UNIVERSITÉ DE STRASBOURG

ÉCOLE DOCTORALE DES SCIENCES DE LA TERRE ET DE L'ENVIRONNEMENT

Institut Terre et Environnement de Strasbourg, UMR7063

En cotutelle avec l'Université de Jilin (Chine)

THÈSE présentée par:

Minghe ZHANG

Soutenue le: **30 Août 2024**

pour obtenir le grade de: **Docteur de l'Université de Strasbourg**

Discipline/Spécialité: **Géophysique**

Techniques for estimating hydraulic parameters of unsaturated soils based on GPR waveform data

THÈSE dirigée par :

M. BANO Maksim	Professeur, Université de Strasbourg
M. FENG Xuan	Professeur, Jilin University

RAPPORTEURS :

Mme. SAINTENOY Albane	Professeur, Université Paris-Saclay
M. LIU Hai	Professeur, Guangzhou University

AUTRES MEMBRES DU JURY :

M. TOUSSAINT Renaud	Professeur, Université de Strasbourg
Mme. LU Qi	Professeur, Jilin University
M. LI Jing	Professeur, Jilin University

Minghe ZHANG

Remerciements

Time flies, and life, in its brevity, spans just a few decades. I've spent nearly thirty years on the path of academics. As I embark on a new chapter at the age of thirty, I am filled with boundless expectations for the future, yet I cannot forget the family, teachers, and dear friends who stood by me during my low moments. Their unwavering encouragement and care have ensured that my journey over these past thirty years was not a solitary one.

First and foremost, I am deeply grateful to my parents. They have been my driving force and my strong support when I felt discouraged. Despite our modest means, my parents never wavered in their support for me. In our rural community, many of their peers are already enjoying a leisurely life. I have sometimes seen the admire in their eyes and asked them about it. Their response has always been, "Don't worry about us. You're grown now, and whatever decisions you make, we trust that you have your reasons." I consider myself incredibly fortunate to have such parents, which is why I was able to pursue multiple international exchanges during my doctoral studies and ultimately earn two PhD degrees. My parents have always told me, "As long as you go high and far, we will support you unconditionally." I am proud to have such parents, and I hope to make them proud in return.

Next, I am thankful to my mentors, Professor Maksim Bano and Professor Xuan Feng. During my doctoral studies, I spent six years in China and two years in France, coinciding with the challenging pandemic period. Regardless of whether I was in China or France, both mentors led by example, generously sharing their academic expertise and providing me with meticulous care in my daily life. From them, I learned invaluable research ethics and virtues, and an earnest and rigorous approach to scientific questions. They taught me never to give up, to face challenges with optimism, and that there is always a solution. I am immensely grateful to my mentors and hope to continue collaborating with them in the future.

I am also indebted to Professor Cai Liu, the leader of group I stayed in China, for his investment and dedication over the years. As a guiding figure, Professor Liu has provided us with an exceptional research and learning environment, offering unwavering support and care both academically and personally. I am grateful and delighted to have had heartfelt conversations with him. Each interaction leaves me in awe of his profound knowledge and provides me with significant insights.

Additionally, I extend my gratitude to Professor Motoyuki Sato of Tohoku University, Japan, who offered me my first opportunity for international exchange. It was an honor to receive guidance from Professor Sato, and I gained firsthand experience of the cultural and scientific differences between countries. This exchange broadened my horizons and enhanced my analytical skills, propelling me further on my scientific research journey.

I am thankful to the members of my doctoral defense and thesis committee, including Professor Renaud Toussaint, Professor Qi Lu, Professor Hai Liu, Professor Jing Li, Professor Albane Saintenoy, for their meticulous guidance and invaluable suggestions, which greatly improved my thesis.

My heartfelt thanks go out to every senior, junior, and peer who has supported me, to my classmates from the class of 2010, to friends both domestic and abroad who aided me during my time overseas, and to my relatives and friends. Every friendship has fueled the sails of my graduation journey, and every act of kindness has laid the foundation for my life's progress.

Words fall short of conveying my immense gratitude to everyone. I wish each of my dear friends to shine brightly on their life paths and to lead a fulfilling and remarkable life!

I acknowledged all the dear teachers and friends:

Baiyu Shi, Benjamin Belfort, Bérénice Vallier, Bingxiu Li, Caihua Liu, Catalina Morales-Yáñez, Cewen Xue, Chaffaut Quentin, Changle Chen, Chao Song, Chao Zhou, Chengcheng Sun, Damian Kula, Dian Wang, Emmanuel Caballero, Enhedelihai Nilot, François Lehmann, Guillaume Modeste, Guodong Jia, Hailong Yu, Han Bai, Han Yu, Hanqing Qiao, Haoqiu Zhou, Honghao Li, Hongxiang Zhu, Huiting Xing, Jean-François Girard, Jianyu Zhao, Jiarun Yang, Josipa Majstorović, Kai Wang, Lilong Zou, Liulei Wang, Mengyan Ding, Neng Lu, Nolwenn Lesparre, Nolwenn Portier, Olivier Razakarisoa, Peihong Xie, Peng Chao, Peng Li, Pengfei Zhao, Qian Liu, Qianci Ren, Qinglin Deng, Shuaishuai Liang, Shuo Pang, Siliang Jing, Silin Wang, Song Cao, Tao Zhang, Teng Luo, Tianshuo Zhao, Ting Liu, Wei Fu, Wenjing Liang, Xianyang Yu, Xiaodan Li, Xiaoman Lu, Xiaoshi Zheng, Xiaotian Li, Xin Wang, Xin Wen, Xinhui Deng, Xuebing Zhang, Xuri Dong, Yafei An, Yang Liu, Ying Wang, Yinghao Zhang, You Tian, Yu Zhang, Yuantao Fang, Yue Yu, Yuheng Wang, Zejun Dong, Zelong Jin, Zhiqi Guo, Zhixi Wang, Zhixin You, Zhixiong Wang, Zhongyu Wei, et al.

Table des matières

Liste des tableaux

Liste des figures

Introduction

0.1 Research background

The Earth’s Critical Zone (CZO) refers to a permeable region near the Earth's surface, which extends from the top of the tree canopy down to the bottom of the groundwater [1-5]. Fig. 0.1 depicts the specific range of the CZO. In this region, extremely complex interactions occur among water, rock, soil, atmosphere, and organisms. These interactions involve multiple fields such as hydrology, geology, and biology, playing a significant role in soil development, water flow and exchange, and chemical and biological cycles. They regulate the natural environment in which organisms and humans live and provide extensive services and essential support for life near the surface, as well as for human daily life and production activities [6]. Therefore, the National Research Council of the United States regards the study of the CZO as one of the most captivating topics in the field of earth sciences in the 21st century. Since 2016, with the initiation of the international collaborative research project between China and the UK on ‘Using Critical Zone Science to Understand Sustaining the Ecosystem Service of Soil and Water’, research on the CZO has begun to develop rapidly in China [7].

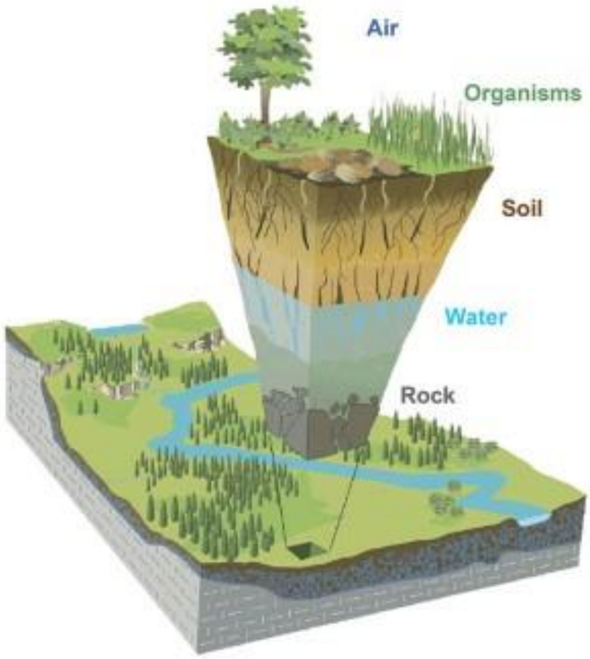

Figure 0.1 The structure of Earth’s Critical Zone [2,5].

Water is the source of life and an indispensable material basis for the survival of plants and animals in nature, as well as for the production and development of human society. With the rapid development of human society, the sustainable use of water resources has come under tremendous pressure. Even though there is a large amount of water on Earth, the available freshwater resources for human daily production and living only account for about 2.5% of the global water volume [8]. About 30% of these freshwater resources are constituted by groundwater [9]. Therefore, groundwater plays an important role in maintaining human survival and development, as well as the sustainable development of the ecological environment.

The vadose zone (also known as the unsaturated zone) is the area between the ground surface and the water table. As a crucial part of Earth's critical zone, the vadose zone controls the exchange of water and energy between surface water and groundwater [10]. In many fields such as hydrology, agricultural science, and soil science, understanding the distribution and changes of soil water in the unsaturated zone is extremely important. The distribution and changes of soil water affect vegetation growth, the transport of underground pollutants, and many aspects of daily human life. Therefore, it has great significance to simulate and predict the dynamic distribution and changes of soil water in the vadose zone.

Soil water content (SWC) and soil hydraulic properties (SHP) are two key factors for characterizing the dynamic distribution and changes of soil water in the unsaturated zone. In traditional hydrology and soil science, SWC and SHP can be determined through laboratory methods [11,12]. However, laboratory methods are often labor- and resource-intensive and may not be representative of real field conditions. It is particularly difficult to obtain soil samples for laboratory measurements when studying deep soil water in the unsaturated zone. Additionally, commonly used methods for measuring SWC and SHP include sensors such as Time Domain Reflectometry (TDR) and neutron probes [13,14]. Although these sensors can accurately determine SWC and SHP, their detection scale is limited and they can be destructive to soil structure. For large-scale assessment of SWC and SHP, remote sensing technology is primarily used. This technology can provide information on SWC and SHP over a large area or even globally. However, the drawback is that the detection depth is relatively shallow, generally only providing information on SWC and SHP within a few centimeters of the surface [15].

In recent decades, geophysical methods have become a very promising technical approaches in the study of soil structure and soil hydrodynamics. Currently, geophysical methods widely used to assess SWC and SHP include Electromagnetic Induction (EMI) [16,17], Electrical

Resistivity Tomography (ERT) [18-21], and Ground Penetrating Radar (GPR) [15,22-25]. Among these, the electromagnetic wave velocity of GPR is very sensitive to changes in SWC. Therefore, GPR technology has become a very promising geophysical method for assessing SWC and SHP. In addition, GPR can provide SWC and SHP information at a medium scale, which fills the gap in measurements of SWC and SHP at this scale [15].

0.2 Objectives and outline

The overall goal of this thesis is to investigate the feasibility for characterizing the soil water dynamics in unsaturated sandy soil, with a particular focus on developing a scheme for estimating and monitoring the SWC and determining the SHP based on time-lapse GPR waveform inversion.

0.2.1 Outline

There are four main research contents:

1. The study proposed a high-precision SWC estimation scheme based on GPR waveform data using the Grey Wolf Optimizer (GWO). We firstly designed three simple four-layer models to perform numerical experiments. The proposed scheme was applied to GPR waveform data both without noise and with noise for high-precision SWC estimation. Then, we established three more complex models, closer to the actual SWC distribution, to perform numerical experiments using the HYDRUS-1D software. Similarly, the proposed scheme was applied to GPR waveform data both without noise and with noise to further study high-precision SWC estimation. Additionally, for the third complex model numerical experiments, we analyzed the uncertainty of GPR data with respect to different inversion parameters (SWC, quality factor, and layer thickness). Subsequently, in order to verify the superiority of the GWO, it was compared with the Particle Swarm Optimization (PSO) Algorithm. Furthermore, we also compared the SWC results based on waveform data and travel time data. Finally, the proposed scheme was applied to the measured GPR waveform data at the Site Contrôlé Expérimental de Recherche pour la réhabilitation des Eaux et des Sols (SCERES) experimental field to test the effectiveness of the proposed scheme.

2. The study investigated the use of time-lapse GPR waveform data for soil water dynamic monitoring. First, we designed two types of experiments to simulate the dynamic changes in

SWC during groundwater level fluctuations and the processes of rainfall infiltration. Then, the time-lapse individual inversion strategy was applied to the measured GPR waveform data from both experiments to monitor the dynamic changes in SWC. However, during the infiltration experiment, we found that the surface soil would first reach saturation. At this point, due to the influence of water, weakening the deeper signal response of the GPR data was weaken, and making it difficult to identify the characteristics of the deeper data. Therefore, a time-lapse double-difference inversion strategy was further applied to monitor the differential changes in SWC at different infiltration times, aiming for more precise dynamic monitoring of SWC during the rainfall infiltration.

3. The study proposed a scheme for direct high-precision estimation of SHP based on GPR waveform data by using GWO algorithm. First, three numerical experiments were designed using the HYDRUS-1D software. The proposed scheme was applied to GPR waveform data without noise and with noise for direct high-precision estimation of SHP. Subsequently, the proposed scheme was further applied to measured GPR waveform data to study the direct high-precision estimation of SHP.

4. The study proposed an improved GWO algorithm to optimize the process for direct high-precision estimation of SHP based on GPR waveform data. It was found that the convergence factor controlling the optimization process of the GWO decreases linearly with the increase in iterations. However, the search process of the GWO does not decrease linearly. In the early stage of GWO, a wide-range global search is ensured, with the convergence curve declining rapidly. In the later stage of the iterations, the convergence curve declines slowly, ensuring local search capability. Therefore, in order to further improve the computational efficiency and accuracy of the GWO, the convergence factor was improved based on the sigmoid function. We test the effectiveness of the improved GWO by using it to optimize the direct high-precision estimation of SHP based on GPR waveform data through three numerical experiments. The results based on the standard GWO were compared with those of the improved GWO. Finally, the improved GWO was applied to measured GPR waveform data to further study its effectiveness.

In order to achieve the overall goal, the thesis is divided into six parts.

The chapter of introduction includes the research background and objectives. We firstly introduced the research background. Then, we summarized the main research contents and the structure of the thesis. Finally, we presented the innovations.

The chapter one firstly introduced the principles of GPR and lists the commonly used GPR systems for SWC estimation. Then, we introduced the main developments of SWC estimation and SHP determination based on GPR.

The chapter two introduced the proposed scheme for SWC estimation based on GPR waveform data using the GWO algorithm. In section 2.1, we presented the petrophysical relationship connecting SWC and relative dielectric permittivity. Then, we described the basic theories for GPR forward modeling which is proposed by Bano in 2004 [26]. Starting from the Maxwell's equation in the time domain in vacuum, the wave equation in frequency domain was derived. Finally, we obtained the GPR echo signals by solving the wave equation and realized GPR forward modeling. In section 2.2, we described the SCERES experimental site where the real data was collected. The RAMAC MALA zero-offset surface GPR system with 500 MHz was used to collected GPR profile. In section 2.3, we designed three simple four-layer model numerical experiments and applied the proposed scheme to both noise-free and noisy GPR waveform data, respectively, to verify the effectiveness of the proposed scheme. Subsequently, we designed three more complex model numerical experiments that better represent the actual distribution of SWC and also applied the proposed scheme to both noise-free and noisy GPR waveform data, further demonstrating the effectiveness of the proposed scheme. In this section, three kinds of parameters were estimated: SWC, quality factor and layer thickness. An uncertainty analysis of the inversion parameters was also conducted for the third complex model numerical experiment. And in order to demonstrate the superiority of the GWO, we compared it with the PSO algorithm. Additionally, we compared SWC estimation results based on waveform data with those based on travel time data, demonstrating that higher-precision estimation of SWC can be achieved based on waveform data. In section 2.4, we further applied the proposed scheme to measured GPR waveform data, also verifying the effectiveness of the proposed scheme.

The chapter three firstly introduced the basic theory of time-lapse inversion in section 3.1, including individual inversion strategy, continuous inversion strategy, and double-difference inversion strategy. Then, in section 3.2 to 3.5, two types of experiments (the imbibition and drainage experiment and infiltration experiment) were designed to simulate the dynamic changes of SWC during groundwater level changes and precipitation infiltration. During the imbibition and drainage experiment, the RAMAC MALA 500 MHz zero-offset GPR system was used to collected GPR profiles. In the infiltration experiment, the RAMAC MALA zero-offset GPR system with 800 MHz was used to monitor the movement of the water. Preliminary results from processed data showed that GPR is an effective geophysical tool for monitoring soil water front. Subsequently, the individual time-lapse inversion strategy was applied to two types of experimental data, successfully monitoring the dynamic changes in SWC. Finally, the double-difference method was introduced for time-lapse GPR waveform data inversion, improving the monitoring accuracy of dynamic changes in SWC during precipitation infiltration by analyzing the differences in SWC at different infiltration times.

In chapter four, we introduced the principles and workflow involved in estimating SHP based on GPR waveform data, including the soil hydraulic model, target function establishment, and improvement strategy of the GWO algorithm based on the sigmoid function in section 4.1. Then, in section 4.2, we designed three numerical experiments and applied the standard GWO algorithm to both noise-free and noisy GPR waveform data to test the effectiveness of the proposed scheme further validating it with real data in section 4.3. In the inversion, the residual SWC, the saturated SWC, and two other soil hydraulic parameters were estimated. Subsequently, the improved GWO algorithm was applied to both noise-free and noisy GPR waveform data for determining SHP in section 4.4. Finally, we compared the results of SHP estimation based on GPR waveform data using the standard and improved GWO algorithms, demonstrating the improvements in computational efficiency and accuracy with the improved GWO algorithm.

In the chapter of conclusions, we provided a comprehensive summary of the thesis and proposed the perspectives for further research work.

0.2.2 Innovations

1. In most current researches, the estimation of SWC based on GPR mainly focuses on utilizing partial information such as travel time or amplitude. In this thesis, we proposed a new inversion scheme to directly estimate SWC based on GPR waveform data. By utilizing the

entire waveform data from the GPR, this proposed scheme improves the accuracy of SWC estimation.

2. During the process of soil water infiltration in the unsaturated zone, the surface soil firstly reaches saturation, making deep GPR signal responses unclear and sometimes difficult to identify. To address this problem, we developed a method for estimating and monitoring changes in SWC using time-lapse GPR waveform inversion based on the double-difference method. By utilizing the differences in data from different infiltration times for inversion, it enhances the ability to extract weak information from deeper layers and improves the monitoring accuracy of changes in unsaturated SWC.

3. In most current researches, the determination of SHP using GPR mainly focuses on utilizing partial information from GPR data, such as travel time information. To improve the efficiency and accuracy of determining SHP based on GPR, this study firstly proposed a scheme for directly determining SHP using GPR waveform data with GWO. Additionally, in the standard GWO, the linear convergence factor does not match the nonlinear update process, leading to local minima and slow convergence speed. In order to address this problem, we proposed an improved GWO based on the Sigmoid function. This ensures a thorough search by the GWO, enhancing both computational efficiency and accuracy of SHP estimation.

Chapter 1 Review of ground penetrating radar applications for water dynamics studies in unsaturated zone

1.1 Principle of GPR

GPR is a non-destructive geophysical detection technology that determines the distribution of underground media based on the propagation of high-frequency electromagnetic waves. It transmits high-frequency electromagnetic waves into the subsurface through a transmitting antenna and receives part of the electromagnetic waves, which have propagated through the underground medium, by a receiving antenna. During the propagation of electromagnetic waves, when encountering subsurface media with different electrical properties, the electrical characteristics of the electromagnetic waves will change. By analyzing the characteristics of the received electromagnetic wave signals (such as changes in waveform, amplitude, and travel time), the structure, depth, spatial position, and morphology of the underground medium can be inferred [27].

Detection depth and resolution are two important factors in estimating the exploration capability of GPR, but they are mutually contradictory. The resolution of GPR is mainly determined by the period of the transmitted pulse, which is controlled by the bandwidth. For a pulse radar system, the bandwidth is generally designed to be the same as the center frequency of the antenna, and the resolution increases with the increase in the center frequency of the antenna. However, due to the influence of the conductivity of the medium, the detection depth of GPR decreases with the increase in the center frequency of the antenna. Therefore, the higher the frequency, the higher the resolution but the shallower the exploration depth. Conversely, the lower the frequency, the lower the resolution but the greater the exploration depth. Thus, it is crucial to find a balance between resolution and exploration in GPR exploration, which is also a significant research challenge. For media with very low conductivity, such as dry sand, a low-frequency GPR system with 50 MHz or 100 MHz is often chosen, which can achieve a detection depth of several tens of meters. When the antenna frequency is 250 MHz or 500 MHz, the detection depth can reach several meters. For a 900 MHz GPR antenna system, the detection depth in dry sand is only a few tens of centimeters [28].

In current research on soil hydrodynamics, the commonly used GPR antenna systems are mainly divided into three categories: surface GPR, borehole GPR, and off-ground GPR. Among them, surface GPR is the most widely used GPR system. In the process of data acquisition, it is directly coupled with the ground, transmitting electromagnetic waves into the ground through a transmitting antenna placed on the surface, and the echoes after the electromagnetic waves propagate underground are received by a receiving antenna, which is also placed on the surface.

Currently, the commonly used observation methods in surface GPR mainly include Common-offset Profiling (COP) or Fixed-offset (FO) measurement, Wide Angle Reflection and Refraction (WARR) measurement, and Common Mid-point (CMP) measurement. Among these, the COP (or FO) is the most commonly used method, as CMP and WARR are more time-consuming and thus less frequently applied. Borehole GPR refers to placing the GPR antenna in a borehole for observations. Compared to surface GPR, borehole GPR can achieve greater detection depth and higher resolution. However, for SWC estimation, borehole GPR can be somewhat destructive to the soil structure and is very time-consuming and labor-intensive. Borehole GPR methods are mainly divided into three categories: Zero-offset Profiling (ZOP) measurement, Multi-offset Profiling (MOP) measurement, and Vertical Radar Profiling (VRP) measurement. Among these, VRP measurement is a single-borehole measurement where the GPR transmitting antenna is placed on the ground and the receiving antenna is placed in a borehole. Compared to the other two measurement methods, VRP is less damaging to the soil and also saves manpower and resources, making it a compromise between surface and borehole GPR. Surface GPR data are affected by direct waves and ground-coupled waves, and cannot effectively observe SWC in the very shallow layers within a few centimeters of the surface. Therefore, off-ground GPR methods, where the radar is suspended in the air at a certain distance from the ground, have emerged. Off-ground GPR collects data at a certain distance above the ground surface, causing less damage to the soil compared to surface and borehole GPR. In addition, off-ground GPR can be mounted on vehicles or low-altitude flight platforms, allowing for rapid, large-area measurements. However, it is significantly affected by terrain, making the elimination of terrain effects a major challenge for off-ground GPR. Fig. 1.1 shows the commonly used GPR systems and measurement modes for different GPR systems.

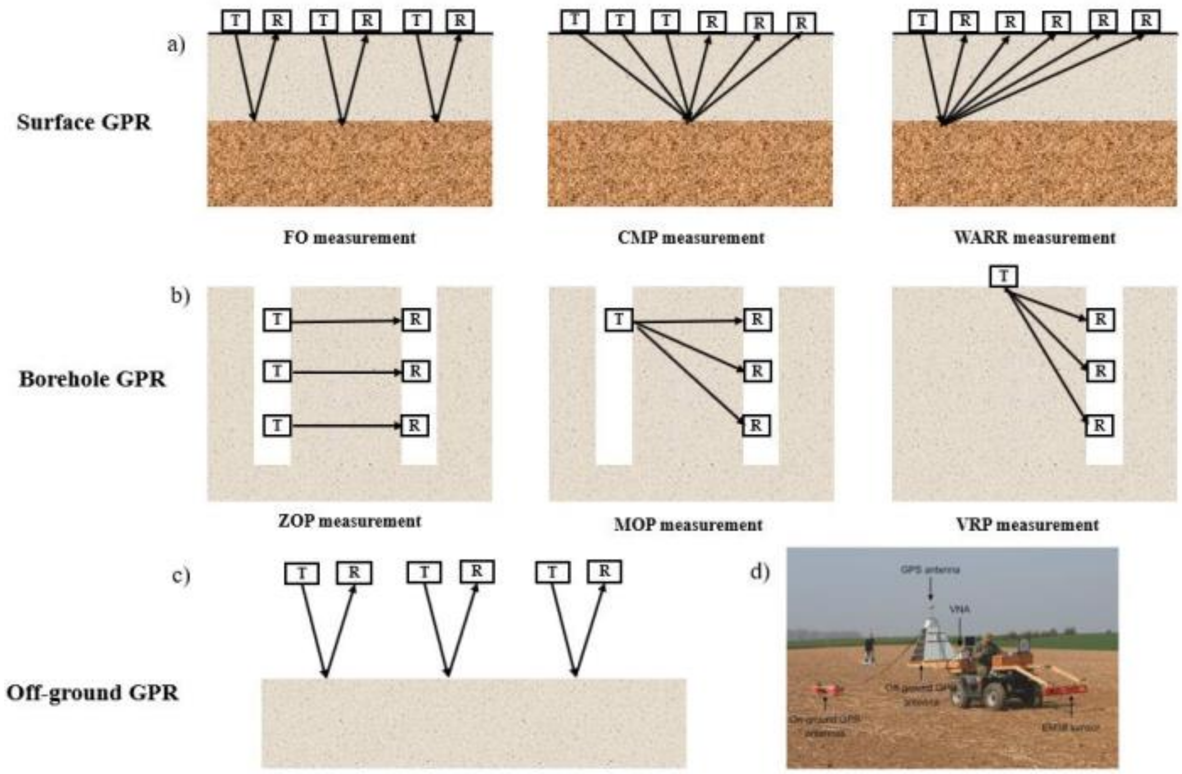

Figure 1.1 Three kinds of commonly used GPR systems in soil hydrodynamic research. a) The surface GPR: FO mode, CMP mode and WARR mode. b) The borehole GPR: ZOP mode, MOP mode and VRP mode. c) The off-ground GPR. d) A field picture presents an off-ground system mounted on a vehicle [15].

1.2 Research developments

Due to the high sensitivity of electromagnetic wave velocity to changes in SWC, the GPR methods have been widely applied in the estimation and monitoring of SWC. There have been several reviews for estimating SWC by GPR [15,28,29]. Table 1.1 summarizes related research work on GPR in SWC estimation and monitoring, which are categorized by antenna structure and observed method. Among them, surface GPR is the earliest and most widely used measured method, followed by borehole GPR. Off-ground GPR is relatively new and, compared to the other two configuration systems, has not yet been widely used in SWC estimation.

Table 1.1 The summary of research development for SWC estimation and monitoring by using GPR.

Configurations of Radar System	**Measured Modes**	**Methods**	**Related References**
Surface GPR	Single Offset	Reflected Wave Method	Vellidis et al., 1990 [30]; Al and Müller, 2000 [31]; Birken and Versteeg, 2000 [32]; Grote et al., 2002 [33]; Gish et al., 2002 [34]; Schmalz and Lennartz, 2002 [35]; Stoffregen et al., 2002 [36]; Loeffler and Bano, 2004 [37]; Makkawi, 2004 [38]; Wollschläger and Roth, 2005 [39]; Lunt et al., 2005 [40]; Turesson, 2006 [41]; Saintenoy et al., 2008 [42]; Irving et al., 2009 [43]; Haarder et al., 2011 [44]; Klenk et al., 2015 [45]; Schmelzbach et al., 2012 [46]; Guo et al., 2014 [47]; Zhang et al., 2014 [48]; Yu et al., 2015 [49]; Shamir et al., 2016, 2018 [50,51]; Ercoli et al., 2018 [52]; Nyquist et al., 2018 [53]; Di Prima et al., 2020 [54]; Mangel et al., 2020 [55]; Zhang et al., 2021a, 2021b [56,57]
		Ground Wave Method	van Overmeeren et al., 1997 [58]; Huisman et al., 2003b [59]; Galagedara et al., 2005b [60]; Grote et al., 2003 [61]; Klenk et al., 2011 [62]; Pan et al., 2012a [23]; Qin et al., 2013 [63]; Ardekani, 2013 [64]; Thitimakorn et al., 2016 [65]
		Average Envelope Amplitude	Pettinelli et al., 2007, 2014 [66,67]; Ferrara et al., 2013 [68]; Algeo et al., 2016 [69]
		Frequency Shift Method	Benedetto, 2010 [70]; Benedetto and Benedetto, 2011 [71]; Benedetto et al., 2013 [72]
	Multi-Offset	Reflected Wave Method	Greaves et al., 1996 [73]; Weiler et al., 1998 [74]; Huisman et al., 2001 [75]; Garambois et al., 2002 [76]; Turesson, 2006 [41]; Strobbia and Cassiani, 2007 [77]; Bradford, 2008 [78]; Gerhards et al., 2008 [79]; Buchner et al., 2011, 2012 [80,81]; Steelman et al., 2012a, 2012b [82,83]; Mangel et al, 2012, 2015 [84,85]; Allroggen et al., 2015 [86]; Iwasaki et al., 2016 [87]; Kaufmann et al., 2020 [88]; Yu et al., 2020 [89]; Saito et al., 2021 [90]
		Ground Wave Method	Huisman et al., 2001, 2002, 2003a, 2003b [28,59,75,91]; Hubbard et al., 2002 [92]; Grote et al., 2003, 2010 [61,93]; Galagedara et al., 2003a, 2005a, 2005b [60,94,95]; Weihermüller et al., 2007 [96]; Steelman et al., 2010, 2012b [83,97]; Thitimakorn et al., 2016 [65]; Cao et al., 2020 [98]
Borehole GPR	Zero Offset		Knoll and Clement, 1999 [99]; Alumbaugh et al., 2000 [100]; Parkin et al., 2000 [101]; Binley et al., 2001, 2002a, 2002b [102-104]; Galagedara et al., 2002, 2003b [105,106]; Rucker and Ferré, 2003, 2004, 2005 [107-109]; Ferré et al., 2003 [110]; Kowalsky et al., 2004 [111]; Looms et al., 2008a [112]; Kuroda et al., 2009 [113]; Wijewardana and Galagedara, 2010 [114]; Haarder et al., 2012 [115]; Klotzsche et al., 2019 [116]; Yu et al., 2020 [89]

	Multi-Offset		Hubbard et al., 1997 [117]; Eppstein and Dougherty, 1998 [118]; Parkin et al., 2000 [101]; Binley et al., 2001, 2002a [102,103]; Galagedara et al., 2002, 2003b [105,106]; Alumbaugh et al., 2002 [119]; Chang et al., 2004 [120]; Deiana et al., 2007 [121]; Looms et al., 2008a [112]; Wijewardana and Galagedara, 2010 [114]; Dafflon et al., 2011 [122]; Haarder et al., 2012 [115]
	Vertical Radar		Knoll and Clement, 1999 [99]; Cassiani et al., 2004 [123]; Dafflon et al., 2011 [122]; Strobach et al., 2014 [124]
Off-ground GPR		Surface Reflections	Chanzy et al., 1996 [125]; Redman, 2002 [126,127]; Serbin and Or, 2004, 2005 [128,129]; Lambot et al., 2004a [130-132]; Weihermüller et al., 2007 [96]; Jadoon et al., 2010 [133]; Minet et al., 2010, 2012 [134,135]; Jonard et al., 2011, 2012, 2013 [136-138]; Tran et al., 2012 [139,140]; Ardekani, 2013 [64]; Moghadas et al., 2014 [141]; Mangel et al., 2015 [85]

1.2.1 SWC estimation with GPR

1.2.1.1 SWC estimation with surface GPR

Surface GPR configuration is the most widely used GPR measurement mode for estimating SWC. In the aspect of technology, the surface GPR includes the most kinds of techniques and is the most comprehensively developed GPR measured mode. Based on measured modes, the surface GPR can be divided into fixed-offset measurement and multi-offset measurement. For each measured mode, there were numerous studies to estimate the SWC based on reflected wave method or ground wave method. Among them, the fixed-offset surface GPR is widely used due to its high measured efficiency compared to multi-offset GPR.

In early studies based on fixed-offset surface GPR, most studies used the reflected wave method to estimate the SWC. For the fixed-offset reflected wave method, a known depth reflector or reflective layer is required to estimate SWC by firstly calculating the velocity of GPR waves from travel time data and then the dielectric constants. Using the depth of the reflector and extracted travel time, the electromagnetic wave velocity in soil and relative dielectric constant can be computed, and then converted into soil moisture content. However, the estimated SWC based on this method is the average SWC between the antenna and the reflector. It is difficult to describe the gradient continuous change of the SWC in detail.

The use of surface GPR for SWC estimation can date back to the 1990s. In 1990, Vellidis et al. [30] realized the monitoring of soil water movement in the unsaturated zone by using fixed-offset surface GPR reflected wave methods. To further quantify the estimation of SWC, Lunt et al. [40] preliminarily calculated the average SWC between the antenna and the reflector by using reflected wave travel time information in 2005. Lateral spatial variation in SWC estimation is a significant challenge in traditional hydrology. In order to observe this variation, two-dimensional, three-dimensional, or even higher-dimensional SWC detection is necessary. In 2000, Birken and Versteeg [32] conducted four-dimensional detection to monitor the change of SWC. To quantify the detection of high-dimensional SWC change, Irving et al. [43] proposed an inversion strategy for quantifying lateral variation of SWC by combining the Markov Chain Monte Carlo (MCMC) method in 2009. In 2012, Schmelzbach et al. [46] proposed an inversion strategy based on GPR reflection amplitude similar to seismic wave impedance inversion techniques to estimate SWC. In 2014, Zhang et al. [48] used time-lapse data from fixed-offset surface GPR reflection waves to monitor seasonal change of SWC. In 2020, Mangel et al. [55] combined automatic GPR data collection technology and reflection wave tomography to estimate the two-dimensional distribution of SWC.

In fixed-offset surface GPR measurement, when direct waves and ground waves can be well separated, it will be a good option by using the ground wave method to measure shallow SWC. The ground wave method estimates the surface SWC through the distance between the transmitted and received antennas and the received travel time information, without requiring a reflector or reflective layer. In 1997, van Overmeeren et al. [58] estimated unsaturated zone SWC by using the ground wave method with fixed-offset surface GPR. In 2005, Galagedara et al. [60] monitored the change of SWC by using the ground wave method with fixed-offset surface GPR. However, in fixed-offset surface GPR measurements, it is difficult to distinguish direct waves from ground waves. Therefore, in order to estimate SWC by using the ground wave method, multi-offset measurement techniques which vary the offset should be employed to collect ground waves for surface SWC measurement and monitoring.

In 1996, Greaves et al. [142] estimated SWC by using CMP velocity analysis techniques with multi-offset surface GPR. In 2012, Mangel et al. [84] extended velocity analysis techniques to the WARR measured mode for the dynamic monitoring of SWC. In multi-offset surface GPR measurement, when a low-velocity layer exists, the guided waves can be generated in the low-velocity layer, significantly reducing the accuracy of SWC estimation based on velocity analysis [143]. In 2007, Strobbia and Cassiani [77] used dispersion analysis techniques to determine SWC through dispersion velocity in the presence of multilayer guided waves. Traditional multi-offset measurement requires moving the antenna for each measurement, which consumes considerable labor and resources. To address the issues of equipment, Buchner et al. [80] designed a multi-receiver GPR measurement system to improve data acquisition efficiency in 2011. Subsequently, a series of multi-receiver systems, including array antenna systems and time-lapse data array monitoring systems, were developed.

In multi-offset measurement modes, the ground wave method is most widely used. Ground wave velocity can be linked to waveform slope. The velocity can be determined and the shallow SWC can be inferred through analyzing the waveform slope. In 2001, Huisman et al. [75] identified ground waves in WARR measurement mode, and inferred SWC by determining ground wave velocity. However, for soils with high electrical conductivity, ground wave attenuation is strong, which will reduce accuracy of estimation. In most cases, ground waves are easily identified in CMP or WARR measurement modes, and thus are still widely used for shallow SWC estimation [60,61,91-93,98].

1.2.1.2 SWC estimation with borehole GPR

Although surface GPR is convenient to operate and causes minimal invasive to the soil, it has certain limitation in the aspect of detection depth. The higher the antenna frequency, the shallower the detection depth. Compared to surface GPR, borehole GPR has a deeper detection depth, which depends on the depth of the borehole. In borehole GPR measurement, the transmitted and received antennas are typically placed in two separate boreholes. By measuring the distance between the antennas and the travel time of electromagnetic waves, the SWC between the two boreholes can be inferred. The borehole GPR methods can be divided into three types: ZOP, MOP, and VRP.

In the ZOP measured mode, the transmitted and received antennas are placed in two boreholes, respectively, and moved simultaneously at the same height during the measurement. This method is relatively simple. In early studies, the SWC between the boreholes could be quickly obtained through the distance between the boreholes and the travel time of direct wave [104,105]. However, in later research, it is found that if the refracted wave propagating along the surface and arrives at the received antenna before the direct wave, which would lead to significant errors in the inverted results. To address this issue, in 2003, Rucker and Ferré [107] proposed using the slope change of travel time and depth to estimate SWC when the refracted wave arrives earlier than the direct wave. Subsequent research further improved the proposed method to enhance the estimation accuracy of SWC, including identifying the travel time of the first arriving refracted wave to improve the accuracy of estimation [108,110]. Recent studies have started using the ZOP mode of borehole GPR for seasonal monitoring of SWC. Under controlled condition of resolution, the ZOP method can provide very detailed information to monitor the spatiotemporal change of SWC. The MOP measured mode has been well applied in obtaining two-dimensional SWC between boreholes. A common method is to improve the estimation accuracy of SWC through tomographic inversion [101,102,112,117,119]. However, since inversion requires a certain amount of times, this method is more suitable for relatively stable soil water condition. The VRP measured mode requires only one borehole, with one antenna fixed on the surface and the other placed in the borehole for data collection. This saves the labor and resources, which makes it considered a compromise between surface GPR and borehole GPR. In 1999, Knoll and Clement [99] demonstrated that VRP method could efficiently and accurately estimate SWC.

Overall, although borehole GPR can achieve the required detection depth, it consumes more labor and resources. Therefore, compared to surface GPR, its application is not as widespread.

1.2.1.3 SWC estimation with off-ground GPR

Compared to surface GPR and borehole GPR, airborne GPR is a relatively new technology for estimating and monitoring SWC. Airborne GPR primarily determine shallow SWC based on the reflection differences between air and surface media. In 1996, Chanzy et al. [125] demonstrated that airborne GPR is a promising method for SWC estimation. Early airborne GPR estimated SWC by measuring the surface reflection coefficient in the time domain [126,128].

In 2004, Lambot et al. [130] proposed a technique for full-wave data inversion in frequency domain by combining airborne ultra-wideband step-frequency continuous wave radar and a monostatic transverse electromagnetic horn antenna. This technique is suitable for large-scale, rapid estimation of SWC distribution. In 2010, Jadoon et al. [133] used this method for field detection and estimation of SWC distribution in agricultural fields. However, this method is susceptible to the influence of surface roughness. In 2012, Jonard et al. [137] considered the impact of surface roughness and made corrections for their effects. Regarding subsequent development of equipment, Moghadas et al. [141] used airborne ultra-wideband step-frequency continuous wave radar with two different frequency bands to determine SWC under condition considering the evaporation of SWC in 2014. In 2015, Mangel et al. [85] introduced a dual-station GPR system, achieving rapid simultaneous acquisition of common offset and common midpoint profiles, thereby improving the monitoring accuracy of soil hydrological process.

1.2.1.4 SWC estimation with other advanced methods

At present, most studies for estimating SWC based on GPR focus on inversion using GPR travel time data, including tomography inversion. However, the variations of SWC not only affect the travel time of GPR data but also affect the amplitude and phase. Therefore, some methods based on GPR amplitude and phase information have also been developed. In surface fixed-offset GPR, it is sometimes difficult to distinguish direct wave and ground wave [61,64]. In 2007, Pettinelli et al. [66] proposed the Average Envelope Amplitude (AEA) method, which determined shallow SWC by analyzing the early amplitude envelope of the signal. In 2013, Ferrara et al. [68] further validated the applicability of this method in clay-rich soils, addressing the inapplicability issues of ground wave and reflectometry methods. In 2023, Lu et al. [144] considered the lateral spatial heterogeneity of SWC and combined the AEA method for large-scale shallow SWC estimation.

The change of SWC also cause the variations in the spectrum of GPR signal. When the SWC increases, the peak frequency of the GPR signal spectrum decreases. In 2010, Benedetto et al. [70] proposed the Frequency Shift method for estimating shallow SWC, which was further applied in agricultural studies for SWC estimation and monitoring [71,72].

With the improvement of computational power, the precision and efficiency of GPR data processing have also been enhanced. The development of GPR full waveform inversion (FWI) has further improved the detection and interpretation accuracy of subsurface medium parameters. The FWI considers the entire GPR waveform information and has been proven to achieve more accurate SWC estimation and monitoring [15]. So far, the determination of SWC using GPR FWI mainly focuses on surface and airborne GPR. In 2004, Lambot et al. [145] proposed building an objective function through the Green's function calculated from waveform to invert subsurface medium parameters based on airborne GPR full waveform data. In 2006, Lambot et al. [131] extended this technique to SWC estimation. In 2007, Weihermüller et al.[96] further applied this technique to SWC estimation based on ground wave data. In 2014, Lambot and André [146] considered that the distance between the airborne antenna and the ground is not very far and further extended this method, proposing SWC estimation based on GPR full waveform data under near-field condition, which improved the accuracy of estimation. However, the above FWI requires calculating the Green's function to construct the objective function. Therefore, in 2021, Zhang et al. [56,57] directly constructed an objective function from GPR waveform data to estimate the SWC.

1.2.2 SHP determination with GPR

SHP is also a crucial factor for studying the soil water dynamics in the vadose zone. It is important to accurately estimate the SHP in various applications including the modeling of soil water and contaminant transport [147,148], and the management of soil and water resources [149]. The research about estimating SHP by GPR can be dated back to 2001 [102]. However, compared to the research about SWC estimation by using GPR, the direct determination of SHP with GPR is still a relatively new technique.

1.2.2.1 SHP determination based on GPR travel time data

To date, most studies on estimating SHP based on GPR have focused on using GPR travel time data. In 2001, Chen et al. [150] used borehole GPR to determine soil hydraulic conductivity in the study area by combining GPR tomography with a Bayesian framework. In 2002, Binley et al. [103] combined GPR with ERT to improve the monitoring accuracy of soil hydrodynamics and the estimation accuracy of soil hydraulic conductivity. SHP estimation based on GPR inversion can be considered as a process to solve an inverse problem. The ill-posed nature and nonlinearity of the inverse problem are inevitable. To deal with these issues, in 2004, Kowalsky et al. [111] proposed an optimization method combining the maximum posteriori probability in statistics, and successfully estimated SHP. In 2020, Cui et al. [151] achieved accurate evaluation of SHP by using data assimilation algorithm.

Time-lapse GPR data can more accurately describe SHP and simulate the change of water flow in the soil. In 2012, Scholer et al. [152] determined the parameters of soil water retention curves (SWRCs) in layered media by using time-lapse GPR data from boreholes combined with the MCMC statistical inversion method. In 2012, Busch et al. [153] predicted water flow and capillary phenomena in the soil based on surface common-offset and multi-offset time-lapse GPR data. They also reduced errors accumulated from multiple forward modeling in the stepwise inversion of SHP based on GPR data through a direct coupled inversion framework.

In addition, early techniques for estimating SHP based on GPR mainly focused on borehole GPR. In 2014, Bradford et al. [154] measured the reflection signals from the soil water transition zone by using surface GPR and found that the transition zone reflection signals were very sensitive to hydrological processes. Since 2014, Léger et al. [155-157] have conducted a series of studies for determining SHP based on surface GPR data and expanded their research to the monitoring of two-dimensional infiltration processes and SHP estimation. In 2018, Jaumann and Roth [24] conducted a series of imbibition and drainage experiment and infiltration experiment, achieving SHP estimation by matching reflection events in the signals. In 2021, Yu et al. [25] compared the stepwise inversion strategy and the coupled inversion strategy of SHP estimation based on GPR, demonstrating that directly inverting SHP through the coupled inversion strategy could avoid the accumulation of errors caused by multiple inversion processes in the stepwise inversion strategy. In 2023, Moua et al. [158] investigate to estimate the hydrodynamic unsaturated soil parameter values and their associated uncertainties based on time-lapse GPR travel time data by using MCMC methods.

1.2.2.2 SHP determination based on GPR FWI

In the area of geophysics, GPR FWI can fully utilize various types of information in GPR data. Compared to inversion that only uses travel time information, GPR FWI improves the accuracy of detection for subsurface targets. In 2006, Lambot et al. [159] proposed a technique for determining shallow SHP based on full waveform GPR data. This technique involves collecting time-lapse data with airborne GPR, then calculating the Green's function of the full waveform GPR data, and finally estimating the shallow SHP by optimizing the objective function constructed based on the Green's function. This method has gradually been applied by many researchers to different field scenarios for validation, achieving the estimation of large-area shallow SHP in the field [160-163]. However, the above studies did not consider the errors caused by the input-output and the model structure itself. Therefore, in 2014, Tran et al. [164] developed a scheme with data assimilation to achieve the determination of SHP. In addition to research on estimating SHP based on airborne GPR full waveform data, in the past decade, inversion based on surface and borehole GPR full waveform data has also gradually been used for determining SHP. In 2013, Dagenbach et al. [165] designed an imbibition and drainage experiment, and applied surface GPR to collect data and estimate SHP. In 2022, Yu et al. [166] began using borehole GPR FWI, establishing an objective function based on GPR waveform data to determine SHP. Numerical experiments verified the effectiveness of the proposed scheme, but it has not been applied to field data.

1.3 Conclusions

In this chapter, we mainly review the development of SWC estimation and monitoring, as well as the development of SHP determination. Firstly, we introduce the principle of GPR including the basic theory of GPR and commonly used GPR measured modes for SWC and SHP estimation. Then, according to the measured modes, we review the development of SWC estimation and monitoring by different GPR systems. Finally, we summarize the development of SHP determination based on different GPR data. The review can give comprehensive understandings for SWC estimation and monitoring, as well as the SHP determination. At the same times, the review provide inspiration for our studies.

Chapter 2 Soil water content estimation by using ground penetrating radar waveform inversion with grey wolf optimizer algorithm

In this chapter, a novel and efficient SWC estimation scheme was proposed based on the GPR waveform inversion with GWO algorithm inspired by the social behavior of grey wolves in nature. In the study of soil water dynamics, GPR is an efficient, nondestructive and promising geophysical technique, which is based on the basic theory of electromagnetic wave propagation. In this chapter, we first introduced the theories used for SWC estimation based on GPR waveform data in section 2.1. In section 2.2, we introduced the SCERES experimental site. In section 2.3, a series of numerical experiments were designed, and the proposed scheme were separately applied to noise-free and noisy GPR data, verifying the effectiveness of the proposed inversion scheme. To further validate the accuracy and efficiency of the proposed scheme, we first compared the results with those based on PSO algorithm, and then compared the results with the inverted results based on GPR travel time data. The results showed that the GWO outperformed the PSO in finding the global optimal solution. In addition, the estimation of SWC based on GPR waveform data was more accurate than that based on GPR travel time data. In section 2.4, the proposed scheme was applied to the real data collected from the SCERES experimental site to further test the applicability of the proposed scheme.

2.1 Theory for SWC estimation based on GPR waveform data

This section starts by introducing the petrophysical relationship which connects SWC and dielectric permittivity, then we present the theories of GPR forward modeling, including Maxwell's equations in time domain and frequency domain. At the same time, this section covers plane electromagnetic wave and the solution to the wave equation. Finally, we introduced the theory of inverse problem and the algorithm used in our study. This section lays a foundation for the subsequent studies.

2.1.1 Petrophysical relationships

The parameter model for forward modeling and inversion in GPR involves the electrical properties of the medium, including relative dielectric permittivity and conductivity. In the forward modeling of GPR, the electrical property model of the medium must first be provided. Then, by solving the electromagnetic wave equation, the forward modeling of GPR is achieved. To study the impact of SWC on GPR data and to evaluate and monitor SWC through GPR data, a petrophysical relationship is required to convert SWC into soil electrical properties. In this study, we did not consider the effect of conductivity and only focus on the relative dielectric permittivity. Compared to conductivity, the relative dielectric permittivity is more sensitive to the change of SWC. This is especially relevant for the characteristic of soil water being continuously distributed in gradients, which sometimes makes the GPR data response very weak and difficult to distinguish. Therefore, the relative dielectric permittivity of the soil, which is highly sensitive to change of SWC, is needed to estimate and monitor the change of SWC.

The Topp equation [167] is a formula that relates volumetric water content to relative dielectric permittivity. As it is derived from fitting a large amount of experimental data from various soils, the Topp equation is generally applicable to most soils. In this study, the Topp equation is used to convert SWC into soil relative dielectric permittivity for the purpose of GPR forward modeling. The most widely used Topp equation is expressed as follows:

$$\kappa = 3.03 + 9.30\theta + 146.00\theta^2 - 76.70\theta^3 \qquad (2.1)$$

where κ is the relative dielectric permittivity and θ is the volume SWC. Fig. 2.1 illustrates the form of the Topp equation, which is a curve showing that the change rate of relative dielectric permittivity accelerates as the increases of volumetric SWC.

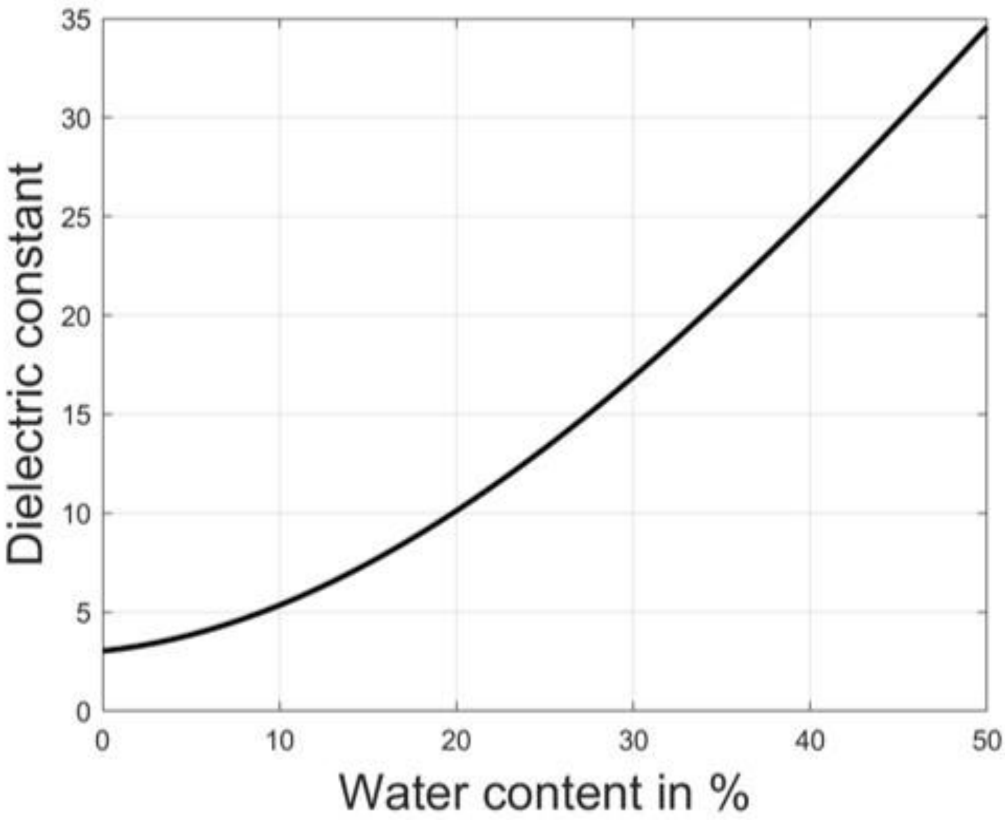

Figure 2.1 The illustration for Topp equation.

2.1.2 Fundamentals of GPR forward modeling

This section mainly introduces the basic theory for GPR forward modeling. First, we introduced the foundational equations for kinematics and dynamics of electromagnetic wave, Maxwell's equations. Then, the electromagnetic wave equation is derived. Finally, by solving the electromagnetic wave equation, we obtained the equations for realizing GPR forward modeling.

2.1.2.1 The time domain Maxwell's equations in vacuum

Based on the fundamental theory of electromagnetic waves, the relationship between the parameters of electric field and magnetic field can be established by using Maxwell's equations [168]. The propagation of electromagnetic waves will consider the variations of these parameters and follow the laws that govern the interactions between electric and magnetic fields. The differential form of time domain Maxwell's equations in vacuum can be expressed as follows:

$$rot\vec{E} = -\frac{\partial \vec{B}}{\partial t} \quad (2.2)$$

$$rot\vec{B} = \mu_0 \left(\vec{J} + \varepsilon_0 \frac{\partial \vec{E}}{\partial t}\right) \quad (2.3)$$

$$div\vec{E} = -\frac{\rho}{\varepsilon_0} \quad (2.4)$$

$$div\vec{B} = 0 \quad (2.5)$$

where $\vec{E}$ $[\mathrm{V \cdot m^{-1}}]$ is the electric field, $\vec{B}\,[\mathrm{T}]$ is the magnetic induction, $\mu_0 = 4\pi \times 10^{-7}$ $[\mathrm{H \cdot m^{-1}}]$ and $\varepsilon_0 = 8.85 \times 10^{-12}$ $[\mathrm{F \cdot m^{-1}}]$ are respectively the magnetic permeability and the dielectric permittivity in the vacuum, $\vec{J}\,[\mathrm{A \cdot m^{-2}}]$ is the vector of current density which is expressed as $\vec{J} = \rho\vec{v}$, ρ is the electric charge density, $\vec{v}$ is the travel velocity of charges, and t $[\mathrm{s}]$ denotes time. The equations (2.2) to (2.5) together express the relationship between magnetic induction and the electric field in vacuum. In fact, they also interact with the surrounding medium. Therefore, when performing the GPR forward modeling, constitutive relations are needed to describe the macroscopic properties of the medium.

2.1.2.2 The time domain Maxwell's equations in medium

In the vacuum, the magnetic field $\vec{H}$ $[\mathrm{A \cdot m^{-1}}]$ and the magnetic induction $\vec{B}$ $[\mathrm{T}]$ are related by the magnetic permeability μ_0, which is expressed as:

$$\vec{B} = \mu_0 \vec{H} \quad (2.6)$$

In the material, the relation of the magnetic field and the magnetic induction still exist. However, the magnetic field element on the right of equation (2.6) includes several magnetic fields. Except the external magnetic field $\vec{H}$, an internal magnetic field, called magnetization $\vec{M}$ $[\mathrm{A \cdot m^{-1}}]$, also has a contribution to the magnetic field element. The magnetization is related to the material and corresponds to the magnetic dipolar moment (linked to each elementary volume of magnetic material) per unit of volume. Therefore, in this case, equation (2.6) can be written:

$$\vec{B} = \mu_0 (\vec{H} + \vec{M}) \quad (2.7)$$

When the magnetization is considered proportional to the magnetic field by the magnetic susceptibility χ_m (without dimension), equation (2.7) will be rewritten as follows:

$$\vec{B} = \mu_0(\vec{H} + \chi_m\vec{H}) = \mu_0(1 + \chi_m)\vec{H} \quad (2.8)$$

Similar to the equation (2.6), we can describe an isotropic medium by using its magnetic permeability $\mu = \mu_0(1 + \chi_m)$. Then the constitutive equation between the magnetic field intensity and the magnetic flux density in a uniform isotropic medium can be obtained:

$$\vec{B} = \mu\vec{H} \quad (2.9)$$

However, except some special minerals like magnetite or hematite, the magnetic susceptibility remains almost zero for most of the underground materials. For GPR detection, the special minerals are rather rare. Therefore, the magnetic permeability of isotropic medium is often considered to be equal to the magnetic permeability in vacuum ($\mu = \mu_0$).

When an electric field is applied to a material, it will cause the appearance of conduction currents due to the movement of free charges. The electrical conductivity $\sigma = [\mathrm{S \cdot m^{-1}}]$ which comes from the generalized Ohm's law relates the electric $\vec{E}$ to a conductive current density $\vec{J_c}$ via:

$$\vec{J_c} = \sigma\vec{E} \quad (2.10)$$

The electrical conductivity is generally a complex parameter $\sigma = \sigma' + \mathrm{i}\sigma''$, σ' represents the real part of the electrical conductivity and σ'' is the imaginary part.

When an electric field is imposed on a rather low-conductive medium (which is also called insulator), there are few free charges. The charges strongly connect with the atoms. The molecules will be distorted by the electric field and the distribution of the charges will also be changed. Therefore, the electric field will change in the dielectric. This phenomenon is called dielectric polarization. In linear, isotropic media, the polarization can be described as the moment vectors. The dipolar moment per unit of volume is called the dipolar vector P which relates to the density of polarization charge by:

$$div\vec{P} = \rho_{pol} \quad (2.11)$$

The dipolar vector can form the electric induction $\vec{D}$ $[\mathrm{C \cdot m^{-2}}]$ by combining with the electric field. The relationship is expressed as:

$$\vec{D} = \varepsilon_0\vec{E} + \vec{P} \quad (2.12)$$

where $\vec{E}$ represents the electric filed and ε_0 is the dielectric permittivity in the vacuum. In the condition of linear and isotropic media, the relation between the dipolar vector and the electric field can be expressed as:

$$\vec{P} = \varepsilon_0 \chi_e \vec{E} \quad (2.13)$$

where χ_e is the dielectric susceptibility of the medium. Therefore, the equation (2.13) can be rewritten as:

$$\vec{D} = \varepsilon_0 (1 + \chi_e) \vec{E} \quad (2.14)$$

Similar to the relation in magnetic field, the dielectric permittivity ε $[\mathrm{F \cdot m^{-1}}]$ can be used to represent the item $\varepsilon_0(1 + \chi_e)$. In other words, the dielectric permittivity, ε, is equal to $\varepsilon_0(1 + \chi_e)$. Therefore, the equation (2.14) can be rewritten as:

$$\vec{D} = \varepsilon \vec{E} \quad (2.15)$$

where the dielectric permittivity is complex $\varepsilon = \varepsilon' - \mathrm{i}\varepsilon''$, ε' represent the real part of the dielectric permittivity, ε'' is the imaginary part.

The equations (2.2) to (2.5) describe the Maxwell's equations in a vacuum, which represent the relationship between the electric field and magnetic flux in a vacuum. By combining equations (2.9) and (2.15), the Maxwell's equations in a medium can be written:

$$rot\vec{E} = -\frac{\partial \vec{B}}{\partial t} \quad (2.16)$$

$$rot\vec{H} = \vec{J_c} + \frac{\partial \vec{D}}{\partial t} \quad (2.17)$$

$$div\vec{D} = \rho \quad (2.18)$$

$$div\vec{B} = 0 \quad (2.19)$$

where ρ_l represents the volume density of free charge.

2.1.2.3 The wave equation in frequency domain

Combining with the constitutive relations, based on equations (2.16) and (2.17), we can obtain the relationship between the electric field intensity and the magnetic field intensity as follows:

$$rot\vec{E} = -\mu\frac{\partial\vec{H}}{\partial t} \text{ ....}(2.20)$$

$$rot\vec{H} = \sigma\vec{E} + \varepsilon\frac{\partial\vec{E}}{\partial t} \text{ ....}(2.21)$$

By taking the curl on both sides of the equation (2.20) and (2.21) simultaneously, we can obtain the electromagnetic wave equations:

$$\Delta\vec{E} = \mu\sigma\frac{\partial\vec{E}}{\partial t} + \mu\varepsilon\frac{\partial^2\vec{E}}{\partial t^2} \text{ ....}(2.22)$$

$$\Delta\vec{H} = \mu\sigma\frac{\partial\vec{H}}{\partial t} + \mu\varepsilon\frac{\partial^2\vec{H}}{\partial t^2} \text{ ....}(2.23)$$

In this study, we only consider the electric field problem. The equation (2.22) represents the control equation for the forward modeling of time-domain GPR.

For a harmonic electric wave $\vec{E}(x, y, z, t) = \vec{E}(x, y, z)e^{-i\omega t}$, we can obtain the wave equation in frequency domain:

$$\Delta\vec{E} + (\mu\varepsilon\omega^2 + i\omega\mu\sigma)\vec{E} = 0 \text{ ....}(2.24)$$

where ω $[\mathrm{rad} \cdot \mathrm{s}^{-1}]$ represents the angular frequency. The equation (2.24) is also called Helmholtz equation of electric field. By introducing the wave number k, the equation (2.24) can be rewritten as:

$$\Delta\vec{E} + k^2\vec{E} = 0 \text{ ....}(2.25)$$

where the wave number $k^2 = \mu\varepsilon\omega^2 + i\omega\mu\sigma$ describes the interactions between the electromagnetic wave and the medium. The equation (2.25) is the control equation for the forward modeling of GPR in frequency domain.

If we suppose that the properties of the medium are real values, we can characterize media in which the nature of currents changes with the signal frequency:

-if $\sigma \gg \omega\varepsilon$, we find $\mu\sigma\omega \gg \mu\varepsilon\omega^2$ and $k^2 \approx i\mu\sigma\omega$. In this condition, the conduction currents predominate, facilitating energy transmission through diffusion. In geophysics, such phenomena are leveraged to assess the subsurface conductivity via methods like magnetotellurics.

-if $\sigma \ll \omega\varepsilon$, we note $\mu\sigma\omega \ll \mu\varepsilon\omega^2$ and $k^2 \approx \mu\varepsilon\omega^2$. The displacement currents dominate, and the energy is transmitted through a propagation mode. The wave equation is used to describe the propagation of electromagnetic waves in GPR.

2.1.2.4 The wave equation in frequency domain

The electromagnetic waves emitted by the source are usually spherical waves. When electromagnetic waves propagate a considerable distance within a medium like the region far from the source, the wave front of the spherical wave can be approximated as a plane wave. Therefore, in a certain sense, complex electromagnetic waves can be considered as composed of multiple plane waves with different frequencies. When the incidence angle of the electromagnetic wave is 0 in GPR and propagates along the z-direction, the solution of equation (2.25) is [26]:

$$E(z,\omega) = E(0,\omega)exp(ikz) = E(0,\omega)\, exp(-\alpha z)\, exp(i\beta z) \qquad (2.26)$$

and k is rewritten as:

$$k = \omega\sqrt{\mu\left(\varepsilon + i\frac{\sigma}{\omega}\right)} = \omega\sqrt{\varepsilon_e\mu} = \beta + i\alpha \qquad (2.27)$$

where α and β are referred to as the factors of attenuation and phase, respectively. $\varepsilon_e = \varepsilon_e' + i\varepsilon_e''$ represents the complex dielectric permittivity. Thus, the first exponential term on the right-hand side of equation (2.26) represents the amplitude attenuation of the electromagnetic wave in the medium, while the second exponential term represents the phase change of the electromagnetic wave in the medium. Therefore, equation (2.26) indicates that the propagation of the plane wave along the z-direction attenuates exponentially according to the attenuation coefficient α, with a phase velocity $V = \omega/\beta$.

Based on the propagation characteristics of electromagnetic waves, when the electrical properties of the subsurface medium change, electromagnetic waves will generate reflection and refraction at the interface of the medium. Ground-penetrating radar utilizes the reflection and refraction properties of electromagnetic waves to achieve propagation of electromagnetic waves within the medium. The reflection coefficient is defined as the dielectric ratio between two media. For non-magnetic materials, the reflection coefficient can be determined by the ratio of the dielectric constants of the two media. Its expression is as follows:

$$R = \frac{\sqrt{\kappa_1} - \sqrt{\kappa_2}}{\sqrt{\kappa_1} + \sqrt{\kappa_2}} \quad (2.28)$$

where κ_1 and κ_2 represent the relative permittivity of two different media. Assuming $E_0(\omega)$ is the complex spectrum of the source wave located at $z = 0$, and a horizontal interface at a depth of $z = z_1$. According to Bano (2004) [26], the complex spectrum of the source wave after being reflected back by the interface can be expressed as:

$$E(\omega, z_1) = G(z_1) R(\omega) E_0(\omega) \exp\left[i \frac{\omega}{V}(2z_1)\right] \exp[-\alpha(2z_1)] \quad (2.29)$$

where G represents geometric attenuation. When $\sigma \ll \omega\varepsilon$, α can be expressed as $\omega/2VQ$, where Q represents the quality factor of the medium. Finally, the echo signal of the GPR can be obtained through the inverse Fourier transform of equation (2.29).

Therefore, the forward modeling of the GPR echo signal is the process of obtaining the GPR received signal by knowing the source wavelet and the electrical characteristics of each medium layer, and calculating parameters such as reflection coefficients. In this study, the dielectric constant is obtained through the SWC, and the GPR received signal is obtained through the above process, achieving the forward modeling of GPR.

2.1.3 Theory of inversion

The purpose of inverse problem is to infer the corresponding system parameters from the observed data in a system. The inverse problem exists in many scientific fields. In geophysics, the inverse problem refers to inferring the parameters of the subsurface medium from the observed geophysical data.

2.1.3.1 The inverse problem in geophysics

In the inverse problem of geophysics, the relationship between the data and the subsurface model is supported by physical theories. In physical theory, the observed data $\mathbf{d}_{\mathrm{obs}}$ and the parameters of the model $\mathbf{m}$ can be related through forward modeling. The relationship can be expressed as follows:

$$\mathbf{d}_{\text{obs}} = \mathrm{F}(\mathbf{m}) \qquad (2.30)$$

where F represents the forward modeling operator.

The solution process of the inverse problem involves solving equation (2.30), which is to estimate the model vector $\mathbf{m}$ from the observed data vector $\mathbf{d}_{\text{obs}}$. In the context of this study, the inverse problem refers to the process of estimating SWC from GPR waveform data.

In general, the solution to the forward modeling problem is deterministic, which means that a unique set of model parameters will yield a unique set of predicted data. However, the inverse problems are typically ill-posed, meaning that a set of observed data may correspond to multiple sets of model parameters, a condition also known as the non-uniqueness of the inverse problem [169]. In addition, in most geophysical inversions, the forward process between the model and the data is nonlinear. Therefore, nonlinear problems are often linearized when using gradient-based optimization algorithms.

The presence of ill-posedness and nonlinearity in geophysical inverse problems is widespread. Therefore, when choosing a solution method, the attributes of the inverse problem itself should be considered to ensure stability, improve solution accuracy, and enhance computational efficiency.

2.1.3.2 The properties of inverse problems

1. Ill-posedness

In practical problems, the solution proper to equation (2.30) does not exist because the physical theory has limitations in describing the real world. The assumption during the forward modeling makes it impossible to accurately reproduce the observed data through numerical modeling. Even if the physical theory is perfect, there is always noise in real data. Therefore, if the theory cannot provide a complete explanation, a true solution cannot be obtained. In this case, the inverse problem can be formulated as inferring the model parameters from the observed data with noise. Due to the presence of noise, equation (2.30) cannot be directly solved. Therefore, an optimization approach is typically employed to solve geophysical inverse problems by transforming them into optimization problems, that is:

$$\mathbf{m} = \min|\mathbf{d}_{\text{obs}} - \mathrm{F}(\mathbf{m})| \qquad (2.31)$$

The equation (2.31) shows that the solution to the inverse problem is to find the parameters of the model m that best explain the data in the sense of a certain norm. The norm measures the distance between the observed data $\mathbf{d}_{\mathrm{obs}}$ and the predicted data $\mathbf{d}_{\mathrm{cal}}$ obtained from the assumed model. Therefore, solving the inverse problem is equivalent to finding the model $\mathbf{m}$ that minimizes the objective function (2.31). In this study, the classical L2 norm based on the Euclidean distance is used to represent the objective function, so equation (2.31) can be transformed to:

$$\Phi(\mathrm{m}) = \|\mathbf{d}_{\mathrm{obs}} - \mathbf{d}_{\mathrm{cal}}\|_2^2 \quad \text{..(2.32)}$$

2. Nonlinearity

If the forward operator F is linear, meaning that the observed data linearly depends on the model parameters, the inverse problem is considered as a linear problem. In the condition of discretization, this linear relationship can be represented by the Jacobian matrix $\boldsymbol{J}$ (or Fréchet derivative). Therefore, the study of linear inverse problems benefits from linear algebra mathematical tools. In particular, the non-uniqueness of the solution can be investigated by examining the kernel (or null space) of the Jacobian matrix [170,171]. Thus, when the L2 norm is used to define the objective function, it behaves as a standard quadratic problem, exhibiting good convexity and uniqueness of the minimum value.

However, most inverse problems are nonlinear. From the perspective of optimization, nonlinearity manifests as the objective function being a multi-valued function, with the presence of multiple local minima (as shown in Fig. 2.2). This effect increases the non-uniqueness of the inverse problem solution and is the main focus of local optimization algorithms. On the other hand, global optimization algorithms treat the solution as a set of possible model parameters, which can avoid the problem of local optimization algorithms getting trapped in local minima [172,173]. For local optimization algorithms, a common operation in practical applications is to linearize the nonlinear problem [174]. Under this assumption, the objective function can be optimized by applying methods for solving linear problems, and obtaining the optimal solution through iterative updates. Therefore, the results of linearized optimization are highly sensitive to the choice of the initial model. As shown in Fig. 2.2, only when the initial model is selected in the same valley as the global minimum, the global optimal solution can be obtained[175]. Otherwise, it may get stuck in a local minimum.

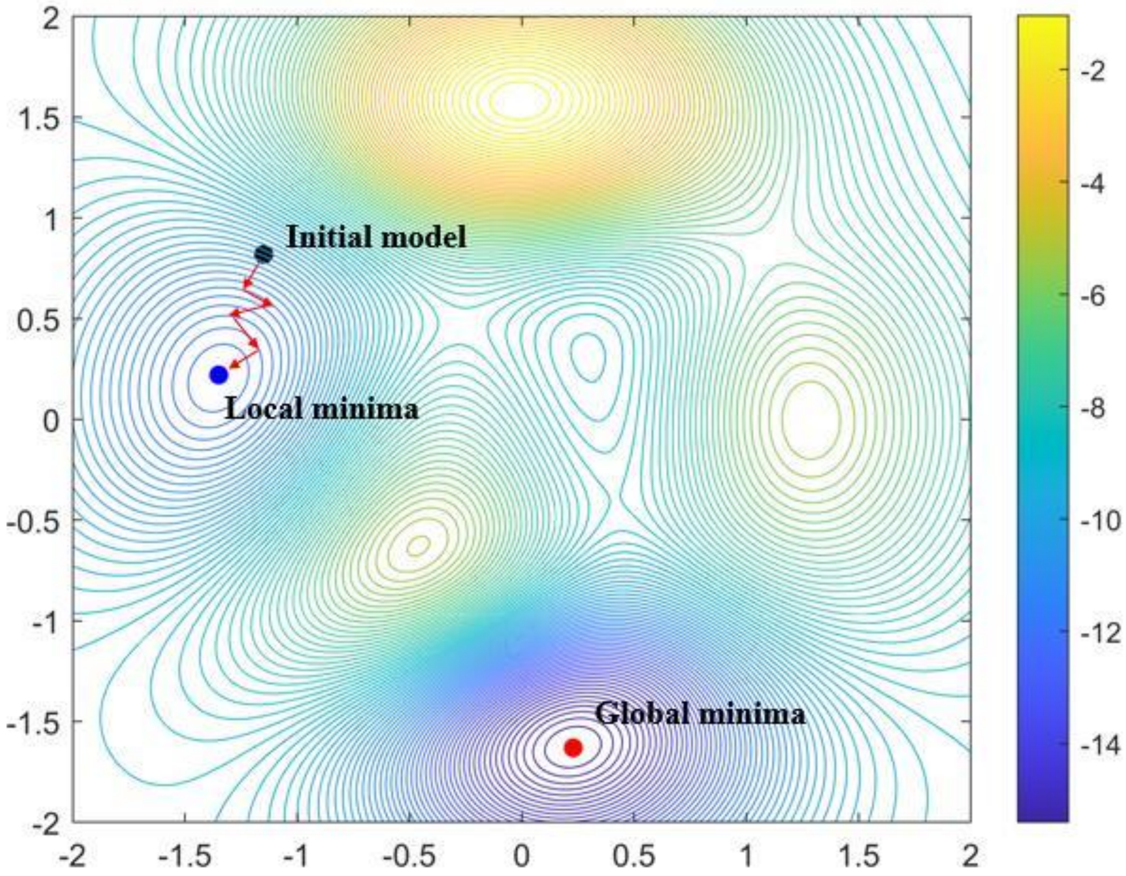

Figure 2.2 The illustration of updating process for local optimization algorithm.

2.1.3.3 The objective function

In real GPR data, the waveform received by the receiving antenna contains information such as the travel time, amplitude, and phase. In this study, we aim to construct the objective function for the inversion problem based on GPR waveform data, in order to fully and effectively utilize the information contained in GPR waveform data and accurately estimate the SWC. Assuming the actual received GPR signal is $\boldsymbol{E}_{obs}$, under the condition of giving the model to be optimized, the forward modeling signal of the model to be optimized, $\boldsymbol{E}_{cal}$, can be obtained through using the relationship between SWC and relative dielectric constant, as well as GPR forward modeling. The objective function of the inversion problem is then defined as the quadratic sum of difference between the measured GPR data and the forward modeling data, as equation (2.33):

$$\Phi(\boldsymbol{\theta}, \boldsymbol{Q}, \boldsymbol{z}) = \|\boldsymbol{E}_{obs} - \boldsymbol{E}_{cal}\|^2 \quad (2.33)$$

where Φ represents the objective function of the inversion problem, while the parameters θ, Q, and z represent the SWC, quality factor, and the layer thickness, respectively.

2.1.3.4 The Grey Wolf Optimizer (GWO)

The GWO is a swarm intelligence optimization algorithm inspired by the hunting behavior of wolves group in nature. Mirjalili et al. (2014) [176] mathematically modeled the natural behavior of wolf populations based on the strict social hierarchy and hunting behavior within a wolf group, and proposed the GWO algorithm. Grey wolves are social animals, and within a wolf group, the most interesting behavior is that the entire population follows a strict social hierarchy, which can be represented by the following structure (as shown in Fig. 2.3).

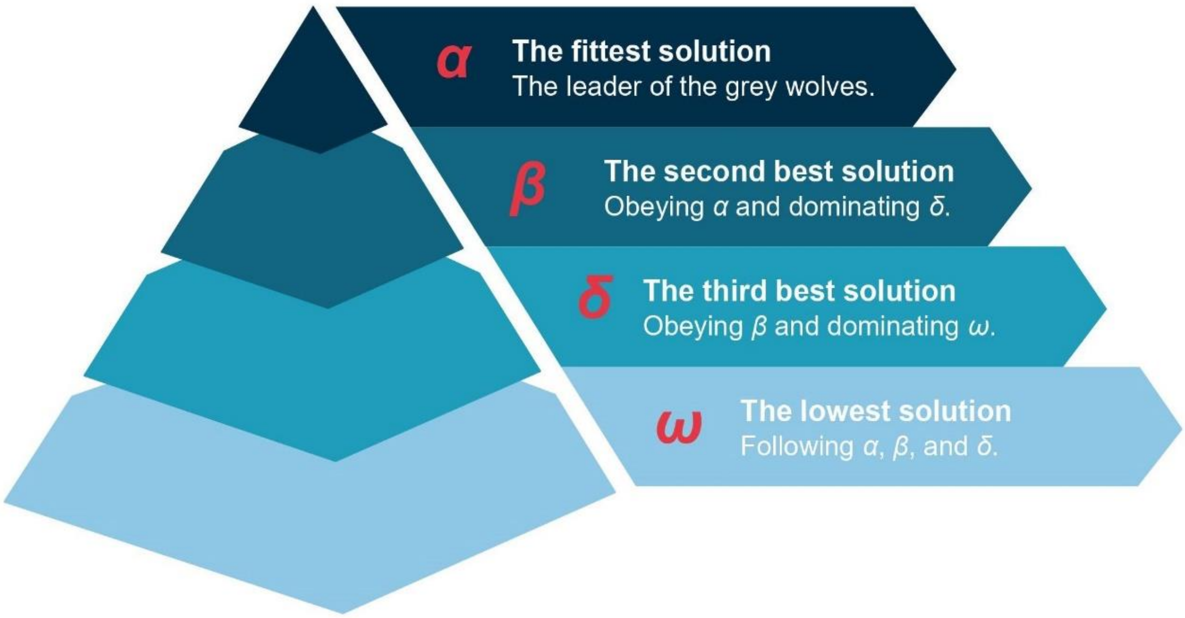

Figure 2.3 The illustration for grey wolf hierarchy (dominance decreases from top to bottom).

In the grey wolf group, there are four classes, represented by α, β, δ, and ω. The first three classes are the leadership hierarchy, with α representing the strongest wolf in the group, responsible for making decisions related to hunting and other survival-related behaviors. The wolves with relatively strong abilities are represented by β, and they assist the α wolf in leading the hunting activities of entire group. The third strongest wolf is the δ wolf, who receives commands from both the α and β wolves, and helps to jointly guide the behavior of the entire group [177]. The ω wolf represents the lowest-ranking wolves in terms of abilities and is also the most numerous in the group. They follow the commands of the top three leaders and participate in the hunting and feeding activities of entire group.

Apart from the strict social hierarchy, another interesting social behavior is the hunting behavior of grey wolves' group. According to Muro et al. [178], the hunting behavior of grey wolves group mainly involves the following stages:

1. Tracking, chasing and approaching the prey

In this stage, the grey wolves group engages in extensive and wide-ranging search within the hunting area to look for potential prey. Once a suitable target is detected, the grey wolves group begins to track the prey. As the grey wolves group reaches the hunting range, they enter the stage of chasing the prey and gradually approach it until a certain distance. In terms of algorithm, this entire process can be seen as the initialization and the initial stage of iteration.

2. Encircling and pursuing the prey

When the prey is driven into the hunting range of the entire wolves' group, according to the leadership mechanism, the leaderships start to command the individual grey wolves with the lowest capability to chase the prey. The prey is forced to move vigorously within the encirclement formed by the wolves. As the vigorous movement reaches a certain degree, the prey's stamina is gradually depleted, and its athletic ability diminishes. The grey wolves' group proceeds to the next step, further narrowing the encirclement to continue exerting pressure on the prey, which causes it to lose further mobility. This enables the subsequent predatory and attacking behavior to take place.

3. Attacking to the prey

After the tug-of-war in the previous two stages, the prey, no matter how large it is, will lose the ability to fight back and escape from the entire wolves' group. Therefore, under the unified command and coordination of the leaderships, the wolves' group will launch an attack and kill the prey. At the end, the entire wolves' group can enjoy a hearty meal. During this attack process, individual wolves in the group update their positions to receive instructions from the leaderships.

Next, we further mathematically formalize the GWO algorithm for optimization. Here is the mathematical modeling of the algorithm:

1. Modeling for encircling prey

In the process of mathematical modeling for the GWO, the social hierarchy of the wolves' group is simulated by defining the most capable α wolf as the optimal solution of the algorithm, while the β and δ wolves are defined as the second and third optimal solutions, respectively. The remaining candidate solutions are represented by ω wolves. In the GWO, the optimization process is directed by the α, β, and δ wolves. From the above analysis, it is evident that the hunting behavior of the grey wolves' group is achieved through individuals gradually encircling their prey. Fig. 2.4 illustrates the process of grey wolves gradually approaching the prey and ultimately surrounding it in a stable structure.

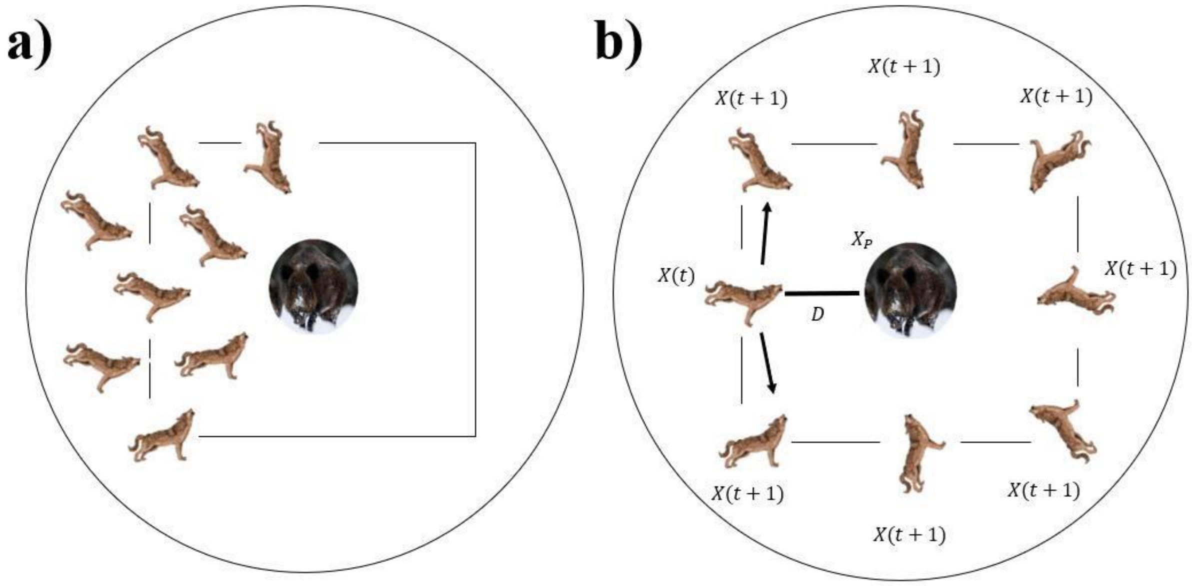

Figure 2.4 Illustration of the process for grey wolves' group to encircle the prey [179].

To describe this encircling behavior from a mathematical perspective, Mirjalili et al. constructed the following formulas:

$$\vec{D} = \left|\vec{C} \odot \vec{X}_P(t) - \vec{X}(t)\right| \qquad (2.34)$$

$$\vec{X}(t+1) = \vec{X}_P(t) - \vec{A} \odot \vec{D} \qquad (2.35)$$

where t represents the current iteration count, $\vec{A}$ and $\vec{C}$ are coefficient vectors, $\vec{X}_P$ represents the prey position vector, $\odot$ stands for term-to-term multiplication, and $\vec{X}$ represents the current position vector of a grey wolf individual.

The coefficient vectors $\vec{A}$ and $\vec{C}$ are calculated by:

$$\vec{A} = 2\vec{a} \odot \vec{r}_1 - \vec{a} \quad (2.36)$$

$$\vec{C} = 2 \odot \vec{r}_2 \quad (2.37)$$

where $\vec{r}_1$ and $\vec{r}_2$ are random vectors uniformly distributed between 0 and 1. Throughout the iteration process, the vector $\vec{a}$ is a control factor that decreases linearly from 2 to 0 as the number of iterations increases. The equation for calculating the vector $\vec{a}$ is given below:

$$\vec{a}(t) = 2 - (2 \times t)/MaxIter \quad (2.38)$$

where t represents the current iteration number and $MaxIter$ represents the maximum number of iterations. Therefore, according to equations (2.36), (2.37), and (2.38), the coefficient vector $\vec{A}$ is a random vector distributed between $-a$ and a, and the coefficient vector $\vec{C}$ is a random vector distributed between 0 and 2.

2. Modeling for hunting

For the hunting behavior of the grey wolves, the strongest α wolf firstly issues commands, followed by random guidance from the second and third leaders in the group. To mathematically simulate the hunting behavior, it is assumed that the α, β, and δ wolves have a very good understanding of the prey's potential location. Therefore, the three best solutions obtained at present will be firstly saved to guide the position updates of the remaining candidate solutions. The entire process is illustrated in Fig. 2.5, and the specific mathematical model is as follows:

$$\vec{D}_\alpha = |\vec{C}_1 \odot \vec{X}_\alpha - \vec{X}|, \vec{D}_\beta = |\vec{C}_2 \odot \vec{X}_\beta - \vec{X}|, \vec{D}_\delta = |\vec{C}_3 \odot \vec{X}_\delta - \vec{X}| \quad (2.39)$$

$$\vec{X}_1 = \vec{X}_\alpha - \vec{A}_1 \odot (\vec{D}_\alpha), \vec{X}_2 = \vec{X}_\beta - \vec{A}_2 \odot (\vec{D}_\beta), \vec{X}_3 = \vec{X}_\delta - \vec{A}_3 \odot (\vec{D}_\delta) \quad (2.40)$$

$$\vec{X}(t+1) = \frac{\vec{X}_1 + \vec{X}_2 + \vec{X}_3}{3} \quad (2.41)$$

where $\vec{C}_1$, $\vec{C}_2$ and $\vec{C}_3$ are calculated by equation (2.37), $\vec{X}_\alpha$, $\vec{X}_\beta$ and $\vec{X}_\delta$ represent the first three best solutions at current iteration t, $\vec{A}_1$, $\vec{A}_2$ and $\vec{A}_3$ are calculated by equation (2.36), $\vec{D}_\alpha$, $\vec{D}_\beta$ and $\vec{D}_\delta$ are calculated by equation (2.34).

3. Modeling for attacking the prey

The behavior of encircling and attacking prey of the grey wolves' group is controlled by the parameters $\vec{a}$ and $\vec{A}$, with the coefficient vector $\vec{A}$ varying with changes in the parameter $\vec{a}$.

According to Mirjalili et al., when $|A| \geq 1$, the GWO primarily conducts a global search, with the parameter $\vec{A}$ controlling the wolves to search for the best possible prey within the search space. This stage is usually referred to as the exploration of GWO. Conversely, when $|A| < 1$, the grey wolves' group is forced into local search, constrained within a known search area for an in-depth search to find the best prey. This process is known as the exploitation of GWO.

Another parameter that plays an auxiliary role in enhancing the search capability of the GWO is the coefficient vector $\vec{C}$, representing the random weight of the prey. When the coefficient vector $\vec{C} > 1$, it indicates that the prey is trying to escape from the wolves' encirclement and attack as much as possible. When $\vec{C} \leq 1$, it suggests that the prey has a low likelihood of escaping from the wolves' encirclement and attack. The coefficient vector $\vec{C}$ determines the random behavior of the prey within the entire search space, with values randomly distributed between 0 and 2. This ensures that the exploration capability is strengthened in the early iterations, while the exploitation capability is also enhanced in the later iterations. Therefore, the random coefficient vector $\vec{C}$ is very helpful in preventing the algorithm from falling into local minima.

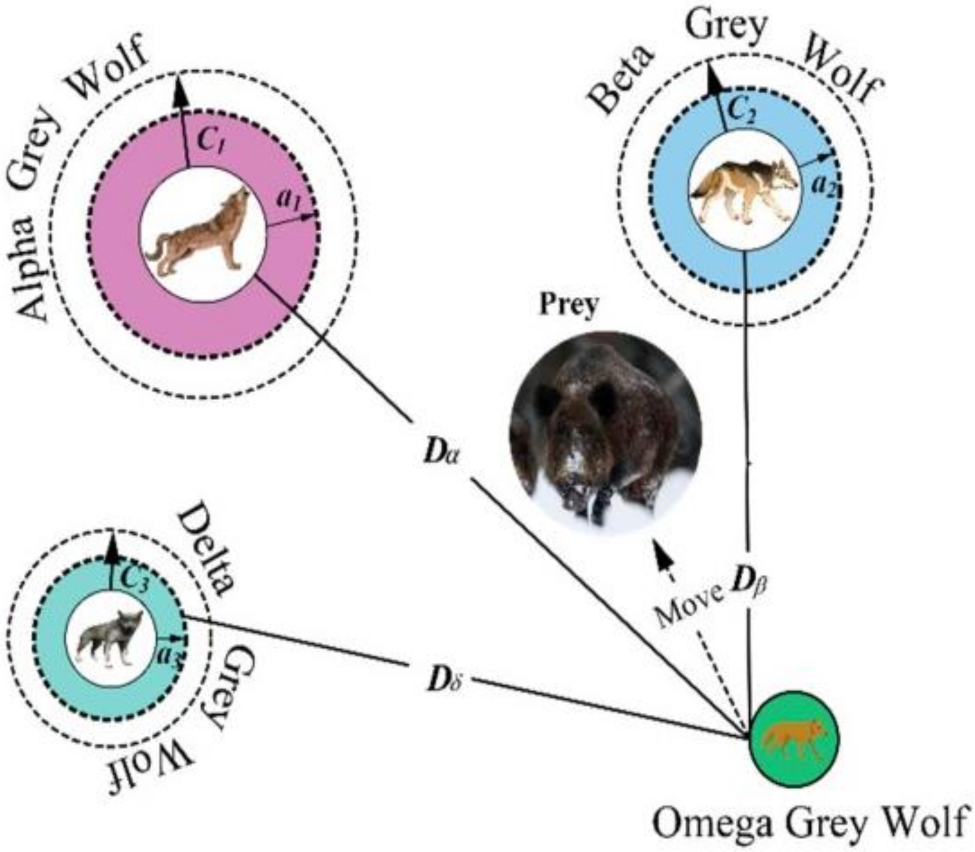

Figure 2.5 The illustration of the hunting process of grey wolves [179].

The flowchart of the GWO is shown in Fig. 2.6. Additionally, to implement the GWO on a computer, we have provided the pseudocode for the GWO as shown in Fig. 2.7.

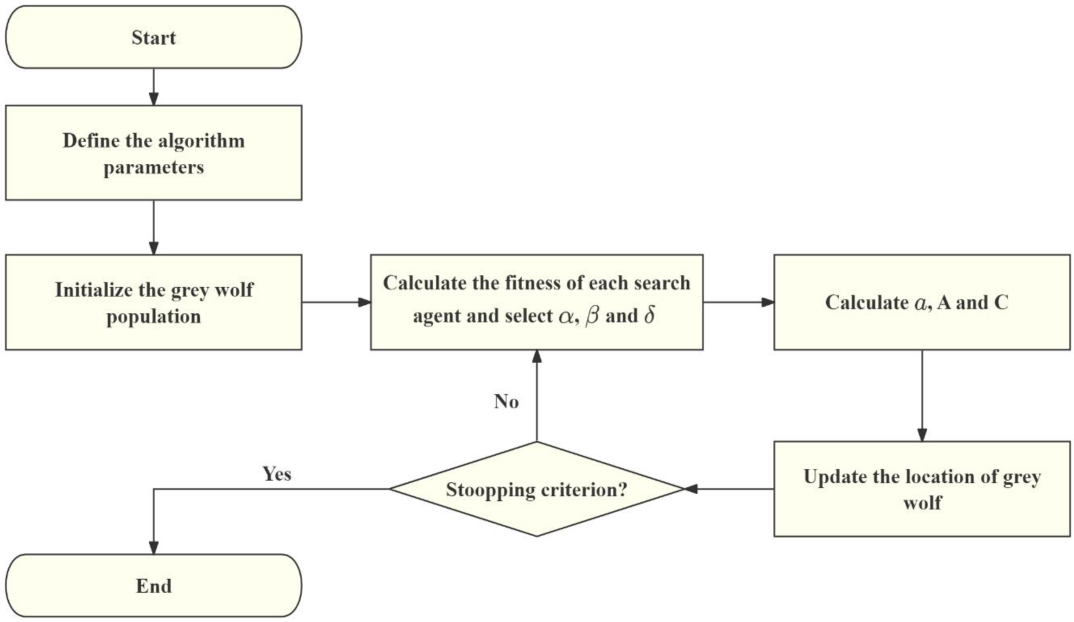

Figure 2.6 The flowchart for standard GWO.

GWO pseudocode:

Initialization of grey wolves' group $X_i (i = 1,2, \dots, N)$ and parameters of a, $\vec{A}$ and $\vec{C}$
Calculating the fitness $f(X_i)$ of individual grey.
X_α=the best grey.
X_β=the second best grey.
X_δ=the third best grey.
  while $(t < t_{max})$
    for $i = 1{:}\,N$
      Update the current position of individual grey according to equation (2.41).
    end
    According to equations (2.38), (2.36) and (2.37) to update parameters a, $\vec{A}$ and $\vec{C}$.
    Calculating the fitness of each grey in the group.
    Updating X_α, X_β and X_δ.
  end
Returning the final X_α and $f(X_\alpha)$.

Figure 2.7 The pseudocode for standard GWO.

2.1.3.5 The workflow for estimating SWC

The key point of inversion process optimization by GWO is to use the established objective function as the fitness function of the optimization algorithm. When the fitness function is updated to the value closest to zero, the optimal position of the grey wolves' group is the final inversion result. Fig. 2.8 describes the process of estimating SWC based on GPR waveform data. In chapter 2 and 3, all the forward modeling and inversion process will obey the following workflow for all the synthetic experiments and real data. The entire process is divided into five steps:

① Select observed data in time domain. For numerical experiments, a SWC model is firstly needed to be established and obtaining electrical parameters used for GPR forward modeling through petrophysical relationships. Then, the waveform data in time domain are obtained through GPR forward modeling and are used as observed data in the inversion process. For actual inversion, the data collected by GPR is the observed data used in the inversion process.

② Set initial model of SWC, quality factor and the layer thickness. Calculate the corresponding electrical parameters based on petrophysical relationships and obtain the GPR waveform data for the theoretical model through forward modeling.

③ Construct objective function based on observed data and calculated data in time domain.

④ Optimize objective function by GWO and update the initial model parameters to make the objective function close to the minimum value.

⑤ Output the final SWC, quality factor and the layer thickness when the iteration stopping criteria are met. Otherwise, return to step 2 and continue iterative updates.

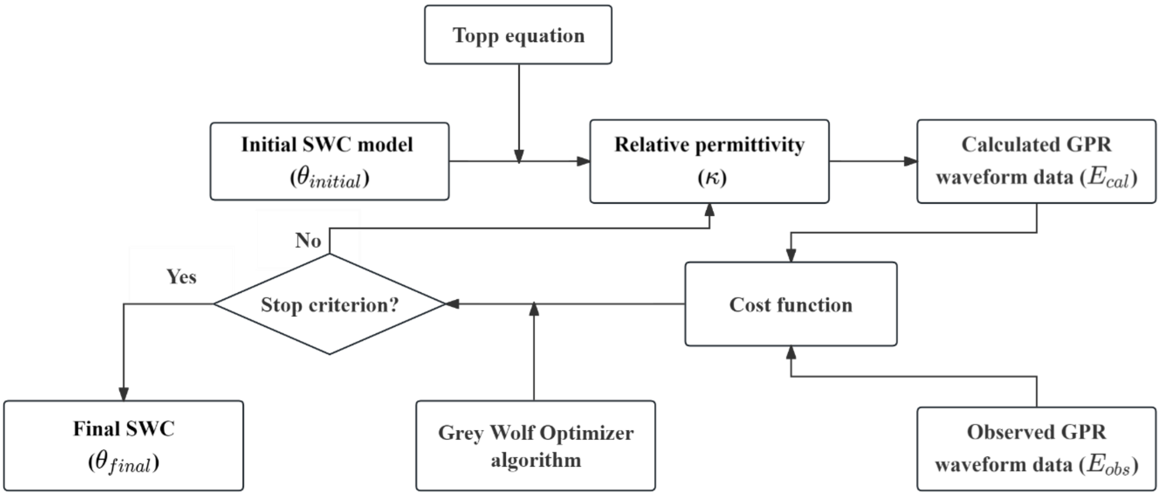

Figure 2.8 The workflow of proposed scheme for SWC estimation based on inversion of GPR waveform data by GWO.

2.2 The SCERES experimental site

To develop methods that improve the quantitative understanding of soil water movement, we collected real GPR data at an experimental site called "SCERES". The SCERES is located at the CNRS campus of the University of Strasbourg in Strasbourg, France. The SCERES is a controlled artificial aquifer contained in a lined concrete sand tank which is specifically designed with a sealant to prevent any leaks to the outside. The inner dimensions of the tank are 25 m in length, 12 m in width and 3 m in depth. Stainless steel partitions are vertically installed 0.5 m from the end walls of the tank. These partitions separate the interior of the tank and can control the water level changes within the tank through two adjustable valves located in the gaps between the partitions and the tank edges. The gaps between the partitions and the tank edges also contain other equipment for managing the aquifer system and monitoring experiments.

The SCERES basin consists of three kinds of medium. The surface layer has the porosity of 43% and the thickness of 0.5 m. The second layer, considered the main medium, has a porosity of 40% and the thickness of 2.0 m. The bottom layer of the basin is a draining layer with a porosity of 38% and the thickness of 0.5 m. Fig. 2.9 shows the field experimental site and vertical distribution of the SCERES basin. From this sketch, the sand tank can be specifically divided laterally into a two-layer area and a three-layer area, which includes a stepped structure. A series of SWC measurement sensors, known as Sentek [180], are installed within the SCERES sand tank. These sensors are used to measure the vertical distribution of SWC and to dynamically monitor SWC changes. This experimental site provides an ideal environment to study and observe the behavior of soil water dynamics and how these changes can be monitored with high-precision equipment.

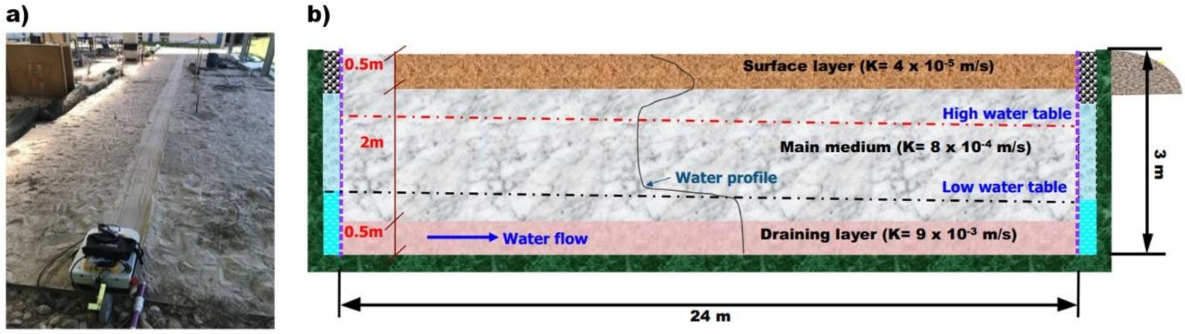

Figure 2.9 a) The illustration of experimental site and setup for data collection. b) The illustration for the subsurface structure of the experimental site. The water is injected and discharged in the third layer to control the water table during monitoring experiments.

2.3 Synthetic data inversion

In order to demonstrate the performance of the proposed scheme, we designed six numerical examples for testing the proposed scheme. The first three models are simple four-layer models used for preliminary performance testing of the proposed scheme. To better approximate the gradient changes in SWC, three nine-layer models were further constructed using HYDRUS-1D hydrological forward modeling software, and the last model was constructed using SWC data measured by Sentek sensors in the experimental field. The six theoretical models are denoted as Models A to F. The schematic diagrams of the specific models are shown in Figs. 2.10b to 2.15b as indicated by the blue dashed lines. For Model A, the SWC gradually increases with depth. In Model B, the SWC of the second layer suddenly decreases, and then gradually increases with depth. In Model C, the SWC increases in the second layer and decreases in the third layer. In Model D, to further approximate changes in SWC, a SWC profile was established using the HYDRUS-1D software. Above 0.65 m, SWC gradually increases with depth. After 0.65 m, the SWC decreases further with depth. This situation simulates the condition when the groundwater table is very deep, and surface water infiltrates to a depth of 0.65 m. For Model E, a SWC profile was also established using HYDRUS-1D software, with the water table at 0.85 m, where SWC gradually increases with depth. Model F uses SWC data measured by Sentek sensors to establish a theoretical underground SWC model, with 0.5 m being the interface between two soil layers in the experimental field. In fact, the experimental field only has three sand layers when divided by the properties of the underground medium. However, even in homogeneous soil, different positions in the soil may have different dielectric constants due to varying SWC, which causes responses in GPR data. Therefore, when inverting the data from the experimental field, we considered this factor. Even though the underground structure is divided into two layers based on medium properties, we divided the initial model's layers based on the different responses caused by varying SWC. Meanwhile, the proposed scheme simultaneously inverts three parameters: SWC, quality factor, and thicknesses of layers. For all the forward modeling in the synthetic experiments, we assumed the GPR system is zero-offset. Because we used the RAMAC MALA GPR system for collecting data, which is also regarded as zero-offset. The parameters for Models A-C are given in the third column of Table 2.1, and the parameters for Models D-F are listed in the second columns of Tables 2.2 to 2.4, respectively.

Table 2.1 The theoretical models' parameters, the search space, the inverted results based on noise free data, the inverted results based on noisy data for Model A to C.

Model	**Number of layers**	**Theoretical models' parameters**		**Search space**		**inverted results based on noise free data**		**inverted results based on noisy data**	
		SWC	z (m)	SWC	z (m)	SWC	z (m)	SWC	z (m)
A	1	0.120	0.300	0.060-0.180	0.150-0.450	0.120	0.300	0.120	0.299
	2	0.196	0.200	0.098-0.294	0.100-0.300	0.196	0.200	0.197	0.203
	3	0.279	0.300	0.140-0.419	0.150-0.450	0.279	0.300	0.288	0.291
	4	0.400	∞	0.200-0.600	∞	0.405	∞	0.415	∞
B	1	0.196	0.300	0.098-0.294	0.150-0.450	0.196	0.300	0.196	0.302
	2	0.120	0.200	0.060-0.180	0.100-0.300	0.119	0.200	0.117	0.199
	3	0.279	0.300	0.140-0.419	0.150-0.450	0.277	0.302	0.288	0.295
	4	0.400	∞	0.200-0.600	∞	0.399	∞	0.402	∞
C	1	0.120	0.300	0.060-0.180	0.150-0.450	0.120	0.300	0.122	0.299
	2	0.279	0.200	0.140-0.419	0.100-0.300	0.281	0.199	0.276	0.202
	3	0.196	0.300	0.098-0.294	0.150-0.450	0.199	0.297	0.194	0.300
	4	0.400	∞	0.200-0.600	∞	0.402	∞	0.418	∞

* SWC represents the soil water content, Q is the quality factor, z represents the layer thickness,∞ stands for the infinite half-space.

Table 2.2 The theoretical models' parameters, the search space, the inverted results based on noise free data, the inverted results based on noisy data for Model D.

Number of layers	**Theoretical models' parameters**			**Search space**			**inverted results based on noise free data**			**inverted results based on noisy data**		
	SWC	Q	z (m)	SWC	Q	z (m)	SWC	Q	z (m)	SWC	Q	z (m)
1	0.167	140	0.150	0.084-0.251	70-200	0.075-0.225	0.167	169	0.150	0.167	200	0.152
2	0.183	130	0.100	0.092-0.275	65-195	0.050-0.015	0.183	85	0.100	0.184	187	0.098
3	0.195	120	0.100	0.098-0.293	60-180	0.050-0.015	0.197	110	0.116	0.197	122	0.147
4	0.202	110	0.100	0.101-0.303	55-165	0.050-0.015	0.202	70	0.073	0.194	119	0.054
5	0.211	100	0.100	0.106-0.317	50-150	0.050-0.015	0.214	70	0.123	0.205	90	0.150
6	0.210	100	0.100	0.105-0.315	50-150	0.050-0.015	0.217	59	0.084	0.212	140	0.053
7	0.104	180	0.100	0.057-0.156	90-200	0.050-0.015	0.102	176	0.099	0.104	146	0.050
8	0.075	190	0.100	0.057-0.113	95-200	0.050-0.015	0.075	196	0.065	0.098	145	0.050
9	0.073	∞	∞	0.057-0.110	∞	∞	0.078	∞	∞	0.072	∞	∞

* SWC represents the soil water content, Q is the quality factor, z represents the layer thickness,∞ stands for the infinite half-space.

Table 2.3 The theoretical models' parameters, the search space, the inverted results based on noise free data, the inverted results based on noisy data for Model E.

Number of layers	Theoretical models' parameters			Search space			inverted results based on noise free data			inverted results based on noisy data		
	SWC	Q	z (m)	SWC	Q	z (m)	SWC	Q	z (m)	SWC	Q	z (m)
1	0.053	195	0.150	0.045-0.080	98-200	0.075-0.225	0.053	119	0.200	0.051	99	0.093
2	0.055	194	0.100	0.045-0.083	97-200	0.050-0.150	0.051	118	0.103	0.045	128	0.146
3	0.058	192	0.100	0.045-0.087	96-200	0.050-0.150	0.050	139	0.058	0.052	105	0.141
4	0.065	190	0.100	0.045-0.098	95-200	0.050-0.150	0.059	156	0.092	0.049	140	0.090
5	0.077	187	0.100	0.045-0.116	94-200	0.050-0.150	0.073	115	0.103	0.058	144	0.095
6	0.104	170	0.100	0.052-0.156	85-200	0.050-0.150	0.099	191	0.104	0.089	173	0.107
7	0.197	130	0.100	0.099-0.296	65-195	0.050-0.150	0.193	94	0.100	0.180	70	0.106
8	0.429	20	0.100	0.215-0.430	20-30	0.050-0.150	0.430	20	0.057	0.417	24	0.119
9	0.430	∞	∞	0.215-0.430	∞	∞	0.430	∞	∞	0.430	∞	∞

* SWC represents the soil water content, Q is the quality factor, z represents the layer thickness, ∞ stands for the infinite half-space.

Table 2.4 The theoretical models' parameters, the search space, the inverted results based on noise free data, the inverted results based on noisy data for Model F.

Number of layers	Theoretical models' parameters			Search space			inverted results based on noise free data			inverted results based on noisy data		
	SWC	Q	z (m)	SWC	Q	z (m)	SWC	Q	z (m)	SWC	Q	z (m)
1	0.090	184	0.150	0.045-0.135	92-200	0.075-0.225	0.090	99	0.150	0.094	92	0.148
2	0.154	150	0.100	0.077-0.231	75-200	0.050-0.150	0.155	164	0.100	0.165	99	0.096
3	0.230	110	0.100	0.115-0.345	55-165	0.050-0.150	0.231	89	0.099	0.246	88	0.096
4	0.278	85	0.100	0.139-0.417	43-128	0.050-0.150	0.280	74	0.102	0.298	65	0.096
5	0.045	195	0.100	0.034-0.068	98-200	0.050-0.150	0.046	110	0.053	0.062	115	0.140
6	0.075	190	0.100	0.038-0.113	95-200	0.050-0.150	0.078	132	0.143	0.038	128	0.067
7	0.196	128	0.100	0.098-0.294	64-192	0.050-0.150	0.188	115	0.099	0.132	113	0.118
8	0.400	20	0.100	0.200-0.460	20-30	0.050-0.150	0.394	25	0.094	0.301	26	0.102
9	0.400	∞	∞	0.200-0.460	∞	∞	0.390	∞	∞	0.299	∞	∞

* SWC represents the soil water content, Q is the quality factor, z represents the layer thickness,∞ stands for the infinite half-space.

2.3.1 Synthetic data of simple models without noise

We firstly tested the proposed scheme on noise-free synthetic GPR waveform data based on simple models. For each numerical model, we conducted 10 tests, with a population size of 320 and 2000 number of iterations. Figs. 2.10a to 2.12a show the noise-free calculated GPR waveform data from three simple theoretical models (Model A, Model B, and Model C) and the observed GPR waveform data the inverted results. From Figs. 2.10a, 2.11a, and 2.12a, it can be seen that the GPR waveform responses from the inverted results (shown by the red solid lines in Figs. 2.10a, 2.11a, and 2.12a) perfectly match the GPR waveform responses from the theoretical models (shown by the blue star dotted lines in Figs. 2.10a, 2.11a, and 2.12a). Moreover, the SWC were also well recovered by using the proposed scheme (shown by the red solid lines in Figs. 2.10b, 2.11b, and 2.12b). The average errors between the three theoretical SWC and the inverted SWC were 0.13%, 0.10%, and 0.17%, respectively.

At the same time, Figs. 2.10d, 2.11d, and 2.12d show the changes of each parameter with the number of iterations. From the parameter variations, it can be seen that in the early stages of the iteration, the parameters are thoroughly searched within the search space, so the range of parameter changes is large. When entering the later stages of the iteration, all parameters tend to stabilize and the range of changes becomes very small, indicating that the parameters are being locally searched within the search space. Finally, each parameter tends towards a constant value. From the convergence curves, it can be observed that all the convergence curves exhibit the typical characteristics of the GWO algorithm. The convergence curves drop rapidly at the beginning of the iterations and gradually converge to zero in the later stages of the iterations. This demonstrates that the GWO algorithm exhibits both the ability to avoid local minima and the property of fast convergence.

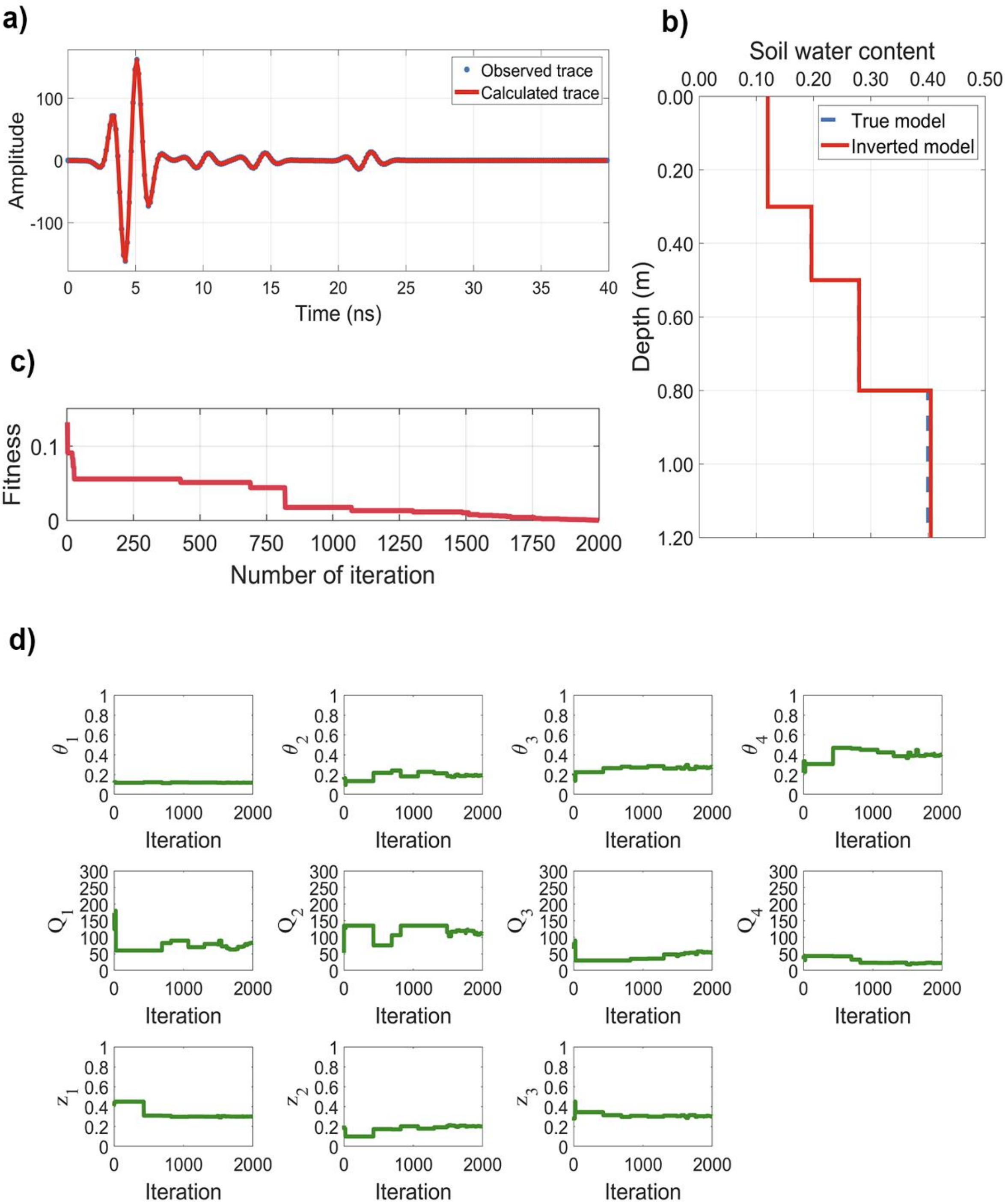

Figure 2.10 The inverted results of noise free data for Model A. a) The noise-free observed data (blue star dotted line) and calculated GPR response (red solid line). b) The true model (blue dashed line) and inverted model (red solid line). c) The fitness curve of iteration. d)-f) The behavior of each parameter versus iteration.

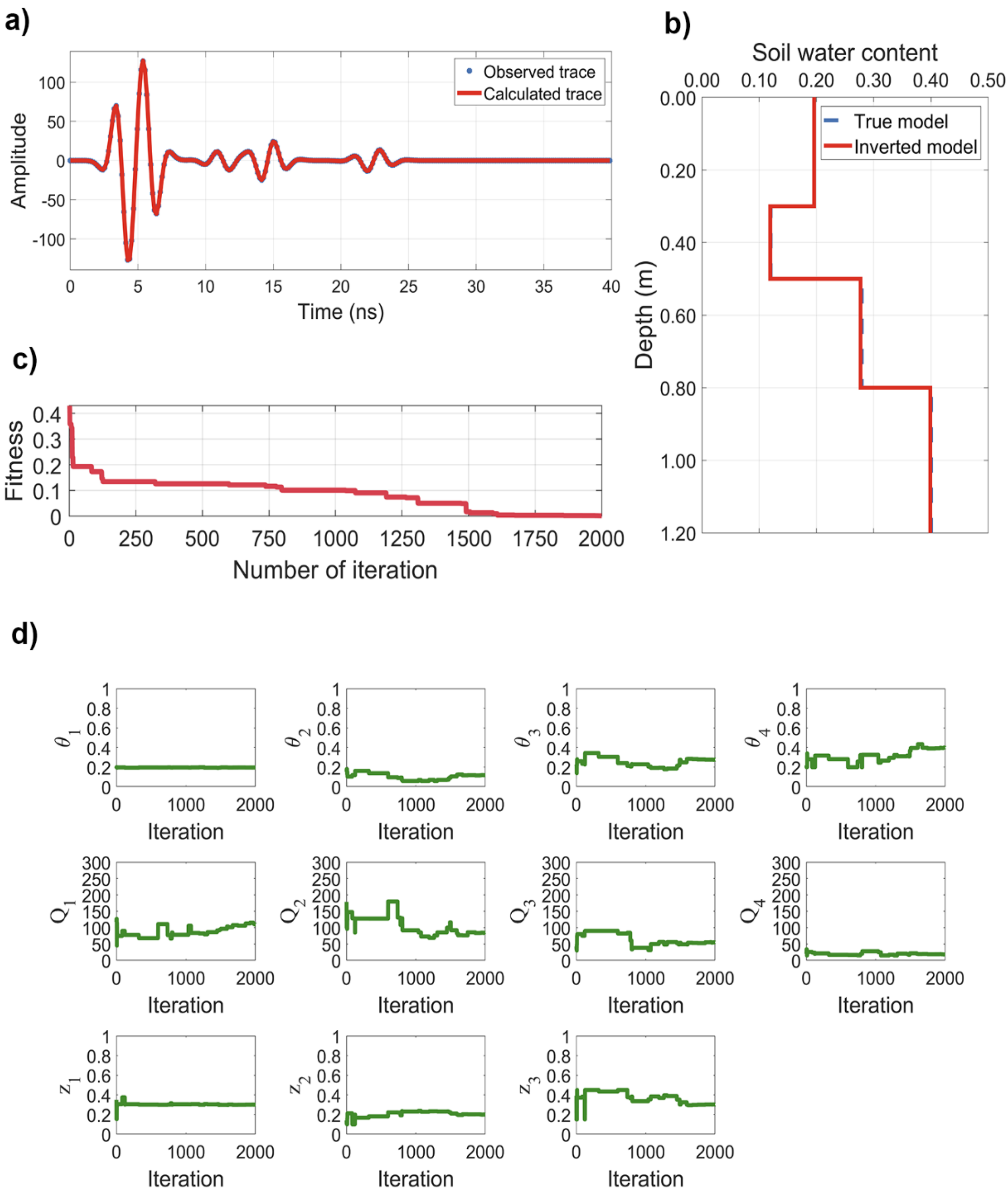

Figure 2.11 The inverted results of noise free data for Model B. a) The noise-free observed data (blue star dotted line) and calculated GPR response (red solid line). b) The true model (blue dashed line) and inverted model (red solid line). c) The fitness curve of iteration. d)-f) The behavior of each parameter versus iteration.

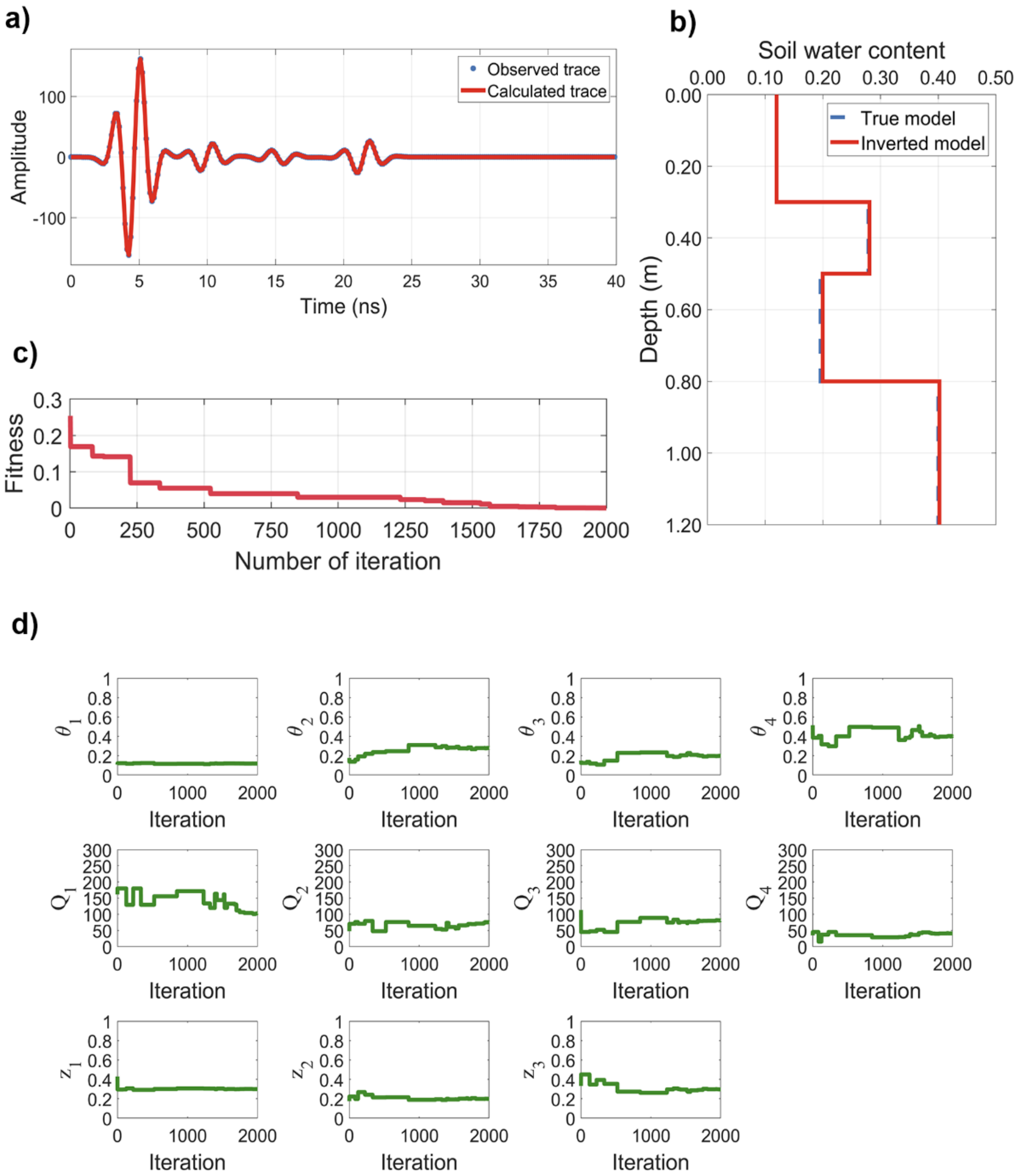

Figure 2.12 The inverted results of noise free data for Model C. a) The noise-free observed data (blue star dotted line) and calculated GPR response (red solid line). b) The true model (blue dashed line) and inverted model (red solid line). c) The fitness curve of iteration. d)-f) The behavior of each parameter versus iteration.

2.3.2 Synthetic data of simple models with noise

In real data, there is noise. To further verify the effectiveness of the proposed scheme, we tested it on synthetic GPR waveform data with noise based on simple models. We added 10% Gaussian white noise to the calculated GPR waveform data from three simple theoretical models. For each numerical model, we still conducted 10 tests, with a population size of 320 and 2000 number of iterations. From the inverted results shown in Figs. 2.13 to 2.15, we found that despite the presence of noise in the data, the proposed scheme was still able to invert SWC well. From Figs. 2.13a, 2.14a, and 2.15a, the GPR waveform responses from the inverted results (shown by the red solid lines in Figs. 2.13a, 2.14a, and 2.15a) still match well calculated GPR waveform responses with noise from the theoretical models (shown by the blue star dotted lines in Figs. 2.13a, 2.14a, and 2.15a). Moreover, for the inverted results using the proposed scheme, the three SWC profiles were still well recovered despite the presence of noise in the GPR data (shown by the red solid lines in Figs. 2.13b, 2.14b, and 2.15b). The average errors between the three SWC models and the inverted SWC were 0.63%, 0.35%, and 0.63%, respectively. Compared to the average errors of the inverted results for noise free GPR waveform data, the average errors of the inverted results for noisy GPR data did indeed increase, indicating a decrease in the accuracy of the inverted results. Table 2.5 lists the comparison of the average errors of the inverted results for the three theoretical models in noise-free and noisy GPR data.

At the same time, Figs. 2.13d, 2.14d, and 2.15d also show the changes of each parameter with the number of iterations. From the parameter variations, it can be seen that, similar to the case in noise free data, in the early stages of the iteration, the parameters are thoroughly searched within the search space, so the range of parameter changes is large. In the later stages of the iteration, all parameters also tend to stabilize, and the range of changes becomes relatively very small. Finally, all parameters tend towards a constant value. From the convergence curves, we can observe that all the convergence curves also exhibit the typical characteristics of the GWO algorithm. The convergence curves drop rapidly at the beginning of the iterations, performing a comprehensive global search, and gradually converge to a constant value in the later stages of the iterations. The results again demonstrate that the GWO algorithm exhibits both the ability to avoid local minima and the property of fast convergence.

Table 2.5 The average errors of inverted results of three simple theoretical models for noise free GPR data and the GPR data with noise.

Type of data	Model A	Model B	Model C
Data without noise	0.0013	0.0010	0.0017
Data with noise	0.0063	0.0035	0.0063

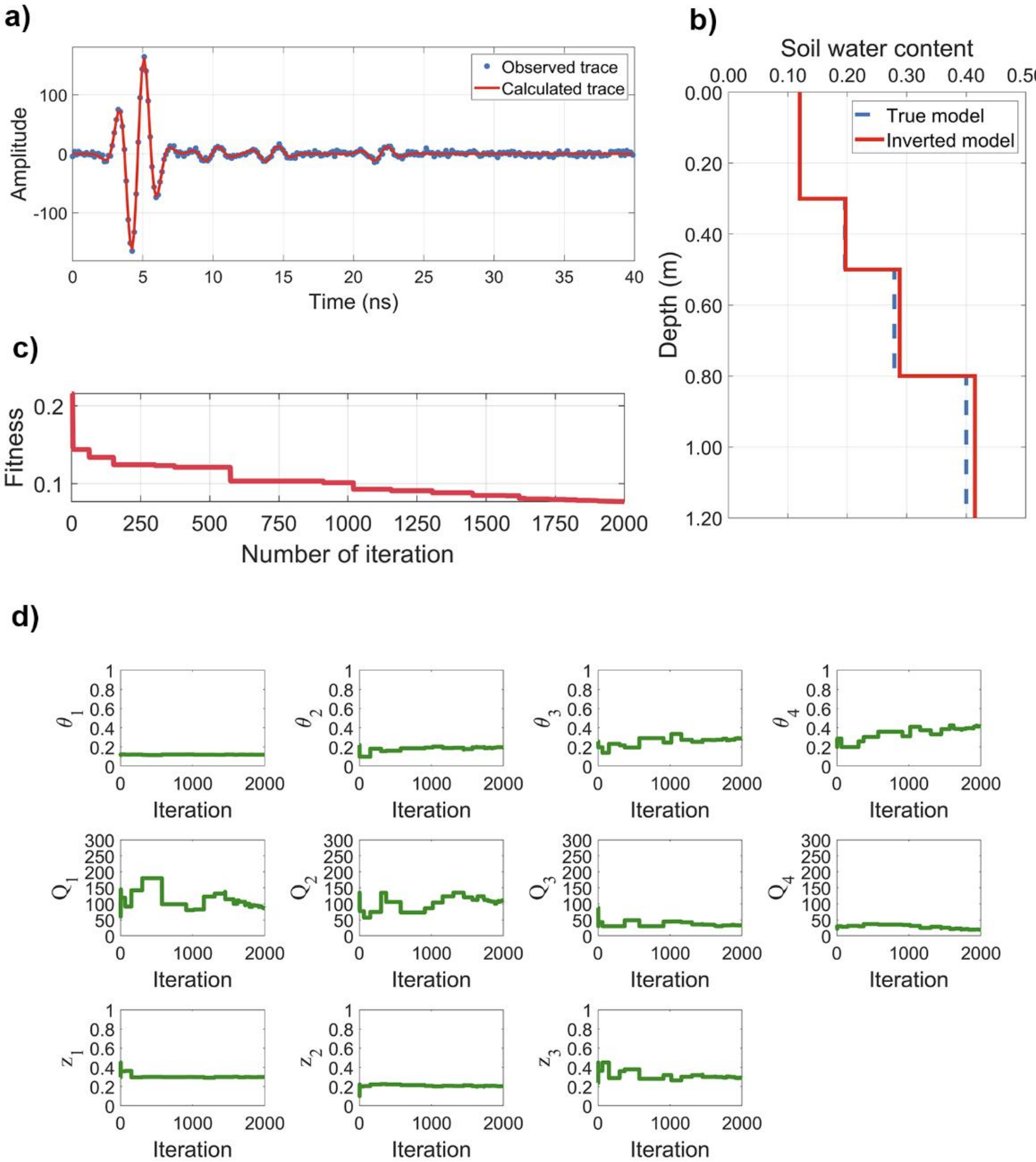

Figure 2.13 The inverted results of data with noise for Model A. a) The noise-free observed data (blue star dotted line) and calculated GPR response (red solid line). b) The true model (blue dashed line) and inverted model (red solid line). c) The fitness curve of iteration. d)-f) The behavior of each parameter versus iteration.

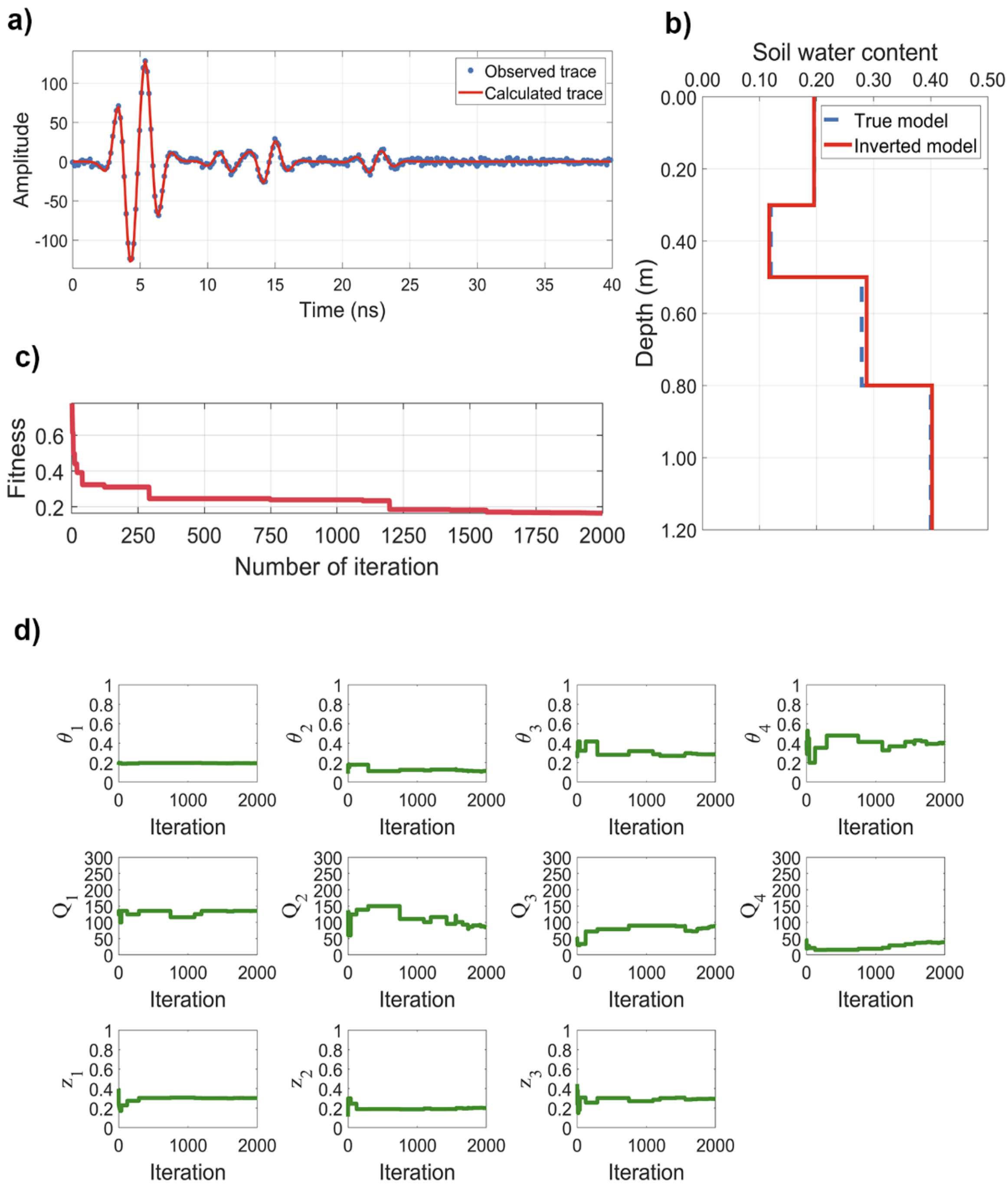

Figure 2.14 The inverted results of data with noise for Model B. a) The noise-free observed data (blue star dotted line) and calculated GPR response (red solid line). b) The true model (blue dashed line) and inverted model (red solid line). c) The fitness curve of iteration. d)-f) The behavior of each parameter versus iteration.

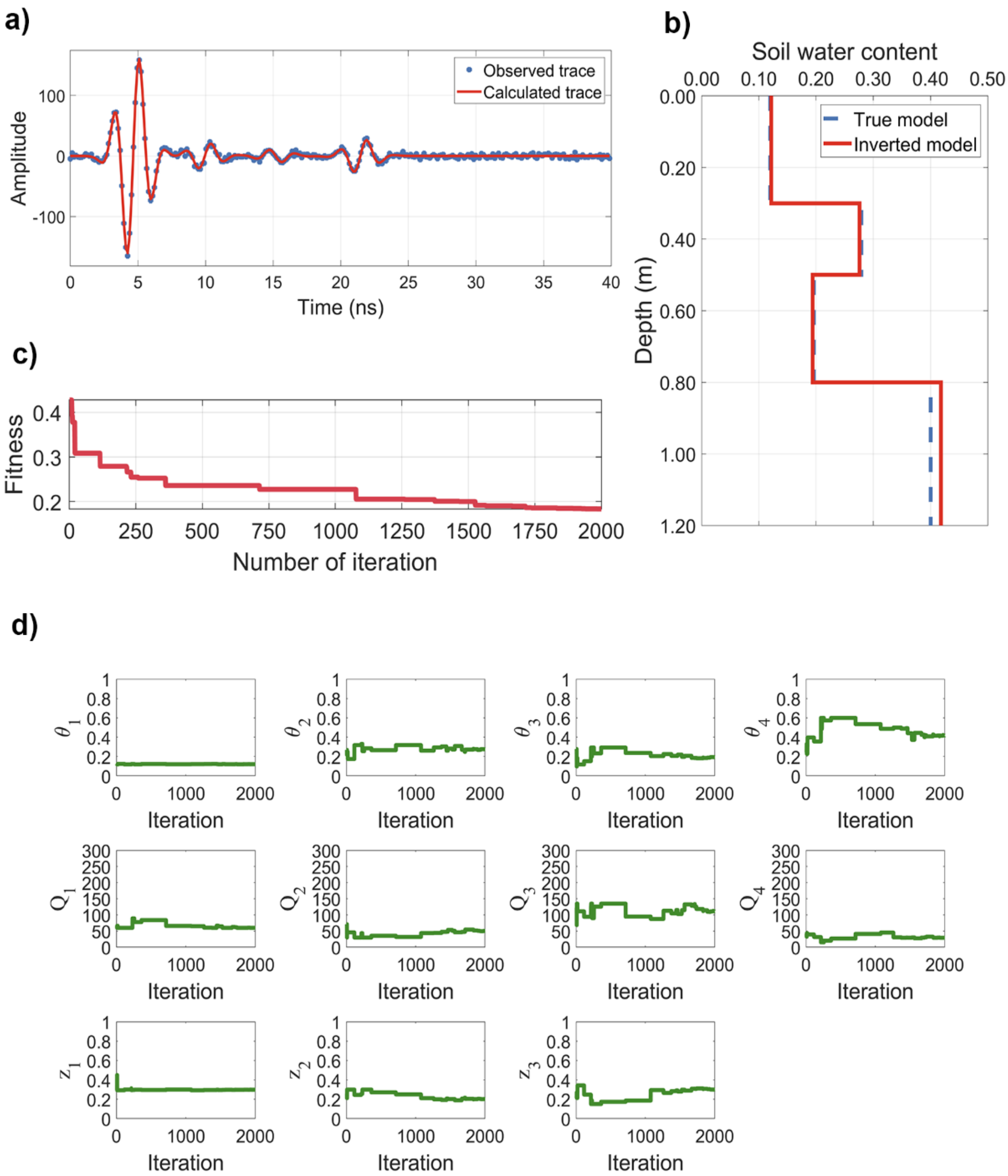

Figure 2.15 The inverted results of data with noise for Model C. a) The noise-free observed data (blue star dotted line) and calculated GPR response (red solid line). b) The true model (blue dashed line) and inverted model (red solid line). c) The fitness curve of iteration. d)-f) The behavior of each parameter versus iteration.

2.3.3 Synthetic data of complex models without noise

In order to more closely approximate the gradient distribution and variation of SWC, we established three more complex multilayer models to test the proposed scheme. Similarly, we first applied the proposed scheme to noise free synthetic GPR data for testing. Each model was tested 10 times. The population size was set to 250, and the number of iterations was 2000. Figs. 2.16 to 2.18 show the three noise-free calculated GPR data from models D, E, and F, as well as the inverted results. From Figs. 2.16a, 2.17a, and 2.18a, it can be seen that the calculated GPR waveform responses from the inverted results (shown by the red solid lines in Figs. 2.16a, 2.17a, and 2.18a) almost perfectly match the observed GPR waveform responses from the theoretical models (shown by the blue star dotted lines in Figs. 2.16a, 2.17a, and 2.18a).

From the inverted results, it can also be observed that the three theoretical models are well recovered (shown by the red solid lines in Figs. 2.16b, 2.17b, and 2.18b). The overall average errors between the theoretical models and the inverted results are 0.016, 0.047, and 0.018, respectively. These results further demonstrate the capability of the proposed scheme to invert SWC from GPR waveform data. The relationship between each parameter and the number of iterations is shown in Figs. 2.16d-f, 2.17d-f, and 2.18d-f. Similarly, the variation of each parameter with the number of iterations was studied. Due to the large number of parameters, similar parameters are plotted on the same graph, with different colored lines representing different parameters. It can be seen that all parameters eventually converge to a stable value, indicating that the proposed scheme can find the appropriate parameter combination during the inversion process. Likewise, from the convergence curves, we can observe that even with increased model complexity, all convergence curves still exhibit the typical characteristics of the GWO algorithm. The convergence curves drop rapidly at the beginning of the iterations and gradually converge to zero in the later stages, indicating that the GWO algorithm has the ability to avoid local minima and converge rapidly.

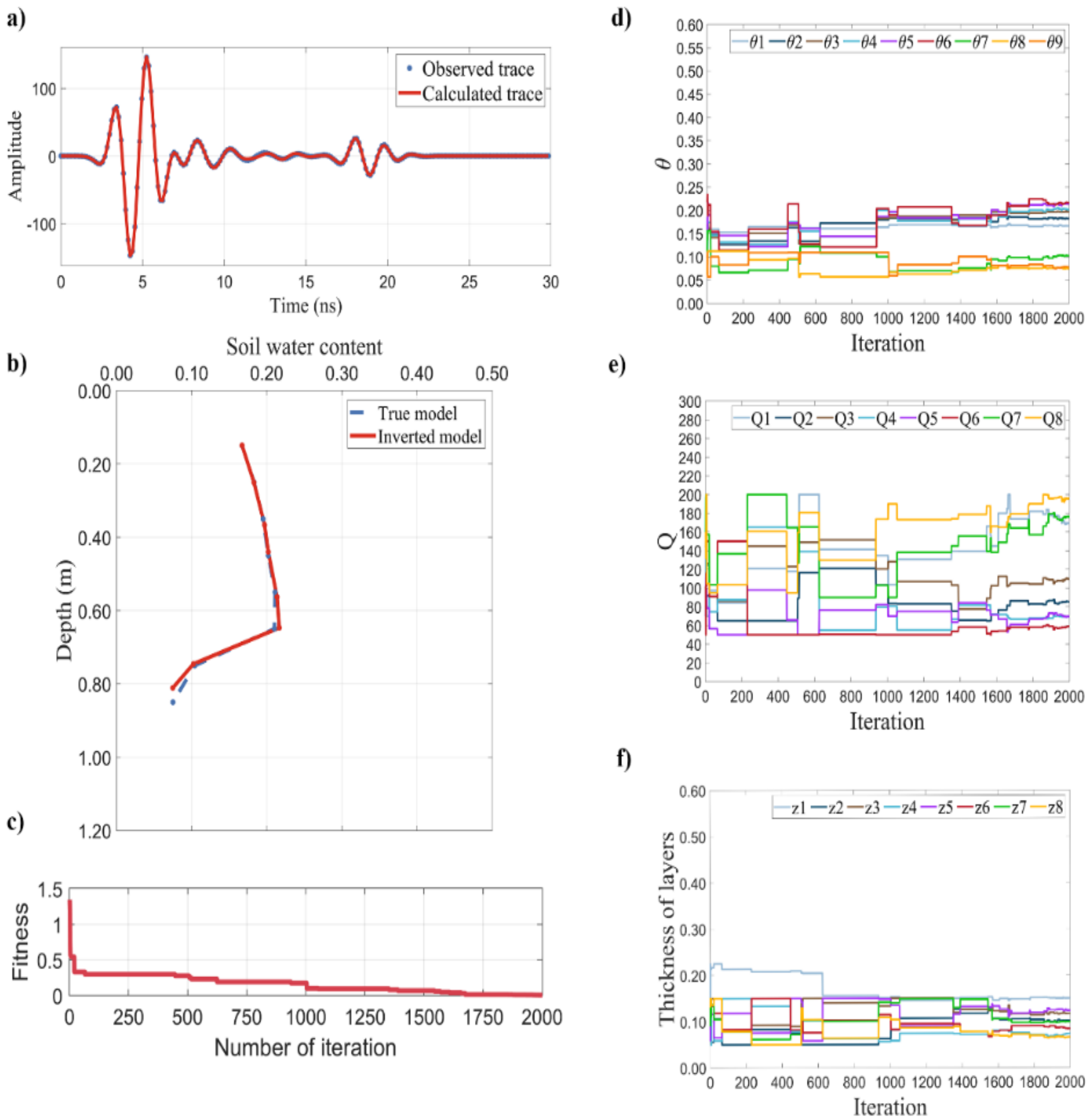

Figure 2.16 The inverted results of noise free data for Model D. a) The noise-free observed data (blue star dotted line) and calculated GPR response (red solid line). b) The true model (blue dashed line) and inverted model (red solid line). c) The fitness curve of iteration. d)-f) The behavior of each parameter versus iteration.

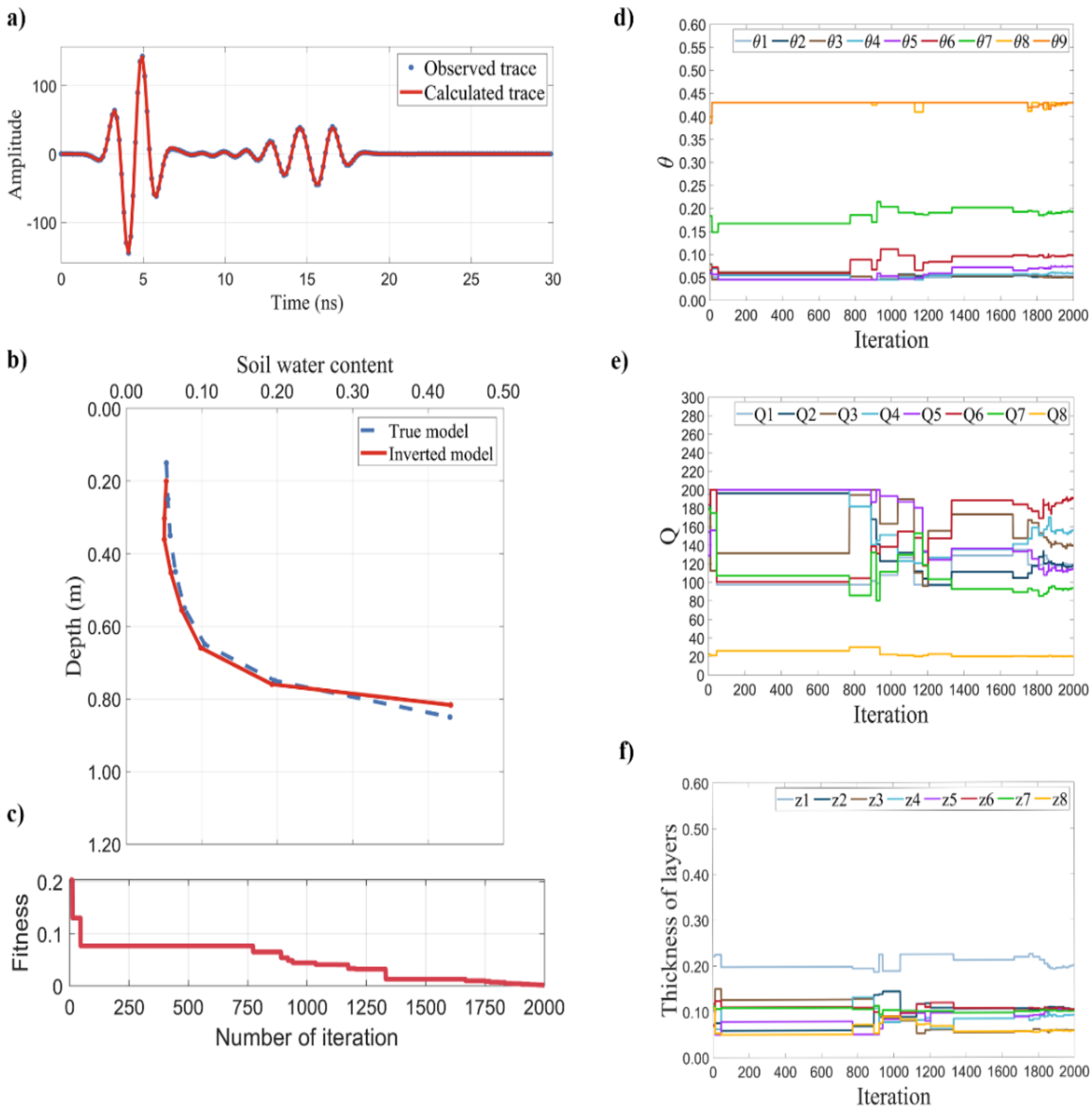

Figure 2.17 The inverted results of noise free data for Model E. a) The noise-free observed data (blue star dotted line) and calculated GPR response (red solid line). b) The true model (blue dashed line) and inverted model (red solid line). c) The fitness curve of iteration. d)-f) The behavior of each parameter versus iteration.

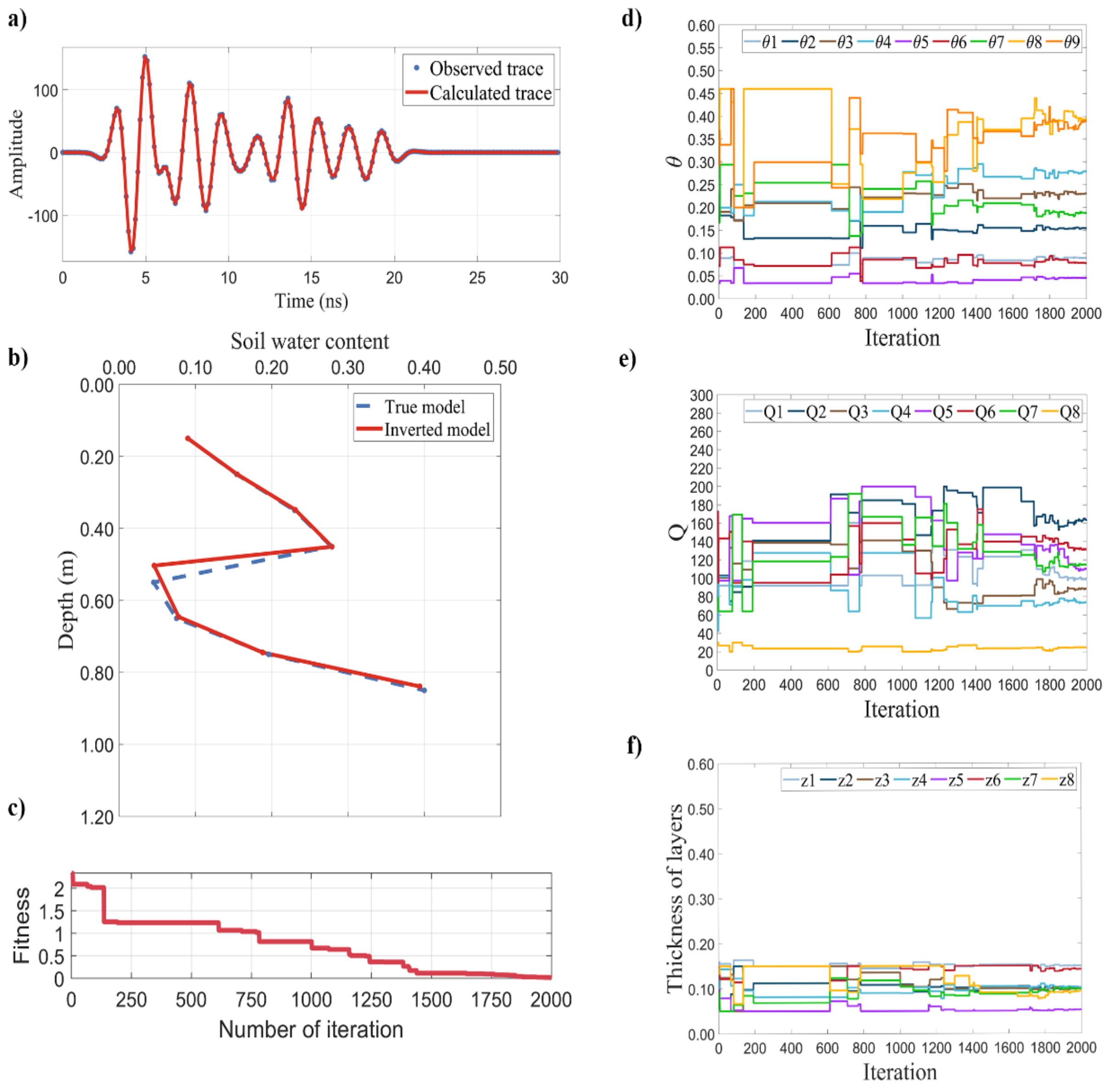

Figure 2.18 The inverted results of noise free data for Model F. a) The noise-free observed data (blue star dotted line) and calculated GPR response (red solid line). b) The true model (blue dashed line) and inverted model (red solid line). c) The fitness curve of iteration. d)-f) The behavior of each parameter versus iteration.

2.3.4 Synthetic data of complex models with noise

Similarly, we tested the proposed scheme on synthetic GPR data with noise. We added 10% Gaussian white noise to the GPR waveform data obtained from the forward modeling of these three complex models. Figs. 2.19 to 2.21 show the inverted results in relatively more realistic scenarios. We can still see that, despite the complexity of the model and the presence of noise in the data, the proposed scheme remains robust. We can still obtain the acceptable solutions through the proposed scheme. The calculated GPR waveform response obtained from the inverted results (indicated by the red solid lines in Figs. 2.19a, 2.20a, and 2.21a) still matches the observed GPR waveform response obtained from the forward modeling of the complex theoretical models (indicated by the blue star dotted lines in Figs. 2.19a, 2.20a, and 2.21a). Despite some minor differences in the final results, the proposed scheme can still effectively invert the SWC from the GPR waveform data (indicated by the red solid lines in Figs. 2.19b, 2.20b, and 2.21b). The overall average relative errors between the complex theoretical models and the inverted results are 0.046, 0.152, and 0.217, respectively. These results demonstrate that, despite the presence of noise in the data, the proposed scheme is capable of correctly inverting the SWC based on the GPR waveform data. From the behavior of each parameter with the number of iterations (Figs. 2.19d-f, 2.20d-f, and 2.21d-f), it can still be seen that all parameters eventually converge to stable values. However, compared to the inverted results based on noise free data, the accuracy and consistency of the inverted results with noisy data have decreased. This may be attributed to the interference caused by the presence of noise in the data, making it more complex to extract accurate information from the data. Table 2.6 lists the average errors of the inverted results for the three complex theoretical models for noise free GPR data and the GPR data with noise.

Table 2.6 The average errors of inverted results of three complex theoretical models for GPR data without noise and the GPR data with noise.

Type of data	Model D	Model E	Model F
Data without noise	0.016	0.047	0.018
Data with noise	0.046	0.152	0.217

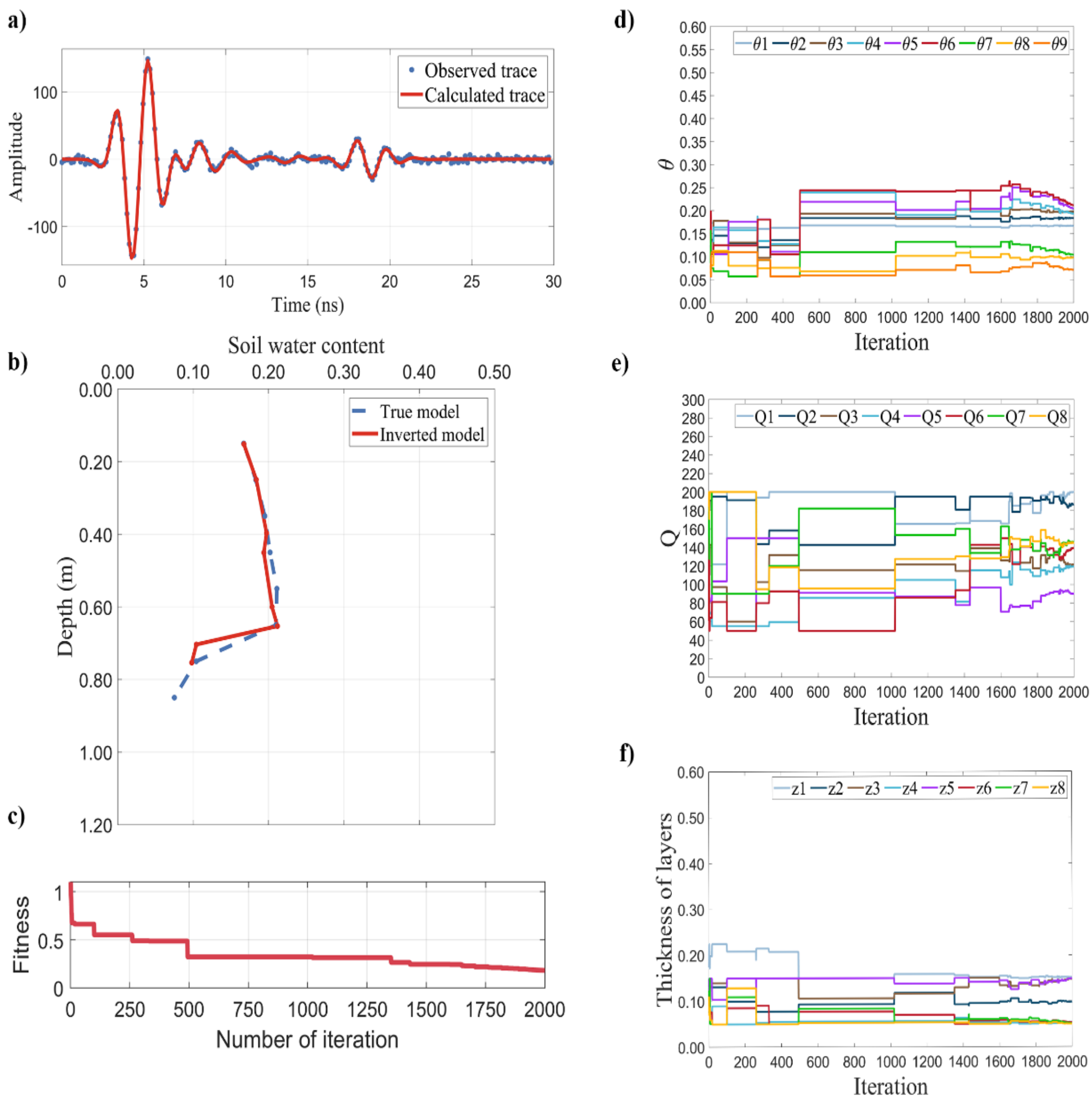

Figure 2.19 The inverted results of data with noise for Model D. a) The noise-free observed data (blue star dotted line) and calculated GPR response (red solid line). b) The true model (blue dashed line) and inverted model (red solid line). c) The fitness curve of iteration. d)-f) The behavior of each parameter versus iteration.

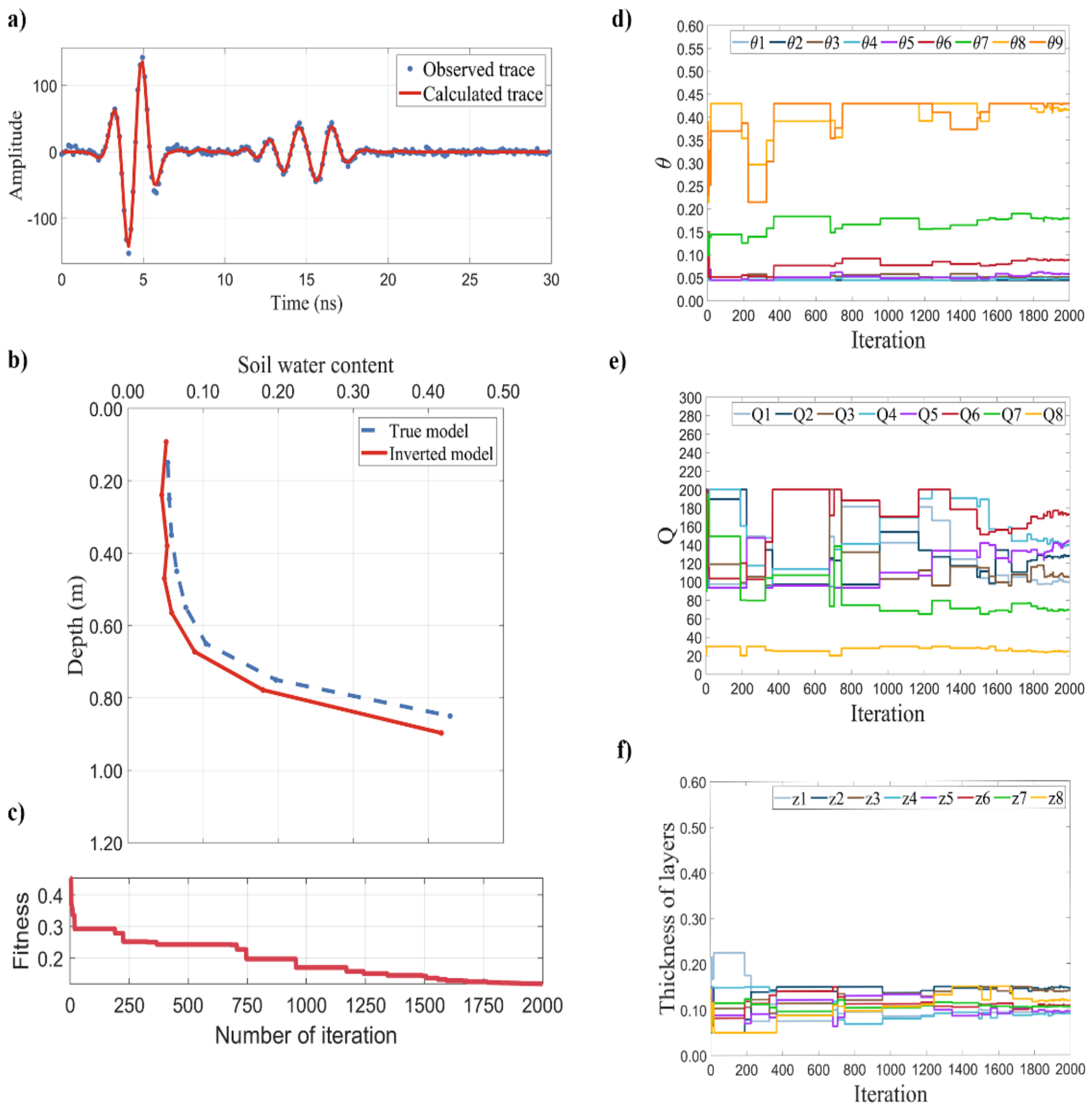

Figure 2.20 The inverted results of data with noise for Model E. a) The noise-free observed data (blue star dotted line) and calculated GPR response (red solid line). b) The true model (blue dashed line) and inverted model (red solid line). c) The fitness curve of iteration. d)-f) The behavior of each parameter versus iteration.

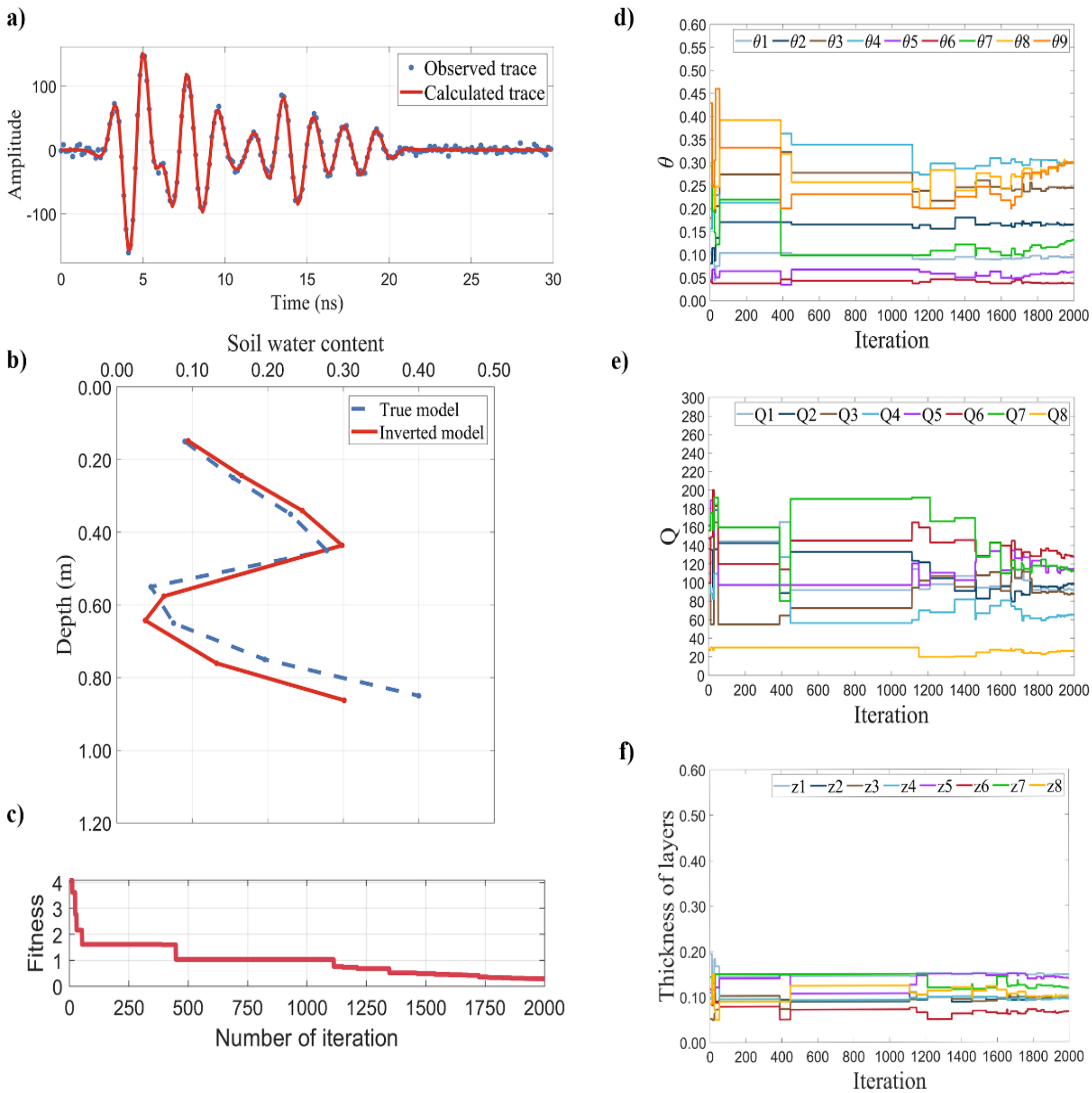

Figure 2.21 The inverted results of data with noise for Model F. a) The noise-free observed data (blue star dotted line) and calculated GPR response (red solid line). b) The true model (blue dashed line) and inverted model (red solid line). c) The fitness curve of iteration. d)-f) The behavior of each parameter versus iteration.

2.3.5 Uncertainty analysis

To investigate the importance of each parameter, we performed a one-dimensional (1D) uncertainty analysis [181] using the inverted results based on the data with noise of complex models. The uncertainty analysis was conducted by comparing the impact of each inverted parameter on the relative error between the noisy GPR waveform data obtained from forward modeling of the three complex models and the observed data. The 1D sensitivity analysis is performed by varying one parameter within a certain range while keeping other's parameters constant. In this study, the target parameter range was chosen between -80% and +80% of the parameter. Figs. 2.22a-c show the results of uncertainty analysis for model D, Figs. 2.22d-f show the results of uncertainty analysis for model E, and Figs. 2.22g-i show the results of uncertainty analysis for model F. Meanwhile, Figs. 2.22a, 2.22d, and 2.22g show the impact of SWC on the relative error, Figs. 2.22b, 2.22e, and 2.22h show the impact of the quality factor Q on the relative error, and Figs. 2.22c, 2.22f, and 2.22i show the impact of layer's thickness on the relative error. From all the figures of uncertainty analysis, it can be seen that the most sensitive parameter is SWC, followed by layer's thickness, and the least sensitive parameter is the quality factor. In Figs. 2.22b, 2.22e, and 2.22h, the change in relative error is slightly larger when the quality factor Q decreases (in the negative percentage direction) compared to when Q increases (in the positive percentage direction). This asymmetry may indicate that the model is more sensitive to the decrease in Q, that is, to the increase of attenuation (α).

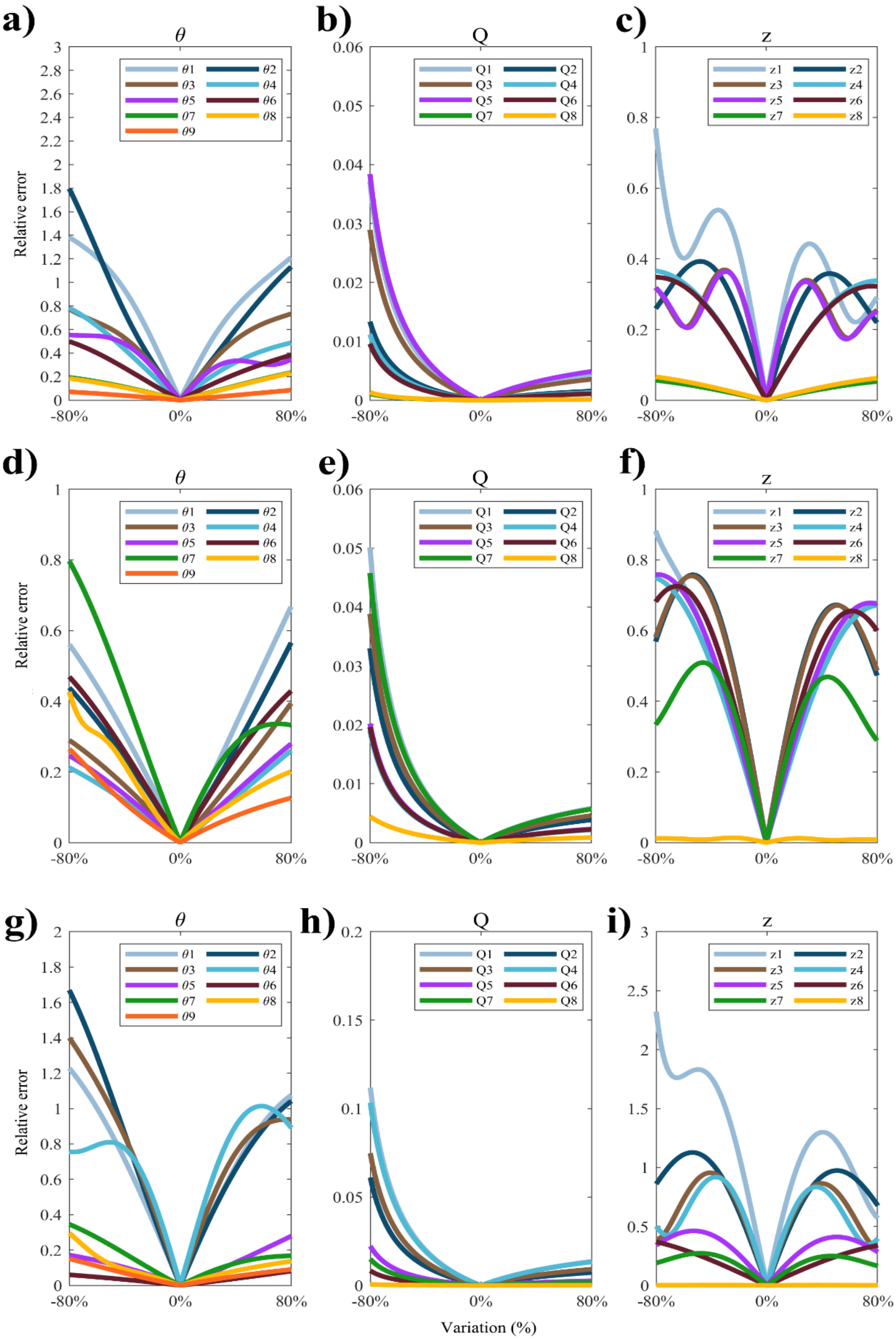

Figure 2.22 The results of 1D uncertainty analysis. a), d) and g) represent the impact of SWC on the relative error for Model D, E and F, respectively. b), e) and h) show the impact of quality factor Q on relative error for Model D, E and F, respectively. c), f) and i) give the impact of layer's thickness on relative error for Model D, E and F, respectively.

2.3.6 Comparing with Particle Swarm Optimization (PSO)

To further verify the superiority of the proposed scheme, we compared the inverted results of the proposed scheme based on the GWO algorithm with the inverted results based on the PSO algorithm. Taking the application of both algorithms to the noise free synthetic GPR data of model F as an example, we set the same size of population and maximum number of iterations for both algorithms. For the PSO algorithm, we set the inertia weight ω to 0.8 and the scaling factors c_1 and c_2 to 1.8 and 2.0, respectively. Fig. 2.23 shows the comparison between the GWO algorithm and the PSO algorithm.

In Fig. 2.23a, it can be observed that the GPR waveform response calculated from the forward modeling of inverted results based on the GWO algorithm (indicated by the red solid line in Fig. 2.23a) matches the GPR waveform response calculated from the forward modeling of theoretical model F (indicated by the blue dashed line in Fig. 2.23a) better, while the GPR waveform response calculated from the forward modeling of inverted results based on the PSO algorithm (indicated by the green solid line in Fig. 2.23a) fits less well with the forward modeling of theoretical model F. The GPR waveform response obtained from the forward modeling of inverted results based on the GWO algorithm closely follows the GPR response from the forward modeling of theoretical model F at all major peaks and troughs, indicating that the GWO algorithm can effectively capture the dynamic changes of the signal during the inversion process. In Fig. 2.23a, the GPR waveform response obtained from the forward modeling of inverted results based on the GWO algorithm is highly consistent with the GPR response from the forward modeling of theoretical model F in terms of shape, demonstrating that the approximation accuracy of the GWO algorithm is higher than that of the PSO algorithm.

Fig. 2.23b shows the comparison between the theoretical SWC, the SWC inverted based on the GWO algorithm, and the SWC inverted based on the PSO algorithm. By comparing the overlap among the three SWC profiles, it is evident that the SWC profile inverted based on the GWO algorithm, represented by the red solid line, is closer to the theoretical SWC, while the SWC profile inverted based on the PSO algorithm shows larger deviations. This further indicates that the GWO algorithm is superior to the PSO algorithm in terms of inversion accuracy for the SWC. This also means that the SWC inverted based on the GWO algorithm can more accurately simulate real conditions. Additionally, we calculated the overall average error between the theoretical model and the inverted models. The overall average errors between the SWC inverted based on the GWO algorithm and the theoretical SWC, and between the SWC inverted based on the PSO algorithm and the theoretical SWC are 0.06 and 0.16, respectively. It is evident that the error between the SWC inverted based on the GWO algorithm and the theoretical SWC is significantly lower than the error between the SWC inverted based on the PSO algorithm and the theoretical SWC, thus proving that the GWO algorithm is superior to the PSO algorithm in this scenario.

Fig. 2.23c further shows the iteration curves of the two algorithms, illustrating the changes in fitness values during the optimization process for both algorithms. The red solid line represents the GWO algorithm, while the blue solid line represents the PSO algorithm. It can be seen that the blue solid line descends to a stable value more quickly, indicating that the PSO algorithm converges faster than the GWO algorithm. However, after reaching the stable value, the PSO algorithm still maintains a higher final fitness value. Combining this with Fig. 2.23b, it can be inferred that the PSO algorithm might have fallen into a local minimum. In terms of the final solution, the red solid line ultimately tends towards a lower fitness value than the blue solid line. Although the blue solid line quickly drops to a stable fitness value, its final fitness value is higher than that of the red solid line. In optimization problems, a lower fitness value usually indicates a solution closer to the optimal one. This also demonstrates that the GWO algorithm can find a better solution.

In summary, we can conclude that in our study, the GWO algorithm outperforms the PSO algorithm in terms of accuracy, model inversion, and convergence. This analysis can provide valuable information for selecting the appropriate optimization algorithm.

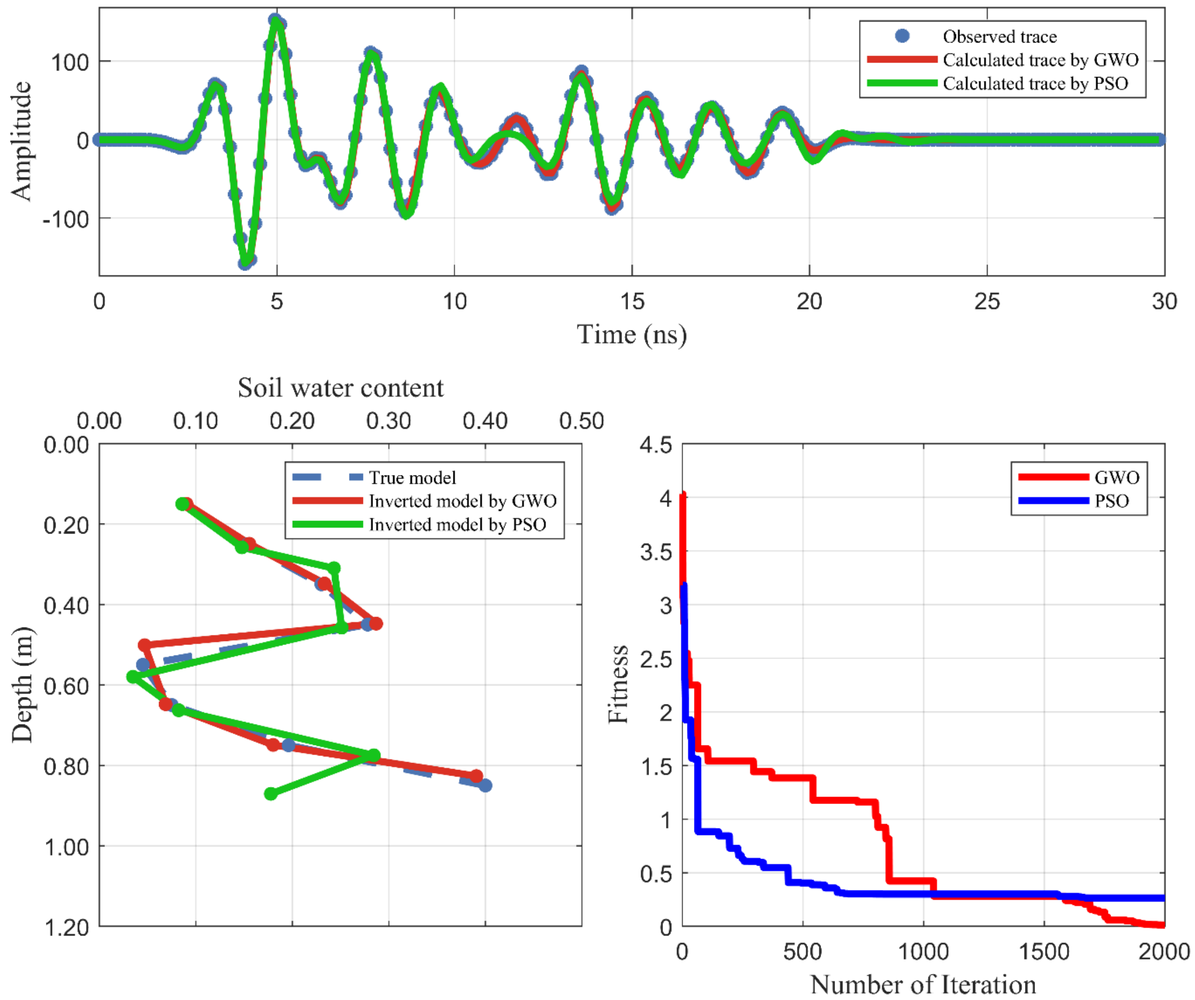

Figure 2.23 The comparison of inverted results based on the GWO algorithm and PSO algorithm in noise free data of model F. a) The GPR waveform response calculated by the forward modeling of model F (blue star dotted line), the GPR waveform response calculated by the inverted result of the GWO algorithm (red solid line), and the GPR waveform response calculated by the inverted result of the PSO algorithm (green solid line). b) The theoretical model F (blue dashed line), the inverted result based on the GWO algorithm (red solid line), and the inverted result based on the PSO algorithm (green solid line). c) The iteration curves of the GWO algorithm (red solid line) and the PSO algorithm (blue solid line).

2.3.7 Comparing with inversion based on traveltime data

We also compare the results obtained from the proposed SWC inversion scheme based on GPR waveform data with the results based on GPR travel time data. Similarly, we take the noise free synthetic GPR data of model F as an example to apply both methods, setting the same size of population and maximum number of iterations for both methods. Fig. 2.24 shows the comparison of the inverted results of the two methods. In Figs. 2.24a and 2.24d, it can be observed that the GPR responses obtained by forward modeling of the final inverted results of both methods (indicated by red dots in Fig. 2.24a and red solid line in Fig. 2.24d) match very well with the GPR responses obtained by forward modeling of the theoretical model (indicated by blue dots in Fig.2.24a and blue dashed line in Fig. 2.24d). Additionally, from the iteration curves in Figs.2.24c and 2.24f, it can be seen that the inversion based on travel time data converges more quickly to a fixed value, with a faster convergence speed than the inversion based on waveform data. However, from the inverted results shown in Figs. 2.24b and 2.24e, it is evident that the SWC profile obtained by waveform data inversion matches the theoretical model better than the profile obtained by travel time data inversion, proving that the results based on waveform inversion are more reliable. This further demonstrates that the accuracy of inverting the SWC based on GPR waveform data is superior to that based on travel time data.

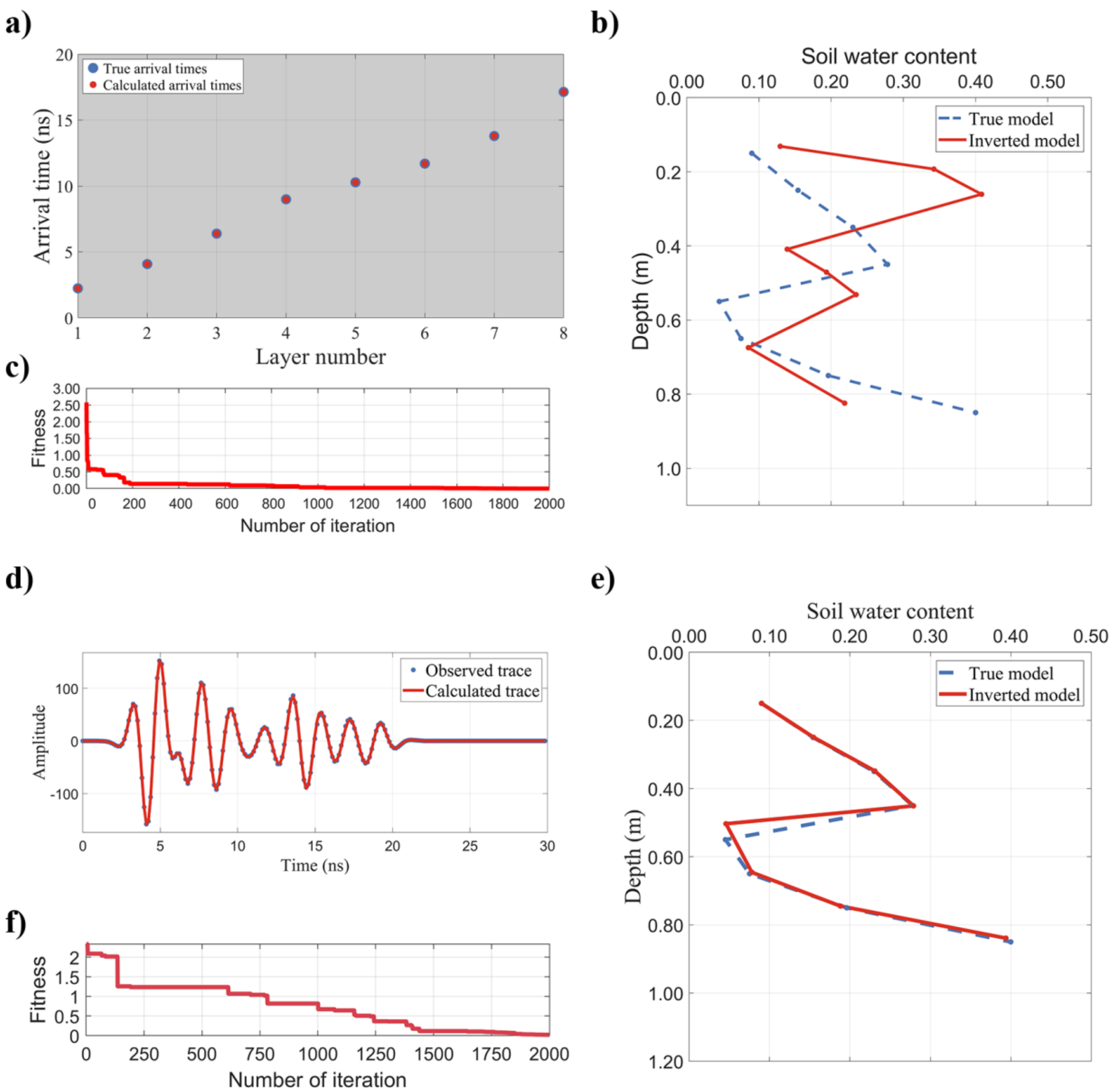

Figure 2.24 The comparison of inverted results based on GPR travel time data and waveform data in noise free data of model F. a) The GPR travel time response from forward modeling of theoretical model F (blue dots) and GPR travel time response from forward modeling of inverted results (red dots). b) The theoretical model F (blue dashed line) and final inverted results based on travel time data (red solid line). c) The convergence curve of inversion based on travel time data. d) The GPR waveform response from forward modeling of theoretical model F (blue dotted line) and GPR waveform response from forward modeling of final inverted results (red solid line). e) The theoretical model F (blue dashed line) and inverted results based on waveform data (red solid line). f) The convergence curve of inversion based on waveform data.

In summary, the research results of this section indicate that, compared to the technique of SWC estimation based on GPR travel time data, the technique based on waveform data encompasses more information from the GPR data. This allows for a higher precision estimation of SWC and a more accurate estimation of the SWC distribution.

2.4 SCERES experimental field data application

In order to further study the applicability of the proposed scheme, it was applied to GPR data collected at the SCERES experimental site. A MALA RAMAC system was used to acquire GPR data from one side to another side of the basin. The data were collected with a shielded antenna of 500 MHz central frequency in fix-offset configuration. The GPR profile was acquired along 24 m long lines. And one trace was recorded at each 0.02 m of the profile. The duration of the GPR recording was 90 ns and each trace had a sampling rate of 0.1414 ns. We applied the DC filter and a constant shift in time for all GPR traces by 20 samples. Fig. 2.25 shows the processed GPR profile.

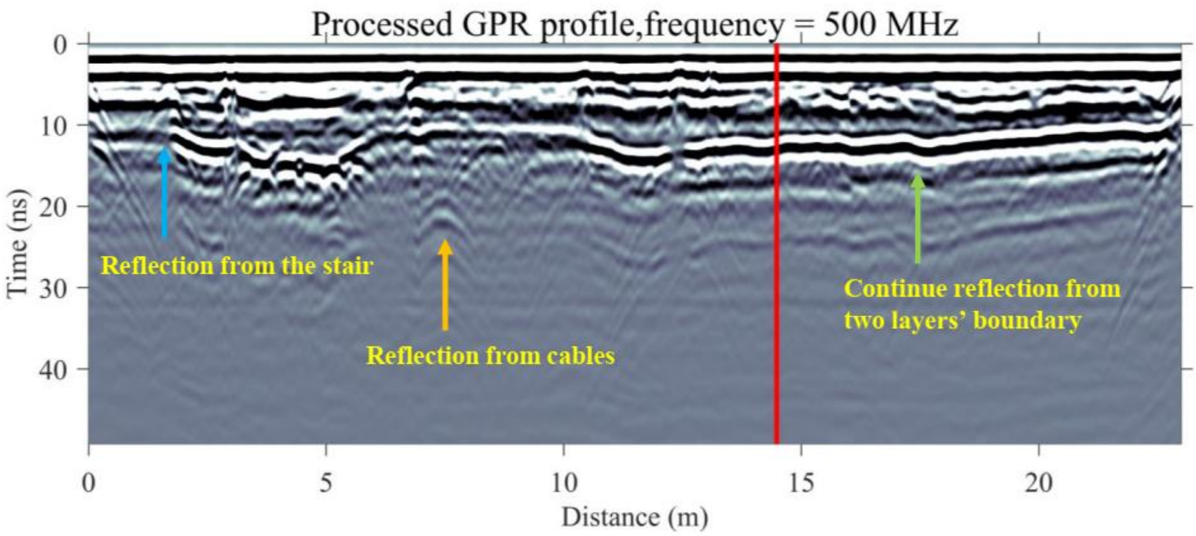

Figure 2.25 The processed observed GPR profiles from experimental site. The red solid line indicates the position of the selected GPR signal used for subsequent inversion (the 700th trace). The arrows of other colors indicate the main reflection events.

We firstly picked up the 700th trace (solid red line in Fig. 2.25) from the GPR profile as the observed trace. We used the similar inverse strategy for the synthetic data to the experimental field data. The SWC, quality factor Q and layer thickness are the parameters to be estimated. According to the test, a 11-layer subsurface structure model is adopted to carry out inversion. The SWC measured by Sentek sensors is used as prior information to set the search space for candidate solutions. The upper and lower limitations of the search space depart 50% from the prior information. This approach allows the inversion process to consider the complexity and uncertainty of the actual underground conditions to some extent while providing guidance for the inversion. By adjusting the search range, it ensures that the inversion process not only explores a sufficiently wide parameter space to find the optimal solution but also takes into account the possible influence of actual soil conditions on the parameters.

In order to obtain the synthetic GPR waveform data, it is necessary to give a source wavelet. We firstly performed a weighted average of all GPR single trace signals in the profile, and then used a Blackman window [182] to extract the wavelet. Finally, a Butterworth band-pass filter was used to further optimize the extracted source wavelet. Fig. 2.26 shows the final extracted source wavelet and its corresponding spectrum. For the real data inversion in chapter 3, we applied the same method to gain the source wavelet for each measured profile during forward modeling.

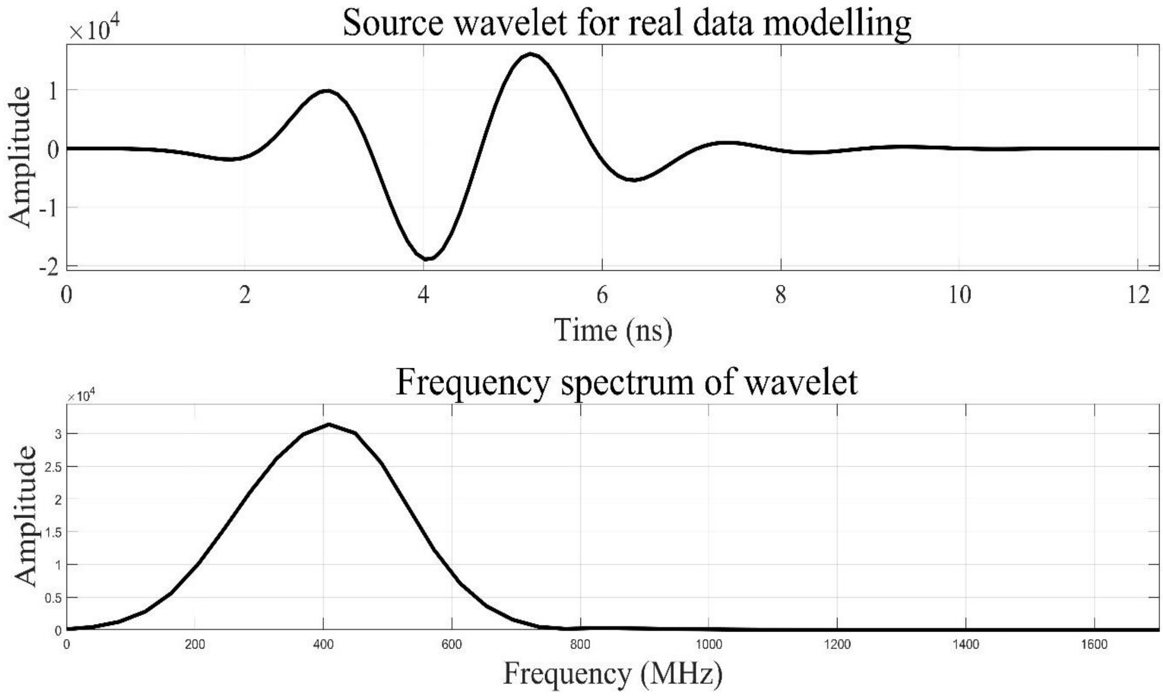

Figure 2.26 The source wavelet and its corresponding spectrum used in the inversion of real data.

Table 2.7 lists the search space for candidate solutions and the inverted results for the real data. From the inverted results, it can be observed that the quality factor Q increases with the increasing of the SWC in overall trend.

Table 2.7 The search space for SWC, quality factor Q and layer thickness z, and the inverted results for real data.

Number of layers	Search space			Inverted results for real data		
	SWC	Q	z (m)	SWC	Q	z (m)
1	0.038-0.113	20-200	0.075-0.225	0.077	30	0.225
2	0.070-0.210	20-200	0.050-0.015	0.078	40	0.063
3	0.100-0.300	20-200	0.050-0.015	0.187	35	0.055
4	0.125-0.375	20-200	0.050-0.015	0.372	81	0.084
5	0.035-0.053	20-200	0.050-0.015	0.040	43	0.075
6	0.038-0.113	20-200	0.050-0.015	0.113	23	0.150
7	0.105-0.315	20-200	0.050-0.015	0.191	137	0.068
8	0.200-0.430	20-200	0.050-0.015	0.418	22	0.126
9	0.200-0.430	20-200	0.050-0.015	0.430	123	0.150
10	0.200-0.430	20-200	0.050-0.015	0.200	93	0.098
11	0.200-0.430	∞	∞	0.430	∞	∞

* SWC represents the soil water content, Q is the quality factor, z represents the layer thickness, ∞ stands for the infinite half-space.

Fig. 2.27 shows the inverted results of real data. As shown in Fig. 2.27b, the inverted SWC from the real data (indicated by the red solid line) is generally consistent with the SWC measured by the Sentek sensors (indicated by the blue dashed line), displaying similar trend. Above approximately 0.50 m (the boundary between two soil layers), the SWC increases with depth. At 0.55 m, the SWC suddenly decreases, probably due to the influence of the boundary and changes in the medium. In the second layer, the SWC continues to increase with depth until reaching the water table. At approximately 0.85 m, there are some minor variations in the inverted results based on GPR data. This may be due to the presence of noise in the data being interpreted as valid signals during the inversion. However, the general trend remains similar. Moreover, the GPR waveform response calculated from the inverted result (indicated by the red solid line in Fig. 2.27a) closely matches the observed GPR waveform response (indicated by the blue star dotted line in Fig. 2.27a). Additionally, at the beginning of the iterations, the fitness curve shows a rapid decline and then gradually converges to a constant value after about 1500 iterations.

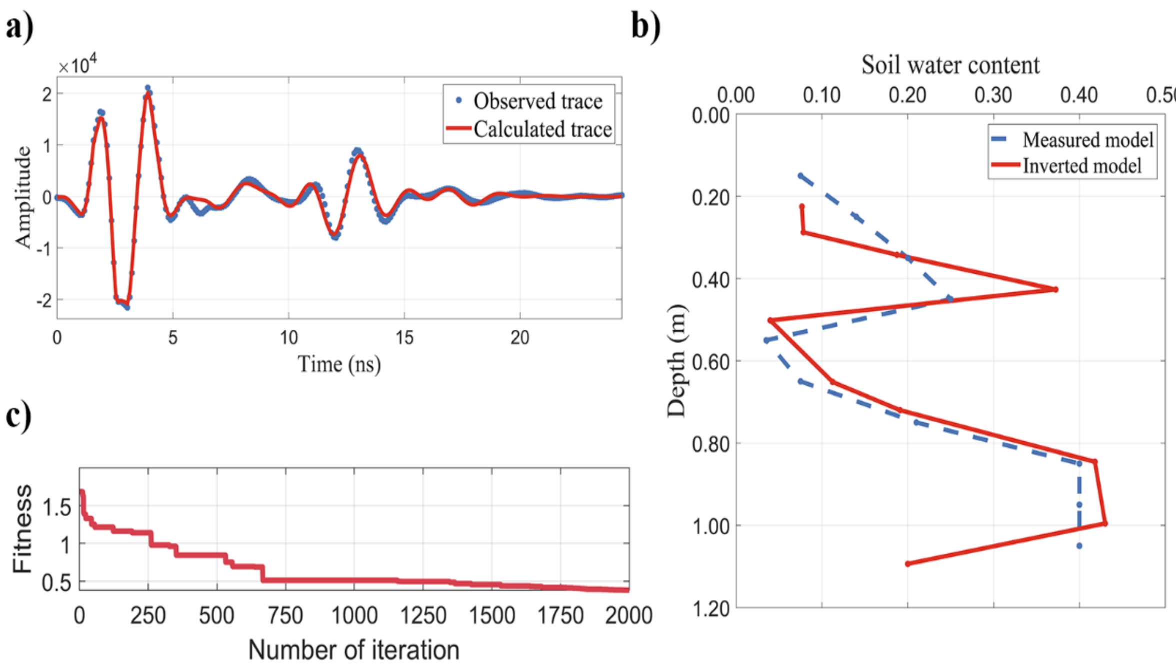

Figure 2.27 A single trace experimental field data inversion result. a) The observed trace (blue star dotted line) and calculated GPR response (red solid line). b) The measured SWC with Sentek sensors (blue dotted line) and inverted SWC (red solid line). c) The fitness curve of iteration.

We further conducted uncertainty analysis on the inverted results of real data. Figs. 2.28a, 2.28b, and 2.28c represent the sensitivity of relative error to SWC, quality factor and the thickness of the layer, respectively. The variation range of the target parameters remains -80% to +80% of their inverted values. The vertical axis still represents the relative error between the calculated GPR waveform data from the inverted results and the observed GPR waveform data. From Fig. 2.28a, we can see that the sensitivity of θ_4 is significantly higher than the SWC of the other layers within the positive and negative variation range, indicating that changes in SWC in this layer have the greatest impact on the objective function. As the SWC increases or decreases, the relative error of θ_4 increases significantly, indicating that the objective function is very sensitive to changes in the SWC of this layer. It is worth noting that for all layers, compared to an increase in parameter values (changes in the positive percentage direction), the relative error growth is smaller when the parameter values decrease (changes in the negative percentage direction). This may indicate that the objective function is less sensitive to decreases in SWC than to increases. In Fig. 2.28b, the sensitivity of parameters Q_1 and Q_4 is significantly higher than that of the other parameters. Although the relative error of the other parameters also slightly increases with the increase and decrease in parameter values, these changes are less noticeable compared to Q_1 and Q_4, indicating that their impact is limited.

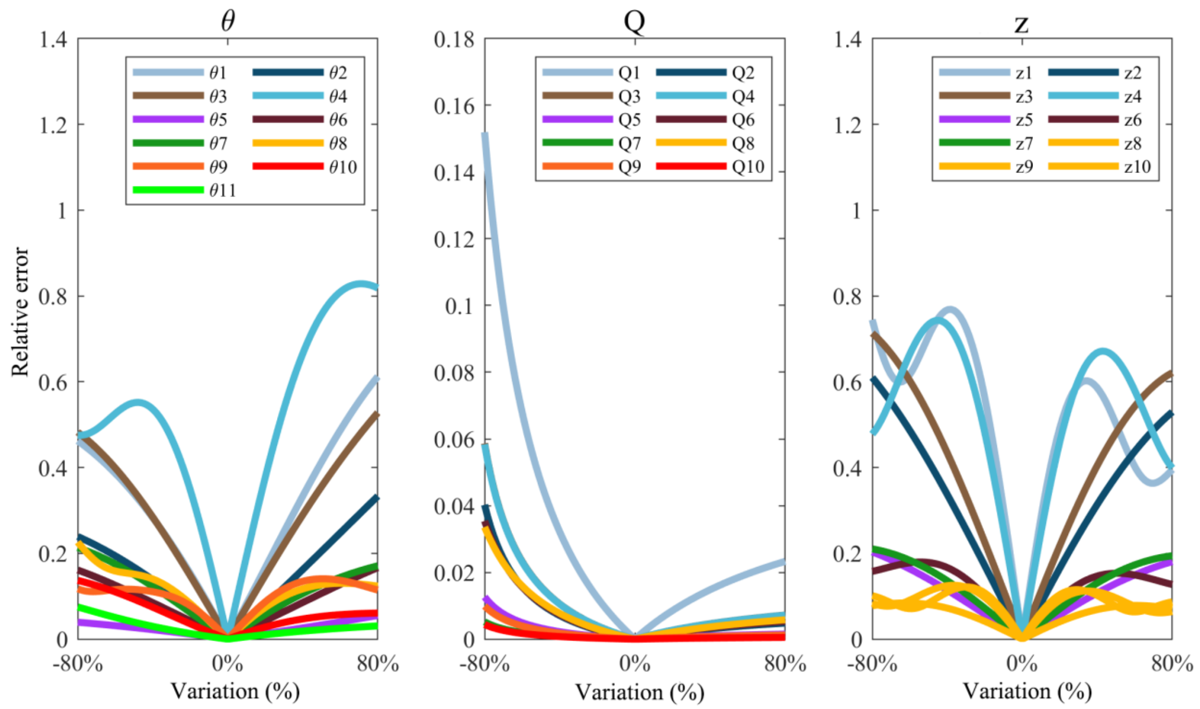

Figure 2.28 The uncertainty analysis of inverted parameters of real data. a) The impact of SWC on relative error. b) The impact of quality factor on relative error. c) The impact of layer's thickness on relative error.

Then, we applied the proposed scheme to two-dimensional (2D) experimental field data. We extracted data between 13 m and 18 m as observed data (as shown in Fig. 2.29). The proposed scheme was then applied to the observed data. Similar to the inversion of 1D GPR data, the inversion parameters were SWC, quality factor, and layer thickness. The subsurface was also divided into 10 layers, and the SWC measured by Sentek sensors was used as prior information. The upper and lower bounds of the search space for candidate solutions remained within 50% of the prior information. Fig. 2.30 shows the 2D inversion results. As shown in the figure, similar to the 1D inversion results, above about 0.5 m, the SWC gradually increases with depth. At the interface of the two soil layers (depth about 0.5 m), the SWC changes suddenly, with the profile color changing abruptly from high water content to low water content. This may be due to changes in the electrical properties between the two soil types. Subsequently, in the second layer, the SWC continues to increase gradually with depth, reaching the water table at about 0.85 m. Since the SWC below the water table is basically saturated, the color distribution of profile is relatively uniform.

From the lateral perspective, there is heterogeneity in the lateral distribution of SWC, which means the horizontal distribution of SWC is uneven. Before approximately 13.5 m, it is difficult to identify the abrupt change in water content caused by changes in soil type at about 0.5 m. This abrupt change is also relatively weak between approximately 16.5 m and 17 m. Between approximately 14 m and 15 m, both at the interface (depth about 0.5 m) and below the water table (depth about 0.85 m), the color of the high SWC area is relatively brighter. Overall, the areas with high SWC exhibit a beaded distribution laterally.

Therefore, it can be concluded that, although each type of soil in our study is considered to be homogeneously isotropic, the results of the study show that the SWC is unevenly distributed not only vertically but also horizontally, leading to an uneven spatial distribution of the dielectric constant. Since the high-frequency electromagnetic waves used in GPR are sensitive to changes in water content, they can effectively identify spatial heterogeneity in SWC, making it an efficient technology for non-destructive assessment of spatial changes in soil.

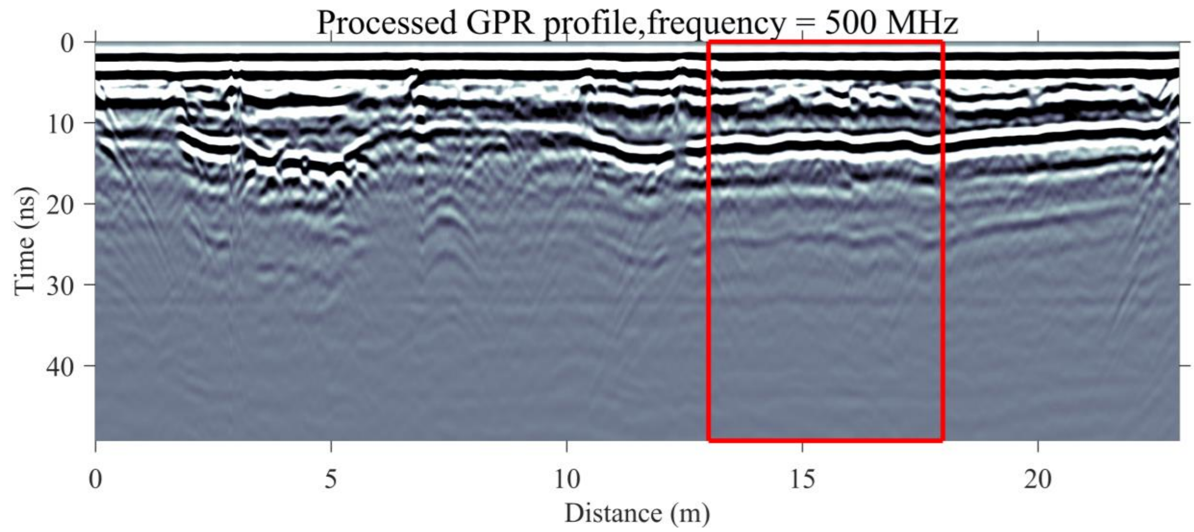

Figure 2.29 The selection of real data for performing 2D inversion of SWC.

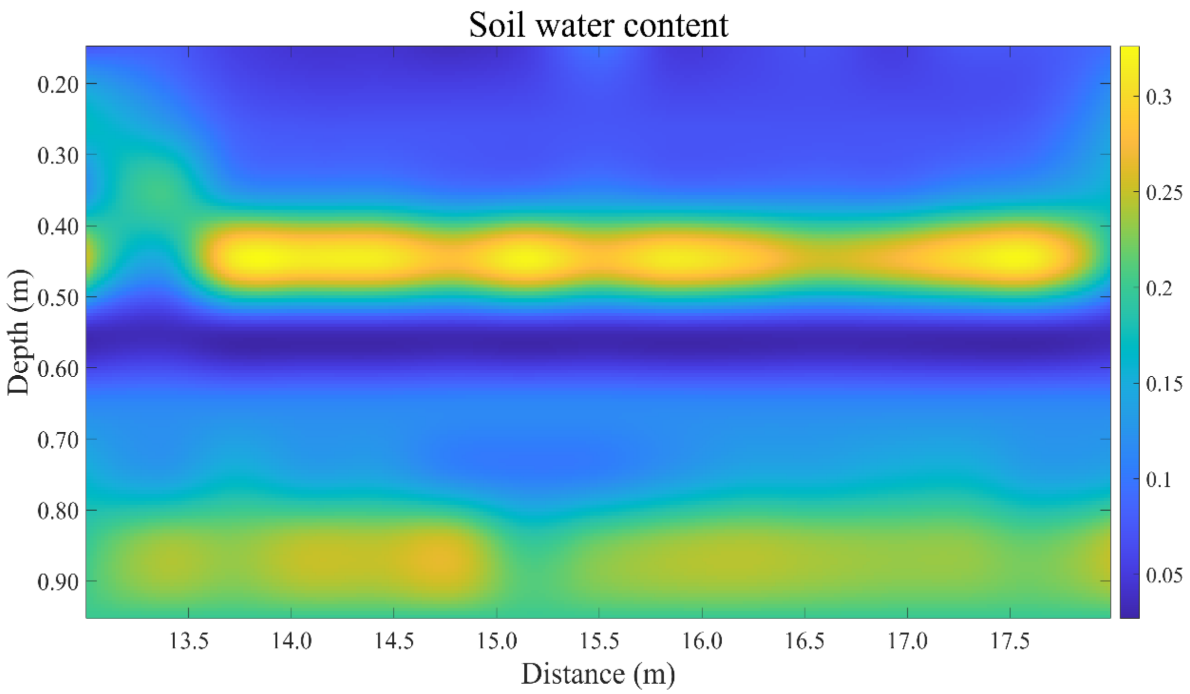

Figure 2.30 The inverted SWC results for 2D GPR data.

In summary, the results in this chapter indicate that the proposed scheme can effectively estimate SWC, quality factor Q, and layer thickness from GPR data. The inverted SWC shows similar trend to those measured by the Sentek sensors, demonstrating the potential of this method for practical groundwater and environmental studies. Furthermore, by applying a multi-layered model suitable for complex subsurface structures, the proposed scheme provides deep insights into soil water dynamics and subsurface characteristics, which are important for improving water resource management and soil conservation strategies.

2.5 Conclusions

This chapter proposed and studied the use of the GWO to optimize the inversion based on GPR waveform data to estimate SWC. First, we introduced the theories of the research process for estimating SWC by GPR, including the petrophysical relationship and how to obtain the GPR echo signals from the Maxwell equations and electromagnetic wave equation. Subsequently, we introduced the inverse problem from the establishment of the objective function. As this study involves the simultaneous inversion of multiple types of parameters, the traditional gradient-based optimization algorithm involves a large amount of computation and is affected by differences in the order of magnitude of the parameters. Therefore, this study utilizes the globally optimized swarm intelligence GWO algorithm to avoid the need for gradient computation. Then, we introduced the SCERES experimental site, where real field data collection was conducted in this study. This experimental site is specifically designed for hydrological experimental research and suitable for the study of most static and dynamic hydrological issues.

To test the effectiveness of the proposed scheme, we designed two types of numerical experiments, including six numerical models. The first three are simple four-layer models, and the latter three are more complex models established using the HYDRUS-1D software, which are closer to the actual underground SWC distribution. The results of all six numerical experiments demonstrate that the proposed scheme can accurately and non-destructively determine SWC. Additionally, uncertainty analysis of the inversion parameters and comparison of the results with the PSO for the last model further verify the effectiveness of the proposed scheme.

Then, in order to further validate the applicability of the proposed scheme, we applied it to real GPR waveform data collected at the SCERES experimental site and conducted 1D and 2D SWC estimation. We also discovered that the SWC is not only unevenly distributed vertically but also heterogeneous horizontally. In future studies, the heterogeneity of SWC distribution in the horizontal direction is also a key issue worthy of attention.

In summary, this is the first time that we attempt to use the GWO algorithm to optimize the inversion based on GPR waveform data for the direct estimation of SWC. The research provides a potential approach for accurate and non-intrusive determination of SWC using GPR waveform data inversion based on the GWO algorithm.

Chapter 3 SWC monitoring by using time-lapse GPR waveform inversion

In chapter 2, it was demonstrated that GPR has the ability to estimate the SWC through numerical experiments and experimental data application. In this chapter, the proposed scheme was then applied to realize monitoring of SWC change from time-lapse surface GPR waveform data. In section 3.1, the basic theory of time-lapse inversion was introduced, including individual inversion, continuous inversion, and double-difference inversion. In section 3.1 to 3.5, two types of experiments were designed in the field: unsaturated soil imbibition and drainage experiment, and unsaturated soil precipitation infiltration experiment. Then, the proposed approach was applied to the GPR data measured during these experiments. The results show that the proposed SWC monitoring technique based on time-lapse GPR waveform data can efficiently monitor SWC changes at the field scale. Finally, by introducing double-difference time-lapse inversion, the accuracy of monitoring soil moisture changes can be significantly improved.

3.1 Theory of time-lapse inversion

The goal of time-lapse inversion is to characterize the dynamic changes of medium within the underground target area by describing the variations of parameters at different time points. The time-lapse inversion includes three commonly used strategies: individual inversion strategy, continuous inversion strategy, and double-difference inversion strategy [183]. This section provides a detailed introduction to each time-lapse inversion strategy.

3.1.1 Individual inversion

In the time-lapse individual inversion, the same initial model is first used to independently invert the parameters based on observed reference data and monitoring data, respectively. The inversion results of the reference data are then subtracted from the inversion results of the monitoring data to obtain the parameter changes in the target area. The advantage of time-lapse individual inversion is that there is no strict requirement on the acquisition parameters for data collection at different time points. However, the drawback is that since the inversions at different time points are independent of each other, it often introduces significant time-lapse artifacts.

Assuming the acquisition time of the reference data is T_1 and the acquisition time of the monitoring data is T_2, with the corresponding data collected at these time points being $\mathbf{d}_{obs1}$ and $\mathbf{d}_{obs2}$. Based on the reference data ($\mathbf{d}_{obs1}$) and monitoring data ($\mathbf{d}_{obs2}$), the inverted models for the time points T_1 and T_2 are $\mathbf{m}_1$ and $\mathbf{m}_2$. By subtracting $\mathbf{m}_1$ from $\mathbf{m}_2$, we can obtain the parameter changes in the target area. Fig. 3.1 shows the flowchart of the time-lapse individual inversion.

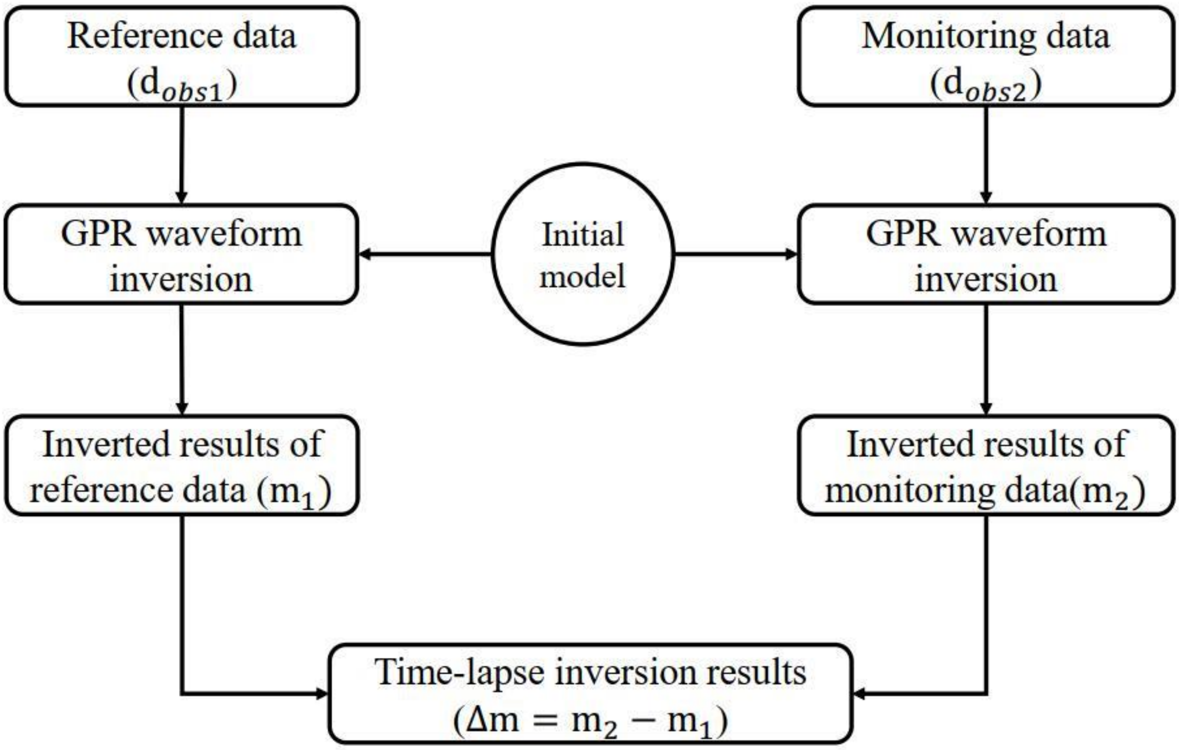

Figure 3.1 The flowchart for time-lapse individual inversion.

3.1.2 Continuous inversion

When the changes of data are small between different time points, the goal of the inversion is to more accurately estimate the parameter changes in the target area while try to avoid the time-lapse artifacts outside the target area. Therefore, it is a good choice by using the inversion results obtained from the previous time point (T_1) as the initial model for the inversion at the subsequent time point (T_2). For most geophysical inversion, the choice of initial model greatly affects the accuracy of the final inversion results. For time-lapse data, the model changes over different time points are localized, with only model changes in certain regions. Therefore, using the model ($\mathbf{m}_1$) obtained from the inversion of the reference data ($\mathbf{d}_{obs1}$) as the initial model for the inversion of the monitoring data in the target area ($\mathbf{d}_{obs2}$) can lead to higher precision in estimating the parameter changes within the target area, while reducing computational costs. The flowchart of the continuous time-lapse inversion is shown in Fig. 3.2.

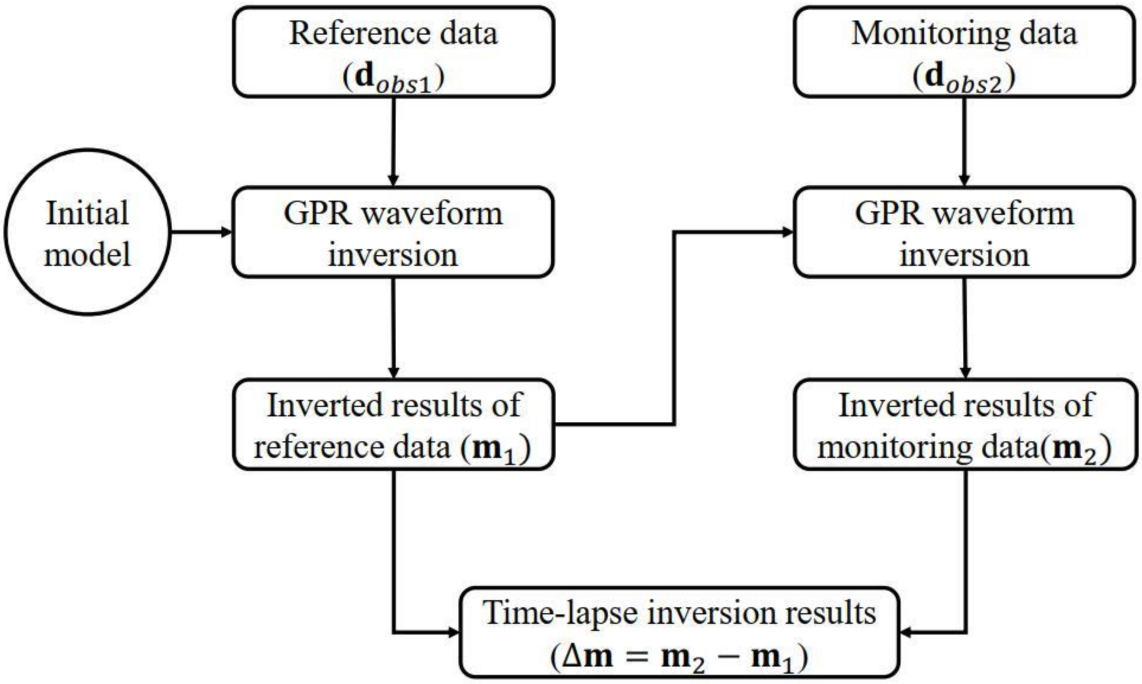

Figure 3.2 The flowchart for time-lapse continuous inversion.

3.1.3 Double-difference inversion

Double-difference time-lapse inversion is proposed by Waldhauser et al. [183] to improve the accuracy of inverting parameter changes in the target area. This method can be considered as a further improvement on the continuous time-lapse inversion method. The method utilizes the forward modeling data of the inversion results from the reference data at the previous time point, together with the differences in the monitoring data collected at the two consecutive time points, to construct GPR waveform data for inversion. This approach aims to minimize the effects from outside the target area, enhance the accuracy of parameter inversion within the target area, and has significant value for analyzing and monitoring dynamic changes in SWC. The time-lapse double-difference inversion can be divided into the following steps:

1) Collect reference data ($\mathbf{d}_{obs1}$) and monitoring data ($\mathbf{d}_{obs2}$) at the previous time point (T_1) and subsequent time point (T_2), respectively. Then, the underground parameter model ($\mathbf{m}_1$) is inverted by using the reference data ($\mathbf{d}_{obs1}$).

2) Perform forward modeling by using the inversion result $\mathbf{m}_1$ of reference data and gain the new reference data $\mathbf{d}^*_{obs1}$. Then, calculate $\mathbf{d}^*_{obs2}$ using the following equation to use as new monitoring data for inverting the underground parameter model at time point T_2.

$$\mathbf{d}^*_{obs2} = \mathbf{d}^*_{obs1} + (\mathbf{d}_{obs2} - \mathbf{d}_{obs1}) \quad (3.1)$$

3) Determine the changes in underground parameters within the target area by analyzing the difference between the underground parameter model $\mathbf{m}_2$and model $\mathbf{m}_1$.

Fig. 3.3 shows the flowchart for the time-lapse double-difference inversion.

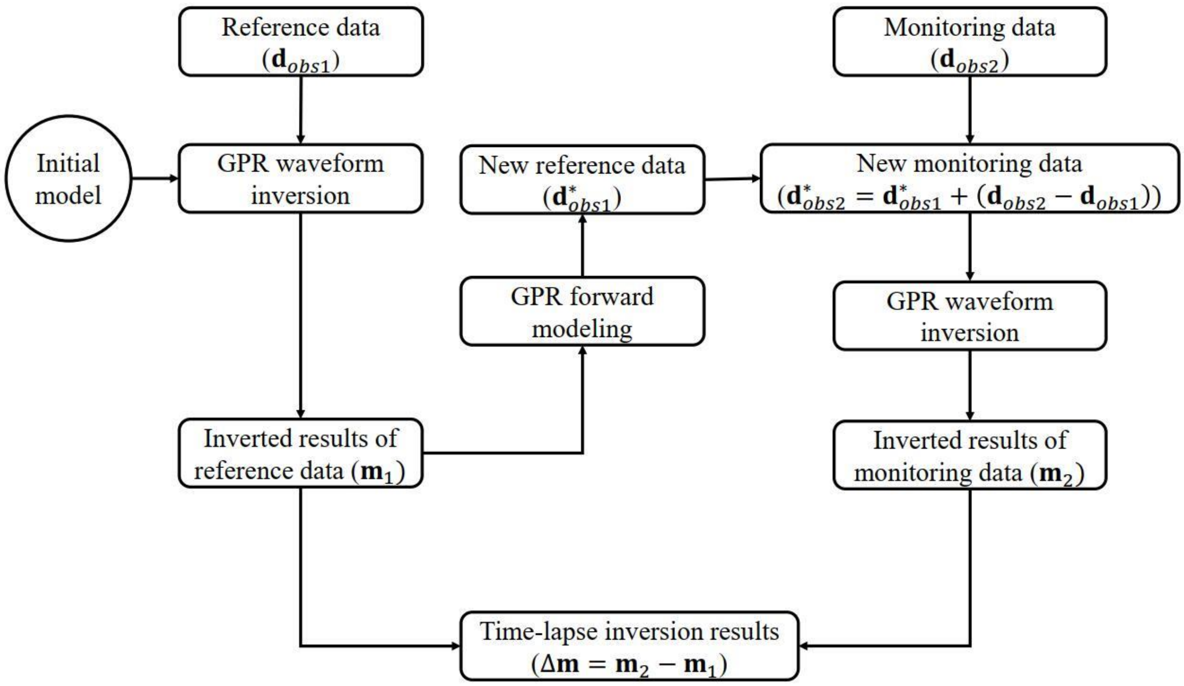

Figure 3.3 The flowchart for time-lapse double-difference inversion.

3.2 Imbibition and drainage experiment for unsaturated soil

3.2.1 Data collection and processing

The imbibition and drainage experiment is still conducted on SCERES experimental site. The level of the water table is manipulated by pumping water in and out of the basin through the bottom layer of the basin for controlling the imbibition and drainage processes. High-resolution common offset measurements were carried out by using a MALA RAMAC surface GPR system, which measures from one side to another side in the basin during a series of imbibition and drainage processes. The length of the line is 24 m. The antenna system was operated at a central frequency of 500 MHz, and the GPR system was set to collect data at intervals of 0.02m per trace.

The imbibition and drainage experiments were performed over two days. On the first day, we conducted the imbibition experiment. A baseline GPR profile was collected at 08:30 prior to beginning the imbibition experiment at 09:00. Then, the water level was raised by using the equipment in the bottom of basin. The profiles were collected every half-hour in the morning. In the afternoon, we measured the profiles every one hour. The water level was maintained overnight after the imbibition experiment for carrying out the drainage experiment on the second day.

For the drainage process, a baseline profile was similarly measured at 08:30 before the drainage experiment at 09:00. In the morning, we still measured profiles every half-hour and each one hour in the afternoon as the water level was lowered. The data processing for all the profiles included the application of a DC filter and a constant shift in time of 20 samples.

3.2.2 Data analysis and interpretation of time-lapse evolution for imbibition experiment

We firstly analyze the changes in SWC and the movement of the wetting front in the soil during the imbibition experiment. Fig. 3.4 displays the temporal evolution of subsurface conditions as measured by GPR during the imbibition experiment on the first day, represented at five distinct time points. Through the overall analysis of the GPR profiles, it can be observed that the overall increase in SWC due to the rise in water level affects the signals in the GPR profiles.

The initial radargram, recorded at 08:30 before the experiment, reveals the interface between two sandy layers via a distinct reflection occurring at approximately 10 ns (see the red arrow in Fig. 3.4a). Additionally, the main structural elements are discernible, such as the step located approximately 2 m from the left edge of the basin and the discontinuous event between 2 m and 6 m horizontally due to the backfilling of the site.

In the rest GPR profiles, it can be observed that as a continuously increasing water level during the imbibition experiment, there is a corresponding increase SWC in the subsurface. And the unsaturated soil gradually becomes saturated, which results in a gradual decrease in signal amplitude on the GPR profiles. By 16:00, the water table has ascended above the interface between the two sandy layers. Consequently, the reflection amplitude associated with this interface diminishes in intensity (as shown by the red arrow in Fig. 3.4) compared to the earlier four radargrams.

In order to observe more clearly, individual traces have been picked up and analyzed from each radargram at the same position. As shown in Fig. 3.5, the arrival time of the reflection (highlighted by the red arrow) gradually shifts to later times as the progress of the imbibition experiment progresses, while concurrently, the reflection amplitude gradually becomes weak. This attenuation of the reflection signal indicates during the imbibition experiment, as the water table rises continuously, the SWC below the water table approaches saturation, leading to a gradual reduction in the difference of SWC between the soil on either side of the interface, thereby causing a gradual decrease in the difference in electromagnetic properties of the soil on either side of the interface.

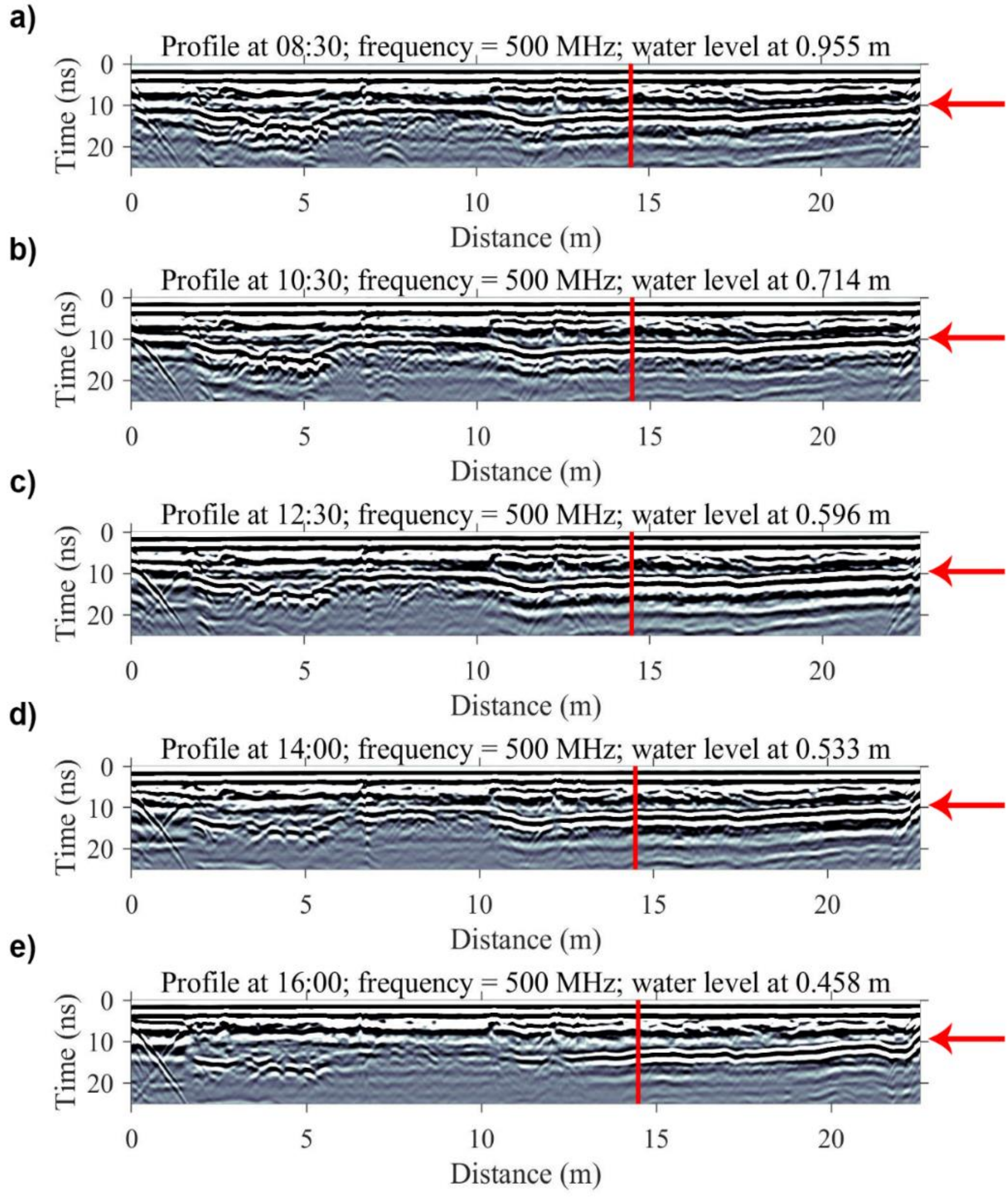

Figure 3.4 The processed GPR profiles at five different time points for the imbibition experiment on the first day. The ground surface is set to be 0 m. The levels of water table are 0.955 m (8 h 30 min), 0.714 m (10 h 30 min), 0.596 m (12 h 30 min), 0.533 m (14 h) and 0.458 m (16 h) at different time points.

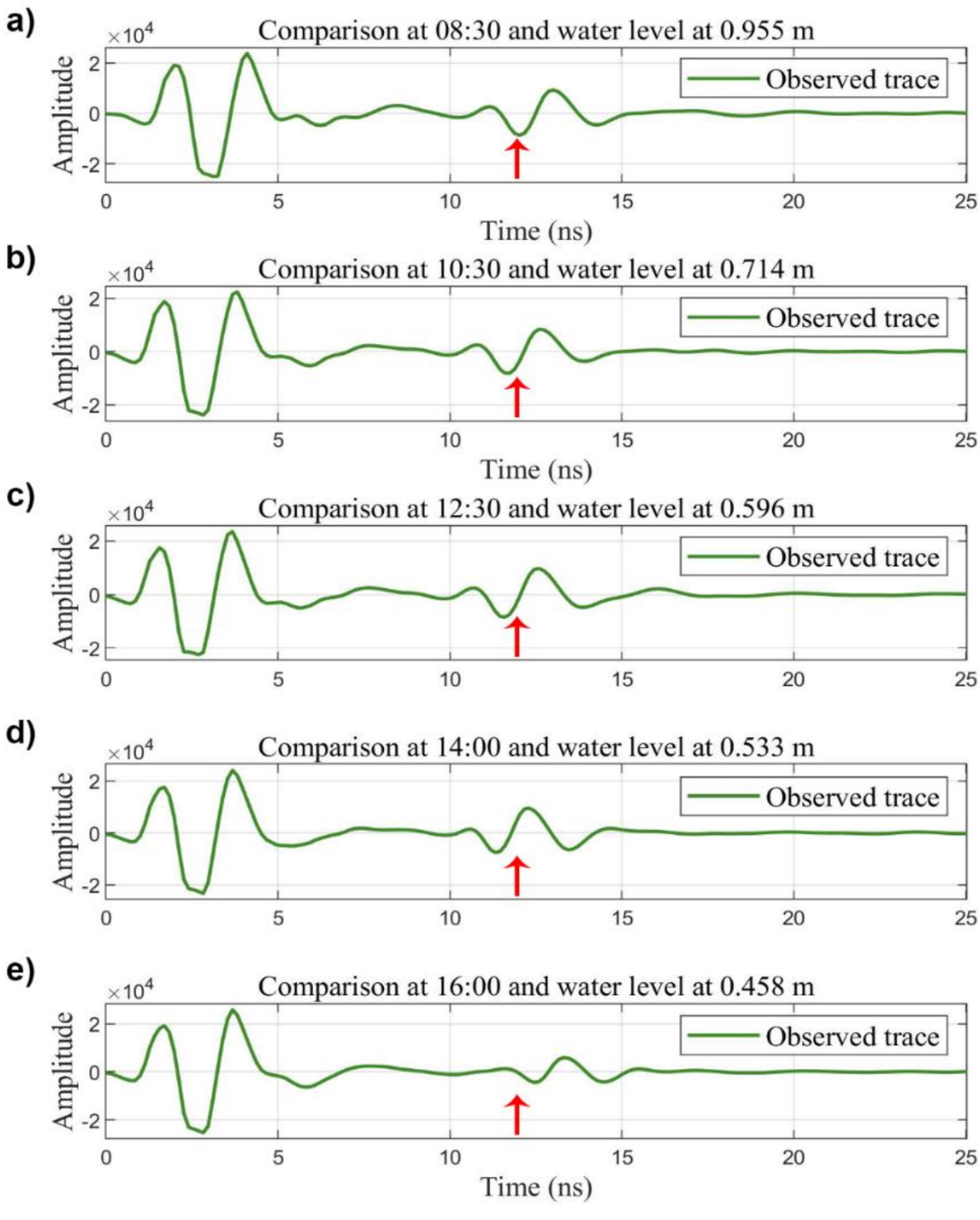

Figure 3.5 The GPR traces picked up from the same position (700th trace) in each processed GPR profiles at 5 different time points during the imbibition experiment on the first day. The ground surface was set to be 0 m. The levels of water table are 0.955 m (8 h 30 min), 0.714 m (10 h 30 min), 0.596 m (12 h 30 min), 0.533 m (14 h) and 0.458 m (16 h).

3.2.3 Data analysis and interpretation of time-lapse evolution for drainage experiment

Fig. 3.6 presents the GPR profiles collected by GPR during the drainage experiment on the second day, still represented at five distinct time points. We conducted an overall of the five profiles, it can be observed that as the groundwater level decrease, the overall SWC gradually decreases, leading to changes in the GPR signals. Similar to the imbibition experiment, the baseline radargram was obtained prior to commencing the drainage experiment at 08:30. However, the reflection from the two sandy layers boundary (around 10 ns) cannot be clearly identified at the beginning of the drainage experiment. The radargram taken at 08:30 shows a faint reflection from this interface (indicated by the red arrow in Fig. 3.6).

From the GPR profiles collected at the five different time points, it can be observed that as the gradual decreasing of the water table, the overall SWC in the upper part of the water table also decrease gradually during the drainage experiment. This results in an increasing difference in electromagnetic properties between the two sand layers, leading to the reflection amplitude becoming clearer over time. In order to more clearly distinguish the changes in the reflection between the two sand layers caused by the lowering of the water table, on trace was extracted from the same position in the GPR profile at each time point further analysis (as presented in Fig. 3.7). In Fig. 3.7, it is evident that the reflection signal becomes more pronounced as the water table descends below the boundary of the two sandy layers (observable in the trace at 10:30). Moreover, the arrival time of the reflection (highlighted by the red arrow) shifts to shorter travel times in the traces recorded after 10:30. Concurrently, the amplitude of the reflection intensifies, demonstrating the changes in the SWC during the drainage experiment.

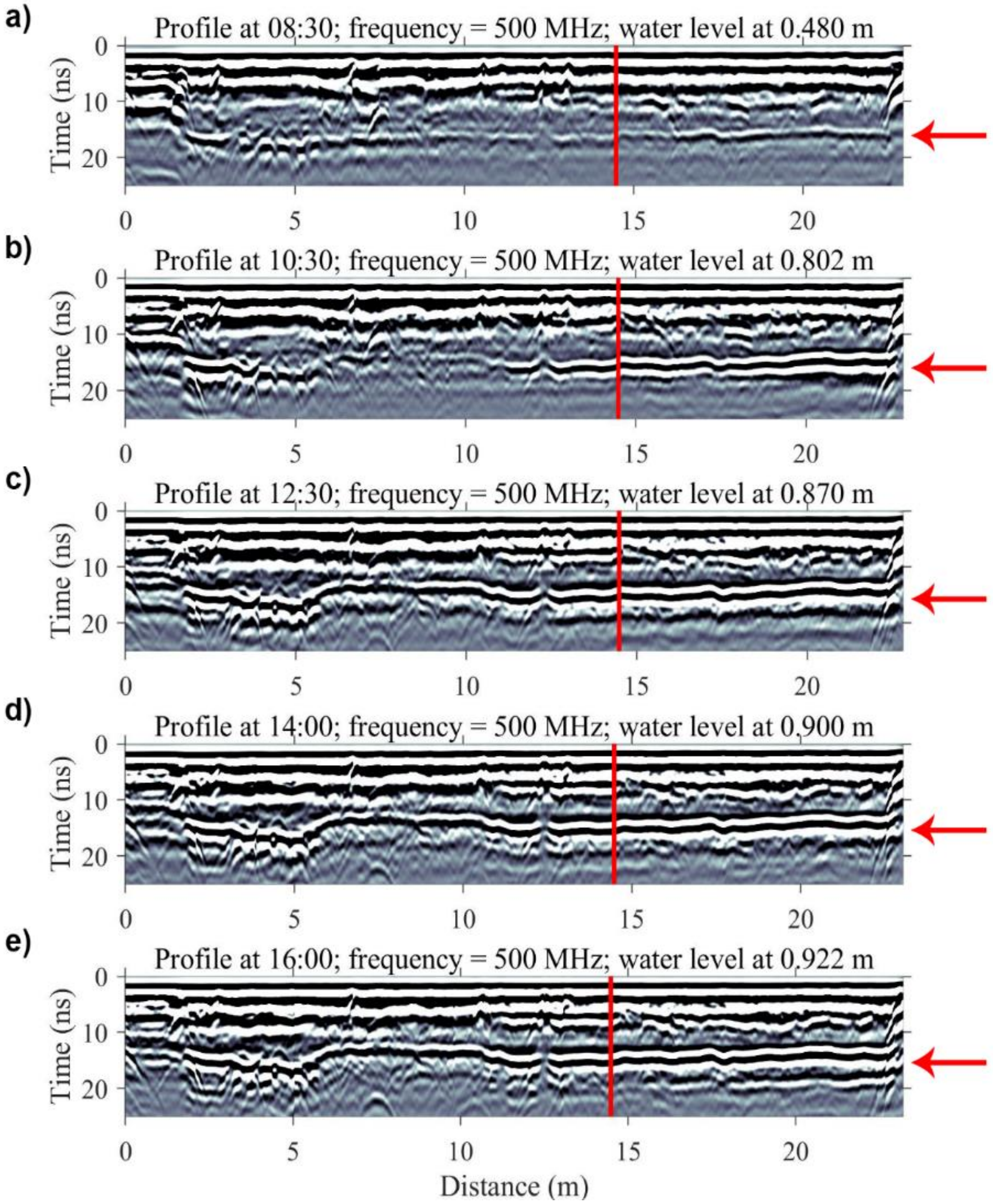

Figure 3.6 The processed GPR profiles at five different time points for the drainage experiment on the second day. The ground surface is set to be 0 m. The levels of water table are 0.480 m (8 h 30 min), 0.802 m (10 h 30 min), 0.870 m (12 h 30 min), 0.900 m (14 h) and 0.922 m (16 h).

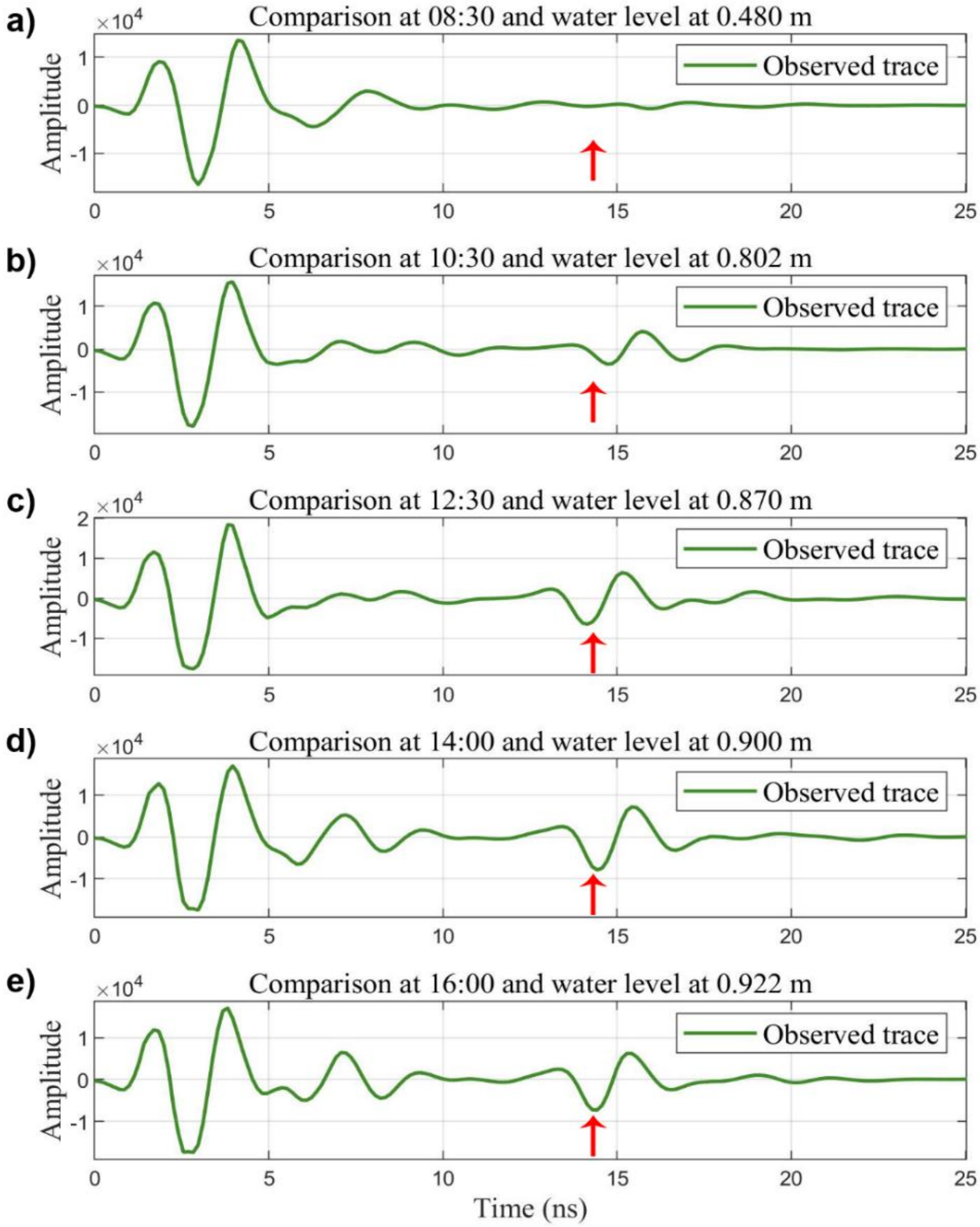

Figure 3.7 The GPR traces picked up from the same position (700th trace) in each processed GPR profiles at 5 different time points during the drainage experiment on the second day. The ground surface was set to be 0 m. The levels of water table are 0.480 m (8 h 30 min), 0.802 m (10 h 30 min), 0.870 m (12 h 30 min), 0.900 m (14 h) and 0.922 m (16 h).

3.3 Results and discussion of imbibition and drainage experiment

In order to estimate and monitor the SWC within the experimental site, we respectively utilized the technique proposed in Chapter 2. The technique was applied on the selected traces from the radargrams corresponding to 10 distinct time points in Figs. 3.5 and 3.7. The SWC, the quality factor and the thickness of each layer were estimated by the proposed technique using the GWO to optimize GPR waveform inversion for non-destructive assessment of SWC. According to the Sentek sensors measurements, the subsurface is divided into 11-layers for the inversion of imbibition and drainage experiments.

For the inversion at each time point, the population size is set to be 320 and the number of iterations is 2000. Each inversion undergoes 10 tests. The SWC values measured by Sentek sensors are integrated as a priori information to provide information for the inversion process. Moreover, the defined search space for the inversion parameters is bounded by upper and lower limits that diverge by 50% from the a priori information. The values in the lower limit below the residual water content were modified to the residual water content, and the values in the upper limit above the saturation water content were modified to the soil saturation water content.

Figs. 3.8 and 3.10 present the fitness between the calculated trace based on the inverted model by the proposed scheme and the corresponding observed trace for each trace at different time points during the imbibition experiment and the drainage experiment, respectively. The figures demonstrate a notable concordance, all the calculated traces match the observed trace well in Figs. 3.8 and 3.10, which indicating the effectiveness of the proposed scheme in monitoring the soil water dynamics throughout the experiments.

Figs. 3.9 and 3.11 show the SWC profiles inverted by the proposed scheme and the measured SWC obtained from Sentek sensors at different time points during the imbibition experiment and drainage experiment, respectively. These SWC profiles play a key role in analyzing the spatiotemporal soil water dynamics throughout the imbibition and drainage experiments.

Firstly, it is evident that the trends observed in the inverted SWC profiles are in good agreement with those from the Sentek sensor measurements. In Fig. 3.9, during the process of imbibition, the change of SWC was firstly observed in the profile at 10:30 and the water level rises from 0.955 m to 0.714 m. The subsequent profile at 12:30 can continue to observe the change in SWC. By 14:00, the water level reaches 0.533 m, the SWC also shows a small increase at the boundary between two soil layers. At 16:00, the SWC measured by Sentek sensors closely becomes saturated at the boundary of two soil layers (around 0.5 m). However, the SWC inverted by the proposed scheme has not reached saturation. This discrepancy indicates that the influence of the boundary is still discernible in the change of SWC inverted by the proposed scheme. From the GPR measured trace presented in Fig. 3.8, a reflected signal from the boundary between the two soil layers at approximately 14 ns is also visible. Consequently, we think that the GPR can identify the SWC more accurately in comparison to Sentek sensors, especially under the influence of sand layer interfaces.

In Fig. 3.11, a similar process to Fig. 3.9 can be observed. In Fig. 3.11, the recession of water level is discernible with the increasing times~~.~~ From the profile at 08:30 in Fig. 3.11, we not only did not observe the change of SWC at the boundary (around 0.5 m) from the SWC measured by Sentek sensors, but also did not observe the phenomenon from the inverted SWC. Furthermore, the signal from the boundary of two soil layers as well did was also not visible on the GPR trace profile in Fig. 3.10 at 08:30. We believe this may be the SWC at boundary reached saturation overnight. Because the water level has been elevated to 0.458 m after the imbibition experiment. In contrast, the 10:30 profile reveals a disparity in both the SWC profile measured by Sentek sensors and the inverted SWC profile at the boundary of two soil layers. In Fig. 3.10, the GPR trace profile at 10:30, exhibits a discernible reflection from this boundary at approximately 14 ns. Indeed, as the water table continued to fall, there is a concomitant decrease in the SWC. The difference of SWC on both sides of the interface gradually increased between the two soil layers, making the difference can be identified by the Sentek sensors and also causing a response in the GPR signal. Throughout the following profiles at 12:30, 14:00, and 16:00, the change of SWC at the boundary can be consistently observed from both the profile measured by Sentek sensors and the inverted SWC profile.

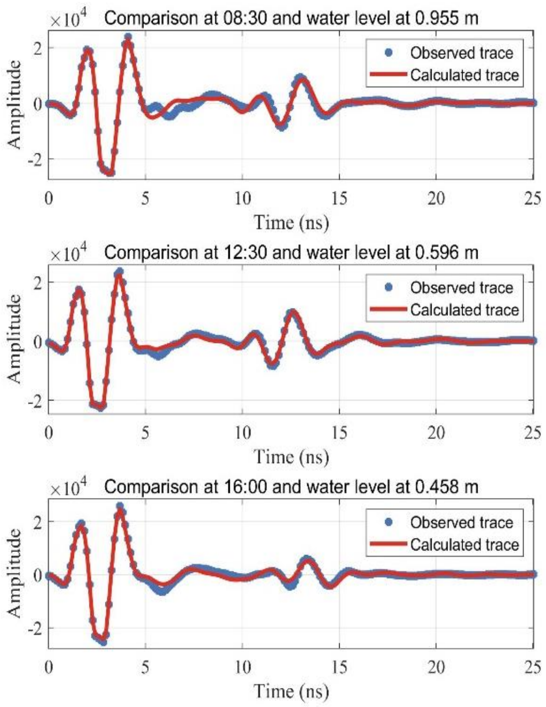

Figure 3.8 The fitness between the observed traces and calculated traces from inverted results at different time points during the imbibition experiment. The solid red lines represent the observed data and the blue dotted lines represent the calculated data.

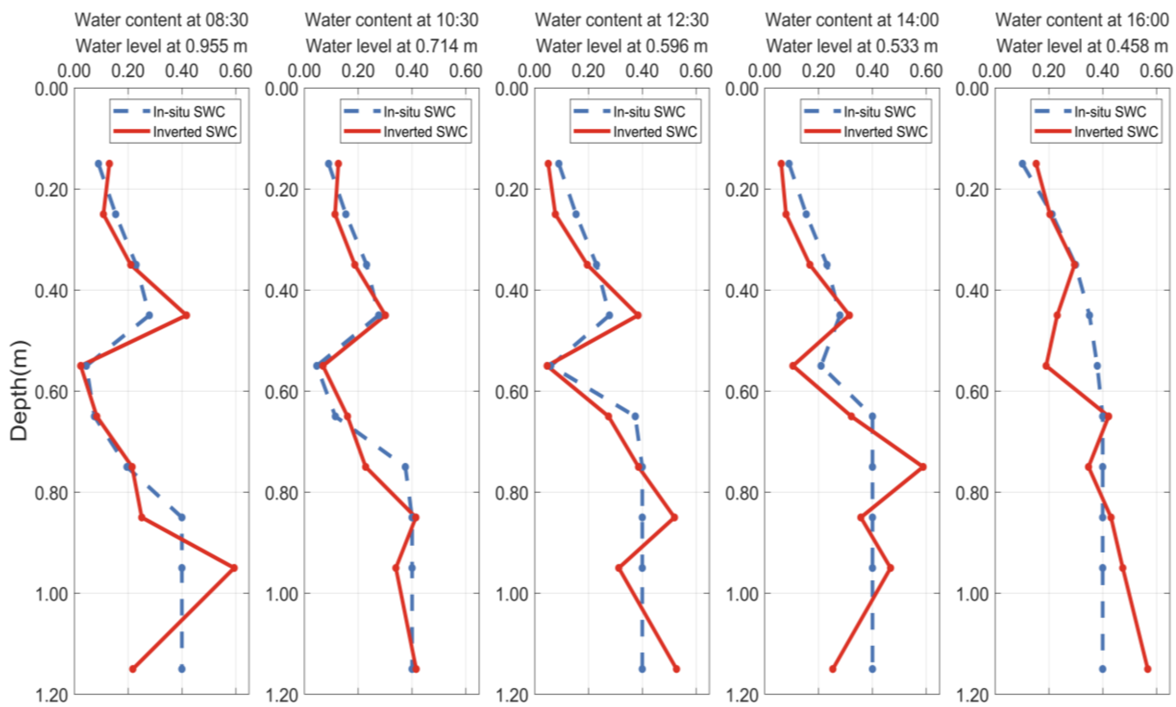

Figure 3.9 The SWC profiles at different time points during the imbibition experiment. The red solid lines represent the SWC measured by Sentek sensors. The blue dashed lines represent the inverted SWC.

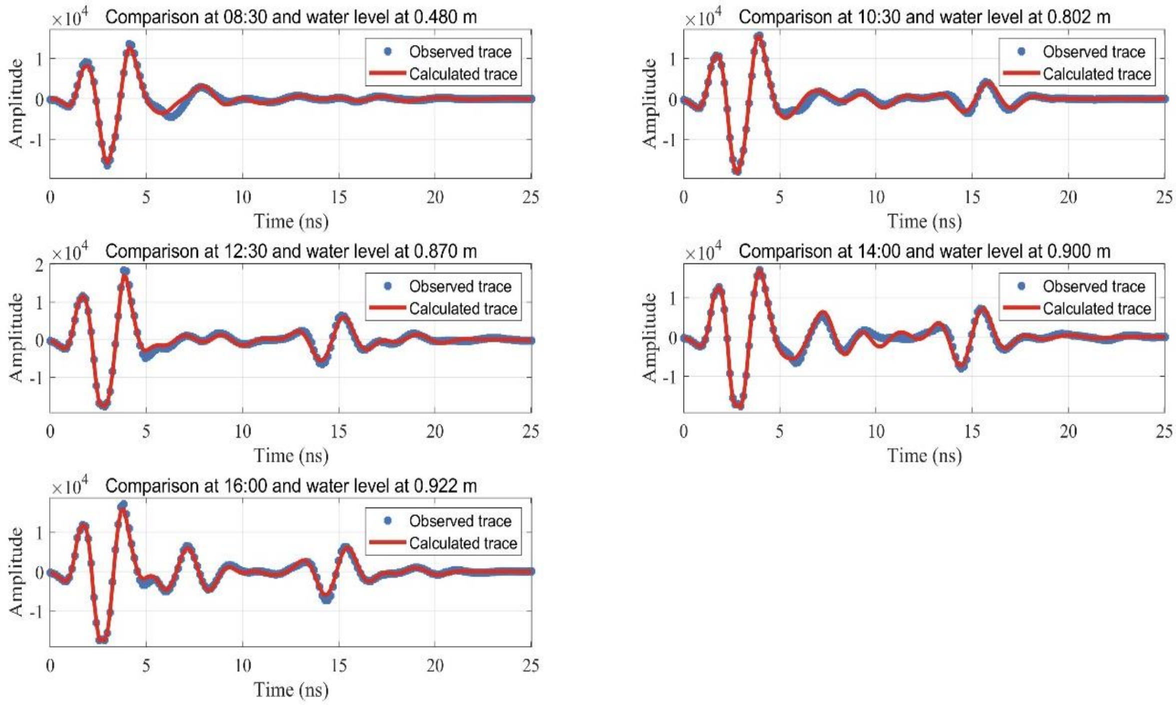

Figure 3.10 The fitness between the observed traces and calculated traces from inverted results at different time points during the drainage experiment. The solid red lines represent the observed data and the blue dotted lines represent the calculated data.

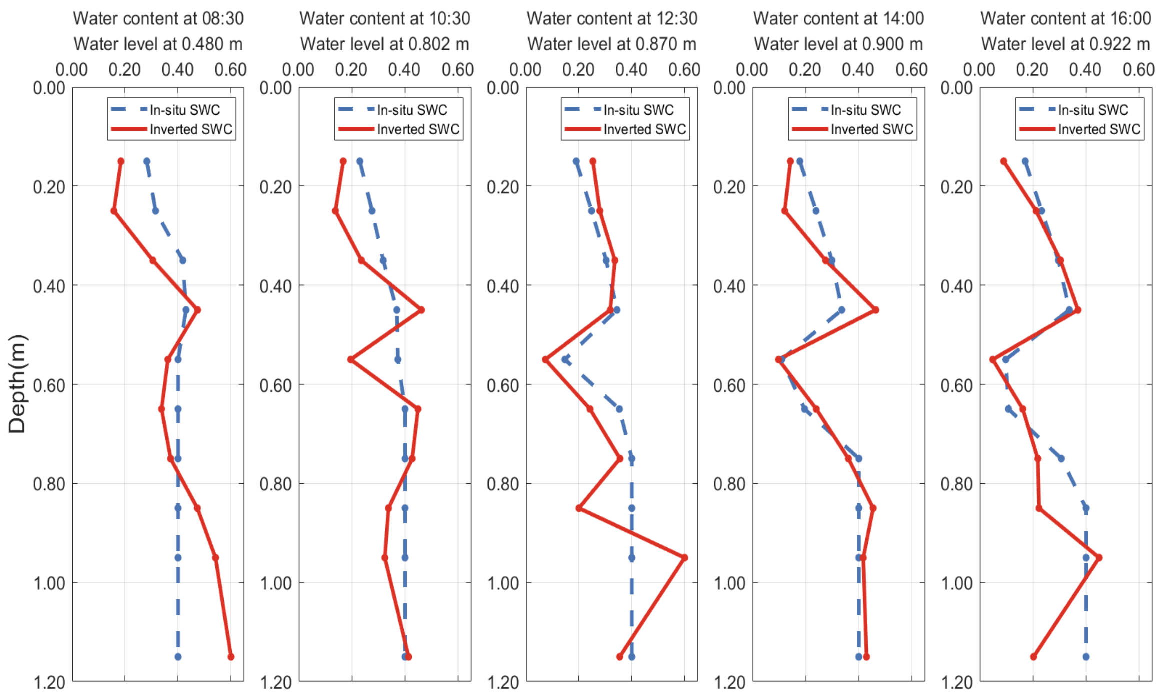

Figure 3.11 The SWC profiles at different time points during the drainage experiment. The red solid lines represent the SWC measured by Sentek sensors. The blue dashed lines represent the inverted SWC.

3.4 Infiltration experiment

3.4.1 Data acquisition and processing

Fig. 3.12 shows the setup for GPR experiment and delineates the position of the GPR during the infiltration experiment. Then, a rectangular wooden box with open top and bottom was set up at the selected location, with gravel laid at the bottom of the box to facilitate subsequent adjustment of the water level inside the box. The dimensions of the rectangular wooden box are 1 m in length and 0.68 m in width.

A high-resolution common offset measurement was carried out by utilizing a surface coupled MALA RAMAC GPR system with a center frequency of 800 MHz. To protect the GPR antenna from water damage and minimize the impact of water during the experiment, it was wrapped in a plastic protective covering and placed was in the wooden box (as shown in Fig. 3.12a) for data acquisition. The GPR data acquisition commenced at 10:46 am when the water was injected into the wooden box. The GPR system was configured to record a trace at 2 s intervals, ensuring the resolution of monitoring the wetting front during the infiltration process over time.

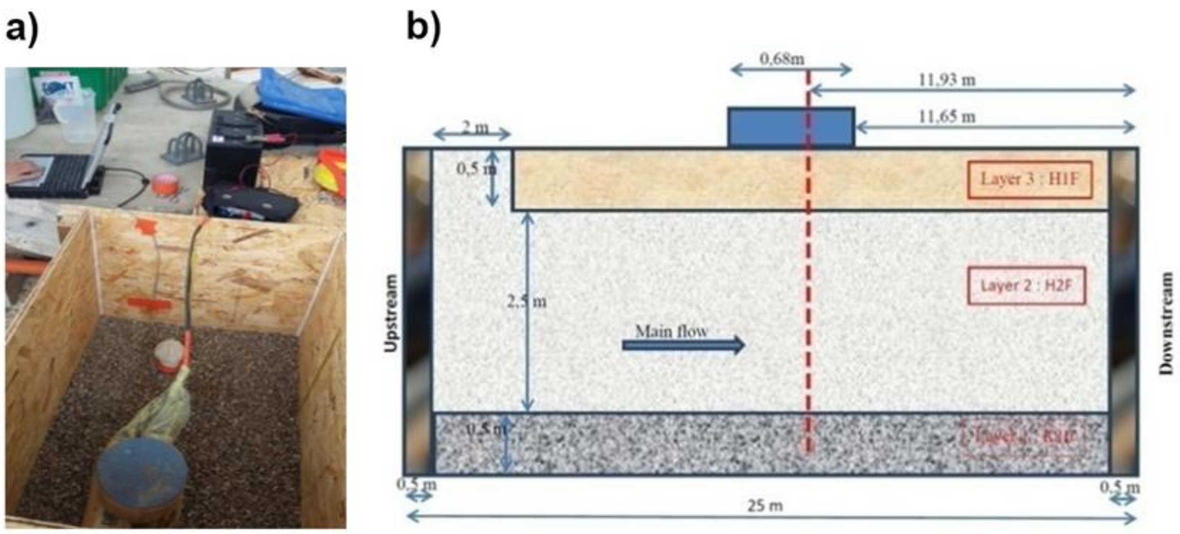

Figure 3.12 a) The illustration of the setup for the infiltration experiment. b) The illustration for the position of the wooden box.

The GPR experiment was divided into two distinct stages: an infiltration phase at constant water height followed by an infiltration phase at descending water height. In the initial phase of constant head infiltration, water was continuously supplied into the wooden box to sustain a consistent water level of 15 cm in the box above the gravel. Transitioning into the second phase, water injection was ceased, permitting the water within the wooden box to percolate downwards freely. During the course of these measurements, a discrepancy was identified between the operational time as recorded by the computer and the actual elapsed time of the experiment. To rectify this for data processing purposes, the initial time interval set between successive traces, originally at 2 s, was adjusted to 3 s to more accurately reflect the real-time soil water dynamics observed during the infiltration experiment. Additionally, a Direct Current (DC) filter was implemented alongside a static time shift correction of 29 samples to refine the data quality.

3.4.2 Data analysis and interpretation

The processed GPR profile is shown in Fig. 3.13. We can figure out the discernible reflection from the boundary between the two soil layers (around 0.5 m deep) and from the water table (approximately 0.85 m). Notably, both the two reflection arrival times exhibit an increment with the infiltration times, attributable to the augmentation of water content within the sand (the velocity of GPR waves is decreasing).

The water front is observed to reach the boundary of the two soil layers at around 1387 s (as indicated by the yellow arrow in Fig. 3.13) and it then arrived at the water table (around 0.85 m) at roughly 3694 s (as denoted by the white arrow in Fig. 3.13). At around 4970 s (as highlighted by the red arrow in Fig. 3.13), the wooden box is devoid of water. At this juncture, we can notice that the overall arrival times of the GPR data shifted upwards, nearly returning to the pre-experiment positions. Particularly, the arrival time of the GPR reflection from the contact of the two-soil layer sand the water table is decreasing with the infiltration times, reflecting the diminishing water content results in an increased velocity of GPR waves and causing the arrival time of reflection to advance.

This insight into the soil water dynamics and capillary action confirms the ability of GPR to capture complex hydrological processes within the subsurface, providing valuable data for understanding soil-water interactions.

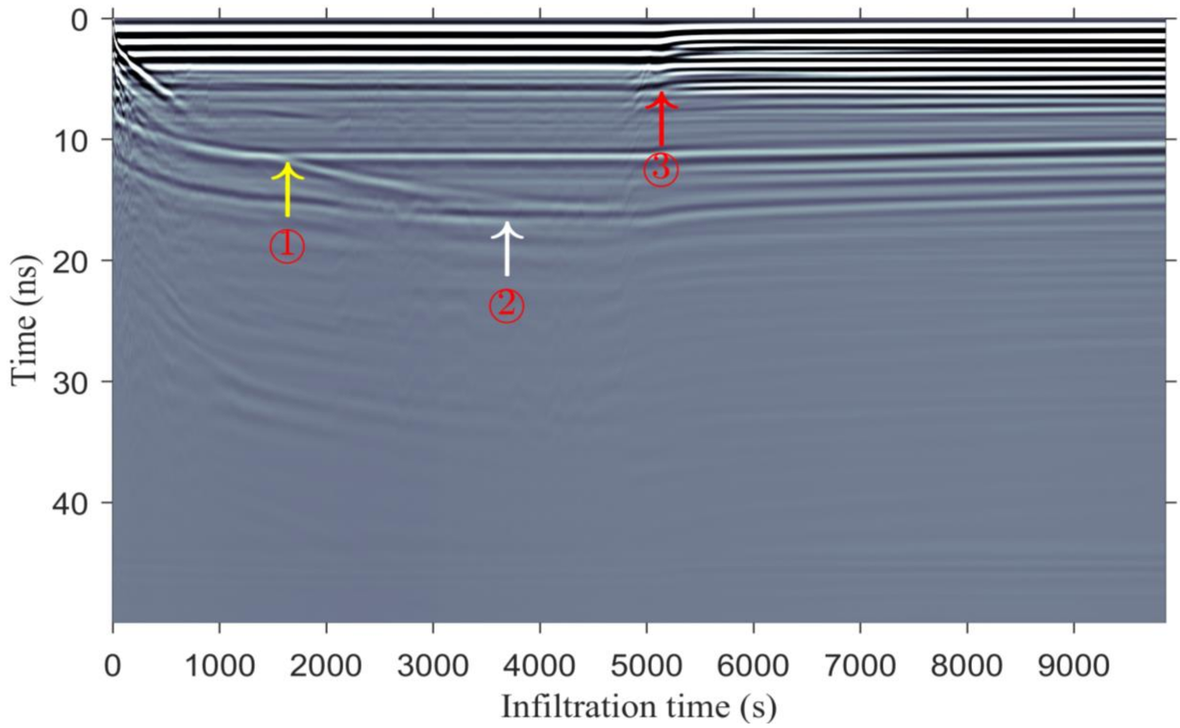

Figure 3.13 The processed profile for infiltration experiment. The yellow arrow presents the time (1387 s) when the water front arrives at the boundary of the two soil layers at 0.5 m. The white arrow shows the time (3694 s) when water front reaches to the water table at 0.85 m. The red arrow indicates the time (4970 s) when there is no water inside the wooden box causing the change of the GPR data.

To enhance the visualization of the water front's progression, we selected six representative traces from different time points during the infiltration process. These traces are presented at the right of Fig. 3.14. Through these selected traces, the advancing movement of the water front is discernible, as evidenced by the incremental increase in the arrival time of reflection across the various traces. The markers labeled 1, 2, and 3 in Fig. 3.14 highlight the GPR reflections attributed to the advancing water front, the boundary between the two soil layers (approximately 0.5 m), and the water table (approximately 0.85 m), respectively.

At the 300 s, the first reflection (labeled as 1) precedes the second and third reflections (labeled as 2 and 3, respectively). By 2400 s, reflection 1 is observed to be situated between reflections 2 and 3. After approximately 3600 s, reflections 1 and 3 coincide, signaling that the water front has reached the vicinity of the water table. Continuing until 4970 s, after the constant head experiment ended and the remaining water in the wooden box was allowed to infiltrate freely. In Fig. 3.14, the GPR signal at 6170 s and 9855 s demonstrated that, as the water moved downward through the medium, the main reflection in the GPR signals gradually decreased and shifted forward. This detailed observation of the traces not only highlights the dynamic nature of the soil water but also emphasizes the efficacy of GPR in monitoring such hydrological phenomena.

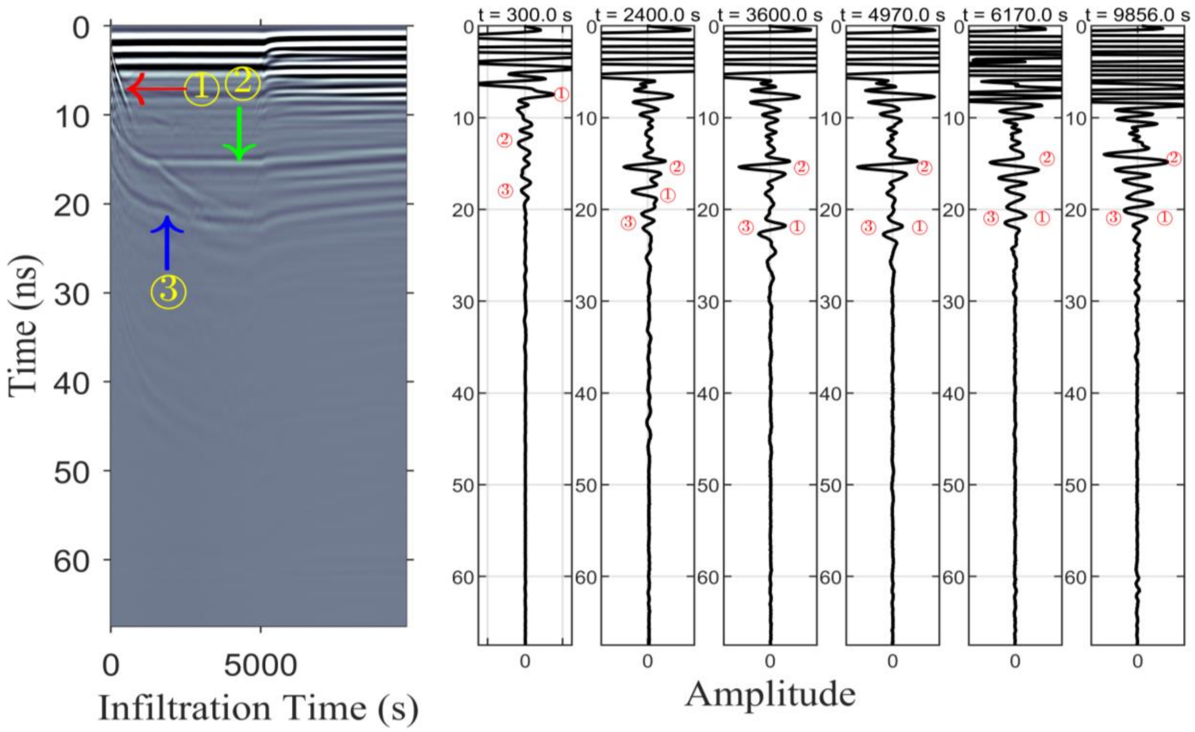

Figure 3.14 The six traces picked up from GPR profile. The signals denoted by 1, 2 and 3 show the reflections from water front, two soil layers boundary (around 0.5 m deep) and water table (around 0.85 m deep), respectively.

3.5 Results and discussion of infiltration experiment

In the infiltration experiment, the analysis approach adopted for each trace mirrored that employed in the imbibition and drainage experiments. To evaluate the efficacy of the proposed scheme in estimating SWC and in monitoring soil water dynamics throughout the infiltration process, and with a particular focus on the soil water dynamics during the constant head infiltration, we further intensified observations during the stage of constant head infiltration. We picked up five traces from the radargram corresponding to five distinct time points: 300 s, 600 s, 1200 s, 2400 s, and 3600 s. These traces were subjected to the estimation of the SWC, the quality factor and the layer thickness through the proposed inversion scheme.

According to the measurements obtained from Sentek sensors, the subsurface was partitioned into 10 layers for the inversion process. This structured approach facilitated a detailed analysis of the SWC variation within each layer across the different time points of the infiltration experiment. For inversion analysis at each time point, the population size was set to be 320, and the number of iterations was set to be 2000, ensuring a comprehensive search for optimal solutions. A total of 10 tests were conducted for each inversion to validate the robustness and reliability of the estimations. The SWC data measured by Sentek sensors served as prior information. The upper and lower limits of the search areas in all inversions were set to deviate by 50% from the prior information. This approach allowed for a flexible yet informed exploration of the parameter space, ultimately yielding more accurate and representative SWC estimations through the proposed inversion scheme.

Fig. 3.15 presents the fitness between the calculated traces derived from the model outcomes of the proposed inversion scheme and the observed traces for each selected time point during the infiltration experiment. This comparison aims to validate the effectiveness of the proposed scheme. As shown in the figure, the calculated GPR trace from the inverted results match very well with the observed trace collected at all time points.

Moving on to Fig. 3.16, the comparison between the inverted SWC obtained through the proposed inversion scheme and the SWC measured by Sentek sensors is presented for various time points throughout the infiltration experiment. This figure helps us understand the distribution and dynamic changes of SWC with depth and over time. The inverted SWC profiles exhibit a trend that closely mirrors that of the measured SWC profiles, indicating the reliability of the inversion process in capturing the dynamics of soil water during the experiment. A detailed observation of the changes in SWC, particularly at a shallow depth of approximately 0.4 m, reveals the initial impact of the infiltration process. In the shallow depth, the SWC decreases with increasing depth at all time points. This is due to the influence of soil pore structure and water tension, which slows down the rate of water percolation deeper into the soil. In the early infiltration stages (300 s and 600 s), the inverted SWC closely match those from the in-situ sensors, especially in the shallower layers (0-0.4 m). This suggests that, in the initial stages of infiltration, the GPR inversion can accurately reflect the actual conditions of soil water. By the 1200 s, there is a noticeable albeit slight increase in SWC at the boundary of the two soil layers (around 0.5 m), but this layer does not yet appear to be significantly influenced by the water front. However, as the experiment progresses to 2400 s and 3600 s, an increase in SWC below the 0.5 m becomes evident. This indicates that the water front has successfully penetrated beyond the boundary between the two soil layers (around 0.5 m). During the progresses (from 1200 s to 3600 s), the difference between the two methods become more pronounced, particularly in the deeper layers (0.4-0.8 m). This may be due to the reduced responsiveness of the GPR to changes in SWC at deeper levels, or because the in-situ sensors have higher sensitivity in these deeper layers. This analysis provides valuable insights into the temporal and spatial variations of SWC.

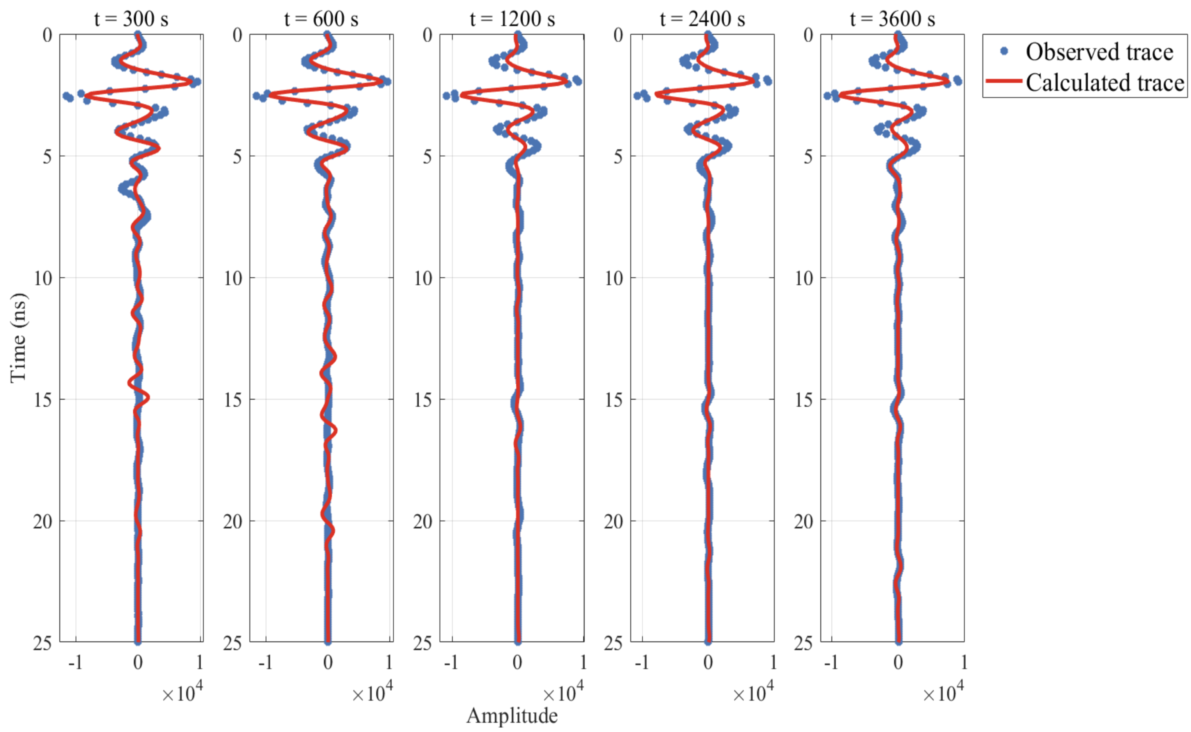

Figure 3.15 The fitness of calculated trace from the inverted results and the observed trace at different time points during the infiltration experiment. The red solid lines represent the observed data and the blue mark dotted lines represent the calculated data.

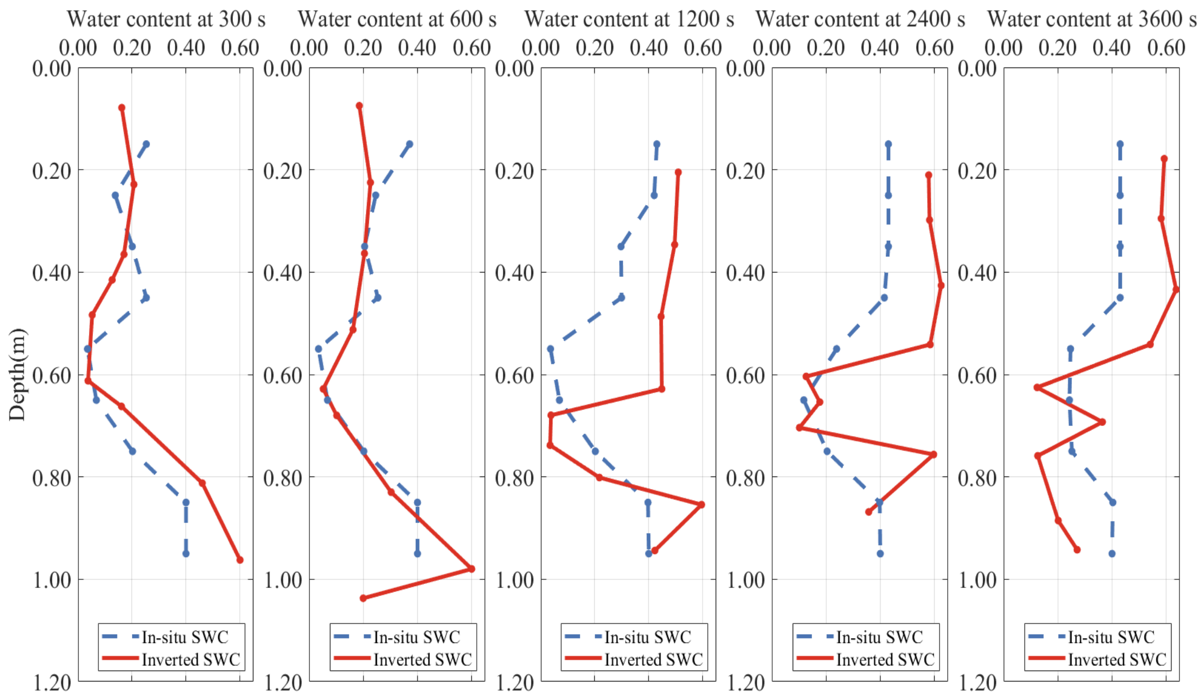

Figure 3.16 The comparison of SWC profiles at different time points during the infiltration experiment. The red solid lines represent the SWC measured by Sentek sensors. The dashed blue lines represent the inverted SWC.

During the infiltration experiment monitored by GPR, we found that it is difficult to identify changes in GPR profile data caused by uneven SWC distribution with the progress of the experiment. In addition, strong reflections between certain media can also weaken the GPR data response caused by SWC differences. And it can be note that the accuracy of GPR inversion in deeper soil may be limited by the resolution and penetration capabilities of the equipment. To improve the accuracy of SWC inversion in deep soil, more improved data processing algorithms might be required. Therefore, we proposed a time-lapse GPR waveform inversion method based on the double-difference method. For this purpose, we re-selected six GPR waveform signals from the processed GPR profiles at six different time points during the constant head infiltration stage: 20 s, 300 s, 600 s, 1200 s, 2400 s, and 3600 s. Similarly, we evaluated SWC, quality factor, and layer thickness. The GPR signal extracted at 20 s was used as the initial data, and the initial model for inversion at each subsequent time point was the SWC obtained from the previous time point. According to the measurements from Sentek sensors, the subsurface soil was divided into ten layers. In the inversion analysis of the GPR signals extracted at each time point, the population size was set to 280, and the number of iterations was set to 2000 to ensure a comprehensive search for the optimal solution. Each inversion was tested 10 times. The SWC measured by Sentek sensors at each time point were used as prior information for the inversion at that time point. The upper and lower limitations of the search domain were set to a 50% deviation around the SWC measured by the Sentek sensors.

Fig. 3.17 shows the fitness between the calculated GPR traces obtained from inverted SWC and the observed GPR traces collected during the infiltration experiment. As shown in the figure, the calculated GPR traces match very well with the observed traces at all time points. Fig. 3.18 compares the inverted SWC obtained at different time points with the SWC measured by the Sentek sensors. As shown in the figure, the inverted SWC and the measured SWC are highly similar and match better compared to Fig. 3.16 at every time point. In the initial 20 s, the SWC is primarily concentrated in the topsoil (0-0.2 m). At this point, the two curves closely align indicating that the inverted SWC closely matches the in-situ measurements, demonstrating high initial validity of the proposed inversion scheme. After 300 s, the water begins to permeate downward to depths between 0.2 and 0.4 m. Although the SWC increases at 0.2 m, its concentration decreases compared to the 20-second mark. The consistency between inverted data and in-situ data remains good at this depth. At the 600-second mark, there is a significant increase in SWC between 0.2 and 0.4 meters, reflecting continued downward seepage. Water begins to appear at a depth of 0.6 meters, although the increase is modest. After 1200 s, the increase in SWC between 0.4 and 0.6 meters becomes more pronounced, indicating that water is progressively moving to deeper soil layers. Despite some deviations, the two curves generally coincide, reflecting the effectiveness of inversion methods in tracking the path of moisture penetration. However, compared to the SWC obtained using separate inversion strategies in Fig. 3.16, the fitness is higher, especially in the shallow layer. At 2400 s the SWC has increased across the soil layers from 0 to 0.6 meters. Notably, the increase in SWC at depths of 0.4 to 0.6 meters is particularly evident. During this period, the deviation between inverted data and measured data slightly increases, possibly due to soil heterogeneity. However, the deviation is smaller than the results in Fig. 3.16. An hour later (at 3600 s), the SWC across the entire measurement range continues to grow. By this time, the deeper soil layers from 0.6 to 0.8 meters also begin to show a significant increase in SWC. Although inverted data is slightly higher than measured data at some depths, overall, the two maintain good consistency.

Next, we calculated the difference between the inversion results of two consecutive time points. As shown in Fig. 3.19, the difference profiles further illustrate the movement of water infiltrated into the soil over time. The difference between the inversion SWC and the SWC measured by the Sentek sensors still shows a very similar trend. At 20 s, it can be seen that the soil water has only infiltrated the surface layer, causing a disturbance in the water content at the depth of 0.2 m. By 2400 s, the SWC at a depth about 0.5 m begins to change slightly, indicating that the wetting front has passed through two soil layer interface. By 3600 s, the wetting front has reached the groundwater level, and the difference in water content observed by both methods still matches well. The results indicate that the time-lapse GPR waveform inversion technique based on the double-difference method can further improve the monitoring accuracy of SWC changes when the GPR data reflection is not particularly significant.

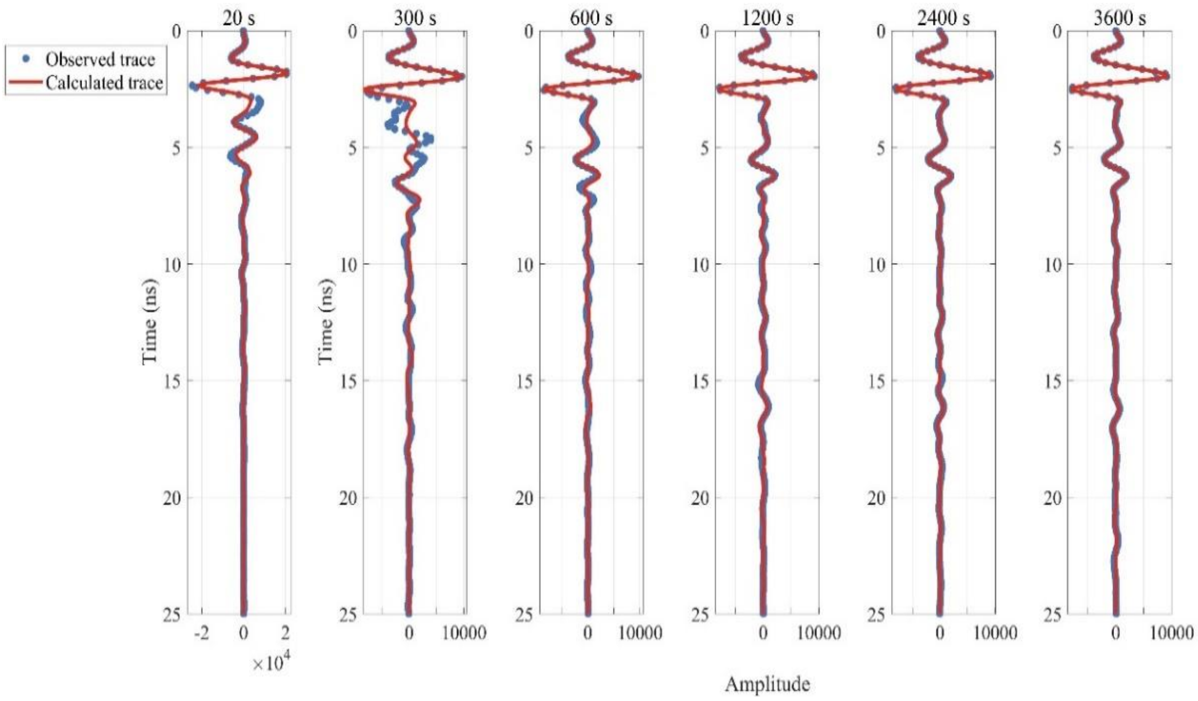

Figure 3.17 The comparison between the calculated GPR traces obtained from the inverted results and the observed GPR traces collected under time-lapse monitoring at different time points during the constant head infiltration experiment. The red solid lines represent the calculated GPR traces, while the blue star dotted lines represent the observed GPR traces.

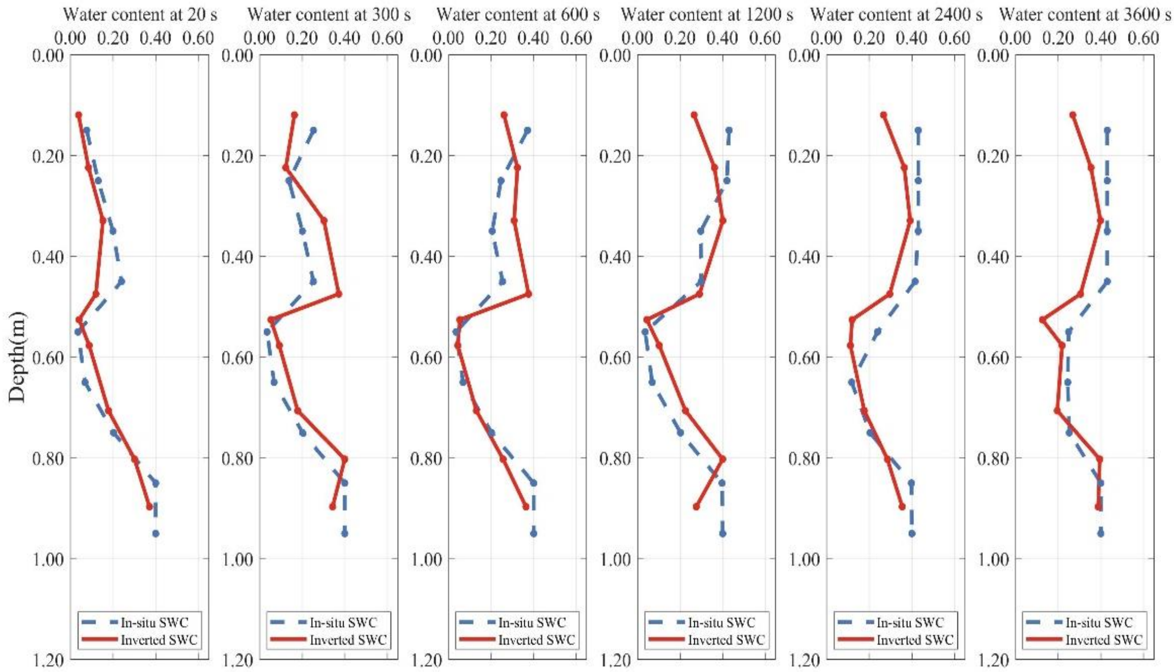

Figure 3.18 The comparison of SWC under time-lapse monitoring at different time points during the constant head infiltration experiment. The red solid lines represent the inverted SWC, while the blue dashed lines represent the measured SWC.

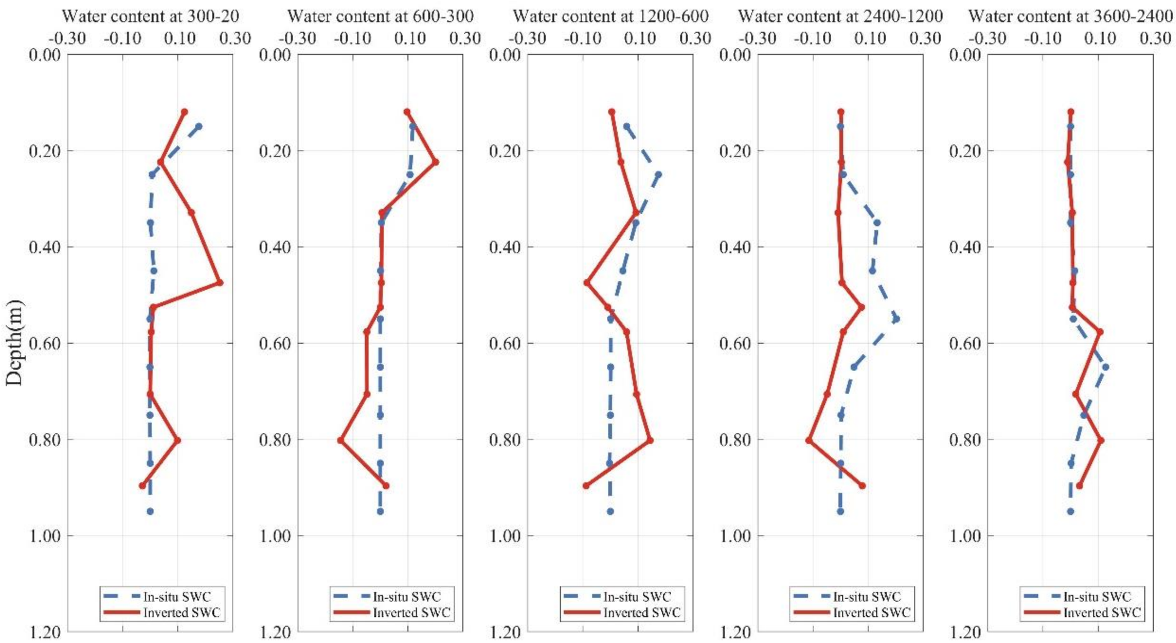

Figure 3.19 The comparison of SWC difference profiles between the double-difference time-lapse inversion results and the SWC measured by Sentek sensors during the constant head infiltration experiment. The red solid lines represent the inverted SWC, while the blue dashed lines represent the measured SWC.

3.6 Conclusions

In this chapter, we carried out high-precision monitoring of dynamic changes in SWC based on high-resolution time-lapse GPR waveform inversion. By combining the time-lapse inversion using the double-difference method with the technical scheme proposed in Chapter 2, we introduced a technique for precisely monitoring the dynamic changes in SWC based on time-lapse GPR waveform inversion with the double-difference method.

First, we introduced the basic theory of time-lapse inversion, including three commonly used time-lapse inversion strategies: individual inversion strategy, continuous inversion strategy, and double-difference inversion strategy. Then, two types of experiments were designed at the SCERES experimental site. One type simulates the spatial distribution and dynamic changes in SWC during the dynamic changes in the groundwater level, and the other simulates the migration of water and the spatial distribution and dynamic changes in SWC during precipitation infiltration from the surface.

For the precipitation infiltration and imbibition and drainage experimental data, we first used the individual time-lapse inversion to monitor the dynamic changes in SWC. However, we found that for the precipitation infiltration experiment, when water infiltrates from the surface, it enhances the amplitude of the direct wave of the GPR, making it difficult to identify deep signals. Therefore, we further introduced the double-difference time-lapse inversion. The results show that time-lapse GPR waveform inversion can monitor the dynamic changes in SWC with high precision, capturing real-time water migration in the soil. Moreover, the double-difference time-lapse inversion can monitor the dynamic changes in SWC more accurately during precipitation infiltration.

Chapter 4 Soil hydraulic properties direct and non-invasive estimation based on GPR waveform inversion

SHP are important factors for characterizing the transport of water and solute in soils, and it is also crucial to accurately estimate these parameters for tracking the movement of water and solute in soils. Traditional methods for determining SHP include laboratory measurements or using sensors buried underground to measure SWC, followed by fitting the SWC to determine the SHP. The disadvantages of these methods are that they can cause damage to the soil structure and are also relatively labor- and resource-intensive. Therefore, GPR has become a potential and non-destructive method for estimating SHP. However, in last decades, only partial information from GPR data is used for determining SHP. In real situation, the change of SWC also cause changes in the waveform and phase information of GPR data. To improve the accuracy of estimating SHP, we proposed to optimize GPR waveform inversion by using the GWO algorithm for directly and non-invasively determining the SHP. However, during the inversion process, we found that the convergence factor of the standard GWO is linear, which does not conform to the nonlinear characteristics of the optimization process for the GWO. Therefore, we further improved the GWO to enhance the assessment accuracy. This chapter firstly introduced the soil hydraulic model and the relative theory for improved GWO. Then we firstly realize the optimization by using the standard GWO, and test the effectiveness of the proposed scheme on numerical experiments and real measured data. Finally, the improved GWO is used to optimize the direct inversion of SHP based on GPR waveform data. The results show that the proposed direct inversion scheme can directly and efficiently determine the SHP from GPR waveform data, and the improved GWO is closer to the search process of the GWO, thereby improving the accuracy of estimating the SHP.

4.1 Theory and workflow

4.1.1 Soil hydraulic model

In practical measurements, the SWRC generally represents the relationship between several pressure heads and their corresponding SWC. However, information about SWC under unmeasured pressure heads is unknown. Thus, it is necessary to obtain a more complete

SWRC by iteratively fitting existed soil pressure head data and corresponding SWC data. In numerous studies, we have found that the van Genuchten model is a SWRC applicable across almost all types of soils, making it the most widely used soil hydraulic model.

In this study, when soil water reaches hydrostatic equilibrium, we adopt the van Genuchten model as the soil hydraulic model to describe the relationship between SWC and depth. The expression of the van Genuchten model is as follows:

$$\theta(h) = \begin{cases} \theta_r + (\theta_s - \theta_r)[1 + |\alpha h|^n]^{-m}, & h < 0 \\ \theta_s & , \ h \geq 0 \end{cases} \quad (4.1)$$

where θ $[\mathrm{m}^3 \cdot \mathrm{m}^{-3}]$ represents the volumetric water content of soil, θ_r $[\mathrm{m}^3 \cdot \mathrm{m}^{-3}]$ and θ_s $[\mathrm{m}^3 \cdot \mathrm{m}^{-3}]$ represent respectively the residual SWC and saturated SWC, h $[\mathrm{m}]$ stands for the pressure head, α $[\mathrm{m}^{-1}]$ and n [–] determine the shape of curve, which are related to the inverse of the air entry value and the width of the pore size distribution. According to Mualem condition, m [–] can be calculated from n [–] by using the following equation:

$$m = 1 - (1/n), \quad n > 1 \quad (4.2)$$

When the depth of the underground water table is z_w $[\mathrm{m}]$, the pressure head h $[\mathrm{m}]$ can be related to the depth z $[\mathrm{m}]$ by using following equation:

$$h = z - z_w \quad (4.3)$$

4.1.2 Constructing objective function

The goal of this chapter is to directly and simultaneously obtain the four unknown SHP (θ_r, θ_s, α and n) in equation (4.1) from GPR waveform data. Therefore, we firstly set the initial values for the four unknown parameters. Then, the profile, which describes the change of SWC with depth, is calculated through soil hydraulic model. According to the Topp equation, the SWC can be converted to soil dielectric permittivity and the GPR simulated data of the present model is obtained by performing GPR forward modeling. Finally, the objective function is constructed using L2 norm between the simulated data and the observed data, and an optimization algorithm is applied to iteratively update the initial model by minimizing the objective function. When a certain iteration criterion is met, the iteration will stop and the present obtained solution is considered as the final inversion result. The objective function is expressed as:

$$\phi(\mathbf{m}) = \sum_{i=1}^{N} \left(E_{obs}^{i} - E_{cal}^{i}(\mathbf{m}) \right)^{2} \qquad (4.4)$$

where $\mathbf{m}$ represent the inverted parameters, which include the SHP (θ_r, θ_s, α and n), the quality factor and the layer thickness, N is the number of time sampling points, E_{obs}^{i} and E_{cal}^{i} respectively stands for the GPR observed data and calculated data at the i^{th} sampling point.

In our study, we firstly applied the traditional GWO algorithm to optimize our objective function. However, we found that the convergence factor of traditional GWO algorithm linearly decreases with the number of iterations during the optimization process. This may lead to insufficient search in the early and later stages for the algorithm. Therefore, we improved the traditional GWO algorithm by making its convergence factor non-linearly decreasing. And in order to validate the effectiveness of the improved GWO algorithm, we also applied the improved algorithm to optimize the objective function.

4.1.3 Improved GWO algorithm based on sigmoid fuction

The Sigmoid activation function, also known as the logistic function, has a geometric shape of an S-curve (as shown in Fig. 4.1). The Sigmoid activation function is a widely used non-linear function in neural networks, which can map any input value to the interval of (0, 1). It can normalize input values and assign them a probabilistic meaning. The expression of the Sigmoid activation function is as follows:

$$f(x) = \frac{1}{1+e^{-x}} \qquad (4.5)$$

From Fig. 4.1, it can be seen that the sigmoid activation function $f(x)$ approaches 0 as the value of x approaches negative infinity. And the $f(x)$ approaches 1 as the value of x approaches positive infinity. When the value of $x$equals to 0, the $f(x)$ equals to 0.5, which means that the activation function is symmetric about the axis of (0, 0.5).

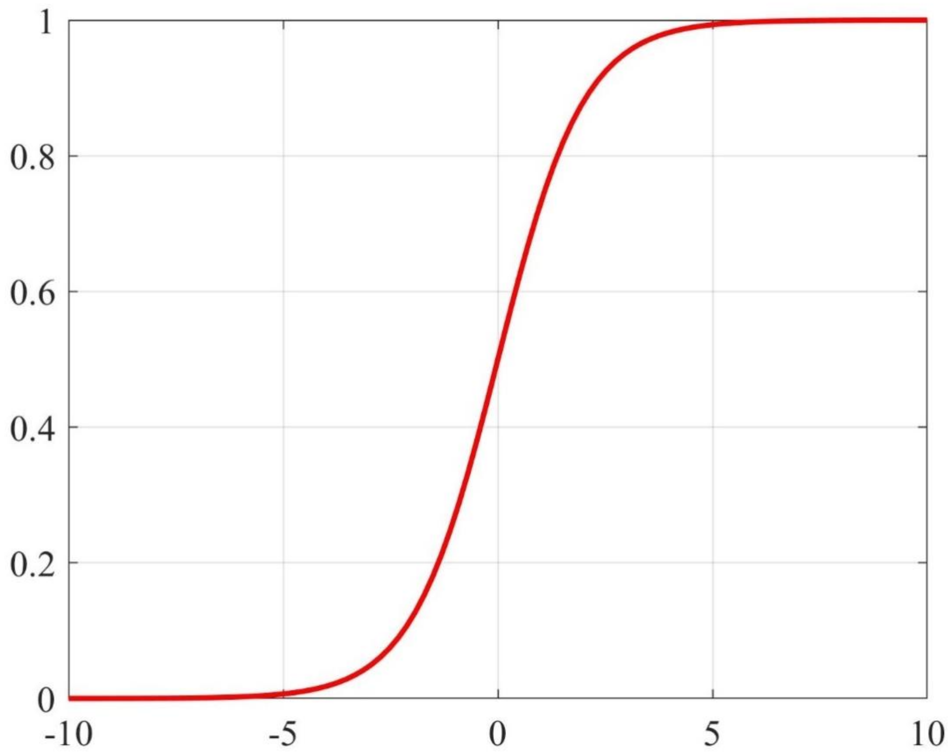

Figure 4.1 The shape of Sigmoid activation function

According to the basic theory of the GWO algorithm, it is known that the coefficient vector $\vec{A}$ determines whether the grey wolves perform global search or local search. When $|A|$>1, the grey wolves conduct global search, expand the search range for prey, and the GWO algorithm converge in a very fast speed. When $|A|$<1, the grey wolves conduct local search. The grey wolves gradually approach the prey and target it for capture. The convergence speed of the GWO algorithm will become slower. Additionally, the coefficient vector $\vec{A}$ changes linearly as the convergence factor a decreases from 2 to 0. However, during the entire convergence process of the algorithm, it can be observed from the convergence curve that the algorithm does not converge linearly with the increase in the number of iterations. Therefore, the linear decrease behavior of the convergence factor does not entirely conform to the actual optimization process of the algorithm. In order to more reasonably allocate the search speed for each stage of the algorithm, we proposed a convergence factor based on the sigmoid activation function, which guides the search process of the grey wolves during the prey hunting stage. At the same time, the proposed convergence factor ensures the GWO algorithm has stronger global optimization capabilities in the early stage and achieve faster convergence speed in the later stage. The improved expression of the convergence factor is as follows:

$$a = a_{final} + \frac{a_{initial} - a_{final}}{1+e^{\left(6\times\left(\left(\frac{2t}{t_{max}}\right)-1\right)\right)}} \quad (4.6)$$

where $a_{initial}$ and a_{final} respectively represent the initial and final value of the convergence factor, which are set to be 2 and 0. t is the present number of iterations. And t_{max} is the maximum number of iterations. The comparison of the improved convergence factor with the original convergence factor is shown in Fig. 4.2.

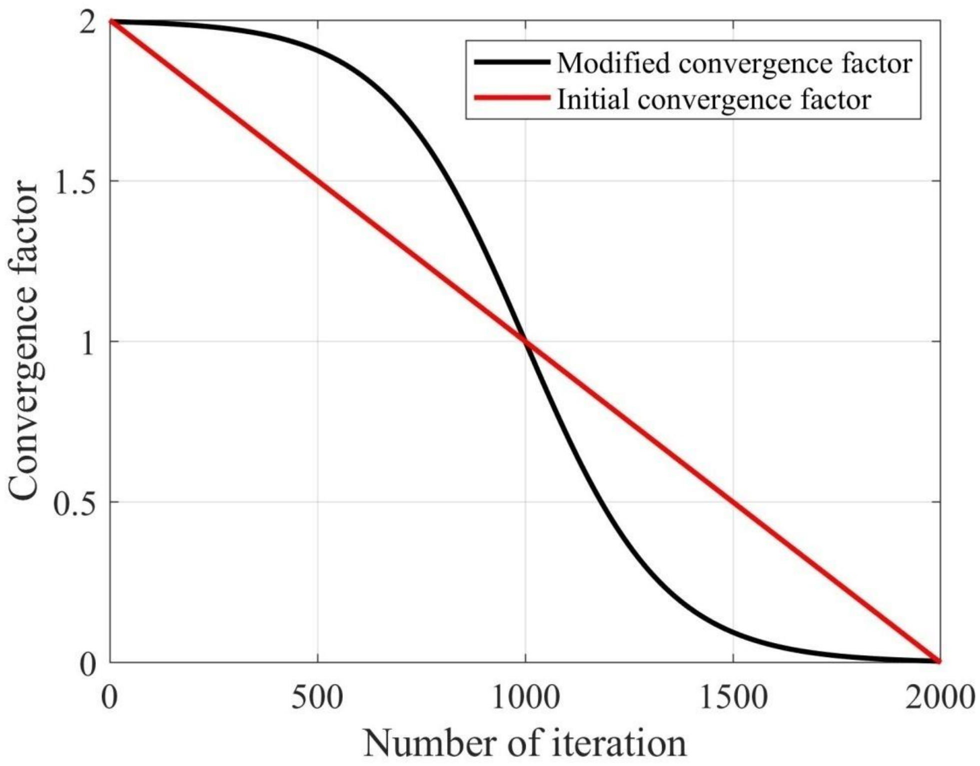

Figure 4.2 The change comparison of the improved convergence factor with the original convergence factor.

In Fig. 4.2, it can be observed that the original convergence factor linearly decreases from 2 to 0 at the same rate with an increase in the number of iterations. In contrast, the improved convergence factor is a curve based on the shape change of the sigmoid activation function. In the early iterations, the convergence factor decreases slowly and maintain a relatively large value for a longer period. This ensures that the coefficient vector $\vec{A}$ maintains larger values for a longer duration, which enhances the global search capability of the algorithm. In the later iterations, the rate of decrease slows down, which allows the convergence factor to maintain a relatively small value for an extended period. This ensures that the coefficient vector $\vec{A}$ maintains smaller values for an extended duration, which improves the local search capability of the algorithm. In summary, the improved convergence factor balances the global and local search capabilities of the GWO algorithm and enhances the overall performance of the algorithm.

4.1.4 The workflow for estimating SHP

The key to optimizing the SHP inversion process based on GPR waveform data using the GWO algorithm lies in using the objective function established in this chapter as the fitness function for the optimization algorithm. Through continuous iteration, when the fitness function approaches zero, the optimal position of the grey wolves' population is the final inverted SHP. The overall workflow is illustrated in Fig. 4.3. The overall scheme is divided into the following five steps:

① Give the initial SHP (θ_r,θ_s,α and n), quality factor and the layer thickness.

② Calculate the SWRC through the soil hydraulic model.

③ Calculate the relative dielectric permittivity from the SWC by using the petrophysical relationship.

④ Obtain the GPR waveform data in time domain by GPR forward modeling.

⑤ Updating the initial SWC model by GWO algorithm to make the objective function close to the minimum value. If the stopping criterion is satisfied, the iteration will be stopped and obtain the final parameters. If not, backing to step ② and continue updating.

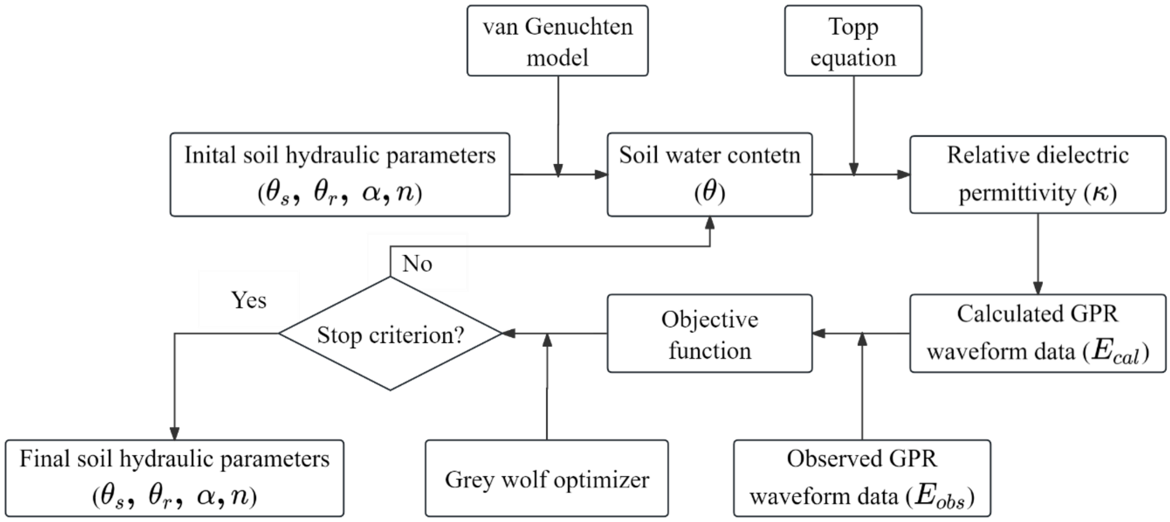

Figure 4.3 The workflow for SHP estimation with the proposed scheme.

4.2 Synthetic data inversion based on traditional GWO

Three numerical simulation experiments were designed for examining the performance of the proposed inversion scheme in directly estimate the SHP. In order to evaluate the performance of the proposed scheme as close to real conditions as possible, two typical soils were selected, namely sandy loam and sandy clay, and three numerical models were designed. The first two models are designed to simulate soil homogeneous half-space. The first model (Model A) only consists of sandy loam and the second model (Model B) only includes sandy clay loam. In the last model, two kinds of soils (sandy loam and sandy clay loam) are combined to construct the model (Model C). The SHP for these soils are defined according to the HYDRUS-1D software [184]. Table 4.1, 4.2 and 4.3 provide the SHP for theoretical Model A, Model B and Model C, respectively. It was assumed that the underground water table is at a depth of 0.85 m, and the soil below the water table is saturated. Then the SWRC are calculated through the soil hydraulic model. Figs. 4.4 and 4.5 present the SWRC (blue dotted line in Figs. 4.4b and 4.5b) and the corresponding GPR forward response (blue star dotted line in Figs. 4.4a and 4.5a) for the model A and model B. Fig. 4.6 shows the SWRC (blue dotted line in Fig. 4.6b) and the corresponding GPR forward response (blue star dotted line in Fig. 4.6a) for the model C. All the numerical examples were conducted with 10 tests. In each test, the size of population was selected to be 10 times the dimension of the solution space, and the number of iterations was chosen to be 2000. In order to simulate real field conditions with minimal prior information constraints, a broader search space boundary for solutions was defined during the inversion process. The upper and the lower values of the search space depart 50% from their true values in all the three numerical models.

Table 4.1 In Model A, the search space of solution, the SHP of theoretical model, the inversion results of synthetic data without noise, and the inversion results of synthetic data with noise.

SHP	Search space	SHP of theoretical model	Inversion results of synthetic data without noise	Inversion results of synthetic data with noise
θ_s (m^3/m^3)	0.205-0.615	0.410	0.406	0.414
θ_r (m^3/m^3)	0.033-0.098	0.065	0.090	0.049
α (1/m)	3.750-11.250	7.500	7.008	5.666
n	0.945-2.835	1.890	2.113	2.081

Table 4.2 In Model B, the search space of solution, the SHP of theoretical model, the inversion results of synthetic data without noise, and the inversion results of synthetic data with noise.

SHP	Search space	SHP of theoretical model	Inversion results of synthetic data without noise	Inversion results of synthetic data with noise
θ_s (m^3/m^3)	0.195-0.585	0.390	0.381	0.309
θ_r (m^3/m^3)	0.050-0.150	0.100	0.121	0.104
α (1/m)	2.950-8.850	5.900	4.419	3.475
n	0.740-2.220	1.480	1.635	1.738

Table 4.3 In Model C, the search space of solution, the SHP of theoretical model, the inversion results of synthetic data without noise, and the inversion results of synthetic data with noise.

SHP	Search space	SHP of theoretical model	Inversion results of synthetic data without noise	Inversion results of synthetic data with noise
θ_s^1 (m^3/m^3)	0.195-0.585	0.390	0.211	0.265
θ_s^2 (m^3/m^3)	0.205-0.615	0.410	0.424	0.441
θ_r^1 (m^3/m^3)	0.050-0.150	0.100	0.150	0.149
θ_r^2 (m^3/m^3)	0.033-0.098	0.065	0.059	0.064
α^1(1/m)	2.950-8.850	5.900	8.687	3.222
α^2(1/m)	3.750-11.250	7.500	10.570	6.936
n^1	0.740-2.220	1.480	2.180	2.018
n^2	0.945-2.836	1.890	1.886	2.157

4.2.1 Synthetic data without noise

The performance of the proposed SHP inversion scheme is firstly investigated on synthetic data without noise. Table 4.1, 4.2 and 4.3 present the inverted SHP based on model A, B and C, respectively. Figs. 4.4a, 4.5a and 4.6a present the fitting between the GPR waveform signals calculated based on the inverted SHP for Model A, B, and C, and the GPR waveform signals calculated based on the theoretical SHP. And Figs. 4.4b, 4.5b and 4.6b show the SWRC calculated through the inverted SHP of Model A, B and C.

From Figs. 4.4a, 4.5a and 4.6a, it can be noted that all the GPR signal responses (red solid lines) calculated from the inverted SHP almost perfectly fit the GPR signal responses (blue star dotted lines) calculated from the theoretical SHP. And in Figs. 4.4b, 4.5b and 4.6b, it can be also noted that all the calculated SWRC (red dotted lines) based on the inverted SHP still well fit with the calculated SWRC (blue dashed lines) based on the SHP of theoretical model.

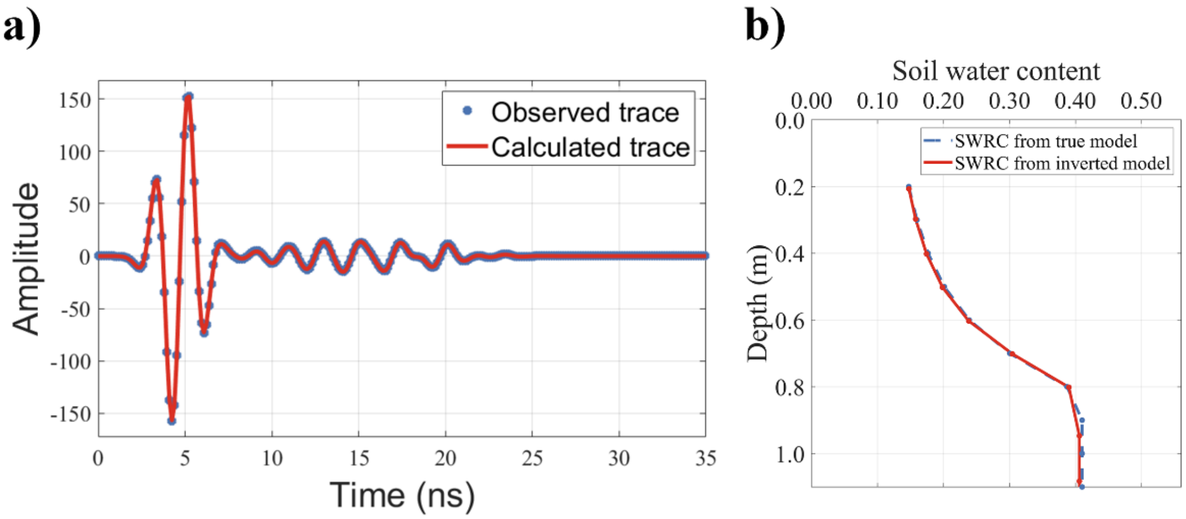

Figure 4.4 The inversion results of synthetic data without noise based on model A. a) The observed trace (blue star dotted line) calculated based on theoretical model and calculated trace (red solid line) from inverted result. b) The SWRC from true SHP of model (blue dotted line) and SWRC from inverted SHP of model (red solid line).

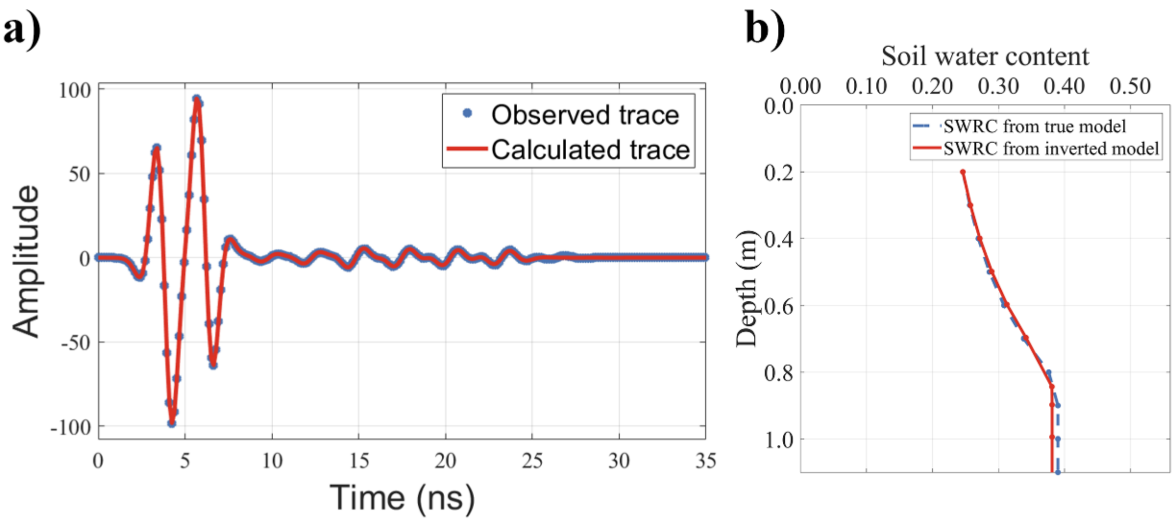

Figure 4.5 The inversion results of synthetic data without noise based on model B. a) The observed trace (blue star dotted line) calculated based on theoretical model and calculated trace (red solid line) from inverted result. b) The SWRC from true SHP of model (blue dotted line) and SWRC from inverted SHP of model (red solid line).

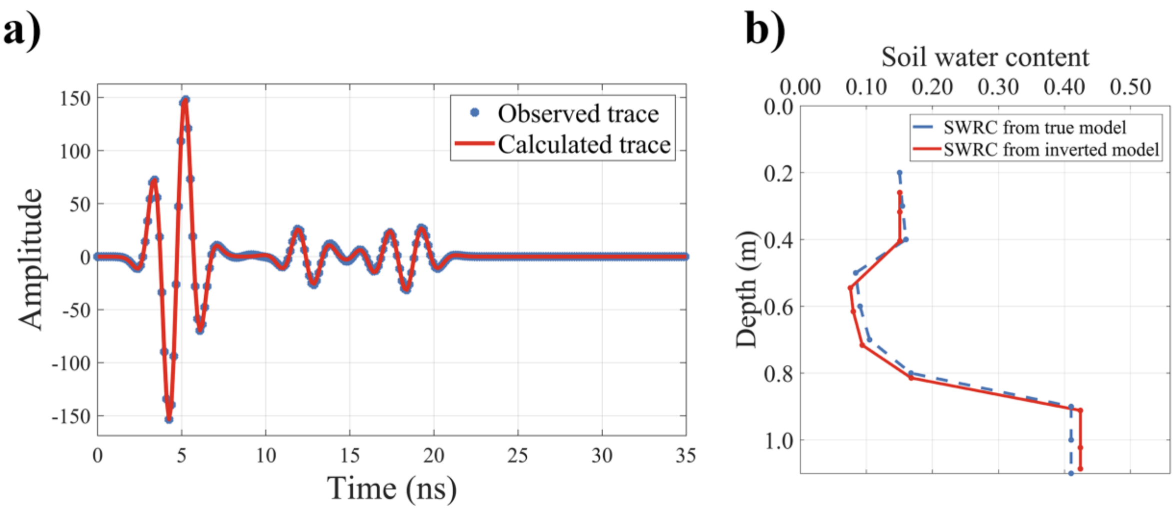

Figure 4.6 The inversion results of synthetic data without noise based on model C. a) The observed trace (blue star dotted line) calculated based on theoretical model and calculated trace (red solid line) from inverted result. b) The SWRC from true SHP of model (blue dotted line) and SWRC from inverted SHP of model (red solid line).

4.2.2 Synthetic data with noise

In real data, the noise is inevitable. Therefore, the performance of the proposed inversion scheme is further tested on synthetic data with noise. A 10% of white Gaussian noise is introduced into the GPR data of the three models. Table 4.1, 4.2 and 4.3 also present the inverted SHP of model A, B and C by the proposed inversion scheme on synthetic data with noise. Figs. 4.7a, 4.8a and 4.9a present the fitness between the observed traces calculated from the theoretical SHP and calculated GPR traces from the inverted SHP of Model A, Model B and Model C. And Figs. 4.7b, 4.8b and 4.9b show the SWRC of model A, model B and model C, respectively, calculated from the inverted SHP. From Figs. 4.7a, 4.8a and 4.9a, it can be noted that all the calculated GPR responses (red solid lines) from the inverted SHP can still match the observed GPR traces (blue star dotted lines) pretty well although the noise exists in the GPR data. And in Figs. 4.7b, 4.8b and 4.9b, it can be also found that all the SWRC (red dotted lines) calculated based on the inverted SHP well fit with the SWRC (blue dotted lines) calculated based on the SHP of theoretical models. These results verify the efficiency of the proposed inversion scheme for determining the SHP based on the inversion of GPR waveform data although there are minor differences between the SWRC from the inverted SHP and the

SWRC from the SHP of theoretical models. Overall, from the results in Tables 4.1, 4.2, and 4.3, it can be seen that the SHP are still well inverted.

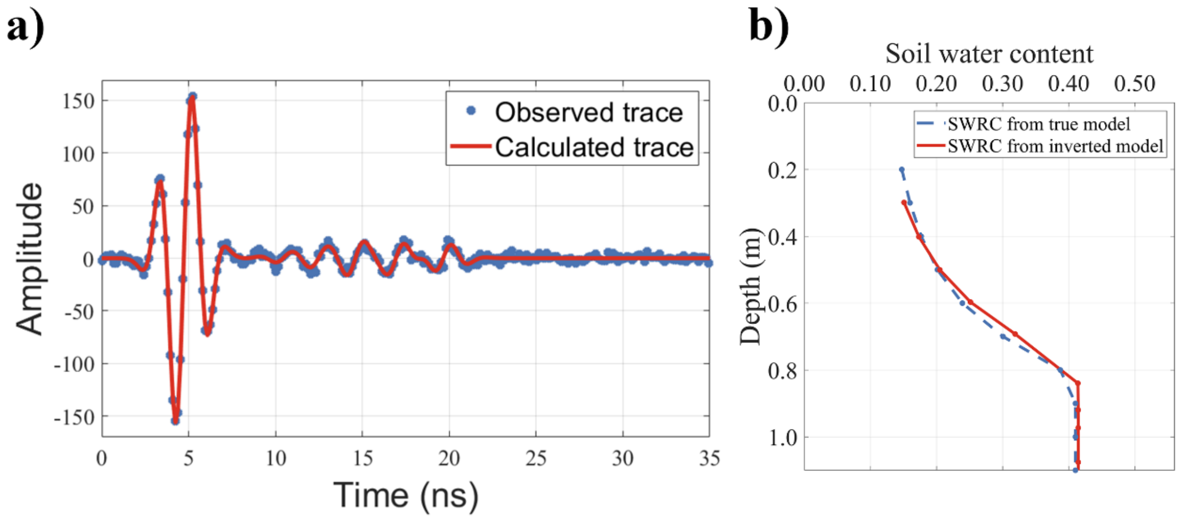

Figure 4.7 The inversion results of synthetic data with noise based on model A. a) The observed trace (blue star dotted line) calculated based on theoretical model and calculated trace (red solid line) from inverted result. b) The SWRC from true SHP of model (blue dotted line) and SWRC from inverted SHP of model (red solid line).

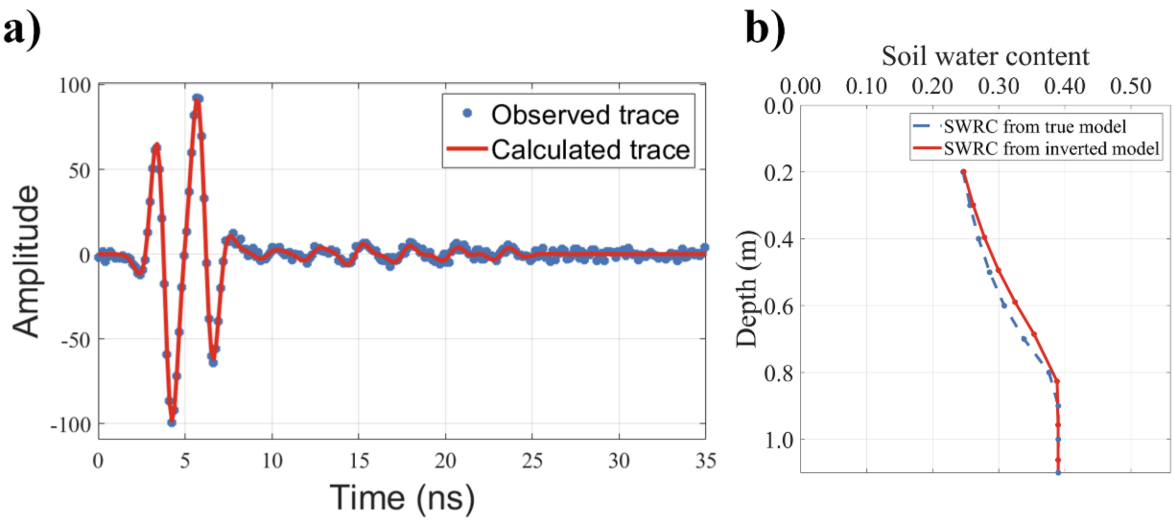

Figure 4.8 The inversion results of synthetic data with noise based on model B. a) The observed trace (blue star dotted line) calculated based on theoretical model and calculated trace (red solid line) from inverted result. b) The SWRC from true SHP of model (blue dotted line) and SWRC from inverted SHP of model (red solid line).

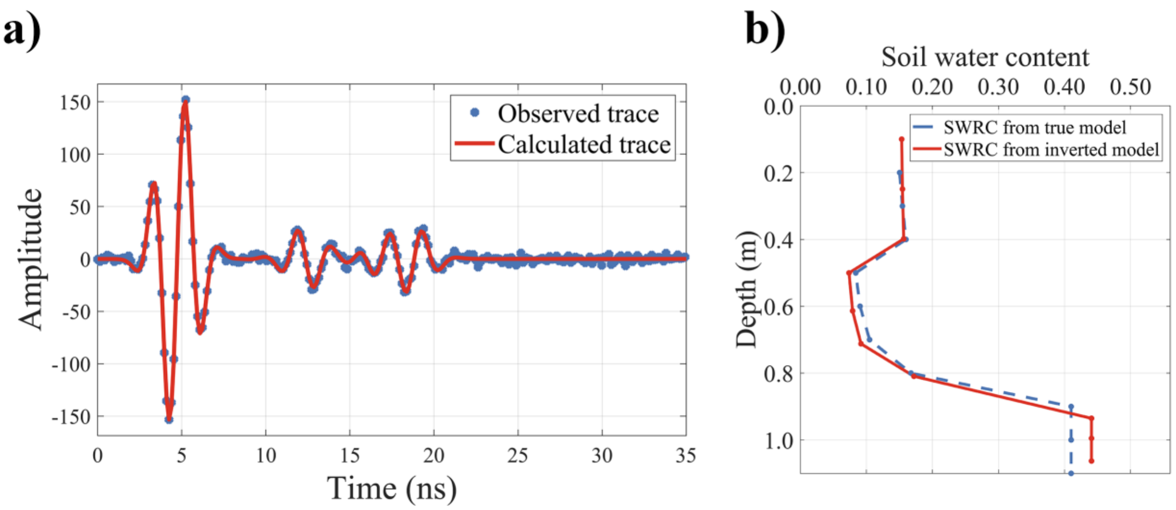

Figure 4.9 The inversion results of synthetic data with noise based on model C. a) The observed trace (blue star dotted line) calculated based on theoretical model and calculated trace (red solid line) from inverted result. b) The SWRC from true SHP of model (blue dotted line) and SWRC from inverted SHP of model (red solid line).

In order to investigate the convergence of the proposed inversion scheme, Fig. 4.10 shows the fitness curve of the data without noise and with noise corresponding to model C. According to the GWO algorithm, the convergence curve should decrease rapidly in the early stages. In Figs. 4.10a and 4.10b, the rapid decrease of the convergence curve can be noted at the early stages, which assists the algorithm to explore the search space extensively. In the later stages, the convergence curve should be gradually reduced to a stable value, which represents the algorithm entry into the local search stage. We can find that the convergence curve gradually becomes stable and converges to zero after around the 600th iteration from the curve of data without noise. From the curve of data with noise, it can be found that the curve gradually becomes stable and converges to a constant value after approximately 1000th iteration. These demonstrate that the GWO shows a good balance between global exploration and local exploitation. The GWO algorithm also has the ability for avoiding a high local optimum and achieving a fast convergence simultaneously.

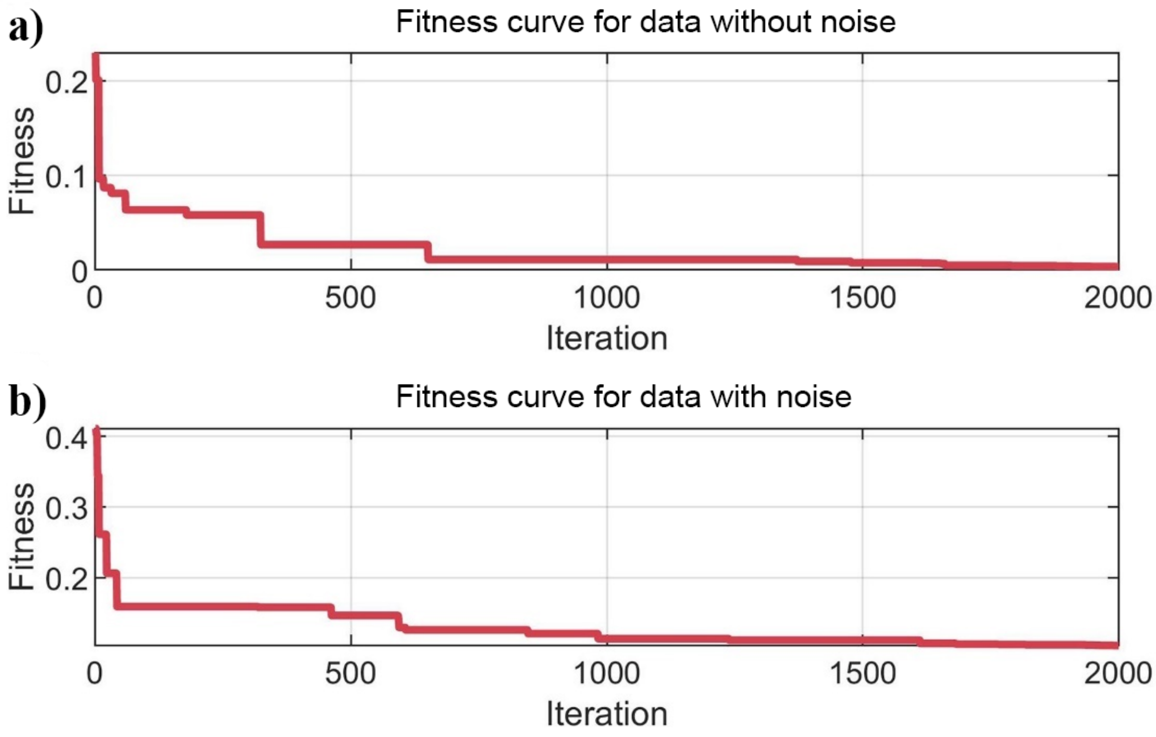

Figure 4.10 The fitness curve corresponding to Model C. a) The curve for data without noise. b) The curve for data with noise.

4.3 Experimental field data inversion based on traditional GWO

In order to further evaluate the applicability of the proposed scheme based on real condition, the real GPR data collected in an experimental field was analyzed using the proposed inversion scheme. The real data is the same as the real data collected in Chapter 2, which was collected by using the MALA RAMAC GPR system with a shielded antenna in fixed offset configuration. The central frequency of the antenna is 500 MHz. Similarly, the 700th trace was selected as the observed trace to realize the inversion by the proposed scheme. Fig. 4.11 shows the collected waveform signal. Table 4.4 provides the search space of alternative solution and the inverted SHP. During the inversion, the underground space is divided into 10 layers.

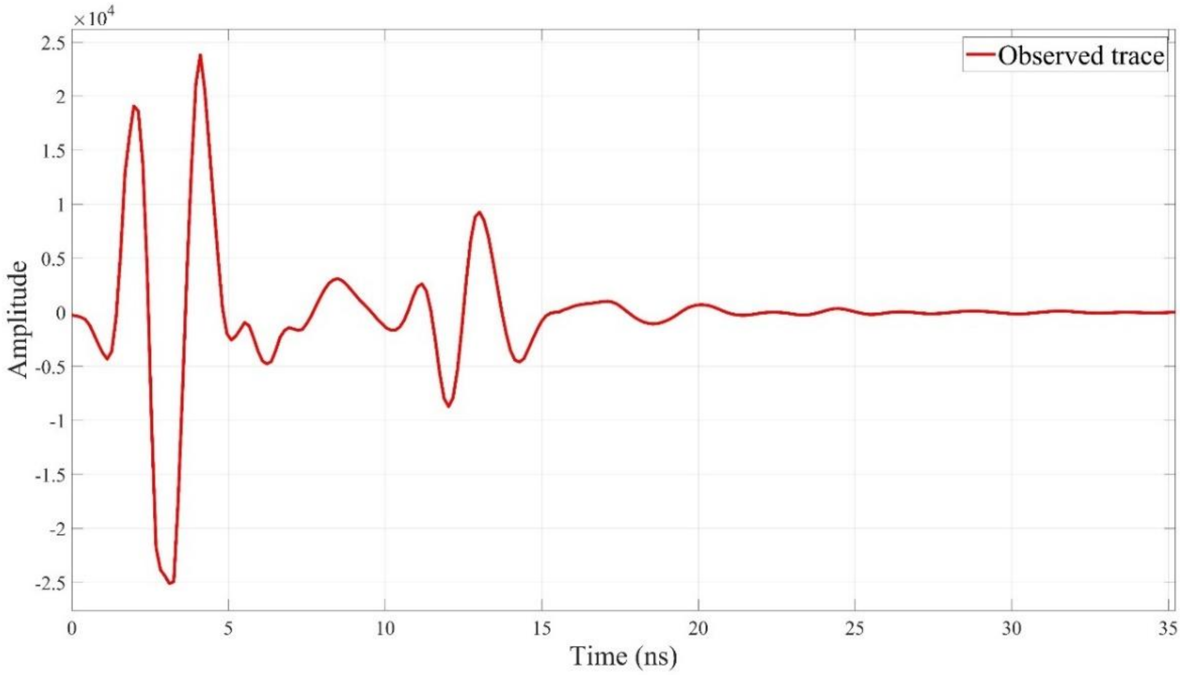

Figure 4.11 The real GPR waveform trace.

Table 4.4 The search space of alternative solution and the inversion results for the real data.

SHP	Search space	Inversion results
θ_s^1	0.350-0.500	0.423
θ_s^2	0.350-0.500	0.465
θ_r^1	0.010-0.100	0.063
θ_r^2	0.010-0.100	0.012
α^1	0.100-20.000	5.381
α^2	0.100-20.000	5.006
n^1	1.000-10.000	2.572
n^2	1.000-10.000	8.701

Fig. 4.12a shows the fitness between the calculated GPR trace from the inverted SHP and the observed GPR trace. And Fig. 4.12b presents the SWRC from the inverted SHP and the SWC profile measured by the Sentek sensors [180]which is installed in the experimental site for measuring the SWC profile. From Fig. 4.12a, it can be observed that the calculated GPR response (red solid line) from the final inverted solution matches reasonably well with the observed GPR trace (blue star dotted line), especially the main amplitudes where the match is quite high. And as shown Fig. 4.12b, the SWRC (red solid line) calculated from the inverted SHP exhibits a similar trend to the SWRC measured by Sentek sensors (blue dotted line). Below a depth around 0.85 m, there is no change of the SWC with increasing depth, which may be due to the soil becoming fully saturated below 0.85 m.

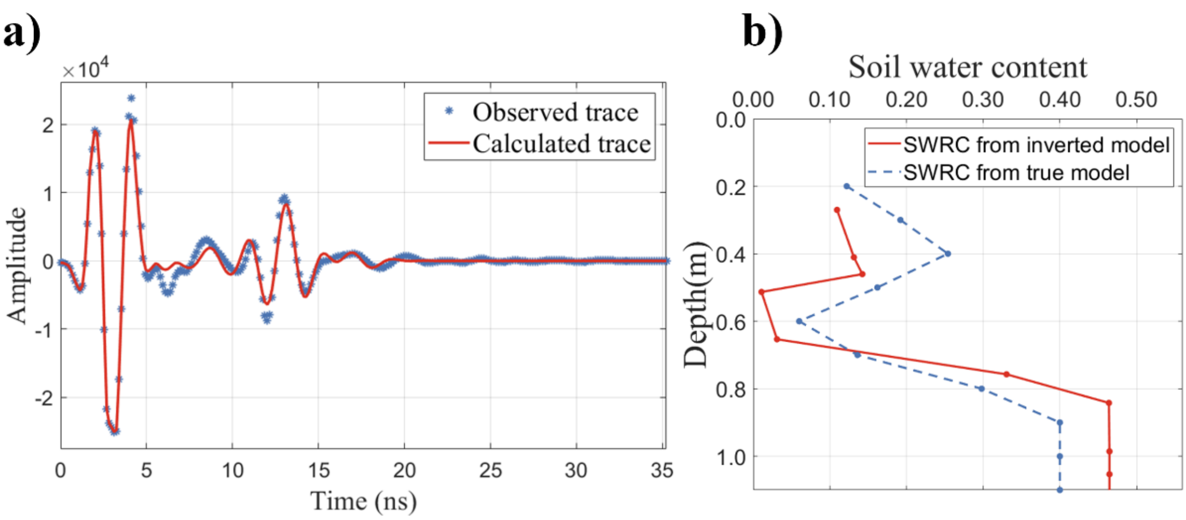

Figure 4.12 The inversion results based on traditional GWO for field experimental data. a) The comparison between the observed trace (blue star dotted line) and calculated GPR response (red solid line) from inverted SHP. b) The comparison between the measured SWRC (blue dashed line) and SWRC (red solid line) from inverted SHP.

4.4 Synthetic data inversion based on improved GWO

Based on the same testing model with the traditional GWO algorithm, we tested the improved GWO algorithm. And we conducted 10 times test for all numerical simulation experiments. The population size was set to be 10 times the data dimension for each test and the number of iterations was set to be 1500. The upper and lower bounds of the search space for alternative solution were set to the left and right 50% of the SHP for theoretical models.

4.4.1 Synthetic data without noise

We firstly conducted performance tests on synthetic GPR data without noise. Tables 4.5, 4.6, and 4.7 present the inverted SHP based on Model A, Model B, and Model C, respectively. Figs. 4.13a, 4.14a, and 4.15a show the fitting between the calculated GPR waveform data from the inversion results and the observed GPR waveform data from the theoretical SHP for the three models. Figs. 4.13b, 4.14b, and 4.15b present the SWRC calculated from the inversion results. From Figs. 4.13a, 4.14a, and 4.15a, it can be observed that the calculated GPR waveform responses (red solid lines) from the inverted SHP match almost perfectly with the observed GPR waveform trace (blue star dotted lines) from the theoretical value of true models. In Figs. 4.13b, 4.14b, and 4.15b, the results demonstrate that the SWRC (red solid lines) calculated from the inverted SHP show a very good match with the SWRC (blue dashed lines) calculated from the theoretical value of true models.

Table 4.5 In Model A, the search space of solution, the SHP of theoretical model, the inversion results of synthetic data without noise, and the inversion results of synthetic data with noise.

SHP	Search space	SHP of theoretical model	Inversion results of synthetic data without noise	Inversion results of synthetic data with noise
θ_s (m^3/m^3)	0.205-0.615	0.410	0.404	0.407
θ_r (m^3/m^3)	0.033-0.098	0.065	0.087	0.062
α (1/m)	3.750-11.250	7.500	6.647	6.312
n	0.945-2.835	1.890	2.122	2.074

Table 4.6 In Model B, the search space of solution, the SHP of theoretical model, the inversion results of synthetic data without noise, and the inversion results of synthetic data with noise.

SHP	Search space	SHP of theoretical model	Inversion results of synthetic data without noise	Inversion results of synthetic data with noise
θ_s (m^3/m^3)	0.195-0.585	0.390	0.388	0.393
θ_r (m^3/m^3)	0.050-0.150	0.100	0.136	0.106
α (1/m)	2.950-8.850	5.900	5.631	4.325
n	0.740-2.220	1.480	1.606	1.732

Table 4.7 In Model C, the search space of solution, the SHP of theoretical model, the inversion results of synthetic data without noise, and the inversion results of synthetic data with noise.

SHP	Search space	SHP of theoretical model	Inversion results of synthetic data without noise	Inversion results of synthetic data with noise
θ_s^1 (m^3/m^3)	0.195-0.585	0.390	0.227	0.321
θ_s^2 (m^3/m^3)	0.205-0.615	0.410	0.396	0.454
θ_r^1 (m^3/m^3)	0.050-0.150	0.100	0.149	0.148
θ_r^2 (m^3/m^3)	0.033-0.098	0.065	0.069	0.053
α^1(1/m)	2.950-8.850	5.900	5.160	5.721
α^2(1/m)	3.750-11.250	7.500	6.070	9.650
n^1	0.740-2.220	1.480	2.132	2.172
n^2	0.945-2.836	1.890	2.053	1.877

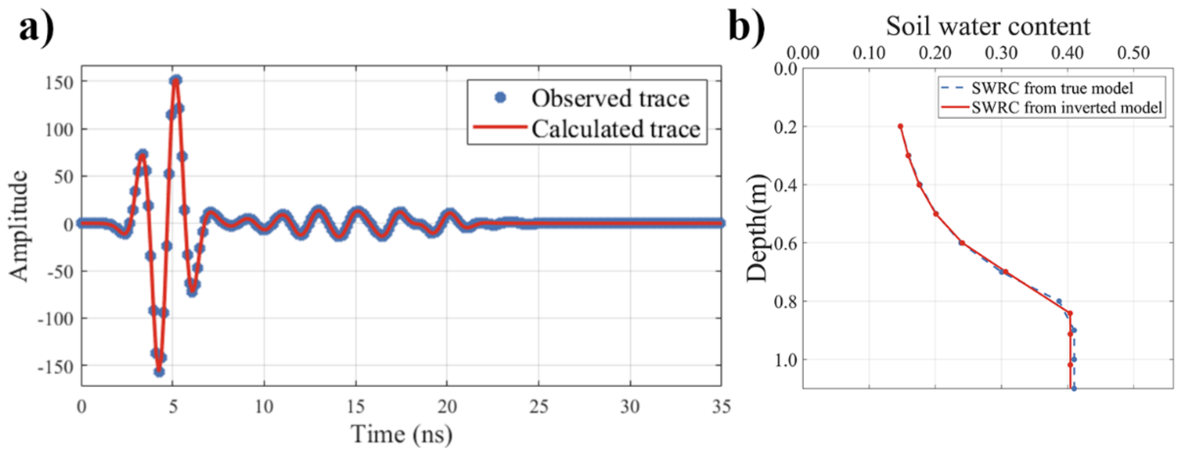

Figure 4.13 The inversion results of synthetic data without noise based on model A. a) The observed trace (blue star dotted line) calculated based on theoretical model and calculated trace (red solid line) from inverted result. b) The SWRC from true SHP of model (blue dashed line) and SWRC from inverted SHP of model (red solid line).

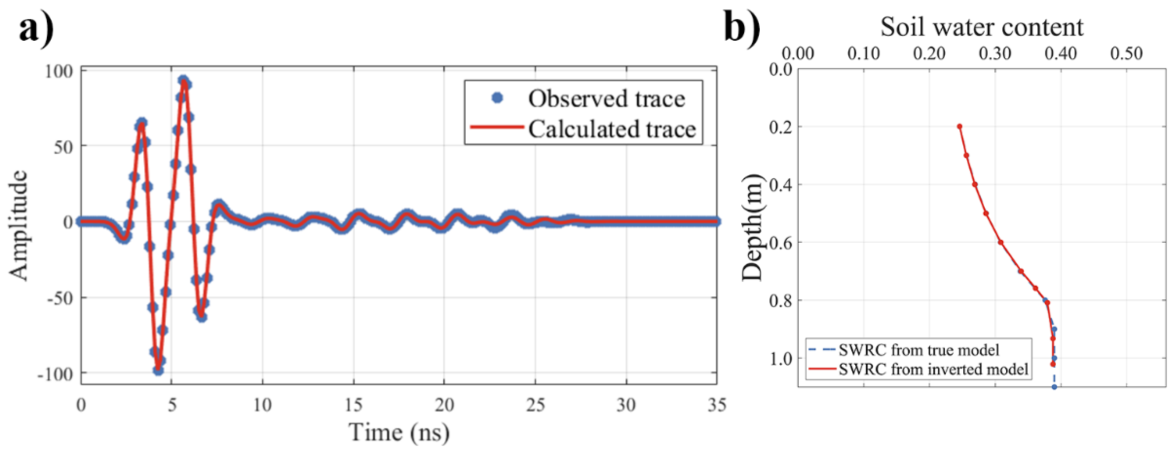

Figure 4.14 The inversion results of synthetic data without noise based on model B. a) The observed trace (blue star dotted line) calculated based on theoretical model and calculated trace (red solid line) from inverted result. b) The SWRC from true SHP of model (blue dashed line) and SWRC from inverted SHP of model (red solid line).

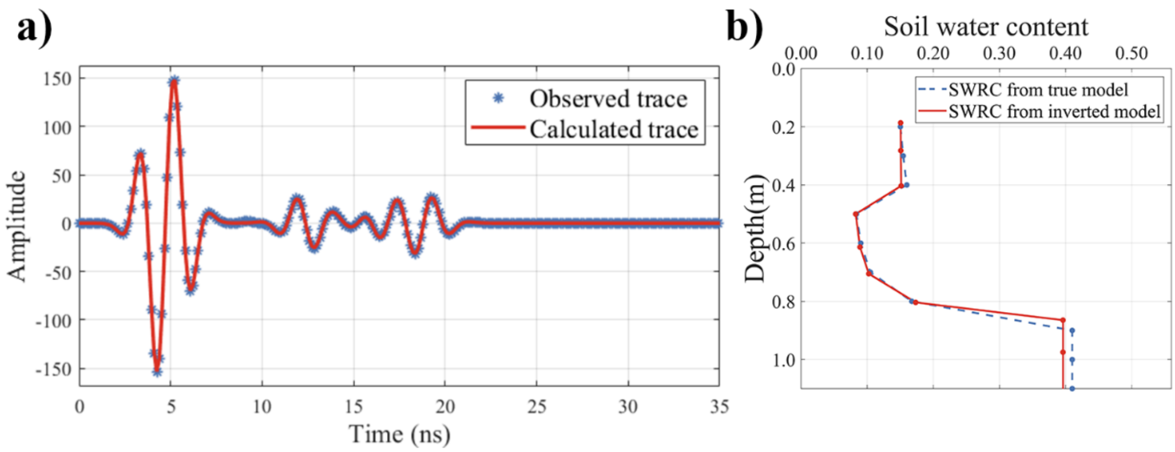

Figure 4.15 The inversion results of synthetic data without noise based on model C. a) The observed trace (blue star dotted line) calculated based on theoretical model and calculated trace (red solid line) from inverted result. b) The SWRC from true SHP of model (blue dashed line) and SWRC from inverted SHP of model (red solid line).

4.4.2 Synthetic data with noise

We further conducted tests on synthetic GPR data with noise. We added 10% Gaussian white noise to the GPR waveform data for the three models. Tables 4.5, 4.6, and 4.7 provide the inverted SHP from the data with noise. Figs. 4.16a, 4.17a, and 4.18a present the matching between the calculated GPR waveform responses from the inversion results and the observed GPR trace calculated from the theoretical value of models, while Figs.4.16b, 4.17b, and 4.18b show the SWRC calculated based on the inverted SHP and the SWRC calculated from the theoretical value of models. From Figs. 4.16a, 4.17a, and 4.18a, it can be observed that despite the presence of noise, the calculated GPR waveform responses (red solid lines) based on the inversion results still match well with the observed GPR trace (blue star dotted lines) from the theoretical value of models. From Figs. 4.16b, 4.17b, and 4.18b, it can be seen that the SWRC (red solid lines) calculated based on the inverted SHP exhibit a very good match with the SWRC (blue dashed lines) calculated based on the theoretical value of models. Although there are some differences between the SWRC calculated based on the inverted SHP and those calculated based on the theoretical value of models, overall, as indicated by the results in Tables 4.5, 4.6, and 4.7, the SHP can still be effectively inverted.

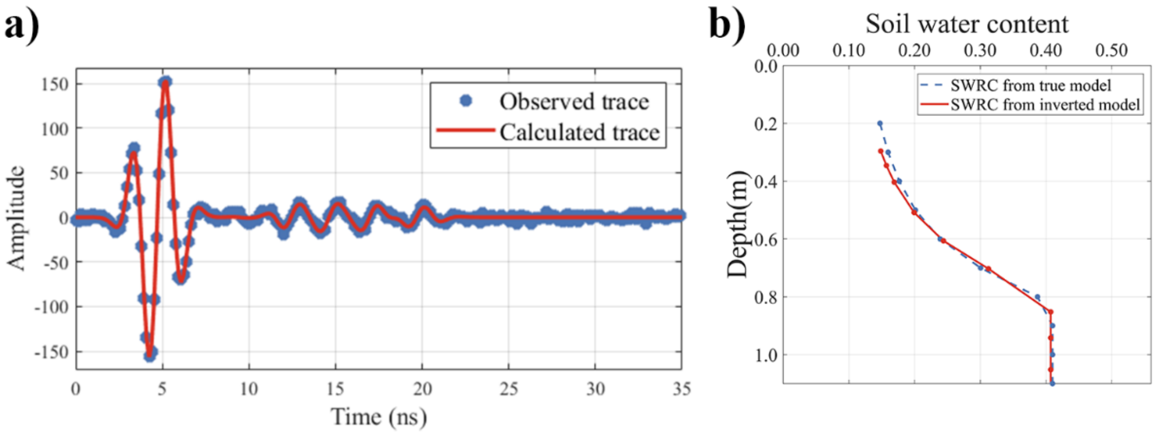

Figure 4.16 The inversion results of synthetic data with noise based on model A. a) The observed trace (blue star dotted line) calculated based on theoretical model and calculated trace (red solid line) from inverted result. b) The SWRC from true SHP of model (blue dashed line) and SWRC from inverted SHP of model (red solid line).

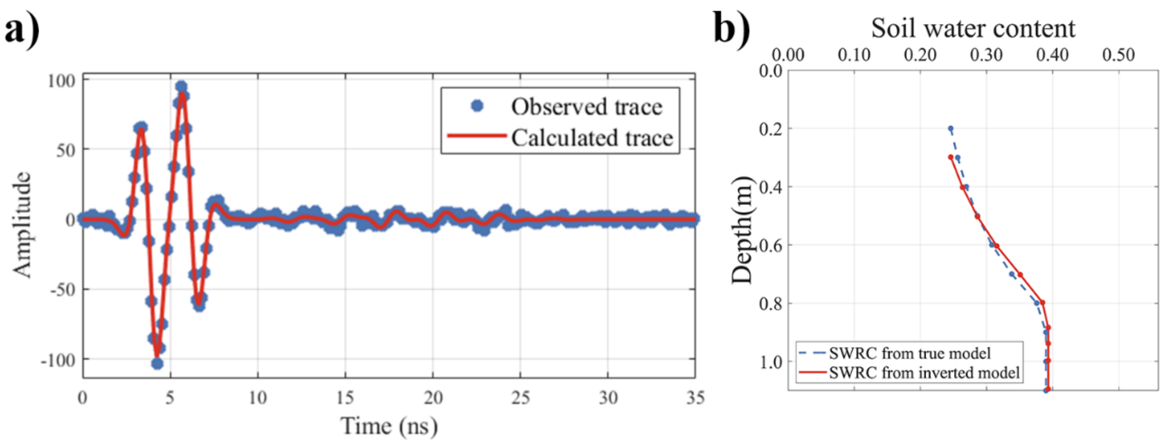

Figure 4.17 The inversion results of synthetic data with noise based on model B. a) The observed trace (blue star dotted line) calculated based on theoretical model and calculated trace (red solid line) from inverted result. b) The SWRC from true SHP of model (blue dashed line) and SWRC from inverted SHP of model (red solid line).

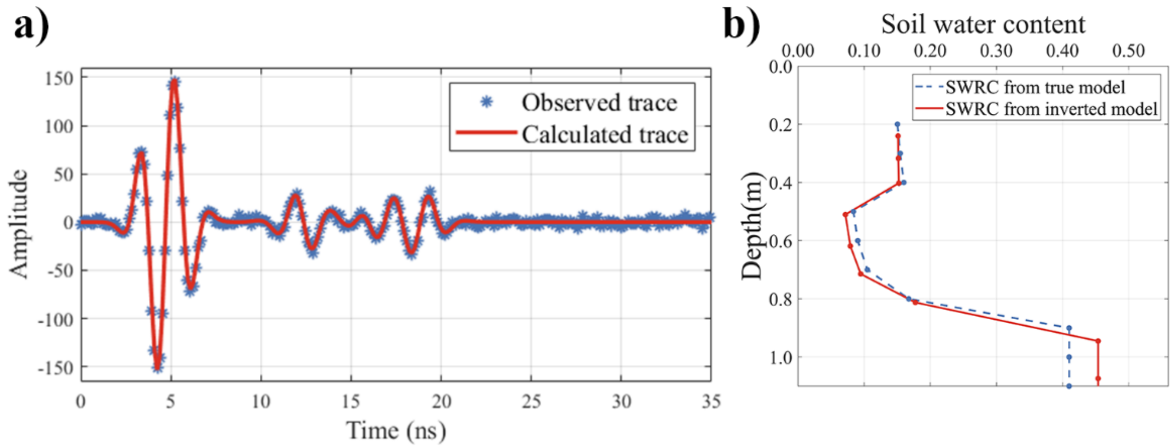

Figure 4.18 The inversion results of synthetic data with noise based on model C. a) The observed trace (blue star dotted line) calculated based on theoretical model and calculated trace (red solid line) from inverted result. b) The SWRC from true SHP of model (blue dashed line) and SWRC from inverted SHP of model (red solid line).

In order to study the convergence of the improved GWO algorithm, Fig. 4.19 shows the variation of fitness with the number of iterations for both noise-free and noisy data corresponding to Model C. From Figs. 4.19a and 4.19b, it can be observed that in the early iterations, the convergence curve still decreases rapidly. In the later stages, the convergence curve gradually stabilizes, indicating the algorithm entering the local search phase. For the convergence curve of noise-free data, it gradually stabilizes and tends to zero after approximately 500th iterations. For the noisy data, the convergence curve stabilizes and approximately converges to a fixed value after around 1000th iterations.

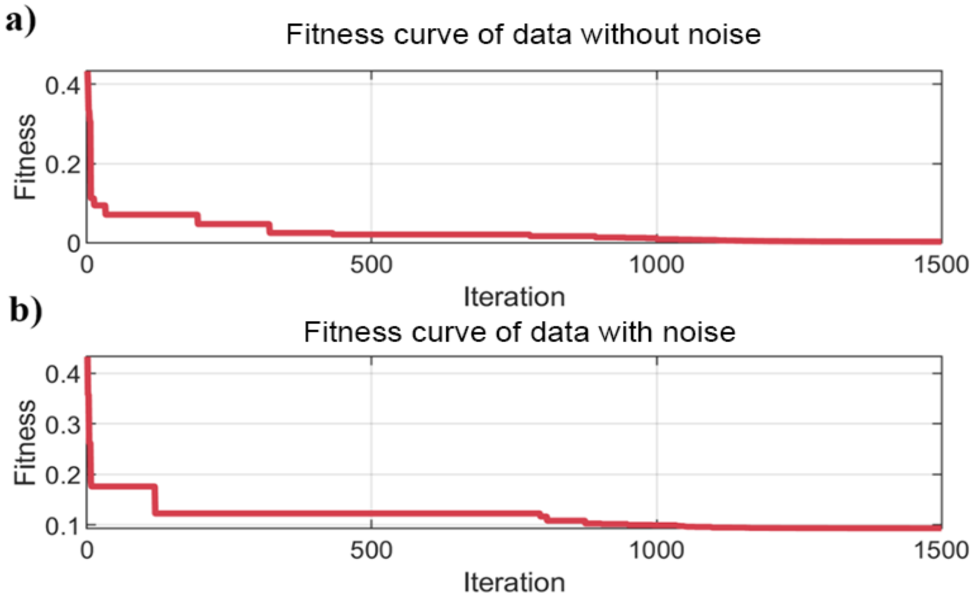

Figure 4.19 The comparison of fitness curve between data without noise and with noise based on model C. a) The fitness curve for data without noise. b) The fitness curve for data with noise.

We compared the traditional GWO and the improved GWO based on the results of Model C. Table 4.8 presents the inversion results by the traditional GWO and the improved GWO. It can be observed that although the accuracy of the inversion results of the improved GWO is lower than that of the traditional GWO in some individual values, overall, the inversion results of the improved GWO are closer to the theoretical SHP. Figs. 4.20 and 4.21 provide the comparison of the inversion results and convergence curves. From Figs. 4.20a and 4.20c, it can be seen that both the GPR waveform responses (red solid lines) calculated from the inversion results of the traditional GWO and the improved GWO match perfectly with the observed GPR trace (blue star dotted lines) calculated from the theoretical value of Model C. In Figs. 4.20b and 4.20d, the matching degree, between the SWRC (red dashed lines) calculated from the inversion results by the improved GWO and the SWRC from the theoretical value of models, is significantly better than that (red solid lines) obtained by the traditional GWO.

Furthermore, from the comparison of the convergence curves in Fig. 4.21, it can be seen that the convergence curve of the improved GWO approaches zero after 1000th iterations, while the convergence curve of the traditional approaches zero after approximately 1600th iterations. These results indicate that the improved GWO better conforms to the nonlinear search behavior of the grey wolves' population. The improved GWO enhances the accuracy of soil hydraulic parameter estimation and improves the inversion speed.

Table 4.8 In Model C, the SHP of theoretical model, the inversion results by traditional GWO, and the inversion results by improved GWO.

SHP	Theoretical SHP	Inversion results by traditional GWO	Inversion results by improved GWO
θ_s^1 (m^3/m^3)	0.390	0.265	0.321
θ_s^2 (m^3/m^3)	0.410	0.441	0.454
θ_r^1 (m^3/m^3)	0.100	0.149	0.148
θ_r^2 (m^3/m^3)	0.065	0.064	0.053
α^1(1/m)	5.900	3.222	5.721
α^2(1/m)	7.500	6.936	9.650
n^1	1.480	2.018	2.172
n^2	1.890	2.157	1.877

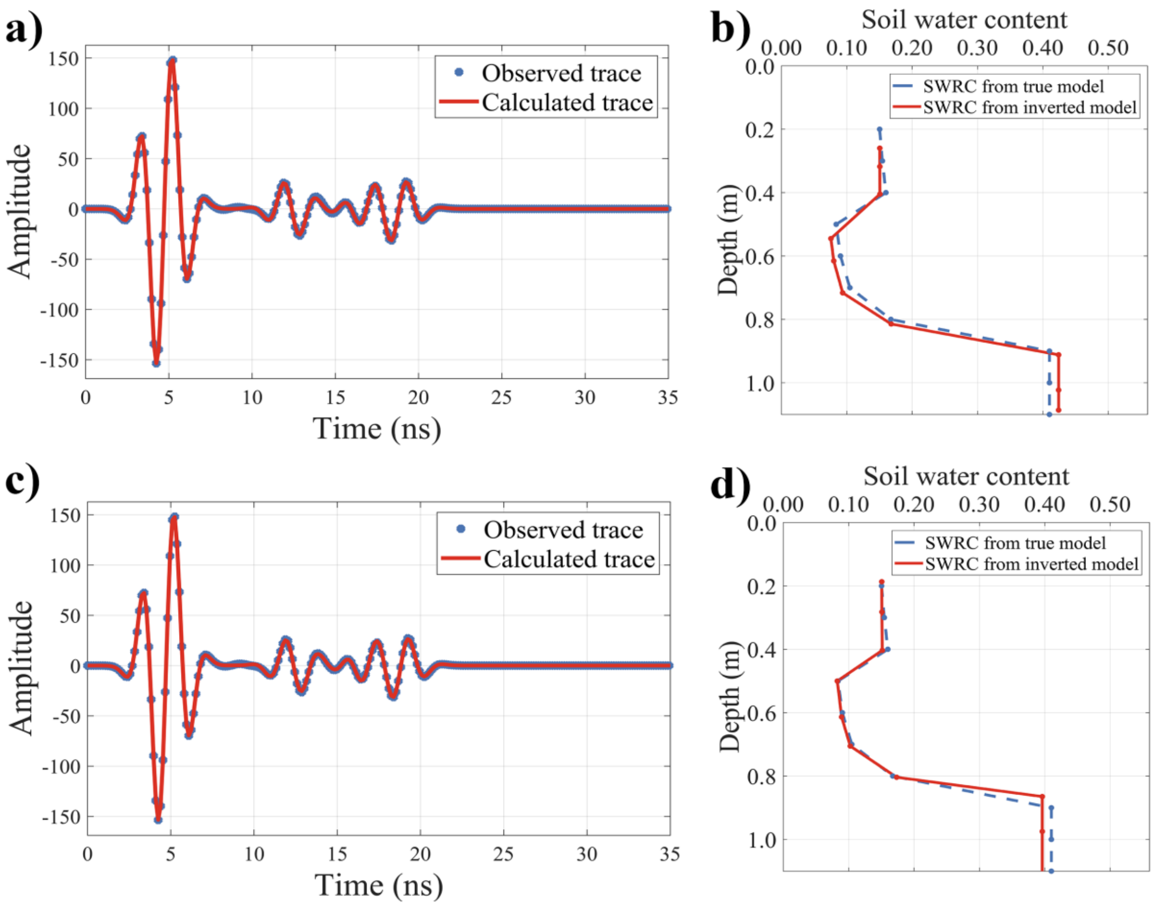

Figure 4.20 The comparison of inversion results between the traditional GWO and the improved GWO based on Model C. a) The calculated GPR response based on the inversion results of traditional GWO. b) The SWRC calculated based on inversion results of traditional GWO. c) The calculated GPR response based on the inversion results of improved GWO. d) The SWRC calculated based on inversion results of improved GWO.

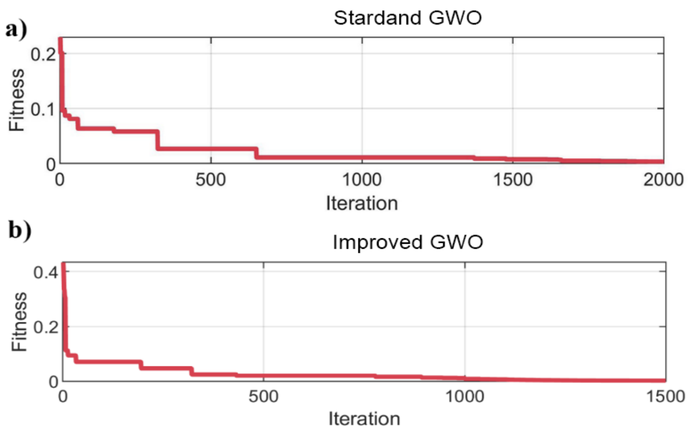

Figure 4.21 The comparison of fitness curve between the traditional GWO and the improved GWO. a) The fitness curve for traditional GWO. b) The fitness curve for the improved GWO.

4.5 Experimental field data inversion based on improved GWO

Similarly, we applied the improved GWO to optimize the inversion process based on the real GPR waveform data. In order to realize the comparison, the GPR waveform data is the same as that used in the optimization process with the traditional GWO, which is the 700th trace of the data profile. Table 4.9 presents the search space and the inverted results of the SHP.

Table 4.9 The search space for alternative solution and the inverted results of real data.

SHP	Search space	Inverted results
θ_s^1(m^3/m^3)	0.350-0.500	0.350
θ_s^2(m^3/m^3)	0.350-0.500	0.3816
θ_r^1(m^3/m^3)	0.010-0.100	0.013
θ_r^2(m^3/m^3)	0.010-0.100	0.022
α^1(1/m)	0.100-20.000	2.688
α^2(1/m)	0.100-20.000	4.498
n^1	1.000-10.000	2.940
n^2	1.000-10.000	6.017

Fig. 4.22a illustrates the fitting between the calculated GPR response from the inverted SHP and the observed GPR trace. Fig. 4.22b displays the SWRC calculated from the inverted SHP and the SWRC measured by the Sentek sensor. From Fig. 4.22a, it can be observed that the calculated GPR response (red solid line) still matches well with the observed GPR trace (blue star dotted line). As shown in Fig. 4.22b, the SWRC (red solid line) calculated from the inversion results still exhibits a similar trend to the SWRC (blue dashed line) measured by the Sentek sensor.

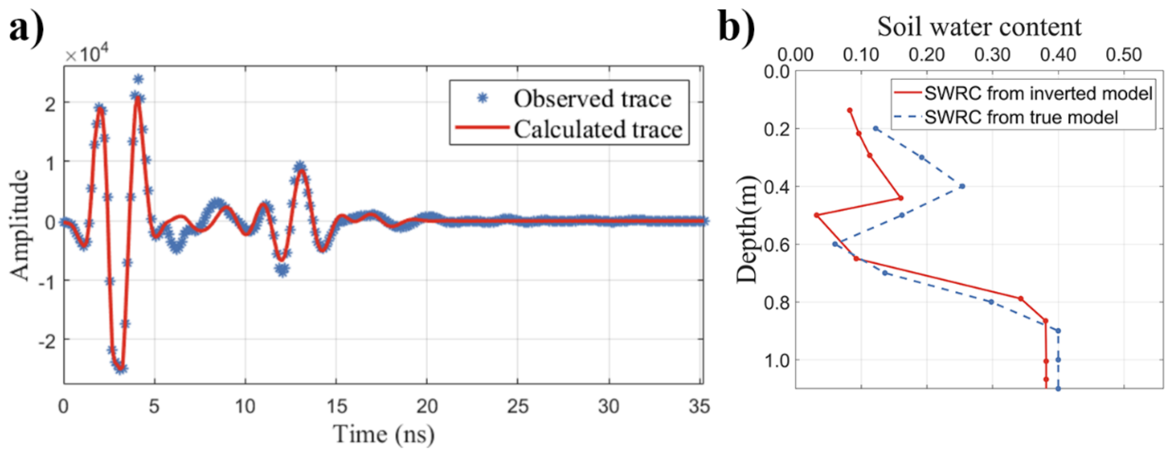

Figure 4.22 The inversion results based on improved GWO for experimental field data. a) The comparison between the observed trace (blue star dotted line) and calculated GPR response (red solid line) from inverted SHP. b) The comparison between the measured SWRC (blue dashed line) and SWRC (red solid line) from inverted SHP.

4.6 Conclusions

This chapter proposed a scheme for direct and high-precision estimation of SHP based on GPR waveform data, and further studied the estimation of SHP by using improved GWO to optimize GPR waveform inversion. First, this chapter introduced the basic theories and workflow involved in this study, including soil hydraulic models that link SHP and SWC, the construction of objective function, as well as the improvement of the GWO based on the sigmoid function. Then, three numerical experiments are designed based on HYDRUS-1D software. The underground structures of the first two experiments are uniform half-space models that only contain one kind of soil, and the third model combines the soils used in the first two models to design a two-layer underground structure with two kinds of soils distributed up and down. The standard GWO is first applied to these three numerical experiments to optimize the inversion process based on both noise-free and noisy GPR waveform data, and verified the effectiveness of direct determination of SHP. At the same time, in order to demonstrate the applicability of the proposed scheme, the scheme of directly estimating SHP by GPR waveform inversion optimized by the standard GWO is also applied to the real data collected from the SCERES experimental site. Afterwards, the improved GWO is applied to these three numerical experiments to optimize the inversion processes still based on both noise-free and noisy GPR waveform data, which verified the effectiveness of the improved scheme. Meanwhile, a comparison is made between the optimization of the standard GWO and the improved GWO. The results showed that the improved GWO improves the estimation accuracy of SHP in the optimization process while also enhancing the computational efficiency of the proposed scheme. Finally, the scheme of directly estimating SHP by GPR waveform inversion optimized by the improved GWO is also applied to the real data collected from the SCERES experimental site, which still demonstrated the effectiveness of the improved scheme.

Conclusions and perspectives

The GPR is highly sensitive to changes in SWC, making it a promising geophysical method for direct, non-destructive estimation and monitoring of soil hydrodynamics. However, most current researches using GPR to estimate SWC and SHP mainly utilizes partial information from GPR data, such as travel time information. In reality, changes in SWC not only affect the travel time of GPR data but also influence the amplitude and phase information. In traditional GPR inversion, a lot of studies have shown that inverting electrical parameters based on GPR waveform data is more accurate than inversion based on travel time data. Therefore, it is possible to improve the accuracy of direct, non-destructive estimation of SWC and SHP by fully utilizing the information in GPR data and performing inversion based on GPR waveform data.

The purpose of this thesis is to develop a technique for directly estimating SWC and SHP by using swarm intelligence GWO algorithm to optimize GPR waveform inversion. Additionally, to achieve high-precision monitoring of dynamic changes in SWC, a high-precision monitoring technique for SWC change based on time-lapse GPR waveform inversion was developed by incorporating the double-difference method. In this thesis, we also enhanced the computational efficiency and accuracy of determining SHP based on GPR waveform data by improving the standard GWO algorithm, providing a powerful tool for research in hydrology, agriculture, and soil science.

Based on the researches in this thesis, we have drawn the following conclusions:

1. Compared with most of the current researches which only use the partial information in the GPR data like travel time. By simultaneously utilizing the travel time, amplitude, and phase information in GPR data and constructing an objective function based on the entire GPR waveform data, the GWO algorithm was used for the first time to optimize the objective function for the estimation of SWC. This proposed approach improves the accuracy of SWC estimation and allows for the determination of SWC in deeper soil layers. Numerical experiments and applications on field data initially validated the effectiveness of the proposed scheme. Uncertainty analysis for the parameters inverted from numerical experiments and field data was also conducted to analyze the sensitivity of GPR data to the derived parameters. Furthermore, a comparison with the PSO algorithm demonstrated that the computational efficiency and accuracy of the GWO algorithm are superior to those of the PSO algorithm. Therefore, using the GWO algorithm for GPR waveform inversion to estimate SWC is both effective and applicable.

2. In order to fully understand the movement of water and solutes in soil, it is necessary to monitor the changes of SWC. This thesis designed two types of experiments: imbibition and drainage experiment, and infiltration experiment. The imbibition and drainage experiment aimed to simulate changes in SWC in the unsaturated zone during groundwater level fluctuations. The infiltration experiment aimed to simulate changes in SWC during surface water infiltration into the ground under rainfall conditions. In the imbibition and drainage experiment, GPR profiles were collected at different time points. From the processed GPR profiles at different time points, we preliminarily observed the influence of SWC changes on GPR signals. In the infiltration experiment, we preliminarily tracked the migration trajectory of the wetting front from the collected and processed GPR profile. To further quantify changes in SWC, the proposed scheme based on GPR waveform inversion for estimating SWC was applied to both types of measured data. The results indicated that the proposed scheme can quantitatively monitor the dynamic changes in SWC.

3. During the infiltration experiment, surface soil firstly reaches saturation due to the water infiltration from the surface, leading to a reduction in the amplitude of deeper waveforms, sometimes making them difficult to identify. This affects the accuracy of quantitative SWC monitoring. Therefore, this thesis proposed a high-precision monitoring technique for the SWC changes based on the double-difference time-lapse GPR waveform inversion. We demonstrated that the double-difference time-lapse GPR waveform inversion could achieve high-precision monitoring of SWC changes by applying the proposed technique to the infiltration experiment data.

4. Most current researches on estimating SHP using GPR mainly focuses on travel time information from GPR data. This thesis proposed a technology for directly estimating SHP based on GPR waveform inversion with GWO algorithm. A series of numerical experiments and applications on field data proved the effectiveness and applicability of the proposed scheme. By the proposed scheme, we can directly estimate the SHP from the entire GPR waveform data. In real condition, this will save times and be less invasive for soil, especially for high-dimensional measurement like 2D.

5. In the process of estimating SHP using GPR waveform inversion optimized by the GWO algorithm, it was found that the convergence factor controlling the optimization process of the standard GWO algorithm decreases linearly with increase in iterations. However,

according to the principles of GWO algorithm, the convergence curve should decrease rapidly in the early stage of iterations to ensure that the wolf group conducts a thorough global search. In the later stage of iterations, the convergence curve flattens and eventually converges to a fixed value to ensure that the wolf group can find the optimal solution. The entire process is a nonlinear search process, but using a linear convergence factor will reduce search efficiency and accuracy. This thesis improved the convergence factor of the GWO algorithm based on the Sigmoid function. The convergence factor will decrease non-linearly, which ensures sufficient global search in the early stage of iteration and searches the optimal solution in the later stage of iterations, thereby improving the efficiency and accuracy of the GWO algorithm. We compared the improved GWO algorithm with standard GWO algorithm, which demonstrates that the improved GWO algorithm is superior in both computational efficiency and accuracy.

Although it has a long history for studying the soil hydrodynamics based on GPR, the research in this area is still not sufficient. In this thesis, we proposed to use the entire GPR waveform data to estimate and monitor the SWC and determine the SHP. In real and future research, we can improve the estimation and monitoring accuracy of SWC, as well as the estimation accuracy of SHP. However, there remains significant space for further exploration. During our research, we also encountered several problems, and we could study in the future from the following aspects:

1. The SWC is not only unevenly distributed in the vertical space but also in the horizontal space. Therefore, in future research, it is necessary to consider the lateral heterogeneity of SWC to more accurately monitor changes in SWC and simulate the soil water movement. In addition, we only applied the proposed scheme on the unsaturated sandy soils. In the sandy soil, the water moves fast. However, in most of the real condition, it is difficult for the water to move in the soil. Therefore, we need to extend the proposed scheme to more kinds of soils and field data for validating the efficient of the proposed scheme.

2. In the process of forward modeling in our study, the calculations at each step are independent of each other. In the future, it is necessary to firstly construct a comprehensive forward modeling equation that directly derives GPR data from SWC and SHP, and then directly invert SWC and SHP. This inversion process will minimize the errors introduced by intermediate processes.

3. With the rapid development of deep learning, we can integrate deep learning algorithms to directly estimate SWC and SHP through GPR waveform inversion in the future.

Bibliographie

1. National Research Council. Basic Research Opportunities in Earth Science. **2001**, 168, doi:doi:10.17226/9981.
2. Chorover, J.; Kretzschmar, R.; Garcia-Pichel, F.; Sparks, D.L. Soil Biogeochemical Processes within the Critical Zone. *Elements* **2007**, *3*, 321-326, doi:10.2113/gselements.3.5.321.
3. Field, J.P.; Breshears, D.D.; Law, D.J.; Villegas, J.C.; López-Hoffman, L.; Brooks, P.D.; Chorover, J.; Barron-Gafford, G.A.; Gallery, R.E.; Litvak, M.E.; et al. Critical Zone Services: Expanding Context, Constraints, and Currency beyond Ecosystem Services. *Vadose Zone J.* **2015**, *14*, 1-7, doi:https://doi.org/10.2136/vzj2014.10.0142.
4. Xu, X.; Liu, W. The global distribution of Earth's critical zone and its controlling factors. *Geophysical Research Letters* **2017**, *44*, 3201-3208, doi:https://doi.org/10.1002/2017GL072760.
5. Ferraro, J.V.; Hoggarth, J.A.; Zori, D.; Binetti, K.M.; Stinchcomb, G. Integrating Human Activities, Archeology, and the Paleo-Critical Zone Paradigm. *Frontiers in Earth Science* **2018**, *6*, 1-4, doi:10.3389/feart.2018.00084.
6. 张甘霖; 朱永官; 邵明安. 地球关键带过程与水土资源可持续利用的机理. *中国科学: 地球科学* **2019**, *49*, 1945-1947, doi:https://doi.org/10.1360/SSTe-2019-0090.
7. 杨顺华; 宋效东; 吴华勇; 吴克宁; 张甘霖. 地球关键带研究评述：现状与展望. *土壤学报* **2024**, *61*, 308-318.
8. Oki, T.; Kanae, S. Global Hydrological Cycles and World Water Resources. *Science* **2006**, *313*, 1068-1072, doi:10.1126/science.1128845.
9. Gleick, P.H. Water and Conflict: Fresh Water Resources and International Security. *International Security* **1993**, *18*, 79-112, doi:10.1162/isec.18.1.79.
10. Vereecken, H.; Huisman, J.A.; Bogena, H.; Vanderborght, J.; Vrugt, J.A.; Hopmans, J.W. On the value of soil moisture measurements in vadose zone hydrology: A review. *Water Resour. Res.* **2008**, *44*, W00D06, doi:10.1029/2008WR006829.
11. Neuzil, C.E.; Cooley, C.; Silliman, S.E.; Bredehoeft, J.D.; Hsieh, P.A. A transient laboratory method for determining the hydraulic properties of 'tight' rocks—II. Application. *International Journal of Rock Mechanics and Mining Sciences & Geomechanics Abstracts* **1981**, *18*, 253-258, doi:https://doi.org/10.1016/0148-9062(81)90980-3.
12. Tamari, S.; Bruckler, L.; Halbertsma, J.; Chadoeuf, J. A Simple Method for Determining Soil Hydraulic Properties in the Laboratory. *Soil Science Society of America Journal* **1993**, *57*, 642-651, doi:https://doi.org/10.2136/sssaj1993.03615995005700030003x.
13. Chanasyk, D.S.; Naeth, M.A. Field measurement of soil moisture using neutron probes. *Canadian Journal of Soil Science* **1996**, *76*, 317-323, doi:10.4141/cjss96-038.
14. Robinson, D.A.; Campbell, C.S.; Hopmans, J.W.; Hornbuckle, B.K.; Jones, S.B.; Knight, R.; Ogden, F.; Selker, J.; Wendroth, O. Soil Moisture Measurement for Ecological and Hydrological Watershed-Scale Observatories: A Review. *Vadose Zone J.* **2008**, *7*, 358-389, doi:https://doi.org/10.2136/vzj2007.0143.
15. Klotzsche, A.; Jonard, F.; Looms, M.C.; van der Kruk, J.; Huisman, J.A. Measuring Soil Water Content with Ground Penetrating Radar: A Decade of Progress. *Vadose Zone J.* **2018**, *17*, 180052, doi:10.2136/vzj2018.03.0052.
16. Brosten, T.R.; Day-Lewis, F.D.; Schultz, G.M.; Curtis, G.P.; Lane, J.W. Inversion of multi-frequency electromagnetic induction data for 3D characterization of hydraulic conductivity. *Journal of Applied Geophysics* **2011**, *73*, 323-335, doi:https://doi.org/10.1016/j.jappgeo.2011.02.004.

17. Moghadas, D.; Jadoon, K.Z.; McCabe, M.F. Spatiotemporal monitoring of soil water content profiles in an irrigated field using probabilistic inversion of time-lapse EMI data. *Advances in Water Resources* **2017**, *110*, 238-248, doi:https://doi.org/10.1016/j.advwatres.2017.10.019.
18. Huisman, J.A.; Rings, J.; Vrugt, J.A.; Sorg, J.; Vereecken, H. Hydraulic properties of a model dike from coupled Bayesian and multi-criteria hydrogeophysical inversion. *J. Hydrol.* **2010**, *380*, 62-73, doi:https://doi.org/10.1016/j.jhydrol.2009.10.023.
19. Brunet, P.; Clément, R.; Bouvier, C. Monitoring soil water content and deficit using Electrical Resistivity Tomography (ERT) – A case study in the Cevennes area, France. *J. Hydrol.* **2010**, *380*, 146-153, doi:https://doi.org/10.1016/j.jhydrol.2009.10.032.
20. Mboh, C.M.; Huisman, J.A.; Van Gaelen, N.; Rings, J.; Vereecken, H. Coupled hydrogeophysical inversion of electrical resistances and inflow measurements for topsoil hydraulic properties under constant head infiltration. *Near Surface Geophysics* **2012**, *10*, 413-426, doi:https://doi.org/10.3997/1873-0604.2012009.
21. Manoli, G.; Rossi, M.; Pasetto, D.; Deiana, R.; Ferraris, S.; Cassiani, G.; Putti, M. An iterative particle filter approach for coupled hydro-geophysical inversion of a controlled infiltration experiment. *Journal of Computational Physics* **2015**, *283*, 37-51, doi:https://doi.org/10.1016/j.jcp.2014.11.035.
22. Hubbard, S.S.; Rubin, Y. Hydrogeological parameter estimation using geophysical data: a review of selected techniques. *Journal of Contaminant Hydrology* **2000**, *45*, 3-34, doi:https://doi.org/10.1016/S0169-7722(00)00117-0.
23. Pan, X.; Zhang, J.; Huang, P.; Roth, K. Estimating field-scale soil water dynamics at a heterogeneous site using multi-channel GPR. *Hydrol. Earth Syst. Sci.* **2012**, *16*, 4361-4372, doi:10.5194/hess-16-4361-2012.
24. Jaumann, S.; Roth, K. Soil hydraulic material properties and layered architecture from time-lapse GPR. *Hydrol. Earth Syst. Sci.* **2018**, *22*, 2551-2573, doi:10.5194/hess-22-2551-2018.
25. Yu, Y.; Weihermüller, L.; Klotzsche, A.; Lärm, L.; Vereecken, H.; Huisman, J.A. Sequential and coupled inversion of horizontal borehole ground penetrating radar data to estimate soil hydraulic properties at the field scale. *J. Hydrol.* **2021**, *596*, 126010, doi:https://doi.org/10.1016/j.jhydrol.2021.126010.
26. Bano, M. Modelling of GPR waves for lossy media obeying a complex power law of frequency for dielectric permittivity. *Geophysical Prospecting* **2004**, *52*, 11-26, doi:10.1046/j.1365-2478.2004.00397.x.
27. 冯晅; 曾昭发; 刘四新; 刘财; 梁文婧; 鹿琪. 探地雷达信号处理. **2014**.
28. Huisman, J.A.; Hubbard, S.S.; Redman, J.D.; Annan, A.P. Measuring Soil Water Content with Ground Penetrating Radar: A Review. *Vadose Zone J.* **2003**, *2*, 476-491, doi:10.2136/vzj2003.4760.
29. Zhang, M.; Feng, X.; Bano, M.; Xing, H.; Wang, T.; Liang, W.; Zhou, H.; Dong, Z.; An, Y.; Zhang, Y. Review of Ground Penetrating Radar Applications for Water Dynamics Studies in Unsaturated Zone. *Remote Sensing* **2022**, *14*, doi:10.3390/rs14235993.
30. Vellidis, G.; C. Smith, M.; L. Thomas, D.; E. Asmussen, L. Detecting wetting front movement in a sandy soil with ground-penetrating radar. *Transactions of the ASAE* **1990**, *33*, 1867-1874, doi:https://doi.org/10.13031/2013.31551.
31. Al, H.; Müller. GPR study of pore water content and salinity in sand. *Geophysical Prospecting* **2000**, *48*, 63-85, doi:https://doi.org/10.1046/j.1365-2478.2000.00180.x.
32. Birken, R.; Versteeg, R. Use of four-dimensional ground penetrating radar and advanced visualization methods to determine subsurface fluid migration. *Journal of*

Applied Geophysics **2000**, *43*, 215-226, doi:https://doi.org/10.1016/S0926-9851(99)00060-9.
33. Grote, K.; Hubbard, S.; Rubin, Y. GPR monitoring of volumetric water content in soils applied to highway construction and maintenance. *The Leading Edge* **2002**, *21*, 482-504, doi:10.1190/1.1481259.
34. Gish, T.J.; Dulaney, W.P.; Kung, K.J.S.; Daughtry, C.S.T.; Doolittle, J.A.; Miller, P.T. Evaluating Use of Ground-Penetrating Radar for Identifying Subsurface Flow Pathways. *Soil Science Society of America Journal* **2002**, *66*, 1620-1629, doi:https://doi.org/10.2136/sssaj2002.1620.
35. Schmalz, B.; Lennartz, B. Analyses of soil water content variations and GPR attribute distributions. *J. Hydrol.* **2002**, *267*, 217-226, doi:https://doi.org/10.1016/S0022-1694(02)00152-X.
36. Stoffregen, H.; Zenker, T.; Wessolek, G. Accuracy of soil water content measurements using ground penetrating radar: comparison of ground penetrating radar and lysimeter data. *J. Hydrol.* **2002**, *267*, 201-206, doi:https://doi.org/10.1016/S0022-1694(02)00150-6.
37. Loeffler, O.; Bano, M. Ground Penetrating Radar Measurements in a Controlled Vadose Zone: Influence of the Water Content. *Vadose Zone J.* **2004**, *3*, 1082-1092, doi:https://doi.org/10.2136/vzj2004.1082.
38. Makkawi, M.H. Integrating GPR and geostatistical techniques to map the spatial extent of a shallow groundwater system. *Journal of Geophysics and Engineering* **2004**, *1*, 56-62, doi:10.1088/1742-2132/1/1/007.
39. Wollschläger, U.; Roth, K. Estimation of Temporal Changes of Volumetric Soil Water Content from Ground-Penetrating Radar Reflections. *Subsurface Sensing Technologies and Applications* **2005**, *6*, 207-218, doi:10.1007/s11220-005-0007-y.
40. Lunt, I.A.; Hubbard, S.S.; Rubin, Y. Soil moisture content estimation using ground-penetrating radar reflection data. *J. Hydrol.* **2005**, *307*, 254-269, doi:10.1016/j.jhydrol.2004.10.014.
41. Turesson, A. Water content and porosity estimated from ground-penetrating radar and resistivity. *Journal of Applied Geophysics* **2006**, *58*, 99-111, doi:https://doi.org/10.1016/j.jappgeo.2005.04.004.
42. Saintenoy, A.; Schneider, S.; Tucholka, P. Evaluating Ground Penetrating Radar Use for Water Infiltration Monitoring. *Vadose Zone J.* **2008**, *7*, 208-214, doi:https://doi.org/10.2136/vzj2007.0132.
43. Irving, J.; Knight, R.; Holliger, K. Estimation of the lateral correlation structure of subsurface water content from surface-based ground-penetrating radar reflection images. *Water Resour. Res.* **2009**, *45*, doi:10.1029/2008WR007471.
44. Haarder, E.B.; Looms, M.C.; Jensen, K.H.; Nielsen, L. Visualizing Unsaturated Flow Phenomena Using High-Resolution Reflection Ground Penetrating Radar. *Vadose Zone J.* **2011**, *10*, 84-97, doi:https://doi.org/10.2136/vzj2009.0188.
45. Klenk, P.; Jaumann, S.; Roth, K. Quantitative high-resolution observations of soil water dynamics in a complicated architecture using time-lapse ground-penetrating radar. *Hydrol. Earth Syst. Sci.* **2015**, *19*, 1125-1139, doi:10.5194/hess-19-1125-2015.
46. Schmelzbach, C.; Tronicke, J.; Dietrich, P. High-resolution water content estimation from surface-based ground-penetrating radar reflection data by impedance inversion. *Water Resour. Res.* **2012**, *48*, W08505, doi:https://doi.org/10.1029/2012WR011955.
47. Guo, L.; Chen, J.; Lin, H. Subsurface lateral preferential flow network revealed by time-lapse ground-penetrating radar in a hillslope. *Water Resour. Res.* **2014**, *50*, 9127-9147, doi:https://doi.org/10.1002/2013WR014603.

48. Zhang, J.; Lin, H.; Doolittle, J. Soil layering and preferential flow impacts on seasonal changes of GPR signals in two contrasting soils. *Geoderma* **2014**, *213*, 560-569, doi:https://doi.org/10.1016/j.geoderma.2013.08.035.
49. Yu, Z.; Dylan, B.; Dryver, H.; Tian, X. Sand moisture assessment using instantaneous phase information in ground penetrating radar data. In Proceedings of the Proc. SPIE 9437, Structural Health Monitoring and Inspection of Advanced Materials, Aerospace, and Civil Infrastructure, 2015; p. 943726.
50. Shamir, O.; Goldshleger, N.; Basson, U.; Reshef, M. Mapping spatial moisture content of unsaturated agricultural soils with ground-penetrating radar. In Proceedings of the The International Archives of the Photogrammetry Remote Sensing and Spatial Information Sciences, 2016; pp. 1279-1285.
51. Shamir, O.; Goldshleger, N.; Basson, U.; Reshef, M. Laboratory Measurements of Subsurface Spatial Moisture Content by Ground-Penetrating Radar (GPR) Diffraction and Reflection Imaging of Agricultural Soils. *Remote Sensing* **2018**, *10*, 1667, doi:10.3390/rs10101667.
52. Ercoli, M.; Di Matteo, L.; Pauselli, C.; Mancinelli, P.; Frapiccini, S.; Talegalli, L.; Cannata, A. Integrated GPR and laboratory water content measures of sandy soils: From laboratory to field scale. *Construction and Building Materials* **2018**, *159*, 734-744, doi:10.1016/j.conbuildmat.2017.11.082.
53. Nyquist, J.E.; Toran, L.; Pitman, L.; Guo, L.; Lin, H. Testing the Fill-and-Spill Model of Subsurface Lateral Flow Using Ground-Penetrating Radar and Dye Tracing. *Vadose Zone J.* **2018**, *17*, 170142, doi:https://doi.org/10.2136/vzj2017.07.0142.
54. Di Prima, S.; Winiarski, T.; Angulo-Jaramillo, R.; Stewart, R.D.; Castellini, M.; Abou Najm, M.R.; Ventrella, D.; Pirastru, M.; Giadrossich, F.; Capello, G.; et al. Detecting infiltrated water and preferential flow pathways through time-lapse ground-penetrating radar surveys. *Science of The Total Environment* **2020**, *726*, 138511, doi:https://doi.org/10.1016/j.scitotenv.2020.138511.
55. Mangel, A.R.; Moysey, S.M.J.; Bradford, J. Reflection tomography of time-lapse GPR data for studying dynamic unsaturated flow phenomena. *Hydrol. Earth Syst. Sci.* **2020**, *24*, 159-167, doi:10.5194/hess-24-159-2020.
56. Zhang, M.H.; Bano, M.; Feng, X.; Lesparre, N.; Girard, J.F.; Razakarisoa, O.; Belfort, B.; Lehmann, F.; Friedmann, P. Estimating water content of unsaturated sandy soils by GPR during a drainage experiment. *IOP Conference Series: Earth and Environmental Science* **2021**, *660*, 012018, doi:10.1088/1755-1315/660/1/012018.
57. Zhang, M.; Bano, M.; Feng, X. Estimating Water Content of Unsaturated Sandy Soils by Ground-Penetrating Radar During an Infiltration Experiment. **2021**, *2021*, 1-5, doi:https://doi.org/10.3997/2214-4609.202120113.
58. van Overmeeren, R.A.; Sariowan, S.V.; Gehrels, J.C. Ground penetrating radar for determining volumetric soil water content; results of comparative measurements at two test sites. *J. Hydrol.* **1997**, *197*, 316-338, doi:https://doi.org/10.1016/S0022-1694(96)03244-1.
59. Huisman, J.A.; Snepvangers, J.J.J.C.; Bouten, W.; Heuvelink, G.B.M. Monitoring Temporal Development of Spatial Soil Water Content Variation: Comparison of Ground Penetrating Radar and Time Domain Reflectometry. *Vadose Zone J.* **2003**, *2*, 519-529, doi:10.2136/vzj2003.5190.
60. Galagedara, L.W.; Parkin, G.W.; Redman, J.D. Measuring and Modeling of Direct Ground Wave Depth Penetration Under Transient Soil Moisture Conditions. *Subsurface Sensing Technologies and Applications* **2005**, *6*, 193-205, doi:10.1007/s11220-005-0006-z.

61. Grote, K.; Hubbard, S.; Rubin, Y. Field-scale estimation of volumetric water content using ground-penetrating radar ground wave techniques. *Water Resour. Res.* **2003**, *39*, 1321, doi:https://doi.org/10.1029/2003WR002045.
62. Klenk, P.; Buchner, J.S.; Roth, K.; Wollschläger, U.; Qin, Y.; Zhou, K. On the reliability of current GPR ground wave methods for determining near-surface water contents. In Proceedings of the 6th International Workshop on Advanced Ground Penetrating Radar (IWAGPR), 22-24 June 2011, 2011; pp. 1-5.
63. Qin, Y.; Chen, X.; Zhou, K.; Klenk, P.; Roth, K.; Sun, L. Ground-penetrating radar for monitoring the distribution of near-surface soil water content in the Gurbantünggüt Desert. *Environmental Earth Sciences* **2013**, *70*, 2883-2893, doi:10.1007/s12665-013-2528-3.
64. Mahmoudzadeh Ardekani, M.R. Off- and on-ground GPR techniques for field-scale soil moisture mapping. *Geoderma* **2013**, *200-201*, 55-66, doi:https://doi.org/10.1016/j.geoderma.2013.02.010.
65. Thitimakorn, T.; Kummode, S.; Kupongsak, S. Determination of Spatial and Temporal Variations of Volumetric Soil Water Content Using Ground Penetrating Radar: A Case Study in Thailand. *Applied Environmental Research* **2016**, *38*, 33-46, doi:10.35762/AER.2016.38.2.4.
66. Pettinelli, E.; Vannaroni, G.; Di Pasquo, B.; Mattei, E.; Di Matteo, A.; De Santis, A.; Annan, P.A. Correlation between near-surface electromagnetic soil parameters and early-time GPR signals: An experimental study. *GEOPHYSICS* **2007**, *72*, A25-A28, doi:10.1190/1.2435171.
67. Pettinelli, E.; Di Matteo, A.; Beaubien, S.E.; Mattei, E.; Lauro, S.E.; Galli, A.; Vannaroni, G. A controlled experiment to investigate the correlation between early-time signal attributes of ground-coupled radar and soil dielectric properties. *Journal of Applied Geophysics* **2014**, *101*, 68-76, doi:10.1016/j.jappgeo.2013.11.012.
68. Ferrara, C.; Barone, P.M.; Steelman, C.M.; Pettinelli, E.; Endres, A.L. Monitoring Shallow Soil Water Content Under Natural Field Conditions Using the Early-Time GPR Signal Technique. *Vadose Zone J.* **2013**, *12*, 1-9, doi:https://doi.org/10.2136/vzj2012.0202.
69. Algeo, J.; Van Dam, R.L.; Slater, L. Early-Time GPR: A Method to Monitor Spatial Variations in Soil Water Content during Irrigation in Clay Soils. *Vadose Zone J.* **2016**, *15*, 1-9, doi:https://doi.org/10.2136/vzj2016.03.0026.
70. Benedetto, A. Water content evaluation in unsaturated soil using GPR signal analysis in the frequency domain. *Journal of Applied Geophysics* **2010**, *71*, 26-35, doi:https://doi.org/10.1016/j.jappgeo.2010.03.001.
71. Benedetto, A.; Benedetto, F. Remote Sensing of Soil Moisture Content by GPR Signal Processing in the Frequency Domain. *IEEE Sensors Journal* **2011**, *11*, 2432-2441, doi:10.1109/JSEN.2011.2119478.
72. Benedetto, A.; Tosti, F.; Ortuani, B.; Giudici, M.; Mele, M. Soil moisture mapping using GPR for pavement applications. In Proceedings of the 7th International Workshop on Advanced Ground Penetrating Radar, 2-5 July 2013, 2013; pp. 1-5.
73. Greaves, R.J.; Lesmes, D.P.; Lee, J.M.; Toksöz, M.N. Velocity variations and water content estimated from multi-offset, ground-penetrating radar. *GEOPHYSICS* **1996**, *61*, 683-695, doi:10.1190/1.1443996.
74. Weiler, K.W.; Steenhuis, T.S.; Boll, J.; Kung, K.J.S. Comparison of Ground Penetrating Radar and Time-Domain Reflectometry as Soil Water Sensors. *Soil Science Society of America Journal* **1998**, *62*, 1237-1239, doi:https://doi.org/10.2136/sssaj1998.03615995006200050013x.

75. Huisman, J.A.; Sperl, C.; Bouten, W.; Verstraten, J.M. Soil water content measurements at different scales: accuracy of time domain reflectometry and ground-penetrating radar. *J. Hydrol.* **2001**, *245*, 48-58, doi:10.1016/S0022-1694(01)00336-5.
76. Garambois, S.; Sénéchal, P.; Perroud, H. On the use of combined geophysical methods to assess water content and water conductivity of near-surface formations. *J. Hydrol.* **2002**, *259*, 32-48, doi:https://doi.org/10.1016/S0022-1694(01)00588-1.
77. Strobbia, C.; Cassiani, G. Multilayer ground-penetrating radar guided waves in shallow soil layers for estimating soil water content. *Geophysics* **2007**, *72*, J17-J29, doi:10.1190/1.2716374.
78. Bradford, J.H. Measuring Water Content Heterogeneity Using Multifold GPR with Reflection Tomography. *Vadose Zone J.* **2008**, *7*, 184-193, doi:10.2136/vzj2006.0160.
79. Gerhards, H.; Wollschläger, U.; Yu, Q.; Schiwek, P.; Pan, X.; Roth, K. Continuous and simultaneous measurement of reflector depth and average soil-water content with multichannel ground-penetrating radar. *GEOPHYSICS* **2008**, *73*, J15-J23, doi:10.1190/1.2943669.
80. Buchner, J.S.; Kühne, A.; Antz, B.; Roth, K.; Wollschläger, U. Observation of volumetric water content and reflector depth with multichannel ground-penetrating radar in an artificial sand volume. In Proceedings of the 6th International Workshop on Advanced Ground Penetrating Radar (IWAGPR), 22-24 June 2011, 2011; pp. 1-5.
81. Buchner, J.S.; Wollschläger, U.; Roth, K. Inverting surface GPR data using FDTD simulation and automatic detection of reflections to estimate subsurface water content and geometry. *GEOPHYSICS* **2012**, *77*, H45-H55, doi:10.1190/geo2011-0467.1.
82. Steelman, C.M.; Endres, A.L. Assessing vertical soil moisture dynamics using multi-frequency GPR common-midpoint soundings. *J. Hydrol.* **2012**, *436-437*, 51-66, doi:https://doi.org/10.1016/j.jhydrol.2012.02.041.
83. Steelman, C.M.; Endres, A.L.; Jones, J.P. High-resolution ground-penetrating radar monitoring of soil moisture dynamics: Field results, interpretation, and comparison with unsaturated flow model. *Water Resour. Res.* **2012**, *48*, doi:https://doi.org/10.1029/2011WR011414.
84. Mangel, A.R.; Moysey, S.M.J.; Ryan, J.C.; Tarbutton, J.A. Multi-offset ground-penetrating radar imaging of a lab-scale infiltration test. *Hydrol. Earth Syst. Sci.* **2012**, *16*, 4009-4022, doi:10.5194/hess-16-4009-2012.
85. Mangel, A.R.; Lytle, B.A.; Moysey, S.M.J. Automated high-resolution GPR data collection for monitoring dynamic hydrologic processes in two and three dimensions. *The Leading Edge* **2015**, *34*, 190-196, doi:10.1190/tle34020190.1.
86. Allroggen, N.; van Schaik, N.L.M.B.; Tronicke, J. 4D ground-penetrating radar during a plot scale dye tracer experiment. *Journal of Applied Geophysics* **2015**, *118*, 139-144, doi:10.1016/j.jappgeo.2015.04.016.
87. Iwasaki, T.; Kuroda, S.; Saito, H.; Tobe, Y.; Suzuki, K.; Fujimaki, H.; Inoue, M. Monitoring Infiltration Process Seamlessly Using Array Ground Penetrating Radar. *Agricultural & Environmental Letters* **2016**, *1*, 160002, doi:https://doi.org/10.2134/ael2016.01.0002.
88. Kaufmann, M.S.; Klotzsche, A.; Vereecken, H.; van der Kruk, J. Simultaneous multichannel multi-offset ground-penetrating radar measurements for soil characterization. *Vadose Zone J.* **2020**, *19*, e20017, doi:https://doi.org/10.1002/vzj2.20017.
89. Yu, Y.; Klotzsche, A.; Weihermüller, L.; Huisman, J.A.; Vanderborght, J.; Vereecken, H.; van der Kruk, J. Measuring vertical soil water content profiles by combining horizontal borehole and dispersive surface ground penetrating radar data. *Near Surface Geophysics* **2020**, *18*, 275-294, doi:10.1002/nsg.12099.

90. Saito, H.; Kuroda, S.; Iwasaki, T.; Sala, J.; Fujimaki, H. Estimating infiltration front depth using time-lapse multioffset gathers obtained from ground-penetrating-radar antenna array. *Geophysics* **2021**, *86*, WB51-WB59, doi:10.1190/geo2020-0590.1.
91. Huisman, J.A.; Snepvangers, J.J.J.C.; Bouten, W.; Heuvelink, G.B.M. Mapping spatial variation in surface soil water content: comparison of ground-penetrating radar and time domain reflectometry. *J. Hydrol.* **2002**, *269*, 194-207, doi:https://doi.org/10.1016/S0022-1694(02)00239-1.
92. Hubbard, S.; Grote, K.; Rubin, Y. Mapping the volumetric soil water content of a California vineyard using high-frequency GPR ground wave data. *The Leading Edge* **2002**, *21*, 552-559, doi:10.1190/1.1490641.
93. Grote, K.; Anger, C.; Kelly, B.; Hubbard, S.; Rubin, Y. Characterization of Soil Water Content Variability and Soil Texture using GPR Groundwave Techniques. *Journal of Environmental and Engineering Geophysics* **2010**, *15*, 93-110, doi:10.2113/JEEG15.3.93.
94. Galagedara, L.W.; Parkin, G.W.; Redman, J.D. An analysis of the ground-penetrating radar direct ground wave method for soil water content measurement. *Hydrological Processes* **2003**, *17*, 3615-3628, doi:https://doi.org/10.1002/hyp.1351.
95. Galagedara, L.W.; Redman, J.D.; Parkin, G.W.; Annan, A.P.; Endres, A.L. Numerical Modeling of GPR to Determine the Direct Ground Wave Sampling Depth. *Vadose Zone J.* **2005**, *4*, 1096-1106, doi:https://doi.org/10.2136/vzj2004.0143.
96. Weihermüller, L.; Huisman, J.A.; Lambot, S.; Herbst, M.; Vereecken, H. Mapping the spatial variation of soil water content at the field scale with different ground penetrating radar techniques. *J. Hydrol.* **2007**, *340*, 205-216, doi:https://doi.org/10.1016/j.jhydrol.2007.04.013.
97. Steelman, C.M.; Endres, A.L. An examination of direct ground wave soil moisture monitoring over an annual cycle of soil conditions. *Water Resour. Res.* **2010**, *46*, W11533, doi:10.1029/2009WR008815.
98. Cao, Q.; Song, X.; Wu, H.; Gao, L.; Liu, F.; Yang, S.; Zhang, G. Mapping the response of volumetric soil water content to an intense rainfall event at the field scale using GPR. *J. Hydrol.* **2020**, *583*, 124605, doi:10.1016/j.jhydrol.2020.124605.
99. Knoll, M.D.; Clement, W.P. Vertical Radar Profiling to Determine Dielectric Constant, Water Content and Porosity Values at Well Locations. In Proceedings of the 12th EEGS Symposium on the Application of Geophysics to Engineering and Environmental Problems, 1999.
100. Alumbaugh, D.; Paprocki, L.; Brainard, J.; Rautman, C. Monitoring Infiltration within the Vadose Zone Using Cross Borehole Ground Penetrating Radar. In Proceedings of the 13th EEGS Symposium on the Application of Geophysics to Engineering and Environmental Problems, 2000.
101. Parkin, G.; Redman, D.; von Bertoldi, P.; Zhang, Z. Measurement of soil water content below a wastewater trench using ground-penetrating radar. *Water Resour. Res.* **2000**, *36*, 2147-2154, doi:https://doi.org/10.1029/2000WR900129.
102. Binley, A.; Winship, P.; Middleton, R.; Pokar, M.; West, J. High-resolution characterization of vadose zone dynamics using cross-borehole radar. *Water Resour. Res.* **2001**, *37*, 2639-2652, doi:https://doi.org/10.1029/2000WR000089.
103. Binley, A.; Cassiani, G.; Middleton, R.; Winship, P. Vadose zone flow model parameterisation using cross-borehole radar and resistivity imaging. *J. Hydrol.* **2002**, *267*, 147-159, doi:10.1016/S0022-1694(02)00146-4.
104. Binley, A.; Winship, P.; West, L.J.; Pokar, M.; Middleton, R. Seasonal variation of moisture content in unsaturated sandstone inferred from borehole radar and resistivity

profiles. *J. Hydrol.* **2002**, *267*, 160-172, doi:https://doi.org/10.1016/S0022-1694(02)00147-6.
105. Galagedara, L.W.; Gary, W.P.; Redman, J.D.; Endres, A.L. Temporal and spatial variation of soil water content measured by borehole GPR under irrigation and drainage. In Proceedings of the 9th International Conference on Ground Penetrating Radar, 2002.
106. Galagedara, L.W.; Parkin, G.W.; Redman, J.D.; Endres, A.L. Assessment of Soil Moisture Content Measured by Borehole GPR and TDR Under Transient Irrigation and Drainage. *Journal of Environmental and Engineering Geophysics* **2003**, *8*, 77-86, doi:10.4133/JEEG8.2.77.
107. Rucker, D.F.; Ferré, T.P.A. Near-Surface Water Content Estimation with Borehole Ground Penetrating Radar Using Critically Refracted Waves. *Vadose Zone J.* **2003**, *2*, 247-252, doi:10.2136/vzj2003.2470.
108. Rucker, D.F.; Ferré, T.P.A. Correcting Water Content Measurement Errors Associated with Critically Refracted First Arrivals on Zero Offset Profiling Borehole Ground Penetrating Radar Profiles. *Vadose Zone J.* **2004**, *3*, 278-287, doi:https://doi.org/10.2136/vzj2004.2780.
109. Rucker, D.F.; Ferré, T.P.A. Automated water content reconstruction of zero-offset borehole ground penetrating radar data using simulated annealing. *J. Hydrol.* **2005**, *309*, 1-16, doi:https://doi.org/10.1016/j.jhydrol.2004.11.008.
110. Ferré, T.P.A.; von Glinski, G.; Ferré, L.A. Monitoring the Maximum Depth of Drainage in Response to Pumping Using Borehole Ground Penetrating Radar. *Vadose Zone J.* **2003**, *2*, 511-518, doi:https://doi.org/10.2136/vzj2003.5110.
111. Kowalsky, M.B.; Finsterle, S.; Rubin, Y. Estimating flow parameter distributions using ground-penetrating radar and hydrological measurements during transient flow in the vadose zone. *Advances in Water Resources* **2004**, *27*, 583-599, doi:https://doi.org/10.1016/j.advwatres.2004.03.003.
112. Looms, M.C.; Jensen, K.H.; Binley, A.; Nielsen, L. Monitoring Unsaturated Flow and Transport Using Cross-Borehole Geophysical Methods. *Vadose Zone J.* **2008**, *7*, 227-237, doi:10.2136/vzj2006.0129.
113. Kuroda, S.; Jang, H.; Kim, H.J. Time-lapse borehole radar monitoring of an infiltration experiment in the vadose zone. *Journal of Applied Geophysics* **2009**, *67*, 361-366, doi:https://doi.org/10.1016/j.jappgeo.2008.07.005.
114. Wijewardana, Y.G.N.S.; Galagedara, L.W. Estimation of spatio-temporal variability of soil water content in agricultural fields with ground penetrating radar. *J. Hydrol.* **2010**, *391*, 24-33, doi:10.1016/j.jhydrol.2010.06.036.
115. Haarder, E.B.; Binley, A.; Looms, M.C.; Doetsch, J.; Nielsen, L.; Jensen, K.H. Comparing Plume Characteristics Inferred from Cross-Borehole Geophysical Data. *Vadose Zone J.* **2012**, *11*, doi:https://doi.org/10.2136/vzj2012.0031.
116. Klotzsche, A.; Lärm, L.; Vanderborght, J.; Cai, G.; Morandage, S.; Zörner, M.; Vereecken, H.; van der Kruk, J. Monitoring Soil Water Content Using Time-Lapse Horizontal Borehole GPR Data at the Field-Plot Scale. *Vadose Zone J.* **2019**, *18*, 190044, doi:10.2136/vzj2019.05.0044.
117. Hubbard, S.S.; Peterson, J.E.; Majer, E.L.; Zawislanski, P.T.; Williams, K.H.; Roberts, J.; Wobber, F. Estimation of permeable pathways and water content using tomographic radar data. *The Leading Edge* **1997**, *16*, 1623-1630, doi:10.1190/1.1437539.
118. Eppstein, M.J.; Dougherty, D.E. Efficient three-dimensional data inversion: Soil characterization and moisture Monitoring from cross-well ground-penetrating radar at a Vermont Test Site. *Water Resour. Res.* **1998**, *34*, 1889-1900, doi:https://doi.org/10.1029/98WR00776.

119. Alumbaugh, D.; Chang, P.Y.; Paprocki, L.; Brainard, J.R.; Glass, R.J.; Rautman, C.A. Estimating moisture contents in the vadose zone using cross-borehole ground penetrating radar: A study of accuracy and repeatability. *Water Resour. Res.* **2002**, *38*, 1309.
120. Chang, P.-Y.; Alumbaugh, D.; Brainard, J.; Hall, L. The application of ground penetrating radar attenuation tomography in a vadose zone infiltration experiment. *Journal of Contaminant Hydrology* **2004**, *71*, 67-87, doi:https://doi.org/10.1016/j.jconhyd.2003.09.011.
121. Deiana, R.; Cassiani, G.; Kemna, A.; Villa, A.; Bruno, V.; Bagliani, A. An experiment of non-invasive characterization of the vadose zone via water injection and cross-hole time-lapse geophysical monitoring. *Near Surface Geophysics* **2007**, *5*, 183-194, doi:https://doi.org/10.3997/1873-0604.2006030.
122. Dafflon, B.; Irving, J.; Barrash, W. Inversion of multiple intersecting high-resolution crosshole GPR profiles for hydrological characterization at the Boise Hydrogeophysical Research Site. *Journal of Applied Geophysics* **2011**, *73*, 305-314, doi:https://doi.org/10.1016/j.jappgeo.2011.02.001.
123. Cassiani, G.; Strobbia, C.; Gallotti, L. Vertical Radar Profiles for the Characterization of Deep Vadose Zones. *Vadose Zone J.* **2004**, *3*, 1093-1105, doi:https://doi.org/10.2136/vzj2004.1093.
124. Strobach, E.; Harris, B.D.; Dupuis, J.C.; Kepic, A.W. Time-lapse borehole radar for monitoring rainfall infiltration through podosol horizons in a sandy vadose zone. *Water Resour. Res.* **2014**, *50*, 2140-2163, doi:10.1002/2013WR014331.
125. Chanzy, A.; Tarussov, A.; Bonn, F.; Judge, A. Soil Water Content Determination Using a Digital Ground-Penetrating Radar. *Soil Science Society of America Journal* **1996**, *60*, 1318-1326, doi:https://doi.org/10.2136/sssaj1996.03615995006000050005x.
126. Redman, J.D.; Davis, J.L.; Galagedara, L.W.; Gary, W.P. Field studies of GPR air launched surface reflectivity measurements of soil water content. In Proceedings of the 9th International Conference on Ground Penetrating Radar, 2002.
127. Redman, D.; Galagedara, L.; Parkin, G. Measuring Soil Water Content with the Ground Penetrating Radar Surface Reflectivity Method: Effects of Spatial Variability. In Proceedings of the 2003 ASAE Annual Meeting, St. Joseph, MI, 2003.
128. Serbin, G.; Or, D. Ground-penetrating radar measurement of soil water content dynamics using a suspended horn antenna. *IEEE Transactions on Geoscience and Remote Sensing* **2004**, *42*, 1695-1705, doi:10.1109/TGRS.2004.831693.
129. Serbin, G.; Or, D. Ground-penetrating radar measurement of crop and surface water content dynamics. *Remote Sensing of Environment* **2005**, *96*, 119-134, doi:https://doi.org/10.1016/j.rse.2005.01.018.
130. Lambot, S.; Rhebergen, J.; van den Bosch, I.; Slob, E.C.; Vanclooster, M. Measuring the Soil Water Content Profile of a Sandy Soil with an Off-Ground Monostatic Ground Penetrating Radar. *Vadose Zone J.* **2004**, *3*, 1063-1071, doi:10.2136/vzj2004.1063.
131. Lambot, S.; Weihermüller, L.; Huisman, J.A.; Vereecken, H.; Vanclooster, M.; Slob, E.C. Analysis of air-launched ground-penetrating radar techniques to measure the soil surface water content. *Water Resour. Res.* **2006**, *42*, doi:https://doi.org/10.1029/2006WR005097.
132. Lambot, S.; Slob, E.; Chavarro, D.; Lubczynski, M.; Vereecken, H. Measuring soil surface water content in irrigated areas of southern Tunisia using full-waveform inversion of proximal GPR data. *Near Surface Geophysics* **2008**, *6*, 403-410, doi:10.3997/1873-0604.2008028.
133. Jadoon, K.Z.; Lambot, S.; Scharnagl, B.; van der Kruk, J.; Slob, E.; Vereecken, H. Quantifying field-scale surface soil water content from proximal GPR signal inversion

in the time domain. *Near Surface Geophysics* **2010**, *8*, 483-491, doi:10.3997/1873-0604.2010036.
134. Minet, J.; Lambot, S.; Slob, E.C.; Vanclooster, M. Soil Surface Water Content Estimation by Full-Waveform GPR Signal Inversion in the Presence of Thin Layers. *IEEE Transactions on Geoscience and Remote Sensing* **2010**, *48*, 1138-1150, doi:10.1109/TGRS.2009.2031907.
135. Minet, J.; Bogaert, P.; Vanclooster, M.; Lambot, S. Validation of ground penetrating radar full-waveform inversion for field scale soil moisture mapping. *J. Hydrol.* **2012**, *424-425*, 112-123, doi:10.1016/j.jhydrol.2011.12.034.
136. Jonard, F.; Weihermuller, L.; Jadoon, K.Z.; Schwank, M.; Vereecken, H.; Lambot, S. Mapping Field-Scale Soil Moisture With L-Band Radiometer and Ground-Penetrating Radar Over Bare Soil. *IEEE Transactions on Geoscience and Remote Sensing* **2011**, *49*, 2863-2875, doi:10.1109/TGRS.2011.2114890.
137. Jonard, F.; Weihermüller, L.; Vereecken, H.; Lambot, S. Accounting for soil surface roughness in the inversion of ultrawideband off-ground GPR signal for soil moisture retrieval. *GEOPHYSICS* **2012**, *77*, H1-H7, doi:10.1190/geo2011-0054.1.
138. Jonard, F.; Mahmoudzadeh, M.; Roisin, C.; Weihermüller, L.; André, F.; Minet, J.; Vereecken, H.; Lambot, S. Characterization of tillage effects on the spatial variation of soil properties using ground-penetrating radar and electromagnetic induction. *Geoderma* **2013**, *207-208*, 310-322, doi:https://doi.org/10.1016/j.geoderma.2013.05.024.
139. Tran, A.P.; Ardekani, M.R.M.; Lambot, S. Coupling of dielectric mixing models with full-wave ground-penetrating radar signal inversion for sandy-soil-moisture estimation. *GEOPHYSICS* **2012**, *77*, H33-H44, doi:10.1190/geo2011-0100.1.
140. Tran, A.P.; Bogaert, P.; Wiaux, F.; Vanclooster, M.; Lambot, S. High-resolution space–time quantification of soil moisture along a hillslope using joint analysis of ground penetrating radar and frequency domain reflectometry data. *J. Hydrol.* **2015**, *523*, 252-261, doi:https://doi.org/10.1016/j.jhydrol.2015.01.065.
141. Moghadas, D.; Jadoon, K.Z.; Vanderborght, J.; Lambot, S.; Vereecken, H. Estimation of the near surface soil water content during evaporation using air-launched ground-penetrating radar. *Near Surface Geophysics* **2014**, *12*, 623-634, doi:https://doi.org/10.3997/1873-0604.2014017.
142. Greaves, R.J.; Lesmes, D.P.; Lee, J.M.; Toksoz, M.N. Velocity variations and water content estimated from multi-offset, ground-penetrating radar. *Geophysics* **1996**, *61*, 683-695, doi:10.1190/1.1443996.
143. van der Kruk, J.; Streich, R.; Green, A.G. Properties of surface waveguides derived from separate and joint inversion of dispersive TE and TM GPR data. *GEOPHYSICS* **2006**, *71*, K19-K29, doi:10.1190/1.2168011.
144. Lu, Q.; Liu, K.; Zeng, Z.; Liu, S.; Li, R.; Xia, L.; Guo, S.; Li, Z. Estimation of the Soil Water Content Using the Early Time Signal of Ground-Penetrating Radar in Heterogeneous Soil. *Remote Sensing* **2023**, *15*, doi:10.3390/rs15123026.
145. Lambot, S.; Slob, E.C.; Bosch, I.v.d.; Stockbroeckx, B.; Vanclooster, M. Modeling of ground-penetrating Radar for accurate characterization of subsurface electric properties. *IEEE Transactions on Geoscience and Remote Sensing* **2004**, *42*, 2555-2568, doi:10.1109/TGRS.2004.834800.
146. Lambot, S.; André, F. Full-Wave Modeling of Near-Field Radar Data for Planar Layered Media Reconstruction. *IEEE Transactions on Geoscience and Remote Sensing* **2014**, *52*, 2295-2303, doi:10.1109/TGRS.2013.2259243.

147. Wagner, B.J. Simultaneous parameter estimation and contaminant source characterization for coupled groundwater flow and contaminant transport modelling. *J. Hydrol.* **1992**, *135*, 275-303, doi:https://doi.org/10.1016/0022-1694(92)90092-A.
148. Vereecken, H.; Kasteel, R.; Vanderborght, J.; Harter, T. Upscaling Hydraulic Properties and Soil Water Flow Processes in Heterogeneous Soils: A Review. *Vadose Zone J.* **2007**, *6*, 1-28, doi:https://doi.org/10.2136/vzj2006.0055.
149. Hartmann, A.; Goldscheider, N.; Wagener, T.; Lange, J.; Weiler, M. Karst water resources in a changing world: Review of hydrological modeling approaches. *Rev. Geophys.* **2014**, *52*, 218-242, doi:https://doi.org/10.1002/2013RG000443.
150. Chen, J.; Hubbard, S.; Rubin, Y. Estimating the hydraulic conductivity at the south oyster site from geophysical tomographic data using Bayesian Techniques based on the normal linear regression model. *Water Resour. Res.* **2001**, *37*, 1603-1613, doi:https://doi.org/10.1029/2000WR900392.
151. Cui, F.; Bao, J.; Cao, Z.; Li, L.; Zheng, Q. Soil hydraulic parameters estimation using ground penetrating radar data via ensemble smoother with multiple data assimilation. *J. Hydrol.* **2020**, *583*, 124552, doi:https://doi.org/10.1016/j.jhydrol.2020.124552.
152. Scholer, M.; Irving, J.; Looms, M.C.; Nielsen, L.; Holliger, K. Bayesian Markov-Chain-Monte-Carlo Inversion of Time-Lapse Crosshole GPR Data to Characterize the Vadose Zone at the Arrenaes Site, Denmark. *Vadose Zone J.* **2012**, *11*, vzj2011.0153, doi:https://doi.org/10.2136/vzj2011.0153.
153. Busch, S.; Weihermüller, L.; Huisman, J.A.; Steelman, C.M.; Endres, A.L.; Vereecken, H.; van der Kruk, J. Coupled hydrogeophysical inversion of time-lapse surface GPR data to estimate hydraulic properties of a layered subsurface. *Water Resour. Res.* **2013**, *49*, 8480-8494, doi:https://doi.org/10.1002/2013WR013992.
154. Bradford, J.; Thoma, M.; Barrash, W. Estimating hydrologic parameters from water table dynamics using coupled hydrologic and ground-penetrating radar inversion. In Proceedings of the 15th International Conference on Ground Penetrating Radar, 30 June-4 July 2014, 2014.
155. Léger, E.; Saintenoy, A.; Tucholka, P.; Coquet, Y. Hydrodynamic Parameters of a Sandy Soil Determined by Ground-Penetrating Radar Monitoring of Porchet Infiltrations. *IEEE Journal of Selected Topics in Applied Earth Observations and Remote Sensing* **2016**, *9*, 188-200, doi:10.1109/JSTARS.2015.2464231.
156. Léger, E.; Saintenoy, A.; Coquet, Y.; Tucholka, P.; Zeyen, H. Evaluating hydrodynamic parameters accounting for water retention hysteresis in a large sand column using surface GPR. *Journal of Applied Geophysics* **2020**, *182*, 104176, doi:https://doi.org/10.1016/j.jappgeo.2020.104176.
157. Léger, E.; Saintenoy, A.; Coquet, Y. Hydrodynamic parameters of a sandy soil determined by ground-penetrating radar inside a single ring infiltrometer. *Water Resour. Res.* **2014**, *50*, 5459-5474, doi:https://doi.org/10.1002/2013WR014226.
158. Moua, R.; Lesparre, N.; Girard, J.F.; Belfort, B.; Lehmann, F.; Younes, A. Coupled hydrogeophysical inversion of an artificial infiltration experiment monitored with ground-penetrating radar: synthetic demonstration. *Hydrol. Earth Syst. Sci.* **2023**, *27*, 4317-4334, doi:10.5194/hess-27-4317-2023.
159. Lambot, S.; Slob, E.C.; Vanclooster, M.; Vereecken, H. Closed loop GPR data inversion for soil hydraulic and electric property determination. *Geophysical Research Letters* **2006**, *33*, doi:https://doi.org/10.1029/2006GL027906.
160. Jadoon, K.Z.; Slob, E.; Vanclooster, M.; Vereecken, H.; Lambot, S. Uniqueness and stability analysis of hydrogeophysical inversion for time-lapse ground-penetrating radar estimates of shallow soil hydraulic properties. *Water Resour. Res.* **2008**, *44*, doi:https://doi.org/10.1029/2007WR006639.

161. Lambot, S.; Slob, E.; Rhebergen, J.; Lopera, O.; Jadoon, K.Z.; Vereecken, H. Remote Estimation of the Hydraulic Properties of a Sand Using Full-Waveform Integrated Hydrogeophysical Inversion of Time-Lapse, Off-Ground GPR Data. *Vadose Zone J.* **2009**, *8*, 743-754, doi:10.2136/vzj2008.0058.
162. Jadoon, K.Z.; Weihermüller, L.; Scharnagl, B.; Kowalsky, M.B.; Bechtold, M.; Hubbard, S.S.; Vereecken, H.; Lambot, S. Estimation of Soil Hydraulic Parameters in the Field by Integrated Hydrogeophysical Inversion of Time-Lapse Ground-Penetrating Radar Data. *Vadose Zone J.* **2012**, *11*, vzj2011.0177, doi:https://doi.org/10.2136/vzj2011.0177.
163. Jonard, F.; Weihermüller, L.; Schwank, M.; Jadoon, K.Z.; Vereecken, H.; Lambot, S. Estimation of Hydraulic Properties of a Sandy Soil Using Ground-Based Active and Passive Microwave Remote Sensing. *IEEE Transactions on Geoscience and Remote Sensing* **2015**, *53*, 3095-3109, doi:10.1109/TGRS.2014.2368831.
164. Tran, A.P.; Vanclooster, M.; Zupanski, M.; Lambot, S. Joint estimation of soil moisture profile and hydraulic parameters by ground-penetrating radar data assimilation with maximum likelihood ensemble filter. *Water Resour. Res.* **2014**, *50*, 3131-3146, doi:https://doi.org/10.1002/2013WR014583.
165. Dagenbach, A.; Buchner, J.S.; Klenk, P.; Roth, K. Identifying a parameterisation of the soil water retention curve from on-ground GPR measurements. *Hydrol. Earth Syst. Sci.* **2013**, *17*, 611-618, doi:10.5194/hess-17-611-2013.
166. Yu, Y.; Huisman, J.A.; Klotzsche, A.; Vereecken, H.; Weihermüller, L. Coupled full-waveform inversion of horizontal borehole ground penetrating radar data to estimate soil hydraulic parameters: A synthetic study. *J. Hydrol.* **2022**, *610*, 127817, doi:https://doi.org/10.1016/j.jhydrol.2022.127817.
167. Topp, G.C.; Davis, J.L.; Annan, A.P. Electromagnetic determination of soil water content: Measurements in coaxial transmission lines. *Water Resour. Res.* **1980**, *16*, 574-582, doi:https://doi.org/10.1029/WR016i003p00574.
168. Loeffler, O. Modélisation géoradar de la proche surface : estimation de la teneur en eau et influence d'un polluant. 2005.
169. Hadamard, J.S. Sur les problemes aux derive espartielles et leur signification physique.
170. Jackson, D.D. The use of a priori data to resolve non-uniqueness in linear inversion. *Geophysical Journal International* **1979**, *57*, 137-157, doi:10.1111/j.1365-246X.1979.tb03777.x.
171. Hansen, P.C. *Discrete Inverse Problems*; Society for Industrial and Applied Mathematics: Pennsylvania, 2010.
172. Sambridge, M. Geophysical inversion with a neighbourhood algorithm—II. Appraising the ensemble. *Geophysical Journal International* **1999**, *138*, 727-746, doi:10.1046/j.1365-246x.1999.00900.x.
173. Malcolm, S. Finding acceptable models in nonlinear inverse problems using a neighbourhood algorithm. *Inverse Problems* **2001**, *17*, 387, doi:10.1088/0266-5611/17/3/302.
174. 冯德山; 王珣; 杨军; 张彬; 李广场. 探地雷达数值模拟及全波形反演. **2021**.
175. Lavoué, F. 2D Full waveform inversion of ground penetrating radar data: Towards multiparameter imaging from surface data. University of Grenoble, Grenoble, 2014.
176. Mirjalili, S.; Mirjalili, S.M.; Lewis, A. Grey Wolf Optimizer. *Advances in Engineering Software* **2014**, *69*, 46-61, doi:10.1016/j.advengsoft.2013.12.007.
177. 晏福. 灰狼优化算法的改进研究. **2024**, doi:10.27060/d.cnki.ghbcu.2020.002331.

178. Muro, C.; Escobedo, R.; Spector, L.; Coppinger, R.P. Wolf-pack (Canis lupus) hunting strategies emerge from simple rules in computational simulations. *Behavioural Processes* **2011**, *88*, 192-197, doi:10.1016/j.beproc.2011.09.006.
179. Li, C.; Zhou, J.; Dias, D.; Gui, Y. A Kernel Extreme Learning Machine-Grey Wolf Optimizer (KELM-GWO) Model to Predict Uniaxial Compressive Strength of Rock. *Applied Sciences* **2022**, *12*, 8468, doi:10.3390/app12178468.
180. Jellali, S.; Muntzer, P.; Razakarisoa, O.; Schäfer, G. Large Scale Experiment on Transport of Trichloroethylene in a Controlled Aquifer. *Transp. Porous Media* **2001**, *44*, 145-163, doi:10.1023/A:1010652230922.
181. Kool, J.B.; Parker, J.C. Analysis of the inverse problem for transient unsaturated flow. *Water Resour. Res.* **1988**, *24*, 817-830, doi:https://doi.org/10.1029/WR024i006p00817.
182. Guillemoteau, J.; Bano, M.; Dujardin, J.-R. Influence of grain size, shape and compaction on georadar waves: examples of aeolian dunes. *Geophysical Journal International* **2012**, *190*, 1455-1463, doi:10.1111/j.1365-246X.2012.05577.x.
183. Waldhauser, F.; Ellsworth, W.L. A Double-Difference Earthquake Location Algorithm: Method and Application to the Northern Hayward Fault, California. *Bull. Seismol. Soc. Am.* **2000**, *90*, 1353-1368, doi:10.1785/0120000006.
184. Simunek, J.J.; Saito, H.; Sakai, M.; Van Genuchten, M. The HYDRUS-1D Software Package for Simulating the One-Dimensional Movement of Water, Heat, and Multiple Solutes in Variably-Saturated Media. **2008**, doi:https://www.pc-progress.com/Downloads/Pgm_hydrus1D/HYDRUS1D-4.17.pdf.

Résumé

La zone critique de la Terre (CZO) est une région perméable située près de la surface terrestre, qui fournit un soutien essentiel à la vie et aux activités humaines de production. L'étude de la zone critique de la Terre a été considérée comme l'un des sujets les plus captivants dans le domaine des sciences de la Terre par le Conseil national de recherche des États-Unis au 21ème siècle. Les ressources en eau douce disponibles pour la production quotidienne humaine et la vie ne représentent qu'environ 2,5 % du volume mondial d'eau, et 30 % de ces ressources en eau douce sont constituées par les eaux souterraines. Par conséquent, comprendre la distribution des eaux souterraines est crucial pour maintenir la survie et le développement humains.

La zone vadose, également connue sous le nom de zone non saturée, est la zone située entre la surface du sol et la nappe phréatique. C'est un canal critique pour l'échange entre l'eau de surface et les eaux souterraines. En tant que zone d'interaction la plus complexe et sensible au sein de la zone critique de la Terre, la zone vadose fournit un soutien essentiel aux espèces et aux activités humaines et influence considérablement l'environnement écologique. Il est donc important de simuler et de surveiller les changements spatiotemporels de l'eau du sol au sein de la zone vadose pour la protection écologique et le développement durable.

Le contenu en eau du sol (SWC) et les propriétés hydrauliques du sol (SHP) sont des facteurs importants pour décrire le transport de l'eau et des solutés dans la zone vadose. Les méthodes traditionnelles de laboratoire pour mesurer le SWC et le SHP sont non seulement laborieuses et consommatrices de ressources, mais aussi particulièrement problématiques lors de l'étude des sols non saturés profonds, où l'obtention d'échantillons est particulièrement difficile. D'autres méthodes, telles que la résonance temporelle du domaine (TDR) pour mesurer le SWC, nécessitent l'installation de capteurs dans le sol, ce qui peut être invasif pour le sol et limité en échelle, en plus d'être consommateur de main-d'œuvre et de ressources. Il est donc nécessaire de trouver des méthodes efficaces et non invasives, telles que des techniques géophysiques, pour estimer le SWC et le SHP dans la zone vadose. Parmi les diverses méthodes

géophysiques, le radar à pénétration de sol (GPR) se distingue par sa grande sensibilité aux changements d'eau du sol, ce qui en fait un outil prometteur pour estimer et surveiller le SWC.

Dans le premier chapitre de cette étude, nous examinons principalement les développements dans l'estimation et la surveillance du SWC, ainsi que les développements dans la détermination du SHP. Nous commençons par introduire les principes du GPR, y compris la théorie de base du GPR et les modes de mesure du GPR couramment utilisés pour l'estimation du SWC et du SHP. Ensuite, nous passons en revue les développements dans l'estimation et la surveillance du SWC à travers différents systèmes GPR et d'autres méthodes avancées, telles que la méthode d'Amplitude d'Enveloppe Moyenne (AEA) et la méthode de Déplacement de Fréquence. Enfin, nous résumons les développements dans la détermination du SHP basés sur différents types de données GPR. Cette revue peut fournir une compréhension complète de l'estimation et de la surveillance du SWC, ainsi que de la détermination du SHP. En même temps, cette revue offre également une inspiration pour notre recherche. Cependant, il est à noter que la plupart des études actuelles utilisant le GPR pour déterminer le SWC et le SHP se concentrent uniquement sur l'utilisation du temps de parcours ou des informations d'amplitude des données GPR. Dans la recherche pratique, il a été observé que le changement dans le SWC n'affecte pas seulement le temps de parcours des signaux GPR, mais influence également l'amplitude et la phase des données GPR. De plus, des études d'inversion ont montré que l'inversion basée sur les formes d'onde peut fournir des informations de paramètres plus précises par rapport aux inversions basées uniquement sur des données de temps de parcours. Par conséquent, il est nécessaire d'utiliser les données de forme d'onde GPR, qui incluent des informations sur le temps de parcours, l'amplitude et la phase, pour améliorer l'exactitude de l'estimation du SWC et du SHP. De plus, lors de la surveillance de l'infiltration par GPR, le sol de surface atteint d'abord la saturation, ce qui amplifie l'amplitude de l'onde directe dans les données GPR et diminue l'amplitude du signal provenant des couches plus profondes, rendant parfois leur identification difficile.

Pour répondre à ces problèmes, l'objectif global de cette thèse est d'explorer la faisabilité de caractériser la dynamique de l'eau du sol dans un sol sablonneux non saturé, en mettant particulièrement l'accent sur le développement d'un schéma pour estimer et surveiller le SWC et déterminer le SHP basé sur l'inversion des formes d'onde GPR en temps-laps. Cette étude a réalisé trois recherches principales, qui sont détaillées dans trois chapitres :

Dans le deuxième chapitre, nous proposons un schéma d'estimation du SWC novateur et efficace basé sur l'inversion des formes d'onde GPR avec l'algorithme GWO inspiré du comportement social des loups gris dans la nature. Cette approche utilise pleinement l'énorme quantité d'informations contenues dans les données GPR, facilitant ainsi une compréhension plus précise des niveaux de SWC en subsurface. Dans la section 2.1, nous introduisons d'abord les fondements théoriques du processus de recherche nécessaire pour estimer le SWC par GPR, y compris la relation pétrophysique et comment obtenir les signaux d'écho GPR à partir des équations de Maxwell et de l'équation des ondes électromagnétiques. Afin d'étudier l'impact du SWC sur les données GPR et d'évaluer et surveiller le SWC par le biais du GPR, une relation pétrophysique est requise pour convertir le SWC en propriétés électriques du sol. Dans cette étude, nous n'avons pas tenu compte de l'effet de la conductivité et nous nous sommes uniquement concentrés sur la permittivité diélectrique relative. Comparé à la conductivité, la permittivité diélectrique relative est plus sensible aux changements de SWC. Nous avons sélectionné l'équation de Topp pour relier le SWC volumétrique à la permittivité diélectrique relative du sol. Après avoir obtenu la permittivité diélectrique relative du sol, nous pouvions fournir le modèle de propriété électrique du milieu pour réaliser la modélisation directe GPR. Ensuite, nous avons introduit la théorie de l'inversion. En géophysique, le problème inverse consiste à inverser les modèles souterrains à partir des données observées. En construisant une fonction objective en combinant les données calculées et les données observées, les modèles finaux peuvent être obtenus en optimisant progressivement la fonction objective à l'aide d'un algorithme d'optimisation. Dans cette étude, le problème inverse se réfère au processus d'estimation du SWC à partir des données de forme d'onde GPR. Comme cette étude implique l'inversion simultanée de plusieurs types de paramètres, l'algorithme d'optimisation basé sur le gradient traditionnel nécessite une grande quantité de calcul et est affecté par les différences d'ordre de grandeur des paramètres, tandis que l'algorithme d'optimisation local a tendance à tomber dans les minima locaux. Par conséquent, cette étude utilise l'algorithme GWO d'intelligence collective globale pour éviter le besoin de calcul de gradient. Semblable à l'optimisation de swarm partiel (PSO), l'algorithme GWO est inspiré de la hiérarchie sociale stricte et du comportement de chasse du groupe de loups gris dans la nature. Enfin, l'ensemble du processus d'estimation du SWC est divisé en cinq étapes : ① Sélectionner les données observées dans le domaine temporel. ② Définir le modèle initial du SWC, du facteur de qualité et de l'épaisseur de la couche. Calculer les paramètres électriques correspondants sur la base des relations pétrophysique et obtenir les données de forme d'onde GPR pour le modèle théorique par le biais de la modélisation directe. ③ Construire la fonction objective sur la base des données observées et des données calculées dans le domaine temporel. ④ Optimiser la fonction objective par GWO et mettre à jour les paramètres du modèle initial pour rapprocher la fonction objective de la valeur minimale. ⑤ Produire le SWC final, le facteur de qualité et l'épaisseur de la couche lorsque les critères d'arrêt de l'itération sont satisfaits. Sinon, retourner à l'étape ② et continuer les mises à jour itératives. Dans la section 2.2, nous avons introduit le site expérimental SCERES, où la collecte de données sur le terrain a été réalisée dans cette étude. Ce site expérimental est spécifiquement conçu pour la recherche expérimentale hydrologique et est adapté à l'étude de la plupart des problèmes hydrologiques statiques et dynamiques. Dans la section 2.3, afin de tester la performance du schéma proposé, nous avons conçu deux types d'expériences numériques, comprenant six exemples numériques. Les trois premiers modèles sont des modèles simples à quatre couches utilisés pour tester les performances préliminaires du schéma proposé. Pour mieux approcher les variations de gradient dans le SWC, trois modèles à neuf couches ont été construits en utilisant le logiciel de modélisation hydrologique HYDRUS-1D, et le dernier modèle a été construit en utilisant les données de SWC mesurées par des capteurs Sentek sur le terrain expérimental. Nous avons d'abord testé le schéma proposé sur des données de forme d'onde GPR synthétiques sans bruit basées sur des modèles simples. Les résultats de toutes les six expériences numériques démontrent que le schéma proposé peut déterminer avec précision et sans destruction le SWC. De plus, une analyse d'incertitude des paramètres d'inversion a été réalisée. Pour vérifier davantage la supériorité du schéma proposé, nous avons comparé les résultats inversés du schéma proposé basé sur l'algorithme GWO avec les résultats inversés basés sur l'algorithme PSO. Nous avons également comparé les résultats obtenus à partir du schéma d'inversion SWC proposé basé sur les données de forme d'onde GPR avec les résultats basés sur les données de temps de parcours GPR. Dans la section 2.4, afin de valider davantage l'applicabilité du schéma proposé, nous l'avons appliqué aux données de forme d'onde GPR réelles collectées sur le site expérimental SCERES et avons effectué une estimation 1D et 2D du SWC. Nous avons également découvert que le SWC n'est pas seulement réparti de manière inégale verticalement mais aussi de manière hétérogène horizontalement. Dans les études futures, l'hétérogénéité de la distribution du SWC dans la direction horizontale est également un enjeu clé qui mérite une attention particulière. Cette recherche fournit une approche potentielle pour une détermination précise et non intrusive du SWC en utilisant l'inversion des données de forme d'onde GPR basée sur l'algorithme GWO.

Dans le troisième chapitre, nous avons effectué une surveillance de haute précision des changements dynamiques du SWC basée sur l'inversion des formes d'onde GPR en temps-laps à haute résolution. En combinant l'inversion en temps-laps utilisant la méthode de double différence avec le schéma technique proposé dans le deuxième chapitre, nous avons introduit une technique pour surveiller précisément les changements dynamiques du SWC basée sur l'inversion des formes d'onde GPR en temps-laps avec la méthode de double différence. Dans la section 3.1, nous avons d'abord introduit les théories de base de l'inversion en temps-laps. L'objectif de l'inversion en temps-laps est de caractériser les changements dynamiques du milieu dans la zone cible souterraine en décrivant les variations des paramètres à différents moments. Il existe trois stratégies d'inversion en temps-laps couramment utilisées : la stratégie d'inversion individuelle, la stratégie d'inversion continue et la stratégie d'inversion par double différence. Dans l'inversion individuelle en temps-laps, le même modèle initial est d'abord utilisé pour inverser indépendamment les paramètres basés sur les données de référence observées et les données de surveillance. Les résultats d'inversion des données de référence sont ensuite soustraits des résultats d'inversion des données de surveillance pour obtenir les changements de paramètres dans la zone cible. Lorsque les changements des données sont faibles entre différents moments, l'objectif de l'inversion est d'estimer plus précisément les changements de paramètres dans la zone cible tout en essayant d'éviter les artefacts en temps-laps en dehors de la zone cible. Par conséquent, il est judicieux d'utiliser les résultats d'inversion obtenus à partir du précédent moment temporel comme modèle initial pour l'inversion au moment temporel suivant. Cette inversion en temps-laps est appelée inversion continue en temps-laps. L'inversion en temps-laps par double différence peut être considérée comme une amélioration supplémentaire de la méthode d'inversion continue en temps-laps. La méthode utilise les données de modélisation directe des résultats d'inversion des données de référence au moment précédent, ainsi que les différences dans les données de surveillance collectées à deux moments consécutifs, pour construire les données de forme d'onde GPR pour l'inversion. Cette approche vise à minimiser les effets en dehors de la zone cible, à améliorer la précision de l'inversion des paramètres au sein de la zone cible et a une valeur significative pour analyser et surveiller les changements dynamiques du SWC. Ensuite, deux types d'expériences ont été conçues sur le site expérimental SCERES. Un type simule la distribution spatiale et les changements dynamiques dans le SWC pendant les variations dynamiques du niveau de la nappe phréatique, et l'autre simule la migration de l'eau et la distribution spatiale ainsi que les changements dynamiques dans le SWC lors de l'infiltration des précipitations depuis la surface. Dans la section 3.2, nous avons d'abord appliqué l'inversion individuelle en temps-laps aux données GPR mesurées pour surveiller les changements dynamiques dans le SWC lors des expériences d'imprégnation et de drainage. Nous avons d'abord sélectionné cinq points temporels distincts et analysé les changements dans le SWC et le mouvement du front humide dans le sol lors de l'expérience d'imprégnation. Grâce à l'analyse globale des profils GPR, il peut être observé que l'augmentation globale du SWC due à la montée du niveau d'eau affecte les signaux dans les profils GPR. Afin d'observer plus clairement, des traces individuelles ont été sélectionnées et analysées à partir de chaque radargramme au même endroit. À partir des traces individuelles, le temps d'arrivée de la réflexion de deux couches de sable se déplace vers des temps ultérieurs lorsque la nappe phréatique monte jusqu'à la limite de deux couches de sable. Lors des expériences de drainage, le mouvement du temps d'arrivée est plus clair. Ensuite, nous avons appliqué le schéma d'inversion proposé sur chaque trace lors des expériences d'imprégnation et de drainage. À partir des résultats d'inversion, nous pouvons observer le changement du SWC pendant les expériences d'imprégnation et de drainage. Les résultats montrent que la technique de surveillance du SWC proposée basée sur les données de forme d'onde GPR en temps-laps peut surveiller efficacement les changements du SWC à l'échelle du terrain. Dans la section 3.3, nous avons d'abord analysé le profil GPR collecté lors de l'expérience d'infiltration. Pour le profil GPR collecté, nous pouvons surveiller le mouvement du front humide. Ensuite, nous avons appliqué l'inversion individuelle en temps-laps aux données GPR mesurées lors des expériences d'infiltration. Cependant, nous avons constaté que pour l'expérience d'infiltration de précipitations, lorsque l'eau s'infiltre depuis la surface, cela renforce l'amplitude de l'onde directe du GPR, rendant difficile l'identification des signaux profonds. Par conséquent, nous avons introduit l'inversion en temps-laps par double différence. Les résultats montrent que l'inversion des formes d'onde GPR en temps-laps peut surveiller les changements dynamiques du SWC avec une grande précision, capturant la migration de l'eau en temps réel dans le sol. De plus, l'inversion en temps-laps par double différence peut surveiller les changements dynamiques du SWC plus précisément lors de l'infiltration des précipitations.

Dans le quatrième chapitre, nous avons étendu le schéma d'inversion proposé au deuxième chapitre et avons proposé un schéma d'inversion pour l'estimation directe et de haute précision des paramètres hydrauliques du sol (SHP) basé sur les données d'onde GPR. Cependant, au cours du processus d'inversion, nous avons constaté que le facteur de convergence du GWO standard est linéaire, ce qui ne correspond pas aux caractéristiques non linéaires du processus d'optimisation pour le GWO. Par conséquent, nous avons amélioré le GWO pour améliorer la précision d'évaluation de l'estimation des SHP. Dans la section 4.1, nous avons d'abord introduit les nouvelles théories de base et le flux de travail impliqués dans ce chapitre. Le nouveau contenu de cette section par rapport au chapitre 2 comprend les modèles hydrauliques du sol, la construction de la fonction objective, ainsi que l'amélioration du GWO basée sur la fonction sigmoïde. Pour estimer les paramètres hydrauliques du sol, nous devons d'abord appliquer un modèle pour relier les paramètres hydrauliques du sol à la teneur en eau du sol (SWC). Dans cette étude, nous avons utilisé le modèle de van Genuchten comme modèle hydraulique du sol pour décrire la relation entre le SWC et la tête de pression. Lorsque nous connaissons la profondeur de la nappe phréatique souterraine, nous pouvons transférer la tête de pression à la profondeur, ce qui nous permet d'obtenir la relation entre le SWC et la profondeur. En utilisant l'équation de Topp, nous pouvons obtenir la relation entre la profondeur et la permittivité diélectrique relative, qui est utilisée comme modèle pour la modélisation directe GPR. Lors de l'inversion pour estimer les paramètres hydrauliques du sol, une fonction objective est toujours nécessaire. En tant que fonction objective pour l'estimation du SWC, nous avons construit la fonction objective en utilisant la norme L2 entre les données simulées et les données observées, et un algorithme d'optimisation est appliqué pour mettre à jour itérativement le modèle initial en minimisant la fonction objective. Le schéma global est divisé en cinq étapes suivantes : ① Donner le SHP initial, le facteur de qualité et les épaisseurs de couche. ② Calculer la SWRC à travers le modèle hydraulique du sol. ③ Calculer la permittivité diélectrique relative à partir du SWC en utilisant la relation pétrophysique. ④ Obtenir les données d'onde GPR dans le domaine temporel par modélisation directe GPR. ⑤ Mettre à jour le modèle SWC initial par l'algorithme GWO pour rapprocher la fonction objective de la valeur minimale. Si le critère d'arrêt est satisfait, l'itération sera arrêtée et les paramètres finaux seront obtenus. Sinon, revenir à l'étape ② et continuer la mise à jour. Dans la section 4.2, nous avons conçu trois expériences numériques basées sur le logiciel HYDRUS-1D pour tester l'efficacité du schéma proposé. Les structures souterraines des deux premières expériences sont des modèles de demi-espace uniforme contenant uniquement un type de sol, et le troisième modèle combine les sols utilisés dans les deux premiers modèles pour concevoir une structure souterraine à deux couches avec deux types de sols répartis en haut et en bas. Le GWO standard est d'abord appliqué à ces trois expériences numériques pour optimiser le processus d'inversion basé sur des données d'onde GPR à la fois sans bruit et avec bruit. Pour tous les résultats des exemples numériques, les données GPR calculées peuvent correspondre assez bien aux données GPR observées, bien que du bruit existe dans les données GPR. De plus, toutes les courbes de rétention d'eau du sol (SWRC) calculées sur la base des SHP inversés s'ajustent bien aux SWRC calculées sur la base des SHP des modèles théoriques. Ces résultats ont vérifié l'efficacité de la détermination directe des SHP à partir des données d'onde GPR. En même temps, nous avons également examiné la convergence du schéma d'inversion proposé basé sur le troisième modèle. Ces résultats de convergence démontrent que le GWO montre un bon équilibre entre exploration globale et exploitation locale. L'algorithme GWO a également la capacité d'éviter un optimum local élevé et d'atteindre une convergence rapide simultanément. Dans la section 4.3, afin de démontrer l'applicabilité du schéma proposé, le schéma d'estimation directe des SHP par l'inversion d'onde GPR optimisé par le GWO standard est également appliqué aux données réelles collectées sur le site expérimental SCERES. Les résultats ont montré que les données GPR calculées à partir de la solution finale inversée correspondent raisonnablement bien aux données GPR observées, en particulier les amplitudes principales où la correspondance est assez élevée. Et la SWRC calculée à partir des SHP inversés présente une tendance similaire à la SWRC mesurée par les capteurs Sentek. Dans la section 4.4, le GWO amélioré est appliqué à ces trois expériences numériques pour optimiser les processus d'inversion encore basés sur des données d'onde GPR à la fois sans bruit et avec bruit, ce qui a vérifié l'efficacité du schéma d'inversion amélioré. Parallèlement, une comparaison est faite entre l'optimisation du GWO standard et celle du GWO amélioré. Les résultats ont montré que le GWO amélioré améliore la précision d'estimation des SHP dans le processus d'optimisation tout en augmentant l'efficacité computationnelle du schéma proposé. Dans la section 4.5, le schéma d'estimation directe des SHP par l'inversion d'onde GPR optimisé par le GWO amélioré est également appliqué aux données réelles collectées sur le site expérimental SCERES, ce qui a également démontré l'efficacité du schéma amélioré.

En résumé, ces résultats de recherche fournissent un soutien théorique et technique pour l'estimation de haute précision du SWC et des SHP utilisant des données d'onde GPR. Sur la base de ces recherches, nous avons tiré les conclusions suivantes :

1. Contrairement à la plupart des études actuelles qui s'appuient sur des données GPR partielles comme le temps de trajet ou l'amplitude, cette recherche utilise simultanément les informations sur le temps de trajet, l'amplitude et la phase. En construisant une fonction objective basée sur les données d'onde GPR complètes et en appliquant l'algorithme GWO pour l'optimisation, la précision de l'estimation du SWC est significativement améliorée. Cette méthode permet de déterminer le SWC dans des couches de sol plus profondes. Les expériences numériques et les applications sur le terrain valident l'efficacité de cette approche. Des analyses d'incertitude ont été menées pour examiner la sensibilité des données GPR aux paramètres dérivés, et des comparaisons avec l'algorithme PSO indiquent que l'algorithme GWO est supérieur tant en efficacité computationnelle qu'en précision.
2. Comprendre le mouvement de l'eau et des solutés dans le sol nécessite de surveiller les changements de SWC. La thèse a conçu deux expériences : l'imbibition et le drainage, et l'infiltration. La première simule les changements de SWC lors des fluctuations du niveau de la nappe phréatique, tandis que la seconde examine les changements de SWC lors de l'infiltration d'eau de surface. Les profils GPR collectés à différents moments ont révélé l'influence des changements de SWC sur les signaux GPR. Le schéma proposé pour l'estimation du SWC a été appliqué aux deux expériences, démontrant sa capacité à surveiller quantitativement les changements dynamiques du SWC.
3. Lors de l'expérience d'infiltration, la saturation du sol de surface due à l'infiltration d'eau peut réduire l'amplitude des ondes plus profondes, compliquant la surveillance quantitative du SWC. Pour remédier à cela, la thèse a introduit une technique de surveillance de haute

précision utilisant l'inversion des ondes GPR à double différence dans le temps, qui a montré son efficacité à surveiller les changements de SWC dans les données de l'expérience d'infiltration.

4. La plupart des recherches sur l'estimation des SHP à l'aide de GPR se concentrent sur le temps de trajet. Cette thèse présente une approche novatrice pour estimer directement les SHP par l'inversion des ondes GPR utilisant l'algorithme GWO. Les expériences numériques et les applications de données sur le terrain confirment l'efficacité de cette méthode, qui facilite l'estimation directe des SHP à partir de données d'onde GPR complètes, économisant du temps et étant moins invasive, en particulier dans des mesures à haute dimension comme 2D.

5. L'étude a révélé que le facteur de convergence dans l'algorithme GWO standard diminue de manière linéaire avec les itérations, ce qui entrave l'efficacité de la recherche. La thèse propose une amélioration basée sur la fonction sigmoïde, permettant une diminution non linéaire du facteur de convergence. Cet ajustement assure une recherche globale efficace lors des premières itérations et une recherche optimale de solutions par la suite, améliorant à la fois l'efficacité et la précision par rapport à l'algorithme GWO standard.

Malgré les avancées dans les études sur l'hydrodynamique du sol basée sur le GPR, des explorations supplémentaires sont nécessaires. Les recherches futures devraient prendre en compte les aspects suivants :

1. Le SWC est réparti de manière inégale à la fois verticalement et horizontalement. Les études futures devraient tenir compte de l'hétérogénéité latérale pour améliorer la surveillance du SWC et simuler le mouvement de l'eau dans le sol. Le schéma proposé devrait être validé à travers divers types de sols au-delà des sols sablonneux, où le mouvement de l'eau est rapide.

2. Les calculs de modélisation directe dans cette étude étaient indépendants. Les efforts futurs devraient se concentrer sur la construction d'une équation de modélisation directe complète qui lie directement les données GPR avec le SWC et le SHP, minimisant les erreurs provenant des processus intermédiaires.

3. L'intégration d'algorithmes d'apprentissage profond pourrait être explorée pour l'estimation directe du SWC et du SHP à travers l'inversion des ondes GPR, tirant parti des avancées dans les techniques d'apprentissage automatique.

Université de Strasbourg

Minghe ZHANG

Techniques for estimating hydraulic parameters of unsaturated soils based on GPR waveform data

Résumé

Le géoradar (GPR) est un outil prometteur pour estimer la teneur en eau du sol (TES) et les propriétés hydrauliques du sol (PHS). Cependant, la plupart des études actuelles utilisant le géoradar pour déterminer la TES et la PHS ne se concentrent que sur une partie des données, comme le temps de parcours. L'inversion basée sur la forme d'onde complète peut offrir des résultats plus précis.

Dans cette étude, nous avons d'abord développé un nouveau schéma d'estimation de la TES basé sur l'inversion de la forme d'onde du GPR avec l'algorithme d'optimisation globale Grey Wolf Optimizer (GWO), puis l'avons validé à l'aide de données synthétiques et expérimentales réelles de terrain.

Ensuite, nous avons appliqué ce schéma aux données GPR en temps réel pour surveiller la TES dans la zone vadose. Enfin, nous avons établi un schéma pour déterminer directement les PHS basé sur l'inversion de la forme d'onde GPR avec l'algorithme GWO testé avec des données synthétiques et réelles. Ces résultats de recherche apportent un soutien théorique et technique à l'estimation haute précision de la TES et des PHS par inversion de la forme d'onde du GPR.

Mots clés: Géoradar, la forme d'onde des données, inversion temporelle, teneur en eau du sol, propriétés hydrauliques du sol

Abstract

Ground Penetrating Radar (GPR) has become a promising tool for soil water content (SWC) and soil hydraulic properties (SHP) estimation. However, most current studies using GPR to determine SWC and SHP only focus on part of data like travel time. Inversion based on the full waveform can provide more accurate results. In this study, we first build a novel SWC estimation scheme based on GPR waveform inversion with the Grey Wolf Optimizer (GWO) global optimization algorithm and validated using synthetic and real experimental field data. Subsequently, we apply this proposed scheme to time-lapse GPR data and realized SWC monitoring in the vadose zone. Finally, we further establish a new scheme for directly determining SHP based on GPR waveform inversion with GWO algorithm and also tested with synthetic and real experimental data. These research findings offer theoretical and technical support for the high-precision estimation of SWC and SHP using GPR waveform inversion.

Keywords: Ground penetrating radar, waveform data, time-lapse inversion, soil water content, soil hydraulic properties